PRESSURE DROP AND FORCED CONVECTIVE HEAT TRANSFER IN HETEROGENEOUS POROUS MEDIA

A thesis submitted in partial fulfilment of the requirements for the degree of
Doctor of Philosophy

Abdulaziz Mosa Gheit

Supervisor: Dr Robert Woolley

Faculty of Engineering
Department of Mechanical Engineering

December 2020

Acknowledgements

Abstract

The primary object of this work is to investigate if it is possible to improve the flow and thermal performance of porous media by combining two different types of media. Aluminuin open cellular materials were combined with woven wire mesh screens and experiments were performed to investigate the pressure drop and thermal performance of the samples. The samples were tested as regenerators where the fluid is passed through the porous media to packed beds.

Thirty-six heterogeneous regenerators were constructed from square woven mesh screens, having mesh sizes 20, 30, 40 pores per inch and combined with six different types of metal foams. The aluminium foam samples were further subdivided on the pore shape: spherical and irregular. Each category consisted of three foam samples having different pore sizes (small pore (1-1.18 mm), medium (1.4-1.7 mm) and large (2-2.36 mm)). Two test rigs were developed to measure the hydraulic and thermal performance of the semi-homogeneous and heterogeneous matrix materials using dry air with velocity from 0.01 m/s to 6 m/s (Darcy permeability based Reynolds number ranged from 0.002 to 80). For the hydraulic performance, the pressure drop profiles against the air velocity were measured under steady-state conditions. Several flow regimes with the transition zone between them were identified. Hydraulic parameters such as permeability and the inertia and form drag coefficients in different flow regimes were determined. Thermal performance measurements were conducted using an unsteady-state technique (single-blow technique). To evaluate the thermal performance a single blow model was solved numerically to predict the number of the transfer unit of each matrix. Furthermore, two data reduction techniques (direct and maximum slope matching techniques) were adopted to predict the thermal characteristics of the tested samples. The hydrothermal performance of regenerator matrices was characterized in terms of volumetric Nusselt number and Reynolds numbers based on the Darcy permeability.

The results indicate that the hydrothermal performance of porous media strongly depends on the physical features of media (porosity and pore size). The results clearly showed that a decrease in either the pore size or porosity leads to enhancement of heat transfer but with the penalty of higher flow resistance. The comparison between the tested samples revealed that stacks of woven screens have

better hydrothermal performance than metallic foams. The hydraulic and thermal performance of the heterogeneous structures varies based on the proportions of materials employed in the structure. The existed semi-empirical available in the literature satisfactory describe the mass and heat transfer behaviour of flow across heterogeneous porous media made of foam slices and wire mesh screens. The 20Mesh stainless steel wire meshes sample tended to have the optimal performance as a regenerator when the weight of the samples is considered.

Contents

List of Figures

List of Tables

Nomenclature

A	Empirical constant in Ergun Equation (Dimensionless)
A_{cs}	The cross-section area of the solid matrix (m^2)
A_{cw}	The cross-section area of the solid matrix (m^2)
A_{cw}	The cross-section area of the solid matrix (m^2)
A_{SP}	Specific surface area (m^{-1})
A_{HT}	Heat transfer surface area (m^2)
A_{cf}	Voids cross-section area available for flow (m^2)
B	Empirical constant in Ergun Equation (Dimensionless)
b	Flow passage perimeter (length)
c_f	Specific heat capacity of fluid (J/Kg. ^{o}C)
c_s	Specific heat capacity of the solid matrix (J/Kg. ^{o}C)
D	Pipe diameter (m)
Di	Diffusion factor (Dimensionless)
D_w	Wire diameter (m)
d	Equivalent or effective particles diameter (m)
d_p	Pore diameter (m)
e	Wire mesh shape factor (Dimensionless)
F	Forchheimer coefficient or the inertial coefficient (Dimensionless)
f	Fanning friction factor (Dimensionless)
$f_{\sqrt{K}}$	Darcy permeability based Fanning friction factor (Dimensionless)
f_{r_h}	Hydraulic radius based Fanning friction factor (Dimensionless)
h	Heat transfer coefficient (W/ m^2. ^{o}C)
h_s	Volumetric heat transfer coefficient of the matrix (W/ m^3. ^{o}C)
K	Specific permeability (m^2)
K_D	Darcy permeability (m^2)
k_s	Thermal conductivity of the solid matrix (W/m. ^{o}C)
K_w	Thermal conductivity of wall (W/m. ^{o}C)
L	The thickness of the solid matrix (m)
Le	Entrance length (m)
M_m	Weight of the solid matrix (kg)

m_f	Fluid weight content within the solid matrix (Kg)
NTU_S	Number of transfer units of the solid matrix (Dimensionless)
$NTUw$	Number of transfer units of the sidewall (Dimensionless)
Nu	Nusselt number (Dimensionless)
P_t	Pitch size (m)
Re_p	Pore diameter based Reynolds number (Dimensionless)
Re_{r_h}	Hydraulic radius based Reynolds number (Dimensionless)
$Re_{\sqrt{K}}$	Darcy permeability based Reynolds number (Dimensionless)
R_{tc}	Ratio Heat capacities of the matrix to heat capacity of the side-wall (Dimensionless)
R_{NTU}	The ratio of the number of transfer units of the side-wall to the matrix (Dimensionless)
r_h	Hydraulic radius (m)
S	Shape factor (Dimensionless)
S_{max}	Maximum slope value (Dimensionless)
$T_f^\star$	Fluid temperature (°C)
$\partial T_f^\star$	Fluid temperature difference (°C)
T_f	Fluid temperature (Dimensionless)
T_{fin}	Inlet fluid temperature (Dimensionless)
T_{fout}	Outlet fluid temperature (Dimensionless)
$T_0^\star$	Initial system temperature (°C)
T_s	Dimensionless solid matrix temperature
$T_s^\star$	Solid matrix temperature (°C)
$T_{t=0}$	The temperature at zero time (Dimensionless)
t	Time (Dimensionless)
t_h	Time equals one on the predictive outlet temperature curve (Dimensionless)
t_{Cent}	Centroid coordinate under the curve (m³)
U	Superficial velocity (m/sec)
V_2	Series expansion function
V_m	The volume of the solid material (m³)
V_S	The volume of the solid matrix (m³)

X	Dimensionless distance (m)
x	Location of temperature at any time (m)
z	Flow passage perimeter for the sidewall (m)
ΔV	Volume difference (m^3)
Δx	Distance increment (Dimensionless)
Δt	Time increment (Dimensionless)
Δx	Distance increment (m)
Δp	The static pressure difference (Pa)
$\dfrac{-\Delta p}{L}$	Pressure gradient
$\Delta \theta_{20-80\%}$	Time difference of 20 – 80 % of outlet temperature curve (Dimensionless)
ΔH_f	Fluid enthalpy change (KJ/mol)
$\partial T_s^\star$	Dimensional temperature difference (Dimensionless)
∂x	Distance difference (m)

Greek symbols

ϵ	The porosity of the solid matrix (Dimensionless)
μ_f	Dynamic viscosity of the fluid (Pa.s)
ρ_f	Fluid density (Kg/m3)
ρ_m	The density of mother materials of the solid matrix (Kg/m3)
ρ_s	The density of the solid matrix (Kg/m3)
β	Form drag coefficient (m^{-1})
$\dot{m}$	Mass flow rate (Kg/sec)
τ_{sys}	System constant (sec^{-1})
τ_i	The measured time constant (sec)
τ	Inlet temperature time constant (Dimensionless)
λ_s	Dimensionless axial conduction parameter of the solid matrix (Dimensionless)
λ_w	Dimensionless axial conduction parameter of the sidewall (Dimensionless)
$\partial\theta$	The real-time difference (sec)

Abbreviations

S	Metal foam sample with a small pore size
L	Metal foam sample with a large pore size
M	Metal foam sample with a medium pore size
PPI	Number of pores per inch liner
$J\text{-}T$	The Joule-Thomson
I_n	Modified Bessel function of nth order
J_0	Bessel function of the first kind of zero-order

CHAPTER 1. Introduction

1.1 Background

Increasing energy costs, the depletion of fossil fuel reserves, and alarming natural signals relating to climate change have all led to the necessity of recovering industrial waste heat [1][2][3]. Waste heat is the thermal energy that is lost through industrial processes and then dumped into the environment. Most lost energy comes from combustion processes, parts, products and the equipment of process units [1].

Several technologies have been proposed to capture and recover the waste heat, while simultaneously raising process efficiencies and controlling environmental emissions [1][4]. One of the most applicable methods is to use thermal regenerators. Thermal regenerators are devices that can be used to transfer thermal energy (enthalpy) between two fluids. The regenerative matrix plays a central role in regenerator performance [5][6]. There are no specific rules for the selection of regenerative matrices. However, an ideal regenerative porous matrix should have large heat capacity; high surface area per unit volume (i.e. compact size); low-pressure drop; low effective thermal conductivity; and high-temperature durability; it should also be lightweight and adaptable to automated high volume production [7][8][9].

Cellular metals are commonly used to build efficient regenerators. The term metallic cellular material refers to any solid metal material containing free spaces, known as voids or pores. Metallic cellular materials are available in a variety of metals and cell geometries [10]. Cellular materials have bulk material properties, such as heat capacity, malleability and thermal/electrical conductivity, as well as porous material properties such as porosity and permeability. They offer unique properties, making them an excellent candidate for high thermal performance heat exchangers, particularly in small spaces [5][11][12][13].

Cellular metallic materials can be classified into two types, based on the configuration of cell structure: periodic cellular metal structures (PCMs) and stochastic structures [10][14][15]. The periodic cellular materials have almost regular topologies and can be subdivided into three main categories, depending on the access to their interior space: prismatic, shell, and truss [10]. Truss types are fabricated from wires

as sheets with fully open cells, almost identical in shape; woven wire mesh is one of the most common types of truss periodic cellular materials. In industrial applications, multiple layers of wire mesh are often stacked on top of each other randomly or at certain angles to obtain a packed bed [16][17][18][19]. Woven wire mesh falls into four groups, based on the arrangement of the warp and weft wires: plain weaves, twill weaves, fourdrinier weaves, and dutch weaves [20]. The plain wire woven sheets are made of bare identical wires called the warp and weft, with their physical properties. They pass alternately over each other, creating fully open cells [20]. Plain-woven meshes are further sub-divided into two classes: square shape wire mesh and diamond shape wire mesh. The square-shaped types are multi-functional materials and are common in the industry. A sketch of a square shape wire mesh screen is shown in Figure 1.1.
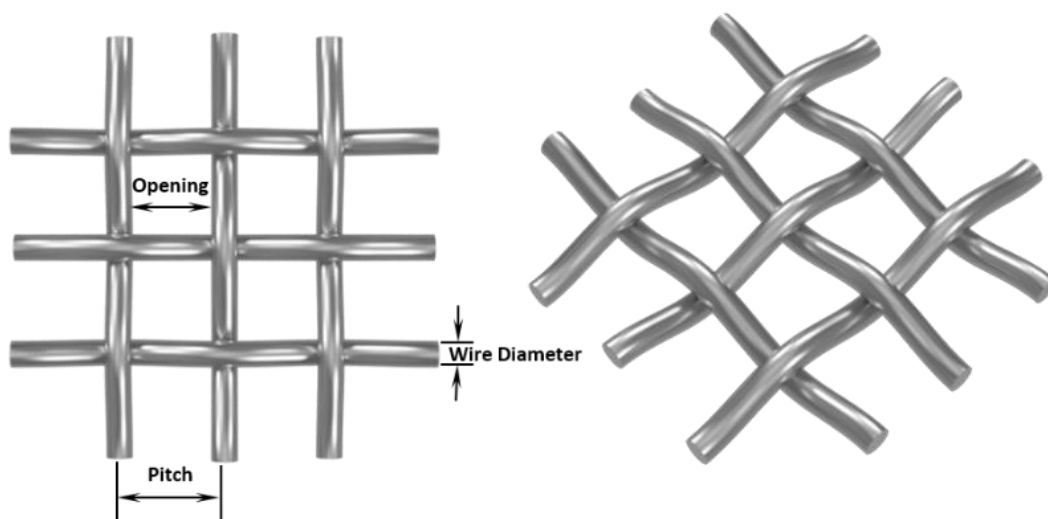
Figure 1.1 Schematic of a square-shaped wire mesh screen.

Fine stainless steel screens have a large pore density per unit of length, hence they are frequently cited as thermal energy absorbers [16][21][22]. One of their main advantages is that they are commercially available on a large scale at a low cost. They are often named according to their pore density per unit of length (the number of openings in one linear inch) [16][17][21][23][24]. Two measurements are required to define the wire mesh screen: wire diameter d_w and the mesh number (M). The wire diameter is the thickness of the wire before weaving, while the mesh number is defined as the number of openings per lineal inch (PPI). The properties of these materials can be controlled by varying mesh size [25][26], weave patterns [17], and wire diameter

[27][28], which allows several structures with a great diversity of porosities and heat transfer surface areas [13][18][21][29].

Advanced manufacturing technology has recently developed a stochastic cellular metal known as metal foam [30][31][31]. Metal foams can be modified to have a wide range of geometries with a variety of mechanical and thermal properties that suit many industrial fields. Until a few years ago, this type of cellular material was limited to aerospace and defence applications due to its high fabrication cost [32][33][34]. The development of manufacturing methods has resulted in an increase in the range of applications and a dramatic decrease in production costs [31][35]. Metal foams are now available in many solid phases, including aluminium, copper, nickel and metal alloys [32].

Similar to periodic structures, stochastic metal foams can be classified into two different types: open cell and closed cell foams. Open-cell foams have a random reticulated-like internal structure, containing thin ligaments, called struts, which are connected through the solid limb. Open-cell aluminium foams, as shown in Figure 1.2, belong to the cellular material family, which is likely to be found in heat exchange applications. This cellular material has recently been introduced as a possible candidate for regenerative heat exchangers [5][36][37].
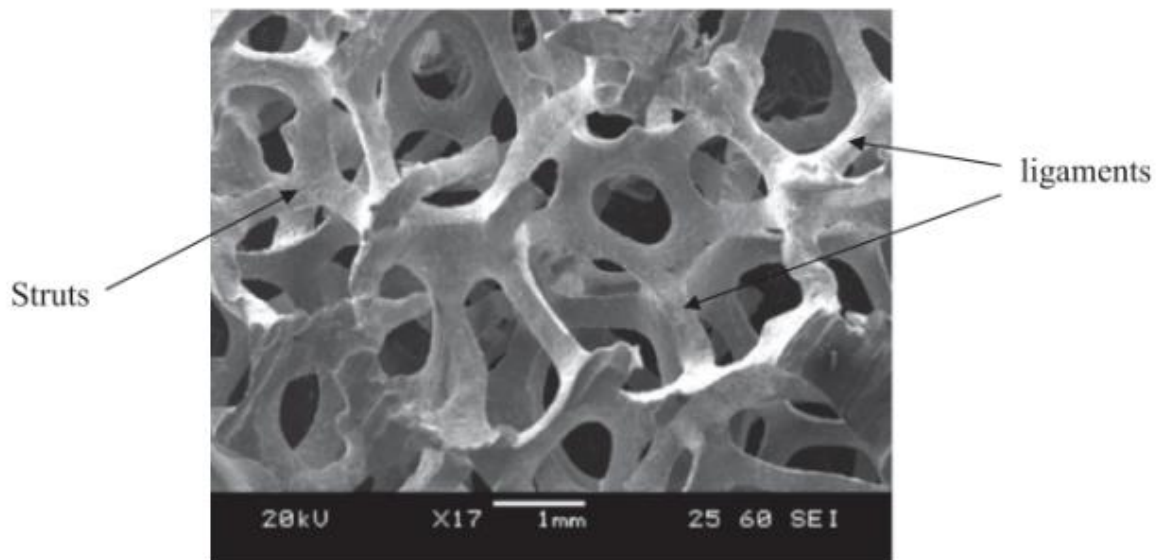
Figure 1.2 Microscopic image of the aluminium metal foam with 40 PPI [38].

The microstructure of these cellular materials can be characterised by porosity, relative density, cell size, cell shape, and ligament morphology, including the ligament diameter and length [39]. Each of these parameters significantly varies by mother material and production method. The scientific terms listed in Table 1.1 are generally used to define the physical properties of the media.

Table 1.1 Common terms and equations used in defining the physical properties of porous materials.

Term	Definition	Equation (Units)
Absolute/True Density	The density of material considering a solid volume only.	$\rho_m = \frac{M_m}{V_m}$ (Kg/ m³)
Bulk/Envelope Density	The density of material considering a solid and pores volume.	$\rho_S = \frac{M_m}{V_S}$ (Kg/ m³)
Void Volume	The volume difference between the bulk and the solid volumes.	$\Delta V = V_S - V_m$ (m³)
Porosity	The fraction of the void volume over the bulk volume.	$\epsilon = \frac{\Delta V}{V_S}$ (dimensionless)
Pore Size/Window size	The distance between the walls of the pore (pore diameter).	By measurement (m²)
Surface Area (depends on media type) (wire meshes as an example)	The area in contact with the working fluid.	$A_{HT} = \frac{4(1-e)V_R}{D_w}$ (m²)
Specific Surface Area	The fraction of the surface area over the bulk volume.	$A_{SP} = \frac{A_{HT}}{V_R}$ (m⁻¹)

1.2 Thermal regenerator

Regenerators have been widely used in heat exchange applications. The regenerator is a storage type heat exchanger in contrast to a recuperative heat exchanger. In the ordinary heat exchanger, the two fluids exchanging heat energy are separated by a solid wall, whereas the characteristic feature of regenerators is that two gases alternatively occupy the same space at different temperatures. During this occupancy, the warmer gas delivers heat to the heat storage medium, called the filler or matrix. The colder gas then picks up this heat energy while occupying the space at another time interval.

There are two types of regenerator: the rotary regenerator [2] and fixed regenerator [40]. The rotating regenerator is usually designed in such a way that heat exchange is accomplished by a wiping action. Heat storage takes the form of a wheel or drum, rotating continuously through warm and cold counter-flowing streams. An

example of the rotating regenerator is the Ljungström air preheater [9], shown in Figure 1.3, and used to preheat the combustion air in power stations.
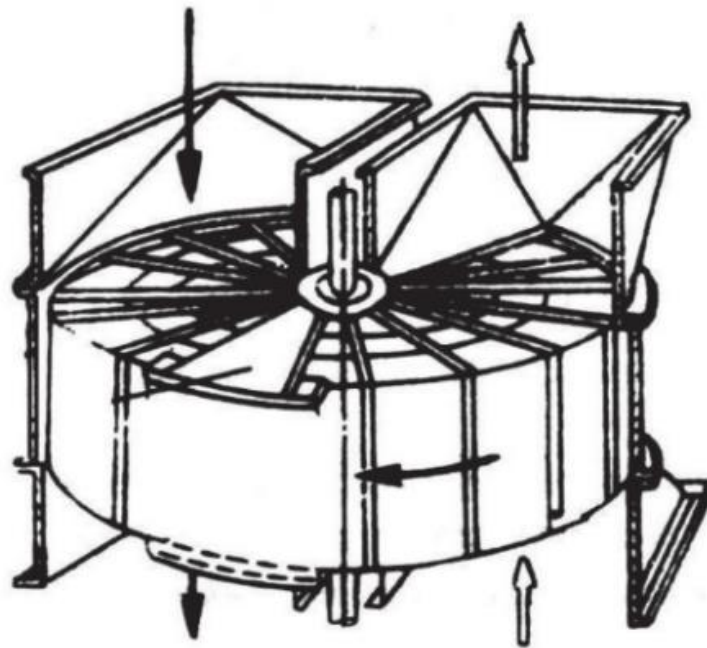
Figure 1.3 Rotary air preheater [41].

The fixed regenerator is usually part of a system where a single fluid stream is reversed, such as in a Sterling engine, or where two fluid streams flow individually through a fixed matrix in sequence. These types of regenerators are more common in the Stirling cooler [42] and the Gifford-McMahon cooler respectively [43], and other applications such as in blast furnaces [4]. A simple diagram of the beta type Stirling engine is illustrated in Figure 1.4. In both types of the regenerator, the matrix is a crucial factor in performance [5][21]. A typical regenerator matrix should be made of a high heat capacity material, resistant to high temperature and corrosion [16]. To increase energy utilisation effectively and reduce the operation cost, a matrix should have the following properties: large heat capacity; large heat transfer surface area; low thermal conductivity; low flow resistance; small size; low weight; and low void volume [5][29].
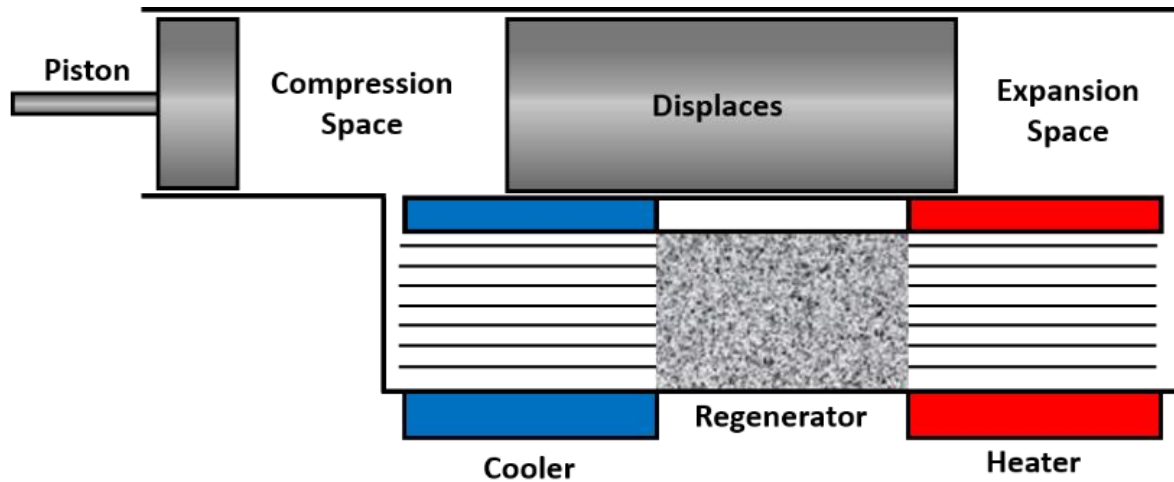
Figure 1.4 Sketch of beta Stirling engine.

1.3 Problem statement

There have been many attempts to develop regenerators and improve their thermal performance. The general trend in development is to reduce the size and weight of the matrix while maintaining relative system performance [44][45][46][47][48][49][50][51][52]. Until the recent past, fine stainless steel wire-woven screens were a common material used to build regenerators. Such screens have a high thermal capacity; large fluid-surface contact area; high convective heat transfer coefficient; and low axial thermal conductance, making them an efficient candidate for energy regeneration [53][54]. The specific surface area of the screens can be increased by increasing the number of screens. Their superior compactness makes them preferable for heat exchangers in limited design spaces [55][56]; however, woven wire mesh matrices have several disadvantages associated with their use as regenerators.

The wire meshes consist of a large number of cylindrical wires submerged behind each other within a fluid flow. This makes velocity developing regions very short and produces separation, wakes, and stagnation zones, resulting in remarkably high flow resistance across the layers [29][57]. Another issue associated with the use of wire meshes is that it is difficult to seal the gap between the circumference of the regenerator and the holder wall. Oversizing the mesh layers has been suggested as a solution to this problem [55]; however, pressure loss is further increased [55]. Moreover, the meshes are heavier than their aluminium metal foam counterparts [15]. In addition, a long assembly time is required to build packed bed regenerators, which

6

results in substantial labour and manufacturing costs that may be prohibitive for mass production [16].

As a result of the above shortcomings of wire mesh aluminium metal foams have been suggested as regenerators [36][37]. Aluminium foam has several potential advantages [5][58]. The most salient of its advantages are its high solid-fluid interface surface area per volume; high strength and rigidity; and high thermal conducting solid phase. Foams can have high porosity (greater than 90%), which enables a significant reduction of the pressure loss [33][36][37][59]. It also exhibits high permeability in the order of 10^{-8} m^2, compared to that of packed beds, which is in order of 10^{-10} m^2. Finally, the nature of aluminium foam internal structure enables mixing for the interacting phase [60][61]. These attributes make aluminium metal foam an attractive material for efficient compact heat exchangers [34][62]. However, metal foams with high porosities are not suitable for heat exchange, so compression is required to lower the porosity to 70-80% in order to achieve improved heat transfer performance [63] however, this increases the pressure loss across the compressed sample [60].

The effective thermal conductivity plays a measurable role in the forced convective heat transfer mechanism between the regenerator matrix and the working fluid [11][32][43][59]. When the matrix has high thermal conductivity, the heat conduction through the solid parallel to the flow direction reduces the temperature difference between the fluid and matrix. This diminishes the energy change between the fluid and solid surface resulting in lower efficiency of the matrix.

Even though constructing an isotropic porous structure is an impossible task [64], the wire mesh packed beds and metal foams have always been treated as idealised structures (homogeneous or isotropic porous structures), probably to avoid the complexity of analysing the internal structure. Some experimental measurements have shown that the diffusional current in the local region is extremely non-homogeneous in a presumed homogeneous porous media [64]. A review of the available literature showed a scientific data shortage for fluid flow in non-homogeneous porous media [60][65][66][67][68][69][70], while fluid flow across heterogeneous media has not been investigated.

1.4 Aims and motivation

The primary aim of this research is to investigate if the performance of the regenerators can be improved using a combination of materials. The performance of regenerators was assessed in terms of their pressure drop and heat transfer. The hydrothermal performance of a regenerator depends on several conflicting features. For better performance, the regenerator should have a large heat capacity, high heat transfer surface area, low thermal conductivity, and as minimal as possible fluid flow resistance. For high heat capacity, the regenerator should have a large mass or be made of a material with a high specific heat capacity. Large mass means an increase in the matrix size or reduction in its porosity. Low porosity results in high fluid flow resistance and high thermal conductivity. The matrix should have a large gas-fluid contact surface area to reduce the thermal resistance and enhance the heat transfer rate. The specific heat capacity of aluminium is almost twice that of stainless steel, (the specific heat of the aluminium is 0.90 kJ/kg K and the stainless steel has a value of 0.46 kJ/kg K) while the density of aluminium is approximately one-third of the stainless steel (2700 kg/m^3 vs. 7750 kg/m^3). For comparison at constant mass, the heat capacity of aluminium is about double of stainless steel, however, when they are compared at the constant solid and fraction volumes, the aluminium has a heat capacity of about one-third of stainless steel [36]. To sum up, it might be possible to design an efficient regenerator, if the material's density and specific heat increase.

Replicated aluminium foams are produced by infiltrating the open space left between bonded leachable particles with a liquid aluminium that is later solidified [71]. They are known for their moderate porosity, which can provide high volumetric heat capacities (the specific heat of the material times the density of the material times the solid volume fraction). However, they have low porosity, which causes high flow resistance [72]. The porosity and pore size in this type of structure can be modified to provide a high surface area [73]. Considering the local temperature distribution within the matrix, the heat transfer scenario becomes more complex. The axial heat conductivity of foams is higher than that of wire meshes [36][74]. Poor contact between adjacent wire screens leads to effective thermal conductivity being much lower than that of foam [36][75]. Both types of open cellular structures have advantages and disadvantages, which makes it difficult to select the best type.

8

A heterogeneous structure made of stainless steel wire mesh screens and aluminium metal foams may lead to improvements that may result in improved regenerator design. Hence, the current work aims to conduct a set of experimental measurements to evaluate the thermal performance of mesh/foam combinations as regenerators, using air. This work can be considered as a fundamental work demonstrating the hydrothermal performance of heterogeneous porous media. The heterogeneous structures in this work were made of low porosity metal foam layers and multi-layers of stainless steel wire mesh screens. The aluminium foam samples were inherited from a previous researcher [37], who used the replication method. The aluminium foam samples were manufactured with different pore shapes (spherical and irregular) and three different pore sizes (small, medium and large).

To produce the heterogeneous structures, the metal foam samples were sliced into three layers with the same thickness using the Electrical Discharge Machining (EDM). All foam samples were tested for their hydraulic and thermal performance before and after slicing to investigate the impact of slicing on the original foam samples. Three types of woven mesh wire screen (20 Mesh, 30 Mesh and 40 Mesh) were combined with the foam layers.

To enable comparison, three-wire mesh packed beds were produced with the same volume as that of the metal foam samples. The heterogeneous structures were produced with the intention of having a similar volume to the semi-homogeneous structures (foams and packed beds of mesh). These structures consisted of one or two layers of metal foam and multi-layers of wire mesh screens. Both semi-homogeneous and heterogeneous porous structures were tested at steady-state flow conditions to measure the pressure drop at a wide range of flow rates. Subsequently, the samples were tested for their thermal performance using the single blow technique.

The primary aim of this study was to quantify the impact on pressure drop and heat transfer of combining different types of porous media. This was to investigate if hybrid samples might perform better than porous media made from parent materials. In order to achieve this, the following objectives were necessary.

1. Investigation of hydraulic performance in semi-homogeneous and heterogeneous porous structures:

   - Design and manufacture of an experimental apparatus to meet the requirements of steady-state conditions for pressure drop measurements.

   - Measurement of the pressure drop at a different flow rate to examine the geometrical parameters on the pressure drop measured data.

   - Determination of the hydraulic and flow resistance parameters at different flow regimes to include the permeability and inertia coefficients.

   - Identification of the four flow regimes: pre-Darcy, Darcy, post-Darcy (Forchheimer) and turbulent flow regimes.

   - Comparison between Darcy and Forchheimer permeabilities for different types of porous media.

   - Examination of the impact of the heterogeneity on the hydraulic parameters.

2. Investigation of thermal performance in semi-homogeneous and heterogeneous porous structures

   - Redesign and modification of inherited experimental apparatus from a previous study to achieve the goals of this study.

   - The experimental measurement under the single-blow transient technique.

   - Development of a model to describe the experimental apparatus and predict the thermal parameters.

   - Review of the four commonly used techniques to reduce the single blow measurements and predict the heat transfer parameters including the number of transfer units, volumetric heat transfer coefficient and volumetric Nusselt number.

   - Demonstrate the influence of modelling parameters (inlet fluid time-temperature variation, axial conduction and side-wall effect) on the heat transfer parameters.

   - Investigate the impact of slicing on the thermal performance of metal foams.

- Determinate the heat transfer parameters, including the number of transfer units, volumetric heat transfer coefficients and volumetric Nusselt number.

- Comparison of heterogeneous porous structure results with those of semi-homogeneous porous structures to determine how well the new regenerators perform at flow rates up to frontal air velocity 6 m/s.

CHAPTER 2. Fluid Flow through Porous Media

Fluid flow through porous media has a long research history. It is an interesting topic relevant to many industrial fields. In mechanical engineering applications, estimating energy dissipation across a porous medium is essential to predict how much energy should be added to the fluid at a specific flow rate [5][76]. Porous media have been found to directly influence heat transfer exchange and the overall efficiency of a system [61]; therefore, a large number of studies have been devoted to understanding the corresponding resistance behind the flow across porous media and the heat transfer mechanisms between the flow and the solid phase.

Flow resistance is often given in terms of pressure drop which itself depends on the nature of the interaction between the flow and solid surface characterised by the macroscopic properties of the solid, and working fluid velocity and its properties [66][68][77][78][79]. Two main theoretical concepts have been adopted to describe the interaction between the fluid flow and the solid surface [80][81][82][83]. The first approach is called 'flow-around', where the solid is considered as an element submerged within the fluid flow. In such a case, the pressure drop is given in the form of the drag coefficient. It is usually applied for a single screen [20][81][84]. The second approach is called the 'flow-through', in which the system is treated as a bundle of tangled channels and the fluid is forced to flow through it [66][85]. An example of this is when a fluid flows into metal foams, or when fluid flows across multiple wire mesh layers. Although both approaches are consistent with very similar terms describing all the relevant transport effects in the porous media, the data and correlations obtained from one approach may differ from the other [81]. The latter approach (flow-through concept) has been adopted in the current study.

Flow resistance through fixed beds has been studied theoretically, following two approaches. The first is the microscopic approach, which considers flow behaviour at the pore level. The second is the macroscopic approach, which deals with the pressure drop–flow rate relationship across the whole structure [86][87]. Theoretically modelling flow resistance involves solving Navier-Stokes equations and using a volume averaging methodology at the macro-scale level [88][89][90]. Furthermore, most of these studies rely on assumptions about isotropic and homogeneous internal structures, or consider ideal geometrical shapes. Even in the almost identical

geometries, constructing a rigorous numerical solution is still challenging [25][91][89]; this is because porous media have complex and irregular internal structures which prevent any exact analytic solutions to the flow problems [39][69][92]. Moreover, the computational costs are expensive for a potential solution [88]. Therefore, the investigators of fluid flow in porous media rely heavily on experiments [63][93][94]. Despite this, fluid dynamics in porous media is still not well understood. There is a severe divergence in the published data in terms of pressure drop behaviour and porous media hydraulics parameters. This divergence has been attributed to the diversity of sample sizes among researchers, different flow regimes, and the fact that each flow regime may present different parameters, or the variety of models used to treat the measured pressure-drop data [61][95].

2.1 Flow regimes and pressure drop relations

Pressure drop of fluid flow through porous media is a critical design parameter in filters, catalysts and heat exchangers. The pressure drop difference across a porous medium is often measured under steady-state conditions. The results are then plotted as a function of the channel or interstitial velocities to approximate the microporous properties of the tested medium [68][92][96]. One of the earliest experimental works in this field was conducted by Henry Darcy in the middle of the 19th century. Darcy performed a lab test to study the movement of water across a pipe packed with sand. Under certain conditions, he found the pressure difference Δp per the bed thickness (L) is linearly proportional to the volume rate of flow per unit area (cross-section area, perpendicular to the flow direction). Darcy first established an empirical relationship written in the following form:

$$\frac{-\Delta p}{L} = \frac{\mu_f}{K_D}\, U \qquad\qquad 2.1$$

Where $-\Delta p/L$ represents the pressure gradient in the direction, U is the volumetric velocity vector (called Darcian velocity), μ is dynamic viscosity and K_D is the hydraulic conductivity coefficient, known currently as Darcy permeability. The Darcian velocity represents the superficial flow velocity that can be defined as the ratio between the mass flow rate ($\dot{m}$) and fluid density ρ multiplied by cross-section area (A_C) of the empty channel as:

$$U = \frac{\dot{m}}{\rho A_C}$$

2.2

Permeability is a term that implies how the size of the pores in a porous medium allows sufficient fluid to transmit itself through. High permeability means low resistance to flow and, consequently, the larger flow rate for the same pressure gradient. The K_D is measured in units of area (length^2) and depends mainly on the porosity of a solid and the characteristics of its pores [96][97]. The Darcy low is the most widely used expression for describing a single-phase flow through a permeable medium at low Reynolds numbers (when the viscous forces dominate the flow resistance). It has been derived theoretically using the volume averaging procedure. No restrictions to homogeneous or spatially periodic porous media were found [98]. To apply the Darcy equation (Equation 2.1), the relationship between the hydraulic gradient and flow velocity must be linear. The steadiness and the laminar status should be stipulated [99]. Unfortunately, at a critical Reynolds number, the pressure drop is no longer linearly proportional to fluid velocity. The classical Darcy's law becomes incompatible in terms of accurately describing the pressure loss across the medium [100][101][102][103]. Boundary layers start developing, and the interaction between the fluid and the solid surface must be considered. Many investigators have confirmed that the flow just after the Darcy regime is still laminar but exerts a wake inertia effect. The relationship between the pressure drop and fluid velocity was found to be describable when a nonlinear correlation is used [92][103].

Using an analogy with fluid flow in a pipe, Forchheimer [104] postulated an empirical quadratic expression, given in Equation 2.3, to analyse his experimental pressure drop data at high-flow velocities.

$$\frac{-\Delta p}{L} = \frac{\mu_f}{K_F}U + \beta \rho U^2$$

2.3

Where ρ is the working fluid density, U is the frontal velocity (Darcy velocity), and β is a form drag coefficient, that depends on the pore size, shape and porosity of the porous material [61]. Sometimes β is written as $F\sqrt{K_F}$, where F is a constant that is known as non-Darcy, Forchheimer coefficient or the inertial coefficient and K_F is Forchheimer permeability. F is believed to be universal, or at least fixed for a given class of porous media [69][105]. The K has been found to be close but not equal to Darcy permeability [94][105]. Both were found to depend strongly on structure

[39][61][66]. The Forchheimer model has been widely accepted for pressure drop description in porous media over a large range of flow rates. This includes flow in packed beds of wire mesh [29][56][106], packed beds of spheres [65][66], and metal foams [63][93][107][108]. The expression has been derived theoretically, based on assumptions of homogeneity of solid and fluid distribution [90][109][110]. Shown in Figure 2.1, is the typical quadratic relationship between the pressure gradient and frontal fluid velocity in the Forchheimer regime.
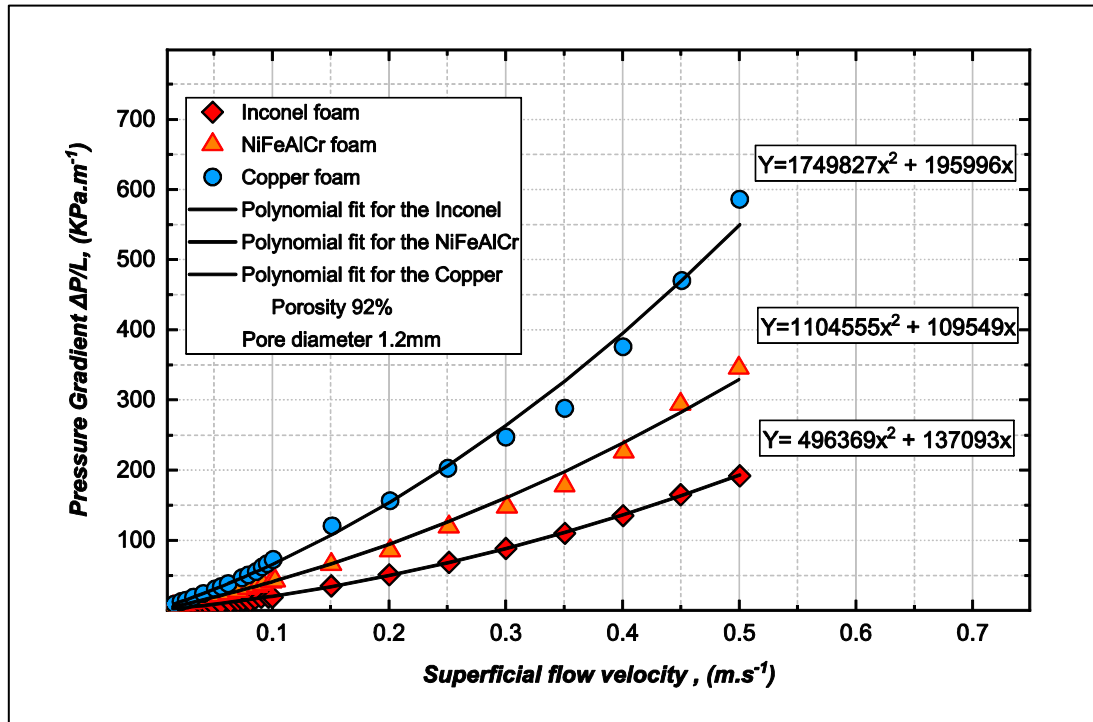
Figure 2.1 Pressure drop versus velocities for several types of metallic foams [111].

The pressure loss along the porous beds can also be represented in terms of solid spherical particles, the porosity of the medium and the flow velocity. Ergun [97] proposed Equation 2.4 to cover all flow types (laminar and turbulent) through packed beds of spheres.

$$\frac{-\Delta p}{L} = A \frac{(1-\epsilon)^2}{\epsilon^3} \frac{\mu_f U}{d^2} + B \frac{(1-\epsilon)}{\epsilon^3} \frac{\rho U^2}{d} \qquad 2.4$$

Where ϵ is the porosity of the porous medium, d is the equivalent or effective particle diameter (the diameter of the spherical particle if spherical particles are identical), and A and B are dimensionless correction factors representing the internal geometry differences in the medium. The applicability of the Ergun equation was found to be dependent on the multipliers A and B. For a gas flow through packed beds of

15

sand and coke spherical particles, Ergun proposed the values 150 and 1.75 for A and B respectively. Fand et al. [65] applied the Ergun model to characterise flow resistance through uniform and non-uniform packed beds of spheres, however, the constants were $A = 182$ and $B = 1.92$. The Ergun model has also been revisited [112]. It was recommended that the term ϵ^3 be replaced by $\epsilon^{3.6}$ for better data point fitness, while the constants were found to be $A = 180$ and $1.8 < B < 4$ based on particle smoothness. In the same study, the researchers found the constants are weakly, functionally dependent on porosity in a range between 0.37 and 0.64. The Ergun model provided a good fit to measured pressure drop data for flows in randomly stacked fibres and metallic foams [113]. The constants were found to be between 100 and 865 for A and between 0.65 and 2.6 for B.

There is a similarity between the Forchheimer and the Ergun equations. Both are used to describe pressure drop in porous media [39][61][94][113]. They exhibit two mean force effects: the viscous effect, which is linear dependent on the superficial velocity, represented by the first term of the right-hand side of the equation; and the inertia contribution, represented by the quadratic dependence term of the superficial velocity. Similar expressions may be found in the literature; however, most of them are manipulated to fit the basic forms of these two equations. Both the Forchheimer and the Ergun models have been statistically examined [109]. The results showed that the correlations are satisfactory to present fluid flow behaviour in porous media, and there is no specific reason to choose one over the other.

Perhaps one of the shortcomings of the Forchheimer equation is that the hydraulic parameters F and K can only be determined empirically. However, the Ergun equation is based on modelling the space between nearly uniform-sized spherical particles. Some researchers argue that as the Ergun equation is a superimposition of the Blake-Kozeny and the Bruke-Plummer equations, the Forchheimer regime is considered a transitional regime between the laminar and turbulent regimes [95]. Thus, if one is interested in the Forchheimer regime, it is more convenient to use the Forchheimer model. When the Ergun equation was applied to predict the pressure drop in ceramic and metal foams, an approximate 40% margin of error was observed in the predicted data compared to the measured data [114]. At a sufficiently high velocity, streamlines start to shift, and fixed eddies begin to form inside closed streamlines [64][78][115]. Sudden enlargements and contractions occur in the

flow paths resulting in a turbulent flow regime [91]. Fand et al. [65] Kececioglu and Jiang [116] indicated that the pressure gradient slope decreases when water flows through sphere beds [65][116]. The decrease in the pressure slope implies a reduction of drag at higher fluid velocities. One expects the opposite flow behaviour as the turbulent regime typically leads to an increase in flow resistance. Contrary behaviour was observed by Lage et al. [92] for air flows through aluminium foams. It might be more convenient to divide the pressure gradient by the superficial flow velocity U and to then plot the results versus the superficial flow velocity U. Equation 2.3 can be rearranged and written as:

$$\frac{-\Delta p}{UL} = \frac{\mu_f}{K} + \frac{\rho F}{\sqrt{K}} U \qquad 2.5$$

This can provide a reasonable meaning to the pressure drop change and help in easily separating flow regimes [93][94][101][115][111]. The quadratic Forchheimer equation is widely regarded as being satisfactory to predict flow behaviour in the turbulent regime but with different coefficients (permeability and Forchheimer coefficient) [61][117][118][94][101]. If the inclination of the pressure drop rate with velocity increases in the turbulent regime, using the Forchheimer model at high velocity would underestimate the pressure drop. Therefore, the applicability of the Forchheimer equation for turbulent flow has been investigated [119]. The values of the Forchheimer coefficients were found to vary with fluid velocity but were not very significant. Lage et al. [92] recommended the cubic-Forchheimer-extended Darcy in Equation 2.6 for better experimental data fitting, in which the permeability K and the inertia coefficient β are similar to those obtained from the Forchheimer model, and c is a cubic coefficient with units Pa s^3/m^4 and accounts for the effect of high velocity.

$$\frac{-\Delta p}{L} = \frac{\mu}{K} U + \beta \rho U^2 + c U^3 \qquad 2.6$$

Porous media structures are random in nature; their hydrothermal behaviour differs remarkably from one class to another [107][120][121][122]. The fabrication techniques of these materials are also found to have impacted their performance [53][75][120]. Because of this, great efforts have been expended to understand the relationship between pressure drop and porous material structures. The general trend is that the pressure drop increases linearly at low flow rates and in quadratic at relatively high flow rates with fluid velocity. This relationship was found to vary based

on the structural parameters of the medium [61][66][68][94][100][101][108][111][116][123].

Pressure drop parameters such as permeability and form/inertial drag coefficients are usually measured as representatives of viscous and form drags, respectively. Darcy permeability has been determined for different types of metallic foam structures with different porosity and pore sizes [70][73][123][124]. A linear relationship between pressure gradient and frontal fluid velocity at low flow rates was observed and the Darcy model was used in Equation 2.1 to determine permeability. Figure 2.2 shows the typical linear relationship of the pressure gradient against superficial fluid velocity at the Darcy flow regime.
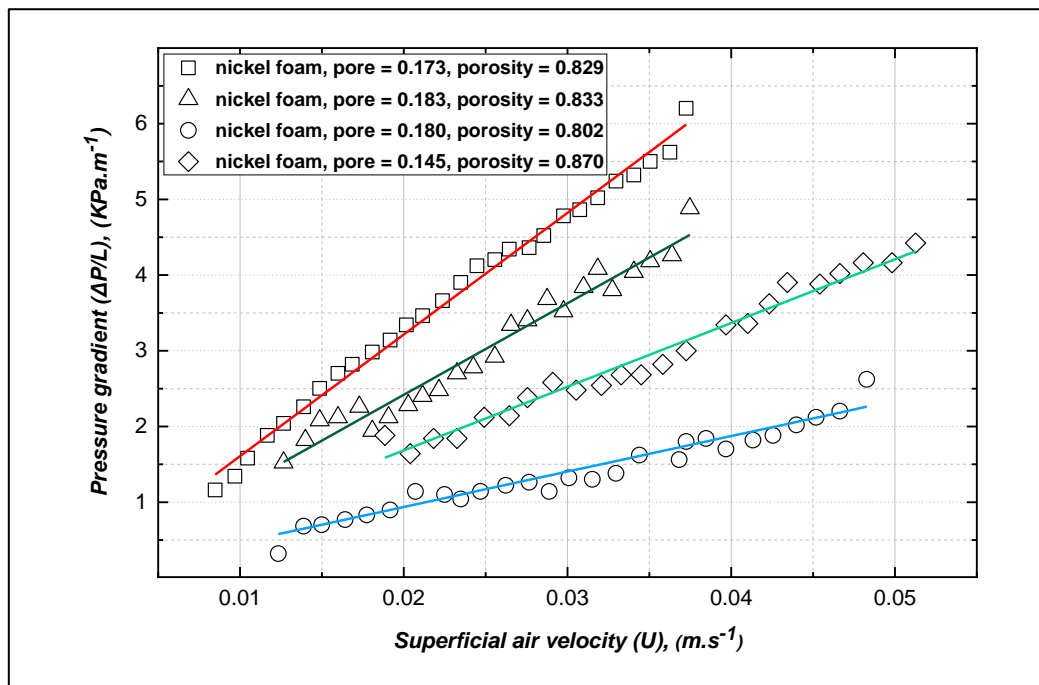
Figure 2.2 The typical linear relationship at Darcy flow regime [123].

A significant amount of work has been directed to determine the pressure drop through multi-layered wire-woven metals. Microstructure parameters such as porosity, wire diameter, pore density (mesh size), and the number of layers were found to influence the penetrating quality of mesh screen packed beds. However, the literature survey showed that pressure drop measurements in packed beds of screens usually only involves friction factor behaviour, and there is limited information about hydraulic parameters in terms of inertia and drag coefficients.

The porosity in screen matrices was found to greatly influence pressure drop and the hydraulic parameters of flow through packed beds of mesh screens. The

porosity has a complicated relationship with other microstructure mesh screen parameters. Similar porosity can be obtained from different combinations of geometrical parameters [25][125]; it can also be produced by changing the number of layers for a given depth of matrix [25][126]. Changing the wire diameter and/or mesh number can further influence the porosity of the screen packed beds [127]. The impact of porosity and wire diameter on fluid flow parameters has been assessed [28][128]. At constant wire diameter, the results showed that increasing the porosity results in a decrease in pressure drop. Keeping the porosity constant and reducing the wire diameter was seen to increase the flow resistance. Permeability was found to increase as the wire diameter increases and the inertia coefficients showed an opposite trend [128]. Miguel [129] experimentally evaluated the impact of screen usage on fluid flow reduction. The flow characteristics of a large number of screen samples with regular rectangular and irregular mesh geometries were determined. His results showed that the shape of the yarns and the mesh geometry have less than 10% influence on flow characteristics of porous screens, and they are mainly a function of porosity. The impact of porosity on the hydraulic parameters in Miguel's study is shown in Figure 2.3. As can be seen, increasing the porosity of the packed beds increases the permeability, whereas the inertia coefficient decreases.
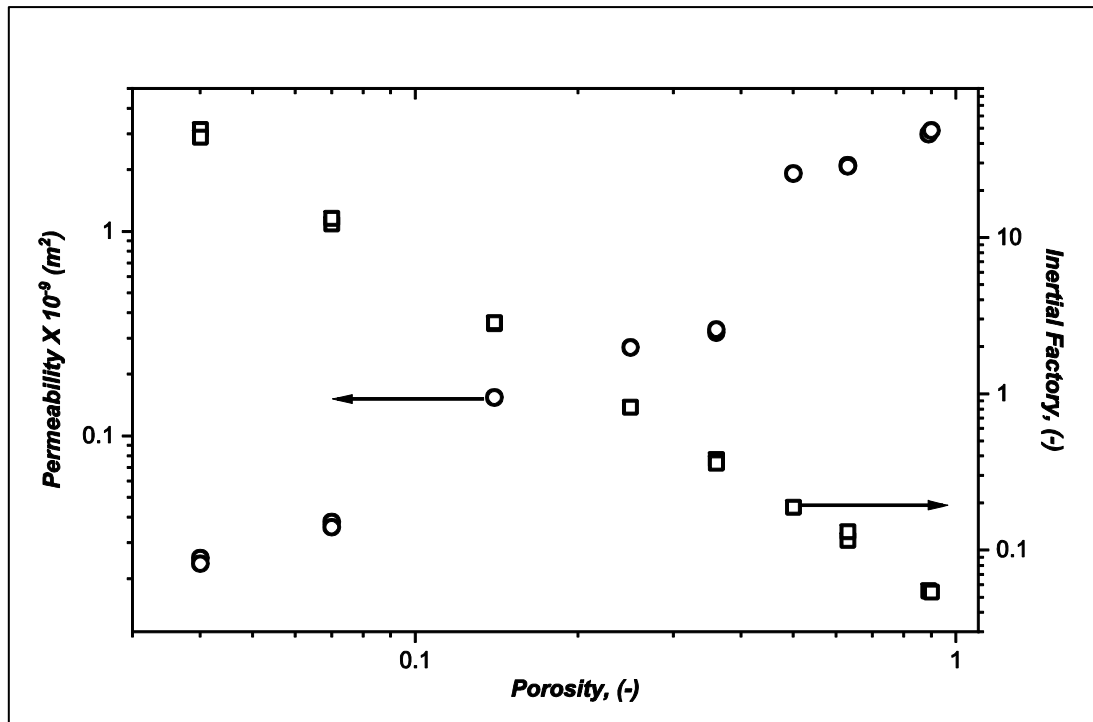
Figure 2.3 Flow characteristics of porous screens as a function of porosity.

The impact of the number of layers and pore densities (mesh size) on pressure drops has also been experimentally examined [25][125][126]. It has been shown that increasing the number of screens and/or pore density leads to more flow resistance and that the pressure drop was a proportional and linear function of the number of screens. Luna's [36] results showed that doubling the number of screens results in a little increase in the pressure drop (less than 15%). In the same study, the researcher warned of the influence of pore density on the pressure drop in packed beds of screens. His results revealed that doubling the pore density might cause a more than 100% increase in the pressure drop. The impact of packing orientation, cell shapes and wire shape [14][130] have also been investigated, but an unmeasurable impact on the pressure drop across was observed.

The literature also includes a large portion of experimental work performed to measure the pressure drop across different types of metal foams; however, most of this work examined foam with high porosity. In contrast, few studies have examined low porosity metal foam only, and at low flow velocities, to identify Darcy permeabilities of the structures [70][73][123][124]. Pressure drop parameters have been found to be very divergent. The permeability and inertia coefficients were also found to vary from one regime to another for foams with the same porosity and microstructure [61][95][108][111]. This was attributed to the flow regime [61][108][131] and the

20

influence of the sample size along and perpendicular to the flow direction [105][107][124]. The form drag and the inertia factor depend strongly on porosity, strut thickness and shape, and pore diameter [32].

Similar to flow in packed beds, the relationship between the pressure drop and geometrical parameters in metallic foams is non-monotonical, and a similar pressure drop can be induced with different porosity pore sizes [132]. The porosity changes depending on manufacturing techniques and different base materials, thus, struts of different shapes and thicknesses are produced [38]. The shape of a fibre cross-section has also been strongly linked to porosity [32]. The porosity has a measurable impact on permeability and inertia coefficients in metal foams. Increasing the porosity means more void volume within a medium, which results in a lower pressure loss due to the inertial and drag effects, while the permeability increases. This concept was confirmed in different base material metal foams with porosities in the range of 0.68 and 0.97 with different pore sizes [39][58][63][79][69][93][101][107][132]. Subsequently, Bhattacharya et al. [32] showed that the inertia coefficient only depends on porosity, if the aluminium foams have porosities between 0.906 and 0.97 and pore densities between 5 and 40.

Figure 2.4 illustrates the impact of pore density PPI (the number of pores per linear inch) on the pressure drop across different aluminium foam samples. As is clear from the graph, increasing the number of pores from 10PPI to 40PPI at constant porosity results in doubling in the pressure drop gradient.
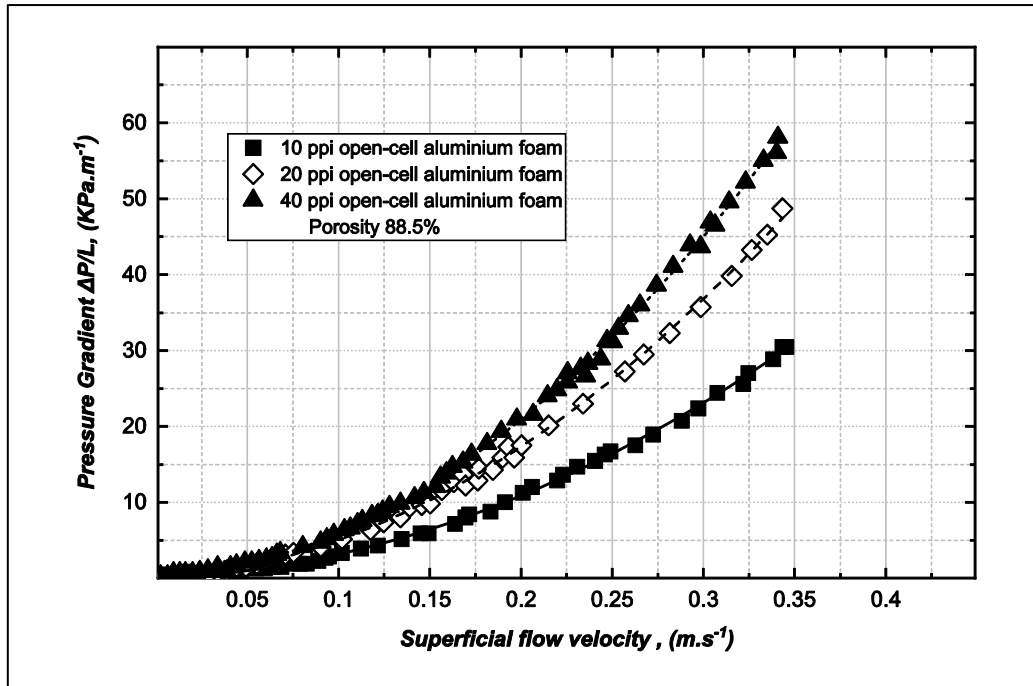
Figure 2.4 Pressure drop per unit length versus average velocity for 10, 20 and 40-PPI aluminium foam [101].

Increasing the pore diameter creates lower pore density (PPI) and less blockage in the fluid path. As a result, the permeability increases while the inertia and drag coefficients decrease [58][63][93][101][133]. The inertia coefficients in the metal foam were also found to differ with the microstructure of the porous media [68][92][134]. The roughness, cell and shape of the ligament have been reported to influence the magnitude of the inertia and drag coefficients. The form drag force during fluid flow over the ligaments forming the porous network is quantified by the inertia factor [32][38][111]. High porosity metal foams have also been compressed in order to reduce the porosity to enhance the specific area [68][135]. Increasing the compression ratio caused an increase in the form and inertia coefficients, but a reduction in permeability [68][108].

2.2 Flow resistance correlations in non-dimensional forms

Similar to fluid flow in pipes, fluid resistance can be expressed in dimensionless form as a log-log relationship between the friction factor and Reynolds number [61][65][94][97][100][102]. The subject of fluid flowing through porous media is further complicated as different researchers have adopted different characteristic lengths to express their research results [70][94][108]. Many geometrical dimensions have been quoted in the literature as bases for the definitions of Reynolds number and friction

22

factor. This includes: the layer thickness [24][136]; duct dimensions [11][14][91]; and hydraulic radius or diameter [16][125][126][137]. These dimensions are easy to measure and provide an acceptable description for simple cases (homogenous porous media). The experimental flow rate expressed as a pore diameter based Reynolds number, and which was proposed by Ergun [97], is as follows:

$$Re_p = \frac{\rho U d_p}{\mu}(1 - \epsilon) \qquad\qquad 2.7$$

and as a hydraulic radius based Reynolds number:

$$Re_{r_h} = \frac{\rho U r_h}{\mu} \qquad\qquad 2.8$$

Where d_p is the equivalent pore or wire diameter and r_h is the hydraulic radius of the tested bed. The hydraulic radius for packed wire mesh screens can be written as:

$$r_h = \frac{\epsilon d_w}{4(1 - \epsilon)} \qquad\qquad 2.9$$

The hydraulic radius is the common characteristic length used to analyse the pressure drop through woven screen matrices; however, there is a considerable deviation in the results when it was used as a scale length: this deviation is attributed to the variation of mesh bed porosity [19]. As can be seen from Equation 2.9, the hydraulic radius depends on the porosity value. The intermediate gap between two consecutive mesh screens may result in a doubtful value of porosity and results in misestimating the hydraulic radius. The average ligament diameter and average pore size have also been proposed as a way of obtaining the Reynolds number and flow friction correlations in metal foams [32][58][102][138]. However, there is no agreement about any of these dimensions for describing flow patterns in metal foams: ligament cross-sectional area was found to be uniform [39] and pore diameter was shown to be an inappropriate characteristic length for metal foam [58].

The diversity of characteristic lengths leads to an ambiguity that impedes a fair comparison between different experimental data. Hence, there is still a necessity for overall characteristic lengths acceptable for all classes of porous media. In order to

compare the performance of different types of porous materials, it is fundamental that the properties of the matrices are defined in a consistent way. Perhaps the most acceptable suggestion is the square root of Darcy permeability $\sqrt{K}$ [100]. Many investigators have employed the square root of Darcy permeability to characterise several types of permeable media [29][61][66][68][74][94][101][108][111][123]. Dybbs and Edwards [102] found that the nature of the flow in the purely viscous Darcy regime can be determined by local geometry, and permeability in this regime has a constant value. In packed beds of spheres, the permeability square root over the porosity was found to be the appropriate characteristic length rather than the sphere diameter (in that less variation in the dimensionless pressure drop date was noticed) [116]. It showed the least divergent values when the square root of the permeability was used to characterise the flow regime in metal foam [108]. The modified Reynolds number, which includes the square root of Darcy permeability $\sqrt{K}$ as the porous media characteristic length scale, can be written as:

$$Re_{\sqrt{K}} = \frac{\rho U \sqrt{K}}{\mu}$$

2.10

Similar to the Reynolds number, the definition of the friction factor differs slightly as the characteristic length changes. Nevertheless, they are all based on the definition of the Fanning friction factor [16][125][126][137]. The simplest expression one can look to is the fanning friction factor based on the hydraulic radius [16][125][126][137].

$$f = \frac{-\Delta p}{L} \frac{2r_h}{\rho U^2}$$

2.11

Ergun [97] successfully recast the flow resistance to the dimensionless form by rearranging Equation 2.4. He expressed the friction factor as:

$$f = \frac{-\Delta p}{L} \frac{d}{\rho U^2} \frac{\epsilon^3}{(1-\epsilon)}$$

2.12

Other investigators non-dimensionalised the experimental pressure drop based on the square root of the permeability using the following expression [94][100][101]:

$$f_{\sqrt{K}} = \frac{-\Delta p}{L} \frac{\sqrt{K}}{\rho U^2}$$

2.13

Several expressions have been proposed to predict the relationship between the modified Reynolds number and the modified fanning friction factor. One is based on Ergun Equation 2.4, and can be written as:

$$f = A\frac{(1 - \epsilon)}{Re_p} + B \qquad\qquad 2.14$$

Where A and B are the adjustable parameters similar to those in the Ergun equation and equal to 150 and 1.75, respectively. Using a large set of experimental data obtained from testing packed-bed spheres and metallic foam, Dybbs and Edwards [102] and Dukhan et al. [94] confirmed, respectively, the validity of this model for describing the friction factor behaviour against the Reynolds number. However, the original constants in the Ergun model accurately described the friction behaviour in wire sheets when the porosity was less than 50%, but not in high porosity mesh beds [83]. Armour and Cannon [91] demonstrated the satisfaction of the model for a single layer of different woven mesh types. However, the adjustable parameters A and B were found to be specific for each type and have to be found individually [83]. To generalise the model, they recommended A and B being 8.61 and 0.52, respectively.

Several models similar to that of Ergun have claimed to describe the arbitrary friction factor versus the Reynolds number in wire mesh screens [20][26]. They all have identical shapes, as does the Ergun model, but none of them accurately describes the friction factor and Reynolds number relationship in packed screens. Several comparisons have been conducted between some cited models in the literature and used to predict the hydraulic resistance across wire mesh screens [80][81][83][139]. Among the compared models Armour and Cannon model [91] was found the most accurate model. Even though the Armour and Cannon model illustrated a rather high level of generality in mesh screens, it might be inaccurate for other porous media types as has been observed in the current study. The non-dimensional form of the Forchheimer equation (Equation 2.15) has been used to predict the relationship between the permeability based Fanning friction factor $f_{\sqrt{K}}$ and the permeability based Reynolds number $Re_{\sqrt{K}}$ [39][61][68][69][94][101][124][133].

$$f_{\sqrt{K}} = \frac{1}{Re_{\sqrt{K}}} + F \qquad\qquad 2.15$$

Where $f_{\sqrt{K}}$ and $Re_{\sqrt{K}}$ are the Darcy permeability based friction factor and Reynolds number, respectively, and can be obtained from Equations 2.10 and 2.13. In the absence of the inertial effects, this equation can be simplified to the following form:

$$f_{\sqrt{K}} = \frac{1}{Re_{\sqrt{K}}}$$

2.16

Some expressions have been demonstrated in terms of the permeability based friction factor as a function of the Reynolds number [74][100][140][141]. These expressions have been tested by many researchers and none of them was found to be satisfactory to describe the measured data [61][74][123][133]. This is likely due to the differences in the material microstructure [123][133]. Sets of the friction factor data for different types of porous materials were gathered from the literature and plotted in Figure 2.5. It is clear that the friction factor decreases with an increase in Reynolds number. At low values of the Reynolds number, the friction factor can be described by the $1/Re_{\sqrt{K}}$ expression. At a relatively high Reynolds number, the inertia takes a role and the friction factor tends to a constant value which is likely the inertia coefficient [61][133]. The different definitions of the friction factor prevent a general expression to quantify the friction factor and validate the experimental results [58].

The literature survey showed that limited published data about non-dimensional variables $f_{\sqrt{K}}$ and $Re_{\sqrt{K}}$. Nonetheless, the majority of the data sets did not include data in the Darcy regime. Therefore, the result from this study was compared with the four correlations reported in the literature using the friction factor based on the square root of permeability (measured in the Darcy regime) and the Reynolds number based on the same characteristic length.
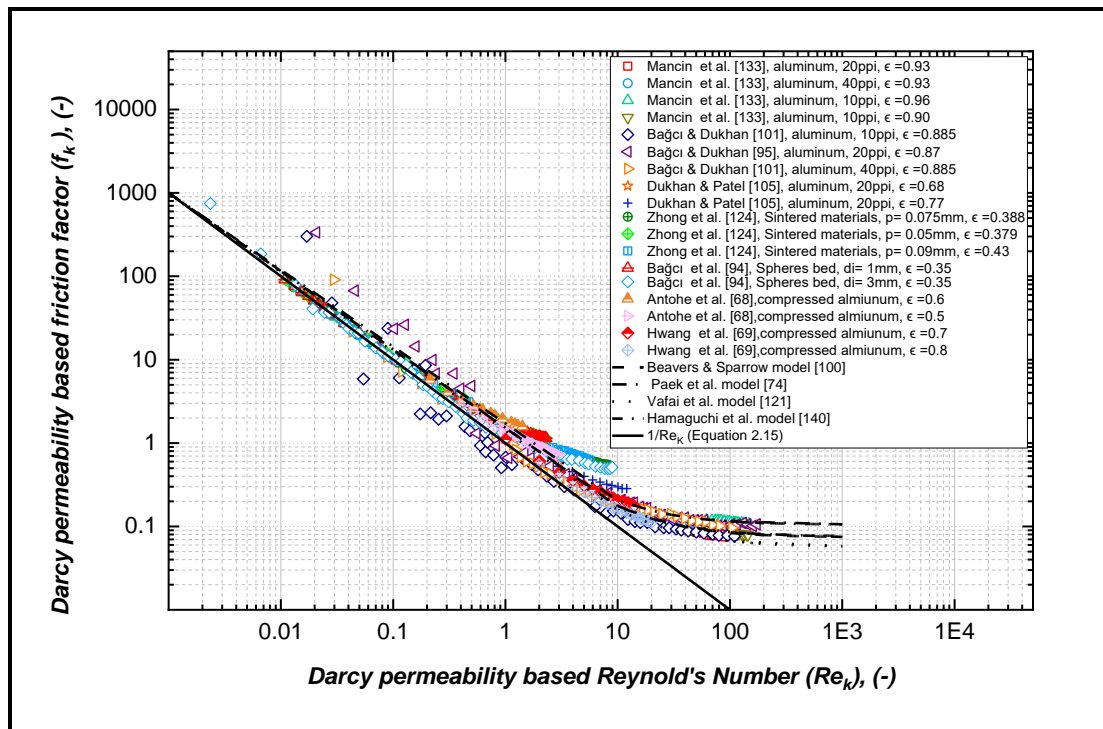
Figure 2.5 Friction factor vs. Reynolds number – data sets compiled by the author from literature.

2.3 Summary

This chapter covered a part of the literature relevant to the pressure drop of fluid flowing through different rigid, open-cell, porous media. A wide review of available correlations for computing pressure drop during single-phase flow in stacks of woven metal screens and metal foams was presented. At low flow rates, the Darcy law seems to be more suitable to estimate the pressure drop within a different structure. Other equations (Ergun and Forchheimer equations) may represent the quadratic flow behaviour through porous media at large flow rates. Despite the similarity between the two equations, the formulation suggested by Forchheimer seems to have less uncertainty. The non-Darcian parameters (Forchheimer permeability, inertia and form drag coefficients) can be determined by fitting experimental data with the quadratic model. The values of these parameters are significantly affected by the geometrical parameters of the specimens (pore size and porosity). Flow-through porous media can also be described in a dimensionless form as a relationship between the friction factor and Reynolds number. Various formulations have been referenced in the literature, from different laboratories. The proposed expression gives the same trends; however, they may not fit well the experimental data for fully developed turbulent flow of air at steady-state conditions.

CHAPTER 3. Heat Transfer in Porous Media

3.1 Introduction

Metallic porous media are excellent candidates for heat transfer enhancement applications because of their high surface density [53][61][101][142]. They are been widely used in many engineering fields such as solar collectors, compact heat exchangers, and packed bed regenerators [125][126][143]. Metallic plain-weave wire mesh screens are generally highly porous, with a large specific surface area. They are usually stacked in an inline or staggered configuration to create a highly tortuous flow path so as to circulate the fluid and enhance the heat transfer [21][144][145]. In the past century, this type of material has been developed to increase the heat transfer area density of heat exchangers without increasing their volume. In situations where the weight of the heat exchanger is an important factor in design, cellular metallic foams are more attractive than wire screens. Cellular metallic foams have open cells and hollow cell ligaments that promote eddies and provide an enhanced mixing which allows for more heat to transfer [30][146][147]. These features make them attractive and highly desirable for compact heat exchangers.

There are two extreme packing methods, namely in-line stacked and staggered stacked, used to form 3D multiple layers wire meshes of different thicknesses. In the in-line configurations, the mesh laminates are all stacked parallel and perpendicular to the facesheets, with flow directed along with the aligned square pores, while in the staggered configuration, the mesh laminates are also stacked parallel to the facesheets, but the passage of fluid flow is through the stagger-shaped pores between the stacked laminates. The influence of the packing method hydrothermal performance of wire screens has been examined [14][18][24][57][144][148][149]. The results showed that the staggered configurations provide higher performance than that of the inline configurations, particularly at a high Reynolds number [11][14][144]. This was attributed to two likely reasons: the staggered structures having lower effective thermal conductivity and the high turbulent flow due to the uncompleted vortexes behind the mesh wires [11][17][75][150].

Overall, heat transfer in porous media is a complex topic and the heat transfer mechanism inside the medium has not been fully explored. Several competing mechanisms contribute to the heat transfer between a through-flowing fluid and

cellular metals: solid conduction, thermal radiation, fluid conduction and thermal convection between the solid and the fluid. The contribution of these mechanisms to the transferred heat differs depending on the physical and dynamic parameters of both the fluid and solid phase [30][56]. Considering all these mechanisms in one study is difficult and the problem cannot be solved [7][151][152]. Consequently, the problem is usually simplified fundamentally to a single direction convective heat transfer problem [60][125][126][153][154]. The reported data showed that the forced convection heat transfer between the solid and the fluid is governed by the geometrical parameters of the medium, fluid properties, and the nature of the interaction between the fluid flow and solid surface [12][21][56][66][155].

Furthermore, the average heat transfer rate can be described by several dimensionless parameters including the number of transfer units (NTU_s) [55][156][157][158][159][160], heat transfer coefficient (h) [38][69][87][161][147], and a Nusselt number (Nu) [38][69][147][153][161][162]. The number of transfer units (NTU_s) has been frequently used as an indicator of the heat transfer rate between the fluid flow and regenerator matrix. It refers to the size of the heat exchanger or thermal regenerator and how much thermal energy can be transferred between the solid and the working fluid. The NTU_s is equal to the ratio of the convective heat transfer rate from a solid to the heating capacity rate of an adjacent fluid and usually given as:

$$NTU_s = \frac{h_s A_{HT}}{\dot{m}_f c_p} \tag{3.1}$$

The averaged heat transfer coefficient has also been commonly used as a principal characteristic to describe heat transfer performance in thermal management systems. Two types of heat transfer coefficients are often employed to characterise the heat transfer in cellular materials: wall heat transfer coefficient and interstitial heat transfer coefficient [69]. The wall heat transfer coefficient, which is known also as the convective or global heat transfer coefficient, is usually utilised to determine heat transfer enhancement due to the attachment of porous media to sidewall surfaces. An example of this is a porous media cooling electronic device [69][136][161][135]. In applications such as in compact heat exchangers or thermal energy storages, the interstitial heat transfer coefficient is commonly used, also called the volumetric heat transfer coefficient (VHTC). The VHTC represents the heat exchange between the

working fluid and the cellular solid surface [36][37][69][147][153]. In most heat transfer applications, the available space for heat exchangers is limited. In such a situation, the VHTCs at a given mass flow rate is usually measured or predetermined. VHTC is defined as:

$$h_v = h_s A_{sp}$$
<div align="right">3.2</div>

Where h_s is the average value of the convective heat transfer coefficient and A_{sp} is the specific surface area per unit volume [137]. Numerous experimental and numerical convective heat transfer studies on open cellular configurations have been reported in the literature. The influence of structural parameters on the number of transfer units, volumetric heat transfer coefficient and volumetric Nusselt number has been measured in different base material types of modern and traditional porous media [7][30][36][43][69][70][147][163][160][164]. The available data showed that the NTU_s value decreases rapidly with increasing flow rate. In addition, increasing the porosity and pore size of the medium leads to a decrease in the NTU_s value [36][37][55][157][158][159][160]. Increasing the porosity or pore size results in a decrease in both the solid-fluid interface area and the local fluid velocity, hence, a lower convective heat transfer rate. However, increasing the flow rate further means adding more energy to the working fluid which then increases the amount of energy that can be transferred between the fluid and solid with respect to the interface surface area.

In the subset of literature dealing with porous media is the nonuniform distribution of voids within matrices [165]. A homogeneous porous medium means the fluid paths inside the medium have a similar mean fluid velocity, thus a similar convection coefficient [160]. Unfortunately, perfect homogeneous porous media cannot be obtained. Porous materials have extremely complicated pore passage geometry which makes it difficult to measure the specific area, window size and pore diameter [18][166]. Moreover, it is rather difficult to measure the geometrical parameters of foam materials such as the specific surface area, mean cell size and mean pore size [167]. Consequently, the complexity of the structure is usually precluded and the heat transfer coefficient per unit volume and the volumetric Nusselt number are used to describe the heat transfer performance [7][30][69][147][164][166][168][169][170].

A series of experimental and numerical studies have been conducted to determine the influence of geometrical parameters on VHTCs for metal foams and screen matrices. The results revealed that there is substantial rise in VHTC with an increase of flow rate and a decrease in porosity [14][30][36][37][43][69][70][137][147] [153][160][161][171]. The increase of the volumetric heat transfer coefficient between the porous matrix and flowing flow has been attributed to two factors: the velocity increase at the inlet and the high turbulent intensity generated by the medium and also to the increase in the interstitial flow velocity (velocity inside the pores) and the surface area density. Increasing the frontal mass flow rate subsequently increases the interstitial flow velocity (velocity inside the pores) while decreasing the porosity most likely results in a decrease in a specific area or increase in the effective conductivity of a sample [69]. Subsequently, these factors work together to achieve a high heat transfer rate [11][171].

The VHTC arises from increasing interstitial velocity and heat transfer area and reduces either by porosity or pore size [7][14][69][137][170][171][172]. It has been reported that the VHTCs increase by decreasing the pore size in different types of metallic foams [7][36][37][147][164][166] and by decreasing the pitch size in packed beds of mesh wire screens [18][36][126][137][171]. Qualitatively speaking, this means that the VHTC is proportional to the interstitial velocity and surface area density and inversely proportional to the porosity and pore size. Figure 3.1 shows some of the compiled data collected by the thesis's author to demonstrate the effect of the different topologies of porous materials with base materials on the VHTCs. The references are provided in the legend.
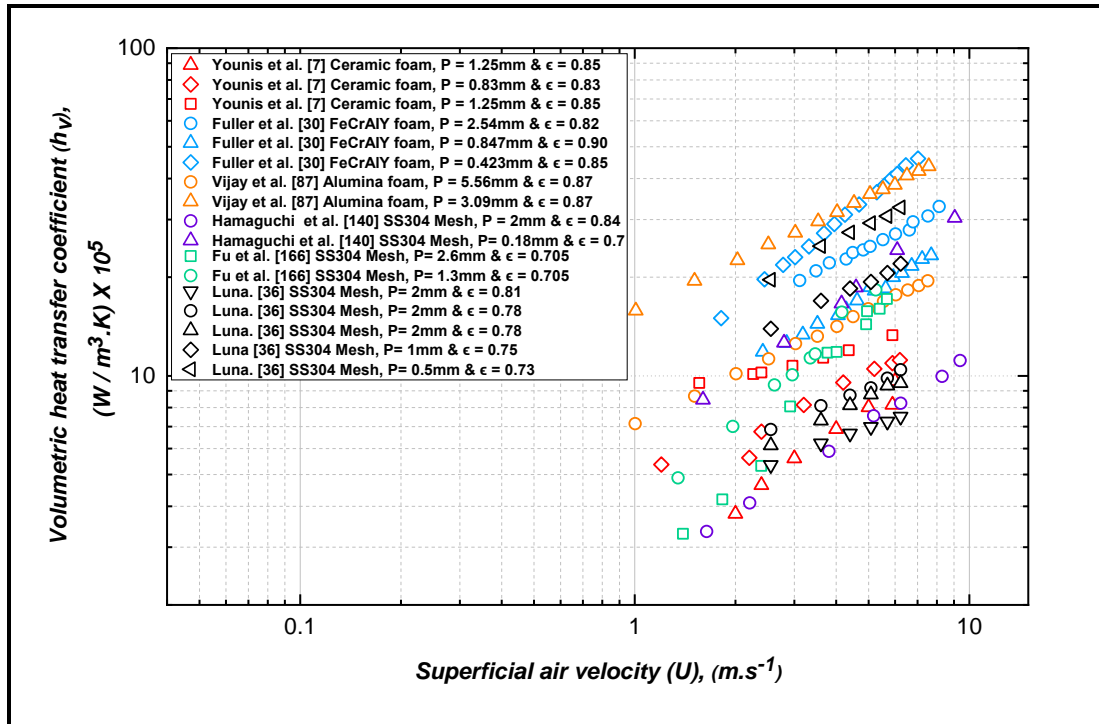
Figure 3.1 The effect of microstructure on volumetric heat transfer coefficient

The convective heat transfer performance in porous media has also been expressed in non-dimensional forms as a relationship between the volumetric Nusselt number parameters and Reynolds number [7][18][30][153][166][168]. The published data revealed that the general trend is that the Nusselt number increases with an increase in the Reynolds number [7][18][30][69]. The published relations for different porous materials cannot be compared due to the technical issue of scaling [166]. More than one kind of characteristic length have been adopted in the reported data and the experimental data has been reduced in several ways. The mean porous or particle diameter has been used to quantify the Nusselt number in metal foams [7][30][69][147][168]. Alternatively, the equivalent strut [164], sample thickness along or perpendicular to the flow [153][161][173][169], average wire diameter [144][174], hydraulic diameter [18][162], hydraulic radius [126][171] and the square root of permeability [175][166] have all been cited as characteristic lengths for the Nusselt number. The pore diameter d_p was seen to be a reasonable choice of the definition of the volumetric Nusselt number without a physical justification being given [30]. The Nusselt number can be written in terms of the VHTC and the average pore diameter as follows:

$$Nu_v = \frac{h_v d_p^2}{K_f} \qquad\qquad 3.3$$

where h_v is the volumetric heat transfer coefficient, d_p is the pore diameter and K_f is the thermal conductivity of the heating or coolant flow. Xia et al. [147] used the pore diameter as a characteristic length to make a comparison of the volumetric Nusselt number between their experimental results and those reported in the literature [7][147][167][176][177][178]. The comparison is represented in Figure 3.2 in which the volumetric Nusselt number is plotted as a function of Reynold's number.
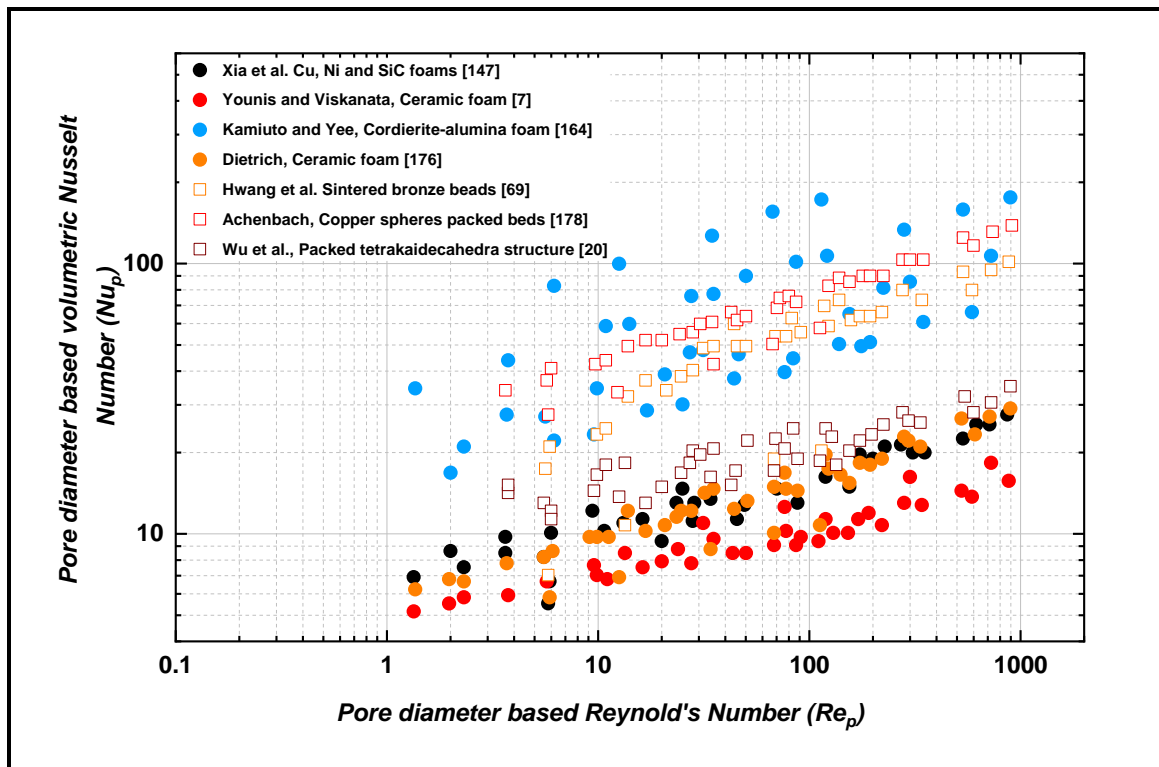
Figure 3.2 Nusselt number vs Reynold's number for different porous media structures [147].

Several experimental studies in the past have attempted to obtain detailed information on the impact of structural parameters on the volumetric Nusselt number. Different combinations of porosity and pore size had a different impact on the volumetric Nusselt number which is predominantly determined by the change in thermal conductivity [30]. The volumetric Nusselt number was found to increase with either decreasing the porosity or pore size [7][30][69][147]. It is proportional to the pore density and increases as the PPI increases (the cell size decreases) [7][147][166]. At constant porosity, the volumetric Nusselt number was found to increases with the specific surface area and mesh size [18]. This has been attributed to the fact that an

increase in the pore density increases the surface area per unit volume and increases the convection heat transfer coefficient, thus, the volumetric convection heat transfer coefficient increased [177]. The Nusselt number has also been shown to depend strongly on the test specimen thickness [7][146][166]. It increased as the thickness decreased which might be due to the impact of the thermal and hydrodynamic entrance [166].

3.2 Measurements of heat transfer coefficient.

It is difficult to measure the local heat transfer coefficients due to the small pore size and the unavailability of sufficiently tiny probes to measure the velocity or surface temperature for a regenerator. Therefore, in most studies on regenerators, the average volumetric heat transfer coefficients are measured to assess their heat transfer performance. The measurement practices involve idealising the experiment facility so initial and boundary conditions are controlled to accurately simulate real-life heat exchanger working conditions. There are two reported techniques for measuring the heat transfer coefficient of porous media: steady-state and unsteady-state techniques (transient technique). Each of these techniques can themselves be further sub-classified.

The steady-state technique has been widely used to produce much data on heat transfer in regenerators, mostly at a high Reynolds number. In this technique, the internal structure of the sample is heated from a source on the substrate walls and measurements are taken when the temperatures of the matrix and the downstream fluid reach the steady-state condition [18][30][57][69][146]. The volumetric heat transfer coefficient can then be obtained from the difference in temperature between the substrate wall and the fluid, using Newton's law of cooling (the energy provided by the heater is compared to the energy gained by the working fluid). This technique involves the difficult task of controlling the conditions for steady-state operation. The testing system should also be thermally insulated while air at a slightly lower temperature flows through it. It has been argued that this technique becomes unreliable at a lower range of Reynolds numbers, the lower temperature difference between the fluid, and when the solid is small [152]. Kays and London [152] argued that the accuracy of this method depends on the error in flow measurement, the point and average bulk temperature due to spatial variation, and also that this method is

restricted for $0.5 < NTU_s < 3$. For $2 < NTU_s < 3$, it was shown a small error in the measured temperature leads to an excessive error in the determination of heat transfer coefficient [179]. Moreover, this technique has implicit limitations as it is strongly dependent on the thickness and the thermal conductivity of the tested sample normal to the flow direction as the heat source located at the side surface of the tested sample [30]. In other words, the central part of the sample might be cooler than the side surface while the volumetric heat transfer coefficient is only based on the side surface temperature.

Subsequently, the unsteady-state technique (known also as transient technique) has become more commonly used. It is believed to be a more effortless and straightforward technique to evaluate the thermal performance of heat exchangers [157][176][180][181][182][183][184][185]. It is cost-effective and less time consuming compared to the steady-state technique. The methodology is simple and is composed of three steps: an experiment, theoretical model and a matching technique [41][186][187]. The experiment requires a constant flow rate of fluid, usually air, that flows through the test heat exchanger. The sample can either be hot with the cold fluid being applied to cool it down, or it can be cold with a hot fluid instantaneously heating it up. Also, the sample and the flowing fluid must be in thermal equilibrium before a perturbation is introduced into the upcoming fluid temperature.

Once the perturbation has been applied, the temperature-time profiles before and after the testing sample are monitored and recorded. Since there is a unique relationship between the temperature-time profiles and the number of transfer units of the heat exchanger NTU_s, the heat transfer coefficient can be determined by employing an inverse analysis with the outlet fluid temperature response as a main input condition [147][157][180][185]. The recorded data can be compared with the predicted data based on an appropriate mathematical model that describes the test heat exchanger and passing air. Consequently, the NTU_s and the average heat transfer efficient h_s can be determined. In contrast to the steady-state technique, the tested sample is assumed to have a uniform temperature in the transverse direction and the results obtained with the transient technique should be more or less independent of the thermal conductivity of the material of the tested sample [30]. However, it has been reported that a transient technique should be used to evaluate the thermal performance of a test heat exchanger for $NTUs > 3$ as if this value were to

35

be lower, it would lead to high uncertainty in the measured data [13]. Fuller et al. [30] compared the transient and steady-state measurement techniques using the Calmidi [161] and Hwang et al. [69] results for aluminium foams. They observed that the values obtained from the transient measurements were about 3 times higher than those from the steady-state measurements. The difference in the results was due to the Biot number effects. They pointed out that the heat transfer coefficient obtained from the transient method is more reliable than that attained by a steady-state.

The unsteady-state technique can be subdivided into two main categories, based on the inlet fluid temperature variation: frequency response (periodic method) [181][188], or single-shot (single-blow method) [53][158][173][189]. The frequency method involves the introduction of sinusoidal changes at the fluid inlet temperature while the exit gas temperature is logged. The heat transfer coefficient h_s may be determined from the amplitude ratio or phase lag of the upstream and downstream temperatures [181]. This technique has been shown to provide reliable results at very high frequencies. However, this may be a misconception since, at very high rates, heat can only penetrate the solid surface [152], which is contrary to the assumed boundary conditions of the appropriate model. In addition, the accuracy of the periodic method depends on the period of oscillation. Large NTU_s values require a longer testing period, and a suitable period selection requires prior knowledge of NTU_s [185]. Therefore, the single-blow transient technique has become a more common transient technique.

3.2.1 Single-blow technique

The thermal performance of heat exchangers and thermal regenerators are commonly evaluated by the single-blow technique. The name 'single-blow' means only one single flow is required. The principal advantages of this technique are that it is simple to perform and cost-effective to generate experimental tests in a short time [55][125][190][191]. Hence, numerous experimental and analytical data have been produced using the same method, making them available for comparison. In this technique, a porous structure is initially prepared to be at a low uniform temperature and in equilibrium with the fluid passing through it. The passed fluid temperature is suddenly changed to a higher temperature using a fast switching method. The fluid and solid temperature histories become a function of time and position along the tested sample. Assuming the heat transfer mechanism is mainly forced convection and the

average heat transfer coefficient h_s remains constant, the heat transfer coefficient h_s can be determined with aid of an appropriate model.

Hausen [192] first formulated the original mathematical model describing the phenomenon as a differential equations system. Schumann [154] first analysed and simplified the problem to derive an analytical solution for Hausen's model for an ideal step change input. The analysis is based upon an energy balance on an element of the porous solid (see Figure 3.3). Assumptions and idealisation he made were:

- An incompressible flow passes in a cylinder consisting of solid crushed material at a uniform rate.
- The heat transfer mechanism is entirely by convection from fluid to solid.
- The solid particles are microscopic or have high thermal diffusivity normal to the flow direction.
- The change of the fluid and solid volumes due to the change in their temperature is equal to zero.
- The transfer of heat by conduction in the fluid itself or in the solid itself is minimal and can be neglected.
- The heat transfer rate from a fluid to a matrix at any point is proportional to the average difference in temperature between the air and the matrix at that point.
- The thermal properties of the fluid and solid are independent of the heat.
- The matrix is initially at a uniform temperature.
- At a time equal to zero, the temperature of the entering fluid changes instantaneously to a different, constant value, i.e., a step-change in fluid temperature.
- The outlet fluid temperature will eventually arrive at the initial temperature of the entering fluid (The matrix boundaries are adiabatic).
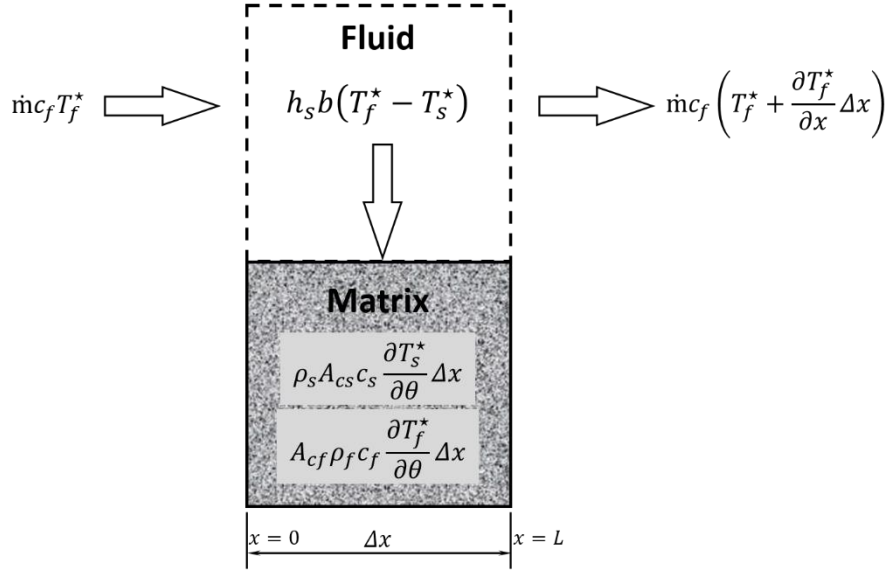
Figure 3.3 Energy balance for fluid and solid body for heater exchanger element.

Based on the energy balance in an element Δx of the control volume, one can have the governing equations for fluid and solid temperatures, respectively, as

$$\dot{m}c_f \frac{\partial T_f^\star}{\partial x} \Delta x + h_s b\left(T_f^\star - T_s^\star\right)\Delta x - A_{cf}\rho_f c_f \frac{\partial T_f^\star}{\partial \theta} \Delta x = 0 \qquad 3.4$$

$$\rho_s A_{cs} c_s \frac{\partial T_s^\star}{\partial \theta} \Delta x - h_s b\left(T_f^\star - T_s^\star\right)\Delta x = 0 \qquad 3.5$$

Where

- $T_f^\star$ and $T_s^\star$ are fluid temperature and solid temperature respectively. Both are functions of time and position.

- b is the flow passage perimeter, θ is time and $\dot{m}$ is the fluid mass flow rate,

- A_c is the cross-sectional area, ρ is density and c is specific heat. Subscripts (s) and (f) indicate solid and fluid, respectively.

- $\rho_s A_{cs} c_s \frac{\partial T_s^\star}{\partial \theta} \Delta x$ is energy adsorbed by solid.

- $h_s b\left(T_f^\star - T_s^\star\right)\Delta x$ is heat transferred to the solid by convection.

- $A_{cf}\rho_f c_f \frac{\partial T_f^\star}{\partial \theta} \Delta x$ is heat accumulated by the fluid within the element.

- $\dot{m}c_f \frac{\partial T_f^\star}{\partial x} \Delta x$ is heat transferred from the fluid by convection.

Schumann introduced two terms to generalise the solution and minimise the number of variables in the energy governing equations - the generalised time equation 3.6) and the generalised position equation (3.7), as follows:

$$t = \frac{h_s A_{TH}}{m_s c_s} \left[\theta - \frac{m_f}{\dot{m}} \frac{x}{L}\right] \tag{3.6}$$

$$X = \frac{hA}{\dot{m}C_f} \frac{x}{L} = NTU_s \frac{x}{L} \tag{3.7}$$

In most practical applications, the energy accumulated by the fluid within the sample at any time is neglected $(A_{cf}\rho_f C_f \frac{\partial T_f}{\partial \tau} \Delta x \simeq 0)$, and the transition time ($m_f xt/\dot{m}L$) is assumed to be equal to zero [183][193][194]. The final form of the generalised time can be rewritten as:

$$t = \frac{h_s A_{TH}}{m_s c_s} \theta \tag{3.8}$$

Letting the fluid, and solid temperatures in the dimensionless form:

$$T_f = \frac{T_f^\star - T_0^\star}{T_{f\,max}^\star - T_0^\star}, \qquad T_s = \frac{T_s^\star - T_0^\star}{T_{f\,max}^\star - T_0^\star} \tag{3.9}$$

The final form of the mathematical model in the non-dimensionalised form can be expressed as:

$$\frac{\partial T_f}{\partial X} = (T_s - T_f) \tag{3.10}$$

$$\frac{\partial T_s}{\partial t} = (T_f - T_s) \tag{3.11}$$

Using the initial and the boundary conditions in Equation 3.12, Schumann's analytically driven solution predicts the temperature distribution for the fluid and solid at any position and time in dimensionless form. Schumann's solution is a function of the modified Bessel function of the first kind of zero-order J_0. Equation 3.13 and Equation 3.14 are Schumann's solutions for the fluid and solid temperatures distribution, respectively.

$$
\begin{aligned}
X = 0 \qquad & T_{fin} = 1 \qquad T_s = 0 \\
t = 0 \qquad & T_s = 0
\end{aligned}
\tag{3.12}
$$

$$T_f = 1 - e^{-(X+t)} \sum_{n=1}^{\infty} X^n \frac{d^n}{d(Xt)^n} \left(J_0 \left(2i \sqrt{Xt} \right) \right)$$

3.13

$$= e^{-(X+t)} \sum_{n=0}^{\infty} t^n \frac{d^n}{d(Xt)^n} \left(J_0 \left(2i \sqrt{Xt} \right) \right)$$

$$T_s = 1 - e^{-(X+t)} \sum_{n=0}^{\infty} X^n \frac{d^n}{d(Xt)^n} \left(J_0 \left(2i \sqrt{Xt} \right) \right)$$

3.14

$$= e^{-(X+t)} \sum_{n=1}^{\infty} t^n \frac{d^n}{d(Xt)^n} \left(J_0 \left(2i \sqrt{Xt} \right) \right)$$

In most transient single-blow problems, the distribution of fluid temperature (T_f) is of particular interest. Curves of dimensionless fluid temperature, shown in Figure 3.4 as a function of X and t have been constructed from computations made by the current author on Equation 3.13. These curves show the dimensionless fluid temperature anywhere within the porous solid at any time.
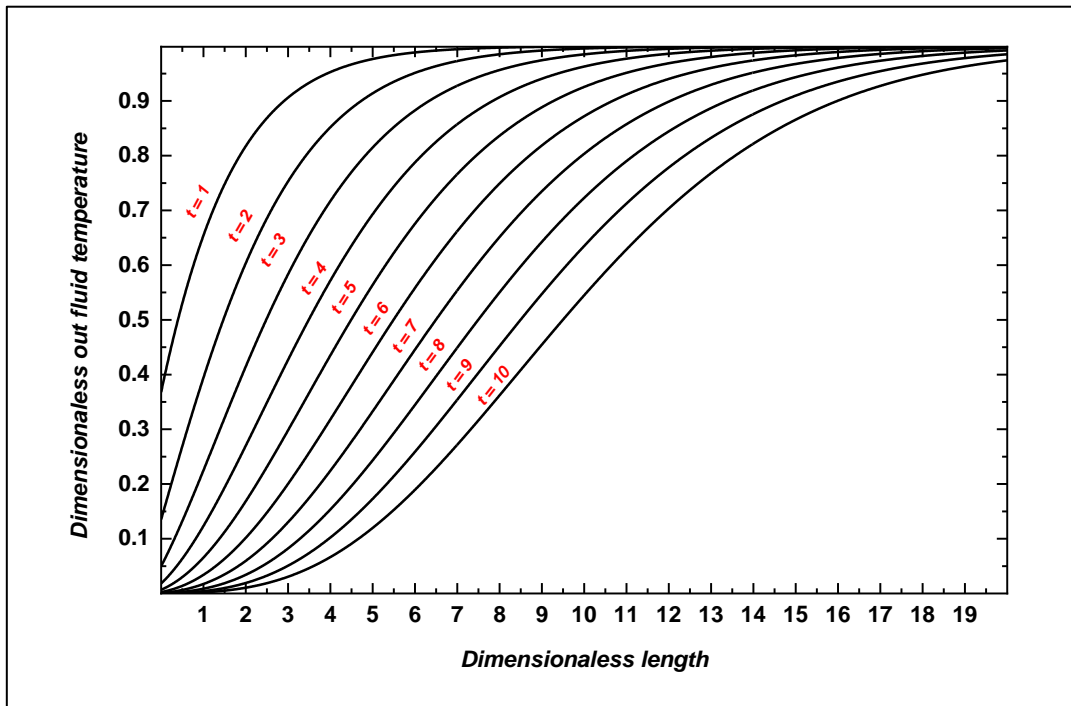
Figure 3.4 Out fluid temperature response against the matrix length at a different time (dimensionless form).

This is the traditional method of presenting Schumann's solution [195]. However, it does not reveal the rate of heat transfer from the fluid to solid. The

standard method is presenting Schumann's solution at the outlet of the tested sample, where $x = L$ and $X = NTU_s$. Moreover, the generalised time is replaced by the modified dimensionless time U, which is merely the physical time in seconds divided by the constant ratio. The constant ratio is called a solid-fluid system constant τ_{sys} and can be obtained from the measured data for any single run:

$$U = \frac{t}{NTU_s} = \frac{\theta}{\tau_{sys}} = \frac{\theta}{\left(m_s c_s / \dot{m} c_f\right)} \qquad 3.15$$

Figure 3.5 shows the response curves for the ideal step change over the complete range of NTU_s values as a function of the modified dimensionless time. The solution has been computed numerically by many researchers, including the current author for the initial and boundary conditions given in Equation 3.12 [180][195]. It is apparent for NTU_s values approximately equal to five that there is a significant instantaneous breakthrough of the outlet fluid temperature at zero time. As the NTU_s increases, the sharpness of the curve becomes more pronounced, which reveals a high heat transfer rate between the fluid and the solid.
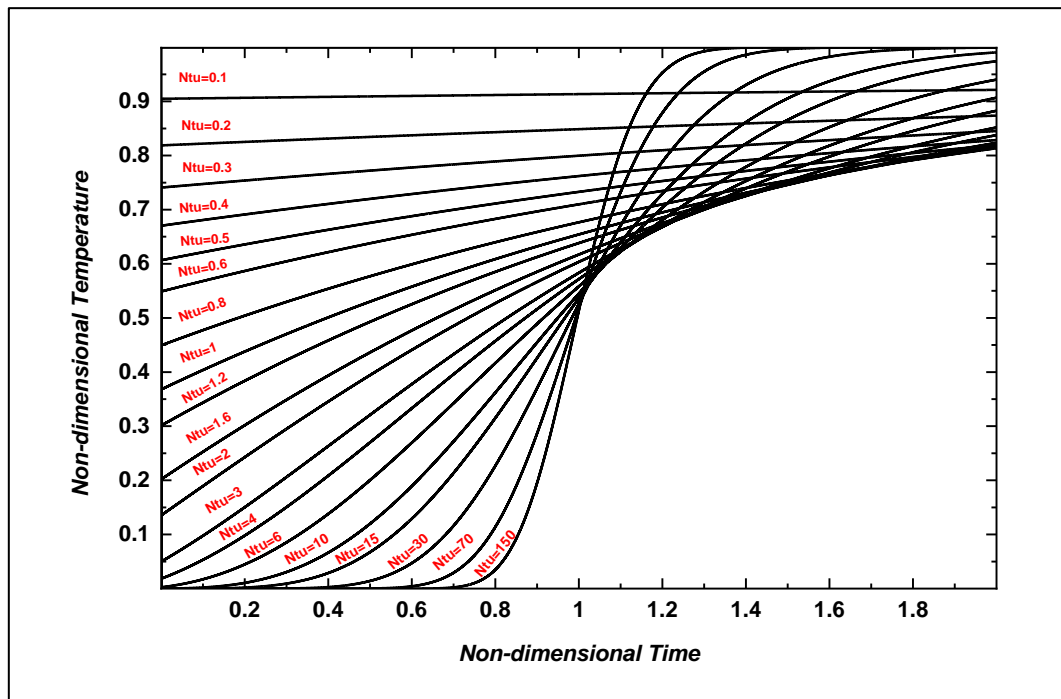
Figure 3.5 Outlet response curves against time at different NTU_s for a step change input (dimensionless form).

3.2.2 Modified Schumann-Hausen model

The simplifications and idealisations in Schumann's mathematical model were seen as somewhat crude and weak. Thus, many investigators have attempted to develop Schumann's model to make it coincide as closely as possible with the actual heat transfer mechanisms. The developed models have taken into account additional parameters which have a measurable impact on the heat transfer mechanism, including the inlet fluid temperature variation, the longitudinal conduction in the test core, the Joule-Thomson effect, and the energy loss of the sidewall [13][158][185][196]. However, different outlet fluid temperature response curves can be obtained from different models. The variation depends on the influence of the considered parameters. Neglecting some of these parameters may result in the mathematical model possibly failing to describe the experiment accurately, and the theoretical solution might not coincide with experiment data [156][181]. Therefore, it is worth understanding the impact of these parameters on the predicted outlet temperature curve.

3.2.2.1 Arbitrary fluid inlet temperature

A stepwise inlet fluid temperature change requires a rapid system to switch the fluid streams from cold to hot or vice versa at zero time. Many investigators have made this assumption without considering its impact on the outlet temperature response curves [181]. As it is nearly impossible, in real life, to achieve a zero-time switching method, time-inlet fluid temperature variation is usually measured; subsequently, it can either be fed directly into the mathematical model or used to determine a well-defined expression that describes the temperature change behaviour. The simplest single-blow model has been developed for two-fluid inlet temperature variations, exponential forcing function, and periodic or arbitrary variation. Whatever the single-blow input type, a dimensionless time constant τ, given in Equation 3.16, is usually used to define how rapid the switching method is in the experiment [181][191]. It is the ratio of the measured inlet fluid temperature time constant τ_i to the solid-fluid system constant τ_{sys}. The time constant τ_i is the measured time in seconds required by the inlet fluid to reach the maximum temperature. If a hot fluid is heated up using a packed-screen heater, the time constant τ is about 0.1.

$$\tau = \frac{\tau_i}{\tau_{sys}} = \frac{\tau_i}{(m_s c_s / \dot{m} c_f)} \tag{3.16}$$

Liang and Yang [191] measured the fluid inlet temperature experimentally. They proposed a first-order exponential function, given in Equation 3.17, to describe the inlet fluid temperature variation with the non-dimensionalised time t.

$$T_{fin\,(t,0)} = 1 - EXP^{(-t/\tau)} \tag{3.17}$$

They were able to derive an analytical solution for the single-blow model considering this forcing function type, using the Laplace transform technique. The detailed process to obtain the analytical solution is very tedious; therefore, a numerical solution was obtained in this study. The initial conditions given in Equation 3.12 were modified to include the exponential function (Equation 3.17) instead of step-change in inlet fluid temperature. The impact of this function on the exit temperature curves is demonstrated in Figure 3.6.
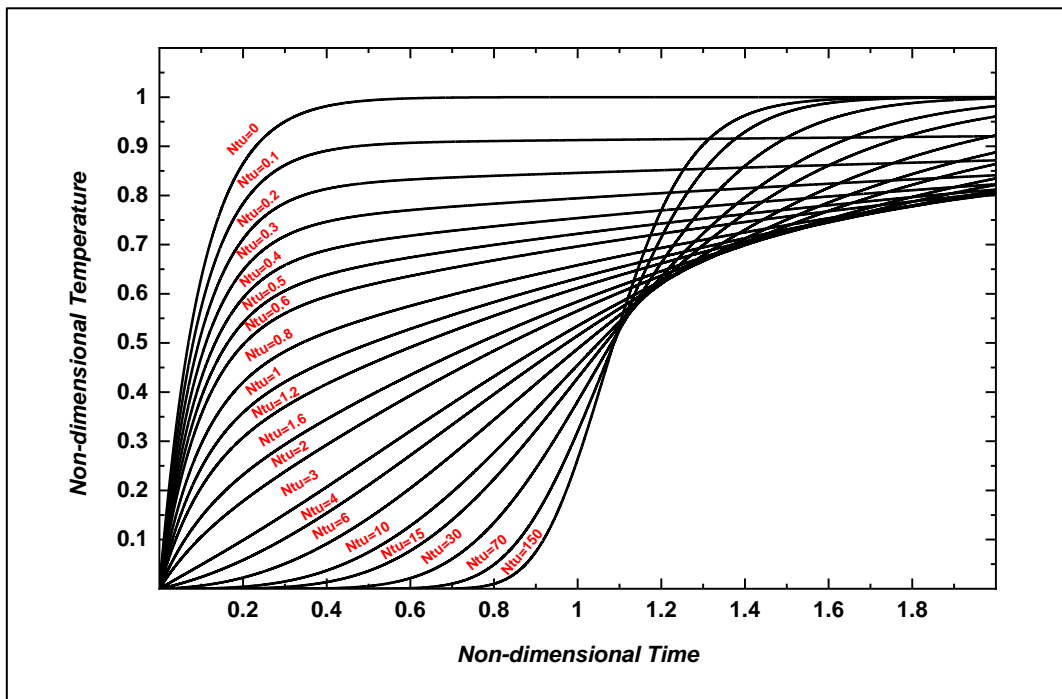
Figure 3.6 Response curves of an exponential inlet fluid temperature change with τ.

By comparing the theoretical response curves in Figures 3.4 and 3.5, it can be seen there is a significant impact on the shape of the outlet temperature curves due to changing the inlet forcing function. All response curves have moved to the right-hand side. As the NTU_s becomes more extensive, the corresponding curves become

less steep in comparison with the ideal step forcing function. Moreover, at infinity NTU_s value, the outlet temperature curve is not vertical as in the step-change case, but the curves' points are displaced in the same way as the inlet fluid temperature points. This means that ignoring this shift in the theoretical curves may lead to a lower estimation of NTU_s value. The magnitude of the discrepancy will increase as the time constant τ becomes greater.

3.2.2.2 Longitudinal conduction effect

Some regenerators have large longitudinal conduction and neglecting this effect may introduce an error in the estimation of the heat transfer coefficient. The earliest workers who considered the longitudinal conduction effect on the outlet fluid temperature distribution were Howard and Pucci [183][196]. A second-order partial differential term, multiplied by the conduction parameter λ_s has been added to the solid energy Equation 3.11, which can be rewritten as:

$$\frac{\partial T_s}{\partial t} - \lambda_s \frac{\partial^2 T_s}{\partial X^2} + NTU_s(T_s - T_f) = 0$$
3.18

The dimensionless constant λ_s can be estimated if the effective thermal conductivity is known and when the geometry has a uniform shape. Otherwise, the modified model becomes a function of two unknown variables NTU_s and λ_s values [185][189][197]. These are modified simultaneously to match theoretical and experimental curves. Once the matching has been achieved, the two thermal parameters are considered as the thermal characteristic of the test core. Adding a second-order partial differential term to the solid equation makes it difficult to solve the problem theoretically. Therefore, the approximation method (the Finite difference scheme) is usually implemented to obtain the solution numerically [69][183][184][198]. Figure 3.7 demonstrates the influence of the axial conduction on the predicted outlet temperature curves. If the axial conduction parameter has a large value, the difference between the inlet and outlet fluid temperatures becomes smaller and the initial temperature rise becomes sharper.

Before proceeding further, it is worthy to note that the following graphs were generated by solving numerically an advanced single blow model for the cases of a step-change in inlet fluid temperature as will be showed in the following chapter.

44
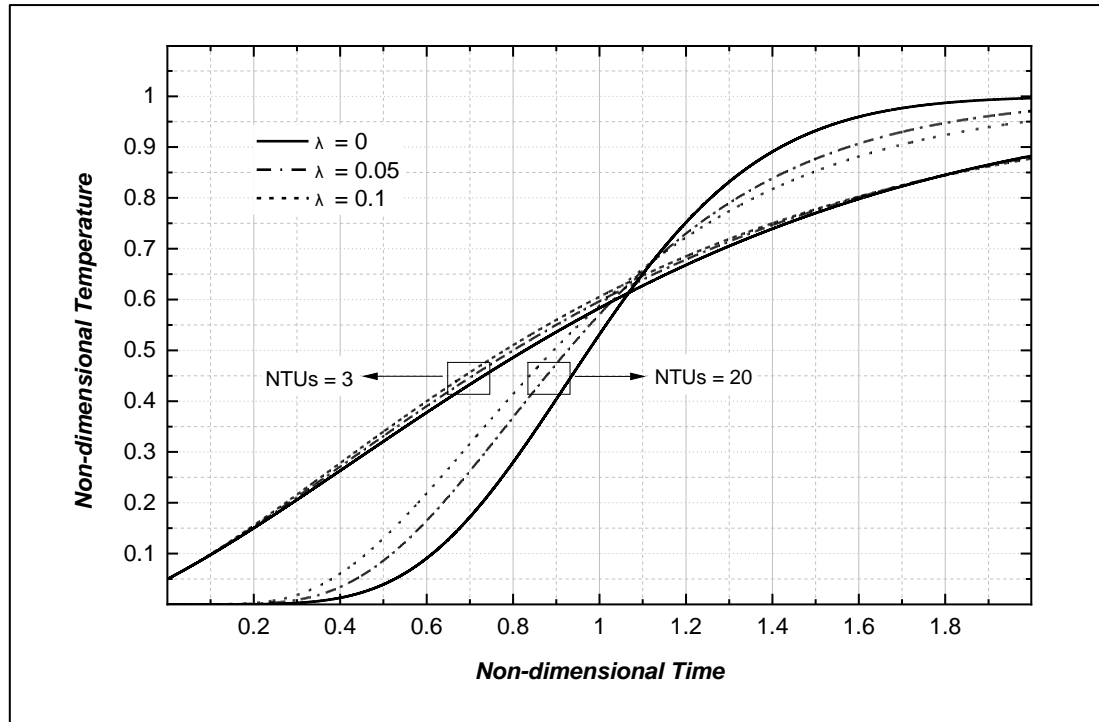
Figure 3.7 Effect of longitudinal conduction on the outlet temperature curves.

For an ideal step in the fluid inlet temperature, Pucci et al. [183] warned of the effect of longitudinal conduction at high NTU_S values as a slight alteration in the conduction parameter λ_s has a marked impact on the estimated NTU_S value. Krishnakumar and Venkatarathnam [197] investigated the axial conduction effect into four perforated hear exchangers consisting of stainless steel and paper plate-spacers for step-change inlet fluid temperature. They found a 10% error in the estimation of λ_s led to 40% overestimation or underestimation of NTU_S. Cai et al. [187] investigated the impact of the longitudinal conduction on the predicted outlet temperature profile but for exponential inlet fluid temperature input. They stated that the axial conduction cannot be neglected for $NTU_S \geq 3$ or if $\lambda_s * NTU_S \geq 0.06$, otherwise the NTU_S value may be underestimated. Mullisen and Loehrke [185] used measured inlet fluid temperature and considered the longitudinal conduction in their model. A large number of parameters were covered ($0.1 \leq NTU_S \leq 20$) and ($0 \leq \lambda_s \leq 30$) to evaluate the thermal performance of heat exchangers. They concluded that when $\lambda_s \geq 10$, the response curve is very close to the exact solution for $\lambda_s = \infty$. Chen et al. [158] showed that for NTU_S in the range between 60 and 150, the predicted outlet fluid temperature curves cannot easily be distinguished, and the curves are even closer once the longitudinal conduction is considered.

45

3.2.2.3 Joule-Thomson effect

The Joule-Thomson effect takes place generally in non-ideal gases operation systems and when the heat exchangers have a large NTU_s value [13][55]. Expansion occurs in the working fluid due to a high-pressure drop $(\Delta p \geq 0.1 MPa)$ along the sample. As a result, the steady passage flow experiences a slight linear decrease in the temperature as it passes through the test core. When this effect was included, an additional constant appeared in the fluid energy equation. It was shown that this constant has no impact on the shape or the slope of the outlet temperature profile, but it results in a shift of the entire curve up or down, which should be considered in the direct matching method.

3.2.2.4 Side-wall effect (non-adiabatic side-wall)

One source of the inaccuracy of the single-blow results is neglecting the side-wall heat capacity. If the tested core is tightly fitted within the case's inner circumference, or when measurement requires a long period of operation, assumptions relating to adiabatic walls may lead to severe errors in the obtained thermal characteristics. Chen et al. [13][55][158][159] carried out a series of investigations on the influence of the sidewalls on the thermal performance of regenerators of packed fine stainless steel wire-screen having large NTU_s, both individually and in combination with other effective parameters. Table 3.1 compares the modelling parameters in each study.

Table 3.1 Series of investigations on the influence of the sidewall.

Ref	Axial conduction	Non-adiabatic side-wall	Axial conduction in the wall	J-T Expansion	Inlet fluid temperature
[13]	No	Yes	No	No	Arbitrary
[55]	No	Yes	No	No	Exponential
[158]	Yes	Yes	Yes	No	Exponential
[159]	Yes	Yes	Yes	Yes	Arbitrary

When the heat flux into the side-wall and Joule-Thomson were considered, an additional time-position dependent temperature equation was added to the single-blow heat transfer system (Equation 3.20). The Joule-Thomson effect μ_j was counted in the fluid Energy equation (Equation 3.19). The side-wall has been represented by three dimensionless groups: the number of transfer units of the wall NTU_w, heat capacities ratio R_{tc}, and wall conduction parameter λ_w and an extra variable T_w. The equation has been given as:

$$\frac{\partial T_f}{\partial X} + NTU_s\left(T_f - T_s\right) + NTU_w\left(T_f - T_w\right) = \mu_j \qquad 3.19$$

$$\frac{\partial T_w}{\partial t} - R_{tc}.\lambda_w \frac{\partial^2 T_w}{\partial X^2} + NTU_w\left(T_w - T_f\right) = 0 \qquad 3.20$$

The dimensionless parameters R_{tc} and λ_w can be determined from the physical and thermal properties of the tested core and the side-wall. The NTU_w can be obtained simultaneously with NTU_s value [55][159] using the curve matching scheme. The finding from Chen et al.'s series of investigations showed that the NTU_s values were underestimated by 31% due to assumptions relating to the adiabatic side-wall.

As there are two unknown parameters, it was practical to introduce a new definition, called R_{NTU}, which is the ratio of the number of transfer units of the side-wall to the number of transfer units of the solid [13][158], expressed in Equation 3.21. The value of R_{NTU} can be assumed as the ratio of the heat transfer surface area of the side-wall to the heat transfer surface area of the solid [158]:

$$R_{NTU} = \frac{NTUw}{NTU_s} \qquad 3.21$$

The impact of side-wall on the outlet fluid temperature response is illustrated in Figures 3.8 and 3.9. It can be seen that the longitudinal conduction into the side-wall does not affect the outlet fluid temperature response for small NTU_s values. Therefore, this parameter can be neglected.
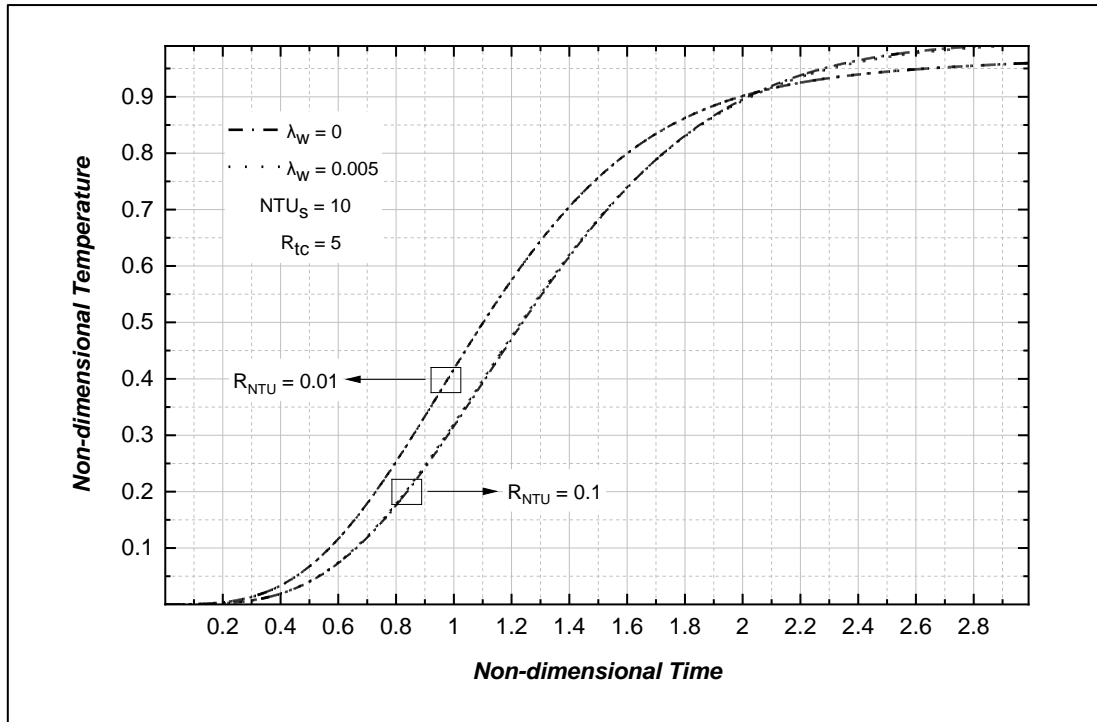
Figure 3.8 Outlet fluid temperature curves with the effect of side-wall and λ_w=0.005.

Figure 3.9 illustrates the effect of the non-adiabatic side-wall on the outlet fluid temperature response curves for a heat exchanger having $NTU_s = 10$. It can be noticed the wall effect increases with R_{NTU} and decreases with R_{tc}. For a small R_{NTU} value, the wall effect on the initial rise of the predicted curves is lower at $t < 1.5$. Once the matrix reaches the thermal equilibrium state with hot fluid $t > 1.5$, the wall effect becomes dependent on the mass of the side-wall. More heat dissipates through the side-wall as the mass of the side-wall increases (a decrease in R_{tc} value). The predicted fluid temperature curves are more sensitive to the R_{tc} value if the R_{NTU} is large. For constant side-wall mass (constant R_{tc}), increasing the side-wall heat transfer surface area (increase R_{NTU}) causes the outlet fluid temperature to reach the maximum temperature more quickly. This is due to a more considerable heat flux from the hot fluid to the side-wall.
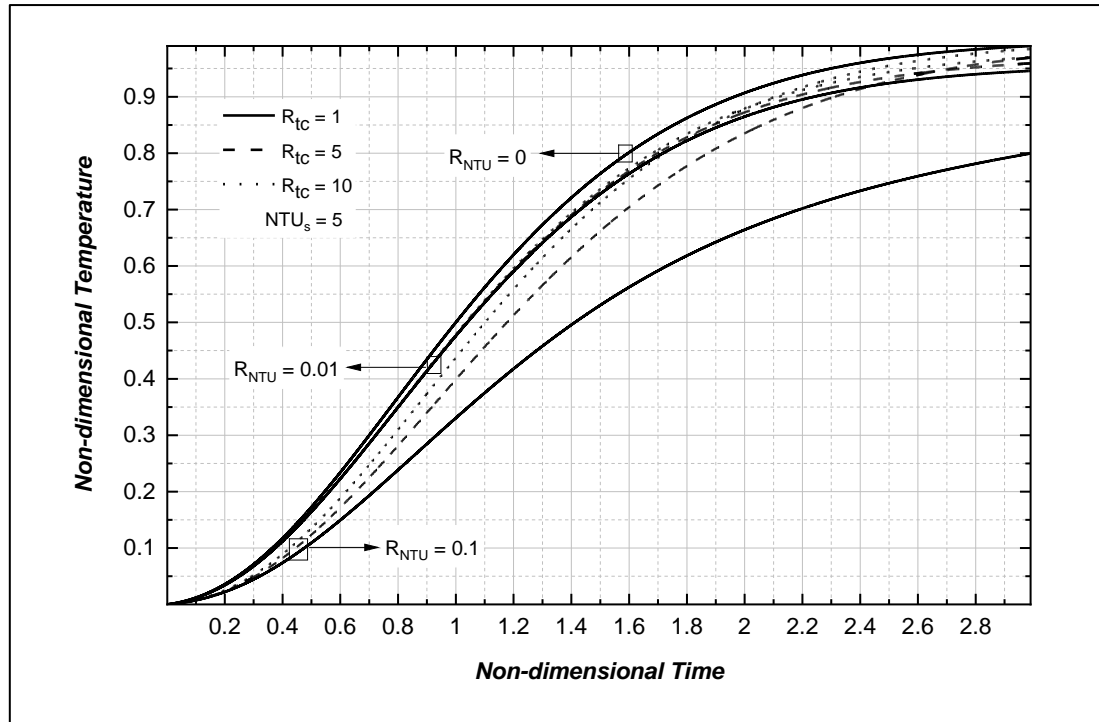
Figure 3.9 Outlet fluid temperature curves with the effect of side-wall and λ_w=0.

3.3 Data reduction for single-blow technique

As mentioned earlier, the single-blow method aims to determine the average heat transfer coefficient by matching the theoretical and experimental outlet fluid temperatures for a sudden inlet fluid temperature rise. Three schemes are commonly adopted to match the experimental data to the theoretical data: direct and indirect matching schemes, and a hybrid-matching scheme which involves both the direct matching and one of the indirect matching schemes.

3.3.1 Direct Matching Method (Curve Matching Scheme)

The Schumann model has been extensively used to determine the heat transfer data experimentally for different geometries of porous structures, including porous media with low mass cores such as heating and cooling heat exchangers and high mass cores as in regenerative type heat exchangers. Furnas [199] made an early experimental study of the heat transfer coefficient h_s between beds of iron balls and a fluid flowing through them. He recorded the temperature-time history of the fluid and compared it to the theoretical curves from Schumann's solution. A value of NTU_s was assumed, and the experimental and predicted curves of time-wise exit temperatures were observed visually. By picking the theoretical curve which fitted the experimental curve within specified limits, Furnas was able to extract the average heat transfer

coefficient of a specific bed. This graphical procedure is known as the direct curve matching approach. More recently, this matching technique has been improved. Instead of matching the entire curve, Liang and Yang [191] suggested selecting five points equally spaced on the experimental temperature to be matched. The points are selected for response times between one and nine seconds. The theoretical and the experimental curves are matched at the first selected point. If the matching coincides with an acceptable limit of accuracy (0.5 per cent or less), a new matching point at a more considerable time is selected, and the procedure is repeated. The arithmetical mean of the five heat transfer coefficients is then taken as the average heat transfer coefficient for the test run.

Cai et al. [187] argued that the uncertainty in the temperature measurements at the five selected points influences the predicted NTU_s value. They proposed selecting five matched points within an optimum matching time interval to minimise the effect. An empirical formula which is a function of NTU_s, an inlet fluid temperature time constant τ and an axial conduction parameter λ_s were derived to determine the optimum time selection. Mullisen and Loehrke [185] performed the direct matching method on a digital computer using a "MATCH" FORTRAN program. They employed an algorithm that treats the error and minimises the area between the experimental and the theoretical outlet temperature curves as a function of the heat transfer coefficient. These researchers recommended this method in a short time test run, so that the sidewall temperature remains constant.

3.3.2 Indirect matching methods

Despite the reliability of the direct matching method, it is still based on human judgement. Moreover, relatively high computational effort and time are required to implement it. Consequently, alternative indirect matching techniques have been proposed by some researchers to reduce the amount of single-blow transient data. In general, the principle of the indirect matching methods is to identify an expression that can describe the experimental outlet fluid temperature as a function the NTU_s value and the dimensionless time only.

3.3.2.1 Maximum slope method

This is the most popular single-value evaluation method, pioneered by Locke [195] in the middle of the 19th century. The maximum slope value S_{max} designates the

maximum value of the first derivative of the dimensionless exit fluid temperature response curve. Locke differentiated Schumann's solution (Equation 3.13) to reveal the unique relationship between the maximum slope values S_{max} and the number of transfer units, shown in Equation 3.22.

$$\frac{d\left(\dfrac{T_f - T_0^\star}{T_{f\,max}^\star - T_0^\star}\right)}{d\left(\dfrac{t}{NTU_s}\right)} = \frac{NTU_s^{\,2}}{\sqrt{NTU_s t}}\left\{-iJ_1\left(2i\sqrt{NTU_s t}\right)\right\}e^{-(NTU_s + t)} \qquad 3.22$$

This approach has gained wide acceptance primarily because of its simplicity. However, it has been shown that this method is potentially error-prone for small NTU_s values and caution should be taken when $NTU_s < 3.5$ [191]. The first derivative of the theoretical exit fluid temperature curves plotted as a function of the modified dimensionless time is shown in Figure 3.10.
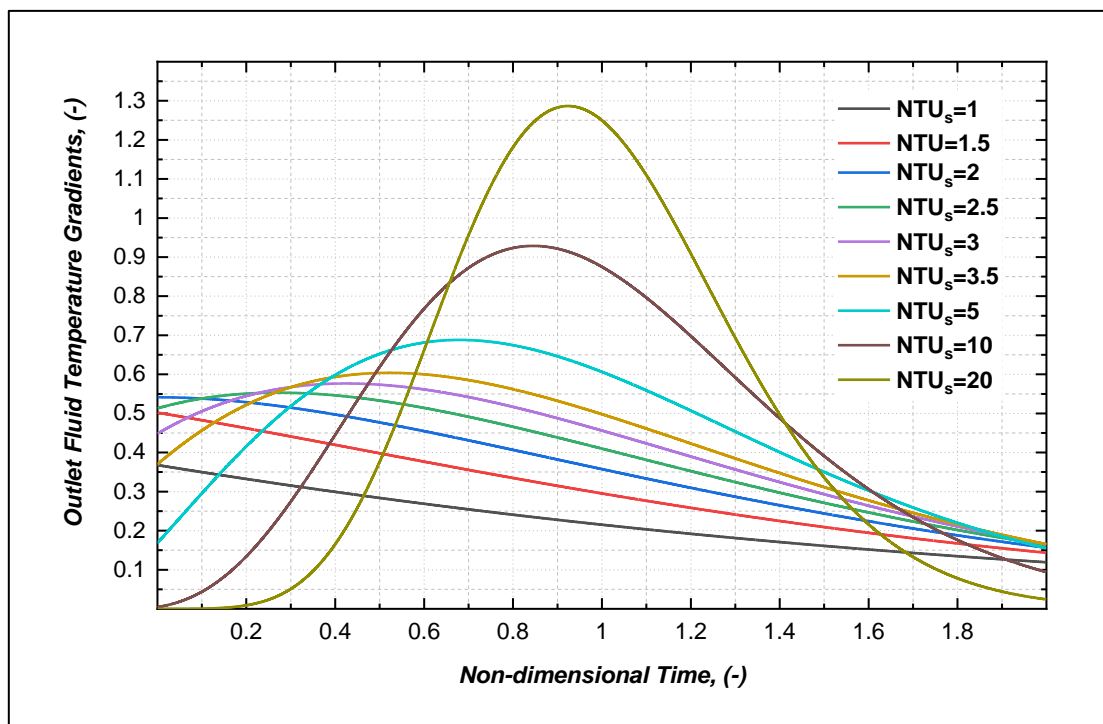
Figure 3.10 The first derivative of the predicted outlet fluid temperature curves versus the dimensionless time.

Kohlmayr [200][201] has driven an exact analytical solution for a single-blow model, assuming an ideal step change for the fluid inlet temperature. The solution was then differentiated to obtain the maximum slope values S_{max} and the reduced time t_{max} at which the maximum slope was achieved. The researcher developed guidelines

for the practical use of this method when the critical value $NTU_s = 2$, and for which the temperature history curve has no inflexion point nor maximum slope value. The author warned of using the maximum slope technique even for $2 < NTU_s < 3$, as small errors in the maximum slope S_{max} may lead to significant failure in the evaluation of NTU_s. Therefore, one must take particular care regarding the number of transfer units in the vicinity of 2.

The plot of NTU_s as a function of the maximum slope is shown in Figure 3.11 for zero longitudinal conduction parameter, adiabatic sidewall and a step-change in inlet fluid temperature. The maximum slope of an experimental curve can be measured and NTU_s can be found in this plot.
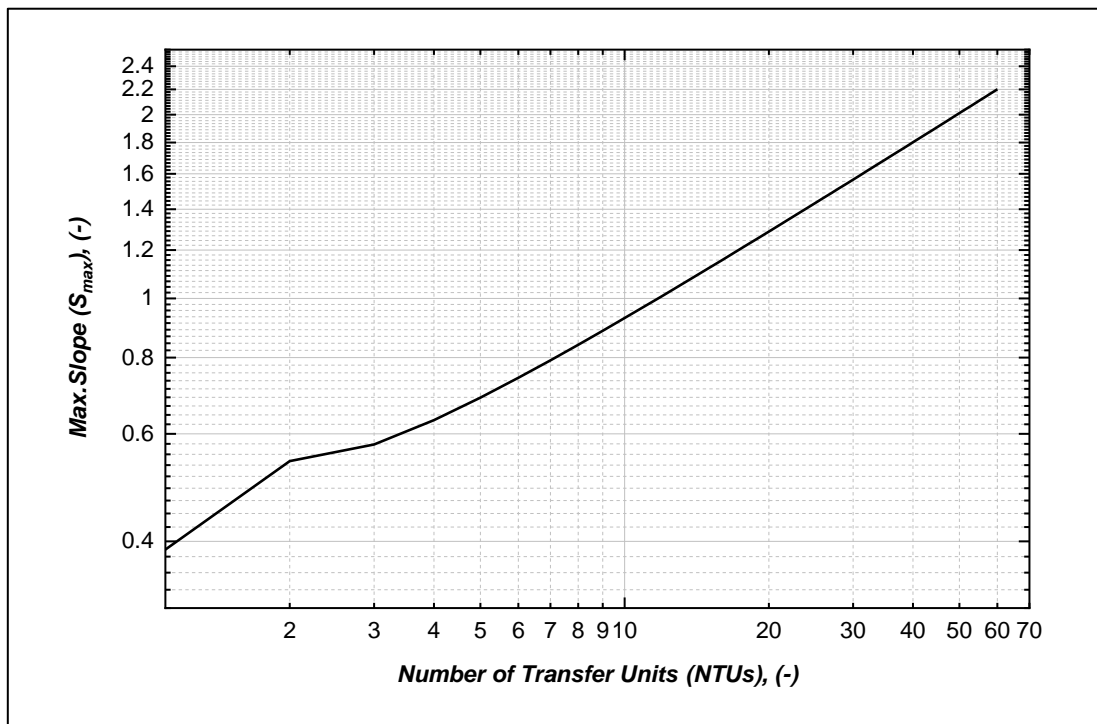
Figure 3.11 Maximum slope as a function of the number of transfer units.

3.3.2.2 The Initial Rise Method

To allow the transient technique to be applied for geometries with low NTU_s values $NTU_s < 3$, for an instant, perforated heat exchanger, Mondt and Siegla [202]

subsequently suggested the first rise method to correlate the outlet temperature curve with the NTU_s.

Looking at Figure 3.5, it can be seen that the fluid outlet temperature curves experience an instantaneous step change at zero time for $NTU_s < 3$. They evaluated the Schumann solution at $t = 0$ to find the relationship between the step temperature rise and the number of transfer units, given in Equation 3.23.

$$T_{t=0} = e^{-NTU_s} \qquad\qquad 3.23$$

It was proven that this relationship is insensitive to the longitudinal conduction parameter λ_s in that range. Mondt and Siegla [202] recommended this method as being highly accurate in the range of $0.16 < NTU_s < 2.3$. However, this method applies only to the case of an ideal step change and when a definite step change can be seen in the outlet temperature curve.

3.3.2.3 The shape factor

Based on the fact that each break-through curve uniquely defines a value of NTU_s, Darabi [152] took advantage of the modified dimensionless time to confirm that time interval between the 20% and 80% points on the break-through curve is solely dependent on the NTU_s. This is demonstrated graphically in Figure 3.12. This time interval is called shape factor S. It can be obtained from the experimental data using Equation 3.24.

$$S = \frac{\dot{m}c_f}{m_s c_s}\Delta\theta_{20-80\%} \qquad\qquad 3.24$$

Darabi [152] employed the Schumann solution to generate the graphical relationship between the shape factor and NTU_s, shown in Figure 3.13. He suggested this method for NTU_s in a range between 1.8 and 20 since at smaller NTU_s the initial rise of the break-through curve is higher than 20% and, for $NTU_s > 20$, the relation between the shape factor and NTU_s becomes insignificant.

53
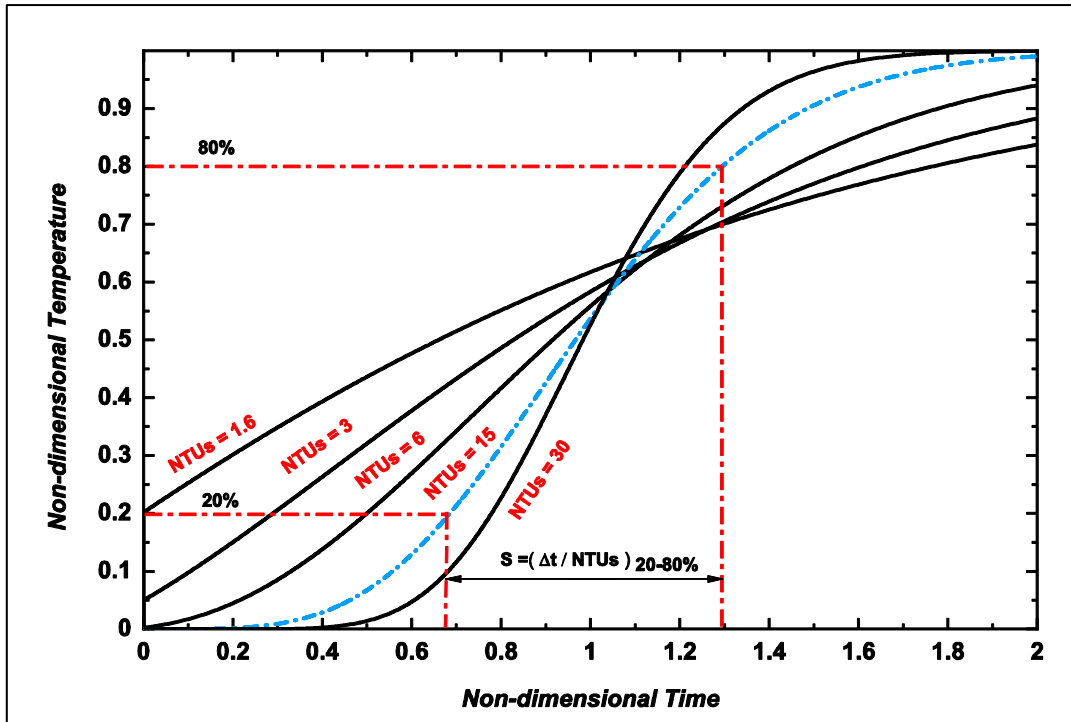
Figure 3.12 Dimensionless time interval between 20% and 80% on the break-through curve.
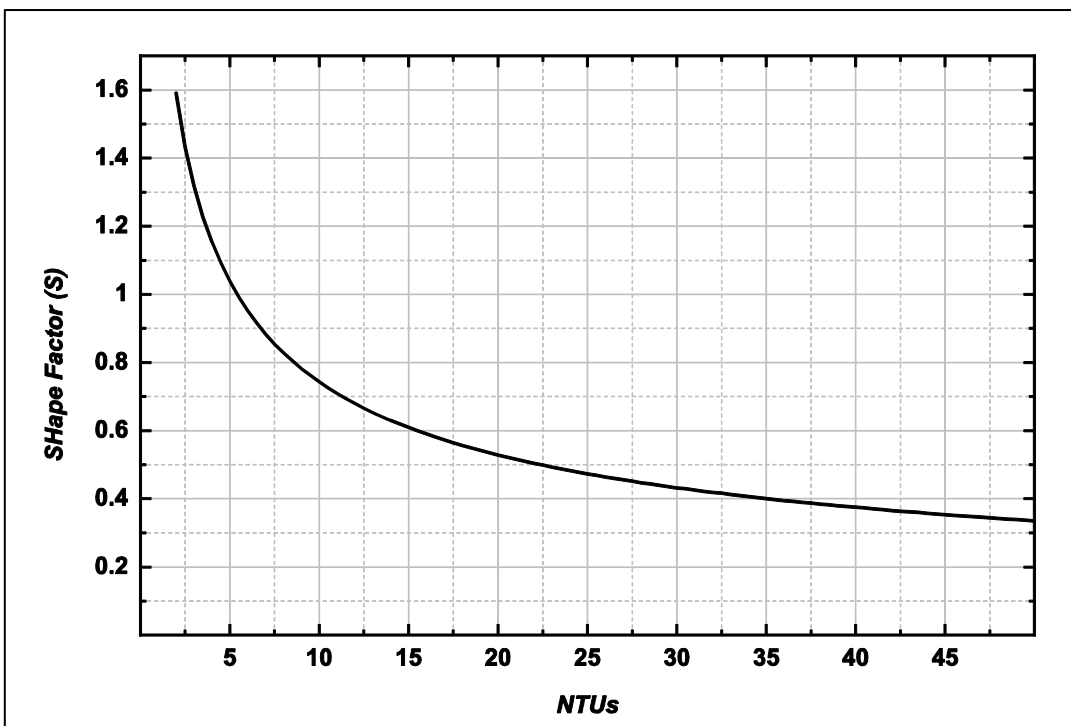
Figure 3.13 The relationship between the shape factors and NTU_s.

54

3.3.2.4 Centroid matching technique

In the previous indirect matching methods, fluid inlet temperature at the test section entrance assumed an ideal step change. This means zero time is required by the fluid inlet temperature to reach the steady-state. In practice, this is not possible, and such an assumption may lead to a significant error as will be shown later. To reduce the uncertainty due to this assumption, Kohlmayr [200][203][193] suggested using a monotonic decrease change as a forcing function to describe the inlet fluid variation in his model. Further, he also proposed another new indirect matching technique, called the centroid matching technique, to reduce the single-blow data in a low range of NTU_s values. This method involves identifying a mathematical function that describes the inlet fluid temperature behaviour as a function of time (monotonic decrease change in the Kohlmayr study). If the outlet fluid temperature is defined mathematically as a function of NTU_s and dimensionless time t, the difference between these two temperatures can be obtained during a particular time, say clip-off at one-tenth of the dimensionless time. It is possible then to determine the total area under the differential curve, shown in Figure 3.14, by performing a computational integration. After that, the first order of moment can be employed to determine the centroid coordinate of that area using Equation 3.25.

$$t_{Cent} = \frac{\int_0^\infty t\big[T_{fout}(NTU_s, t) - T_{fin}(t)\big]dt}{\int_0^\infty \big[T_{fout}(NTU_s, t) - T_{fin}(t)\big]dt} \qquad 3.25$$

Kohlmayr presented values of the centroid coordinate against NTU_s values for the case that the inlet fluid temperature change is a step-function and NTU_s values are in a low range of $0.5 < NTU_s < 5$. It was mentioned that there was a linear error amplification in the analysis because of the integration process. Thus, the relationship between the centroid coordinate NTU_s values were regenerated in this study for an ideal step change (sudden cooling), as shown in Figure 3.15. As can be seen, the centroid coordinate decreases monotonically with NTU_s values. Now, if the centroid coordinate of experimental data is known, the NTU_s value can easily be estimated. There is no evidence in the literature confirming this technique has been used previously.
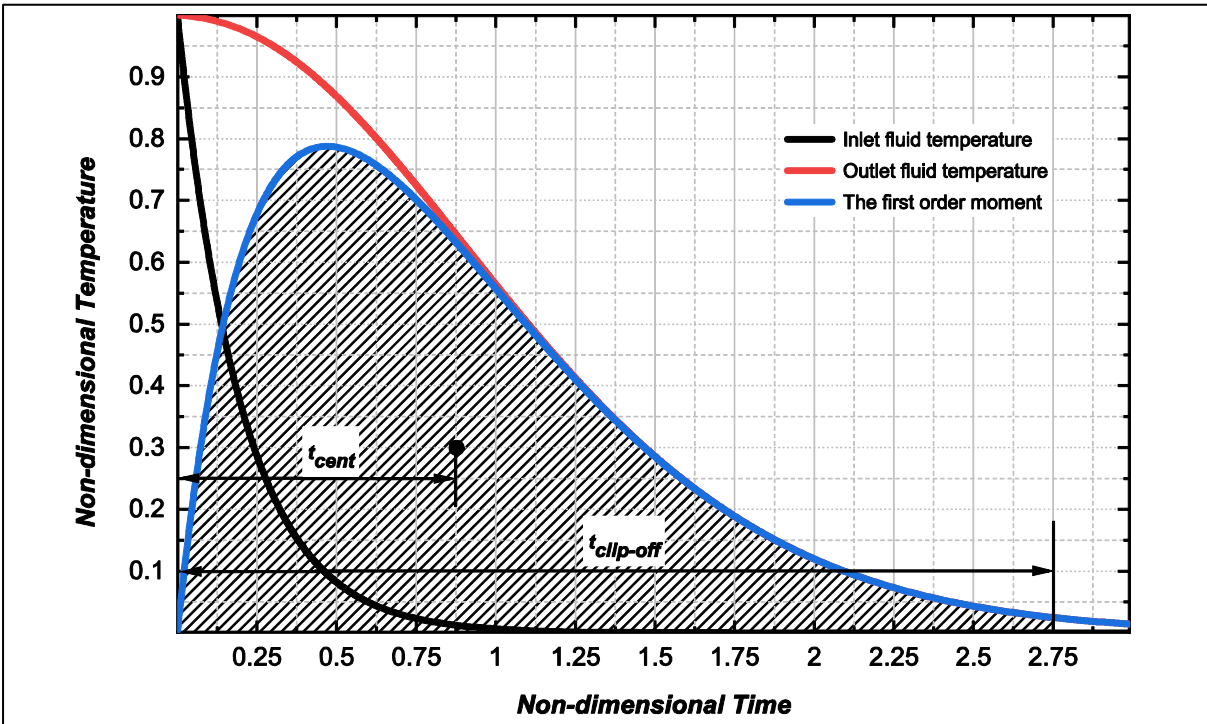
Figure 3.14 Centroid and centroid coordinate NTU_s, for exponential forcing function at $\tau = 0.3$.
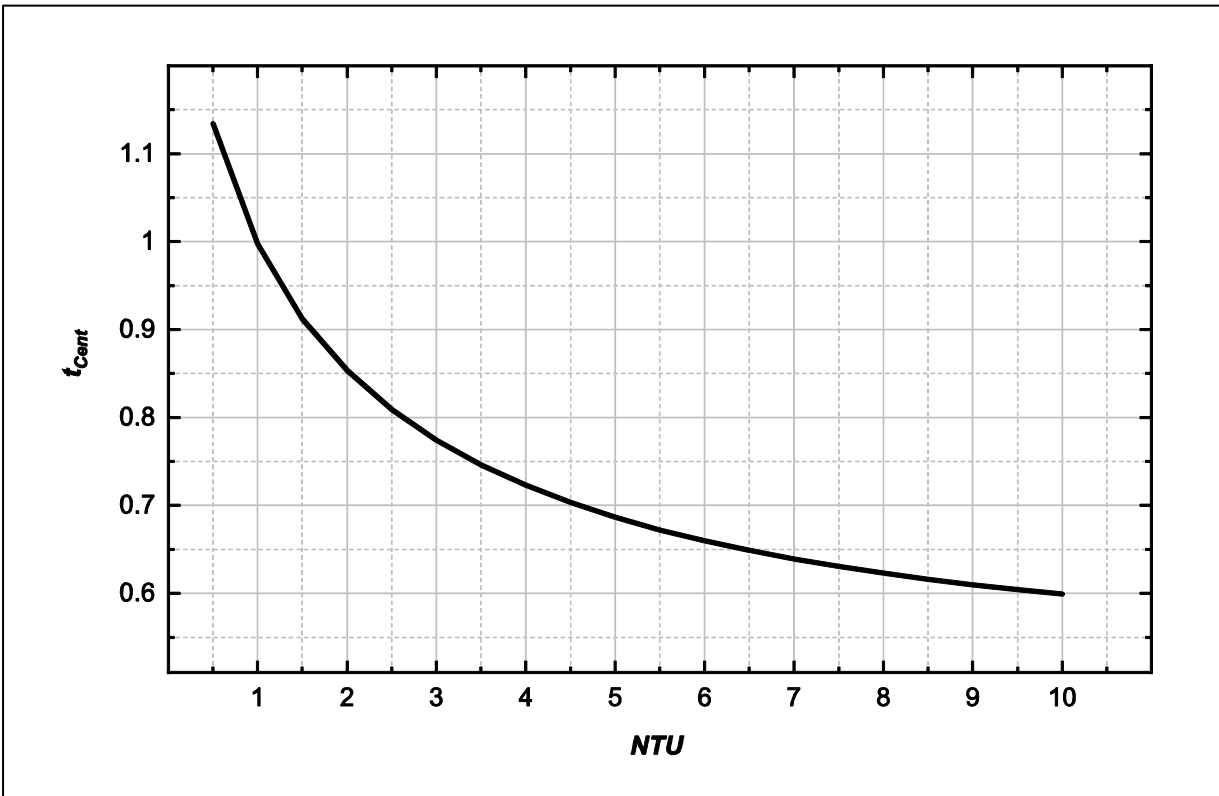
Figure 3.15 Centroid coordinates t_{Cent} vs. NTU_s.

3.3.2.5 The differential fluid enthalpy method

The outlet fluid temperature curve reflects not only the convection heat transfer between the fluid and structure surface area but also the response of the inlet forcing function. The temperature difference between the fluid inlet temperature and the outlet temperature can be used to determine the change of fluid enthalpy ΔH_f. For an exponential inlet fluid forcing function, Baclic et al. [180] developed a mathematical relationship, Equation 3.26 which uses the forcing function time constant to determine the fluid enthalpy change at any given dimensionless time t_h.

$$\Delta H_f(t_h)_{exp} = \Delta H_f(t_h)_{Step} - \tau . \Delta T_f(t_h) \qquad 3.26$$

The left-hand side of the above equation is the total dimensionless fluid enthalpy change. This can be obtained by the conduction integration procedure on the non-dimensional experimental data to evaluate the area between the dimensionless input and output curves, from the start to any considerable dimensionless time t_h, as shown in Figure 3.16.
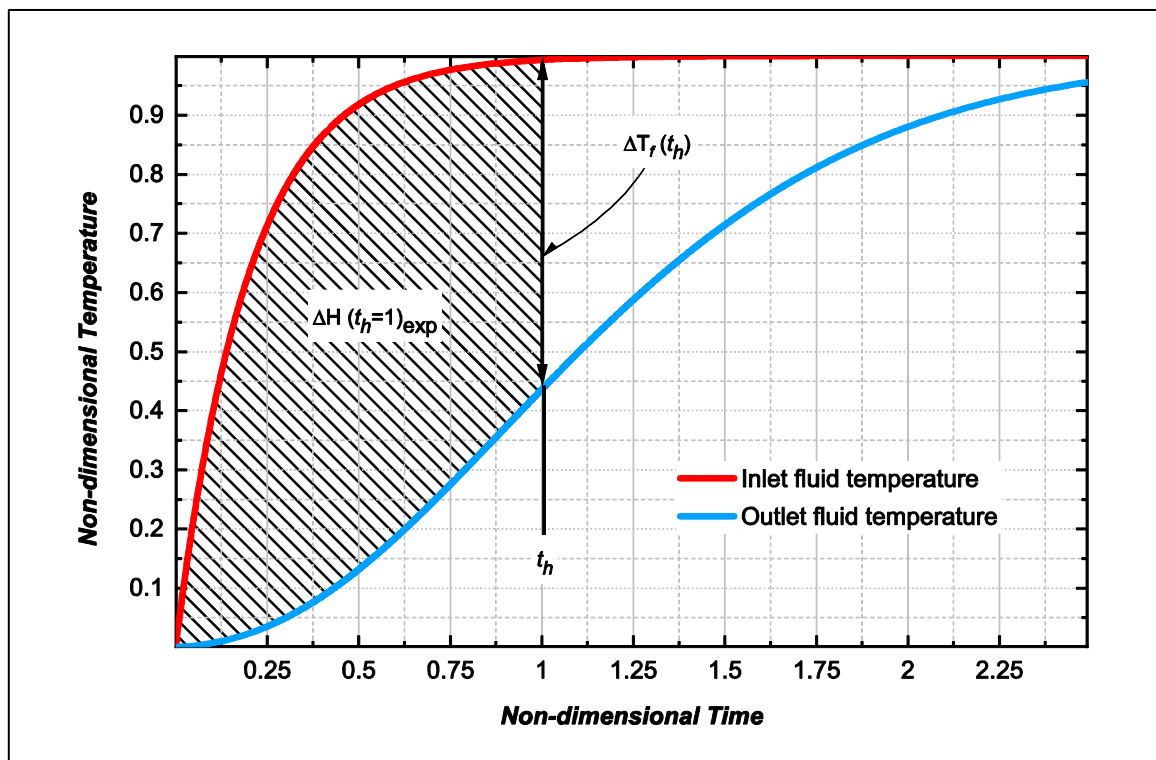
Figure 3.16 The total dimensionless fluid enthalpy change.

The first term after the equals sign is the total enthalpy change for the case of ideal input. This term was presented by a particular series expansion function V_2 written in Equation 3.27. Indeed, this term represents modelling parameters involved in the prediction of the outlet fluid temperature curve NTU_s and t_h. Furthermore, the last term in Equation 3.26 represents the inlet fluid effect, where τ is the dimensionless time constant, which will be described in the next section.

$$\Delta H_f(t_h)_{Step}/t_h = 1 - V_2[NTU_s, NTU_s]/NTU_s \cdot t_h \qquad 3.27$$

By reason of simplicity, Baclic et al. [180] assumed a step-change inlet fluid temperature ($\tau = 0$). They also considered the fluid enthalpy change up to $t_h = 1$, so that the fluid enthalpy change became a function in the NTU_s and was restated as shown in Equation 3.28.

$$\Delta H_f(1)_{Step} = 1 - e^{-2NTU_s}\left(I_0\left(2NTU_s\right) + I_1\left(2NTU_s\right)\right) \qquad 3.28$$

The I_n in the above equation is the modified Bessel function of nth order. The relation between the ideal step fluid enthalpy change and NTU_s values over a wide range of NTU_s values, $0.1 < NTU_s < 1000$, is shown in Figure 3.17.
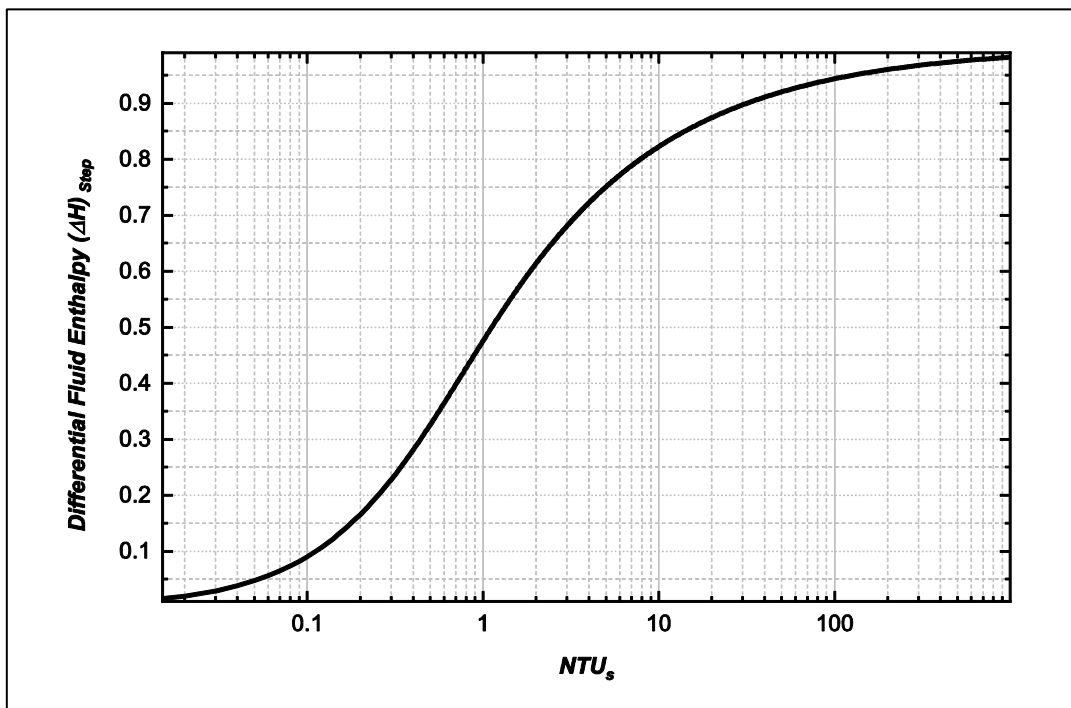
Figure 3.17 Relationship between $\Delta H_f(1)$ and NTU_s.

This reduction technique has distinct advantages over the previous methods, especially in low ranges of NTU_s values. Also, the experimentation time in this method is short because it does not require the system to reach a steady state. However, the analytical expression was derived based on Schumann-Hausen assumptions; thus, several effective modelling parameters were neglected. Moreover, the method was seen to be quite sensitive to the error in the temperature measurements. If the error is kept at 1%, the percentage error in the predicted $0.4 < NTU_s < 10$ is within the range of 1.5% to 9.5%. For NTU_s values > 10 this method presents high uncertainties as the change in the enthalpy becomes very small and cannot be obtained from measured temperature data.

3.3.2.6 Hybrid Matching Method

When the heat transfer between the hot fluid and wall was considered, two unknown $NTUs$ values appeared in the single-blow energy equations, one for the solid, NTU_s, and the other for the case wall NTU_w. The determination of both values can be difficult using a single matching method. Therefore, Chen et al. [55] proposed a hybrid-match technique to determine both values in sequential order. This technique involves both maximum-slope and curve-matching techniques. An initial guess is made for the $NTU_s \ and \ NTU_w$ to predict the outlet temperature curve. The maximum slope value of the theoretical curve is compared with the experimental maximum slope value. If the maximum slope values have coincided, the NTU_s is determined. Otherwise, the values are adjusted, and the process is repeated simultaneously until the correct values are obtained. Alternatively, the curve-matching technique is used to determine the NTU_w value first, and then uses the maximum-slope method to identify the value of NTU_s [13]. This procedure does not take long to converge if one can distinguish between the $NTU_s \ and \ NTU_w$ values. For a typical regenerator, the NTU_s value is much larger than the NTU_w value due to a significant heat transfer area difference.

Several matching techniques have been reviewed by Heggs and Burns [157]. Four indirect matching methods, based on the Schumann model with ideal step inlet fluid temperature input, were employed to estimate the heat transfer coefficients in randomly packed beds of mild steel spheres. This included least squares (direct matching), differential fluid enthalpy, maximum slope, and shape factor methods. Surprisingly, the results showed a significant scatter in the estimated heat transfer

coefficients, even for the same set of data. The results showed that the differential fluid enthalpy method provides the closest approximation to the least-squares process with a 7% increase in the NTU_s values. While the maximum slope and shape methods gave similar prediction results, but were considerably, lower than the least-squares method and the differential fluid enthalpy methods. The NTU_s values obtained from the maximum slope was 9% lower than those obtained by the least-squares method were.

3.4 Summary

To describe the experiments accurately, the numerical model has been frequently developed considering several effective factors such as the inlet fluid temperature variation with time, the longitudinal conduction parallel to the flow direction, the Joule-Thomson effect and the non-adiabatic side-wall. This resulted consequently in advancing the evaluation techniques. Each of these techniques has been developed concerning a certain region of the outlet fluid temperature curve to provide an estimate of the heat transfer coefficients. In addition, each technique has distinct advantages over the other techniques, especially in the range of NTU_s values. Even though all these techniques should provide similar values of the coefficient when applied to the same set of data, this may not be the case. Therefore, the model improvements and the most common evaluation methods were briefly described in this chapter.

CHAPTER 4. Modelling and Reduction Method for This Work

The aforementioned review of the literature revealed that numerous works have been carried out experimentally and numerically to assess the hydrodynamic and thermal performance of wire mesh screens and metal foams. However, the interaction between the fluid and the solid of porous media is yet possible to predict the performance of the regenerator. Therefore, single blow experiments were performed to measure the thermal parameters of the tested samples. The accuracy of the single blow technique may be strongly dependent on the sample parameters, evaluation criteria, and how much the model coincides with the real test conditions [185].

Reviewing the literature showed that the models seldom described the tests correctly. Furthermore, several methods for determining NTU_s have been proposed in the literature, but there is no evidence to show that one reduction method is more accurate than the others. For better consistency, it was recommended not to rely on one single evaluation method [193]. Loehrke [189] carried out a computational study to measure the impact of the modelling parameters and the data reduction method on the estimated NTU_s value. His model accommodated arbitrary inlet fluid temperature variation, longitudinal conduction in the heat exchanger core, as well as core mass effects on the heat transfer coefficient. Moreover, for the sake of comparison, he applied three evaluation methods: direct matching, maximum slope and enthalpy difference evaluation for the same reference set of data.

The error was described as a function of NTU_s value and data reduction method. It was shown that the misdescription of the fluid inlet temperature might have led to a 2% to 50% error in the results. The error due to longitudinal conduction misdescription was 1% to 50%: this error was seen to increase with both the conduction parameter and the NTU_s value when a similar reduction method was used. The error due to the heat transfer coefficient variation and over the measurement of thermal core mass resulted in errors of 4% to 20% and 2% to 50% respectively. Comparison of reduction methods showed that for the NTU_s, the value was generally underestimated, but the maximum slope method gave the closest estimation in most cases. Moreover, even when two different reduction methods gave a similar estimation for NTU_s value, the predicted value was far from the true value.

4.1 Advanced single-blow model for this study

The single-blow technique (transient technique) has many advantages over the steady-state technique, thus, it has been chosen to measure the thermal characteristic of the tested samples. Nevertheless, the accuracy of the single blow transient technique is strongly dependent upon how accurately the mathematical model describes the experiment [189][200]. To reduce measuring uncertainties as far as possible in this work, the most developed mathematical model proposed by Chen et al. [158] was chosen to predict the outlet temperature curves of the tested regenerators. This model takes into account most of the effective modelling variables such as the arbitrary inlet fluid temperature, longitudinal conduction effect and non-adiabatic side-wall. The solution of this model has been utilised to determine the number of transfer units NTU_s in the range 3 to 20. Based on the physical features of the tested samples, the following assumptions have been applied to simplify the mathematical model:

- The air flows at uniform velocity and temperature.
- The fluid is incompressible and has a finite thermal capacity.
- The properties of the fluid and the solid are constant and independent of temperature.
- Uniform inlet air velocity and temperature.
- Only the conduction in the solid structure and the side-wall parallel to the flow direction is considered.
- The radial thermal diffusivity is infinite normal to the flow direction.
- The Joule-Thomson expansion effect is neglected as the pressure drop across the tested samples is low.
- The side-wall is non-adiabatic.

Full details of the advanced model can be found in Appendix 1. The model is a modified version of that described in Chapter 3 with additional terms to include heat transfer to the walls, thermal conduction through the sample and a finite step change in the inlet temperature. The validation of the included physics is also provided in the same appendix. These additional physical processes are highly interdependent and

cannot be treated separately. This interdependence is investigated in the rest of this chapter, it was essential to understand this to ensure the model fit the data correctly. For example, it was theoretically possible to achieve identical solutions with differing modelling constants leading to unrealistic heat transfer predictions. A Matlab code was written to predict the outlet flow temperature response under various assumptions. The numerical code was written to be able to compute the maximum slope values for a wide range of modelling parameters and plotted against dimensionless time.

4.2 Data reduction procedure

As has been previously mentioned, no evidence makes one of the reduction methods better than the others and, besides, it is probably not safe to rely on only one data analysis method [189]. Heggs and Burns [157] compared the four common reduction techniques: the least squares, maximum slope, shape factor and differential fluid enthalpy methods based on the simplest model of the single-blow model (Schumann model). They found consistency between the coefficients predicted from the least-squares and differential fluid enthalpy methods, while the coefficients obtained from the maximum slope and shape factor methods were remarkably lower. However, their model avoided the errors resulting from the deviation of the actual inlet fluid temperature from the step change, although none of the other effective modelling parameters was considered.

The literature showed that even when the same model has been used, different evaluation methods may give a different estimation for the NTU_s values. Loehrke [189] conducted a numerical comparison considering the side-wall effect as an increase in the test core mass. This assumption may be further corrected if the side-wall is represented in the system energy equations. Additionally, Loehrke's analysis was conducted in the 1990s when the computer capability was limited, which might explain why 12 points on the theoretical curve were used based on the analysis. This allows greater room for error when the derivation or integration methods are used. In an era of rapid technological development and the availability of high-speed computers, it would be worth reviewing the work of Heggs, Burns and Loehrke for more rigorous results.

By using an amplification factor, Cai et al. [187] demonstrated that the sensitivity of the NTU_s results in the error in the measured outlet temperature. As the

amplification factor increases, the accuracy of the NTU_s results decreases. The amplification factor was used to determine the optimum time for the curve-matching technique. They concluded that the optimum time is convenient and reliable for cases where the longitudinal heat conduction effect is considered. Chen et al. [158] recommended using the maximum-slope scheme instead of the curve-matching scheme for a regenerator with a large NTU_s value in order to avoid having to choose the time interval.

The maximum slope has been shown to be less sensitive than the direct matching method if the axial conduction effect is neglected [159]. It is an accurate technique for large NTU_s values and it requires less computational effort compared to the direct matching methods. However, it fails for a low range of NTU_s values as will be shown in the next section. The direct curve matching method is valid over the entire practical NTU_s range. The existence of high-speed computers with many effective computational tools means that the direct curve matching method can readily be implemented with better accuracy in a shorter time. Consequently, more recently, the hybrid reduction method, which consists of both the maximum gradient and curve matching techniques, has been recommended to treat experimental data [7][43][55][186]. In this matching procedure, a pair of values of NTU_s and NTU_w were predicted and substituted into the present model to yield an exit fluid temperature profile prediction. Following this, the first derivative of the predicted temperature profile was compared with the measured profile and value. When the two sets of profiles and values matched within specified limits, then the NTU_s, and NTU_w values were registered as the thermal characteristic for the system. These evaluation techniques were adopted in this study to compare the predicted and measured fluid exit temperature histories.

4.3 Effect of the modelling parameters on maximum slope method

A parametric study was performed using the modified model described above to assess the effect of the modelling parameters considered in the current study. The predicted fluid outlet temperature curves were characterised by a maximum gradient and a fluid enthalpy change. The maximum slope S_{max} designates the maximum value of the first derivative of the outlet temperature curve, which can be obtained from the experimental data using Equation 4.1 [156].

$$S_{max} = \frac{dT_f}{d(t/NTU_s)} = \frac{m_s c_s}{\dot{m} c_f} \frac{dT_f^\star}{d\theta}\bigg|_{max} \qquad 4.1$$

The differential enthalpy can be obtained by performing a numerical integration to compute the area between the fluid inlet and outlet temperature curves using the trapezoidal rule. For simplicity, the integration can be conducted up to the dimensionless time equal to unity. Both the maximum slope value and the difference in the fluid enthalpy will be presented as a function in the NTU_s values and the modelling parameters.

4.3.1 Impact of inlet fluid temperature on the maximum slope value.

Various studies have shown that achieving a step-change in the inlet temperature profile is practically impossible. Furthermore, it is not proper to use the assumption of a step change as the effect of the deviation from a step change on the test results is may be considerable [187]. As previously mentioned, Liang and Yang [191] proposed an exponential rise formula shown in Equation 4.2 to relieve the pressure of achieving a step change.

$$T_{fmax\,(t,0)} = 1 - \mathrm{EXP}^{\left(\frac{-t}{\tau}\right)} \qquad 4.2$$

where t is the dimensionless time and τ is an experimentally determined dimensionless constant. The τ depends on the instrumentation's real-time response τ_i and the solid-fluid system constant τ_{sys}. It is often expressed as:

$$\tau = \frac{\tau_i}{\tau_{sys}} = \frac{\tau_i}{\left(m_s c_s / \dot{m} c_f\right)} \qquad 4.3$$

Liang and Yang [191] showed that τ_i is a function of the frontal air velocity of the working fluid. For a given velocity, they used 0.632 of the measured time required by the outlet fluid to reach the maximum temperature in order to calculate τ_i . The exponential fluid inlet variation has been reported by many researchers [158][180][187][189][190]. However, in most cases, the actual fluid temperature profile can be measured and used as an arbitrary inlet fluid temperature change [13][43][159][185]. By knowing the mathematical formulation of the inlet temperature curve, it became possible to accommodate an arbitrary fluid temperature in the single-

blow analysis [157][206]. In this work, the Wiebe function given in Equation 4.4 was found to accurately define the dimensionless measured fluid inlet temperatures.

$$T_{fmax\,(t,0)} = 1 - \text{EXP}^{\left[-a\left(\frac{t}{\tau}\right)^m\right]}$$
4.4

For a reasonable inlet temperature description, the measured inlet temperature data was converted to a non-dimensionless form and fitted using the Wiebe mathematical model. The Wiebe function coefficients (a and m) were adjusted simultaneously to improve the fitness and identify the coefficients for each testing run.

Figure 4.1 shows an example of inlet fluid temperature curve fitness using the exponential and Wiebe functions on typically measured inlet fluid temperature data. As can be seen, the measured inlet fluid temperature deviates from the step change. The response of the Wiebe function perfectly describes the inlet fluid temperature behaviour compared to that of the exponential change. The time constant of the inlet fluid temperature τ was found to vary over a range of $0.03 < \tau < 0.05$, while the Wiebe function coefficients varied in a range of $2.8 - 5.7$ and $1.3 - 1.7$. for a and m respectively. The averaged values of Wiebe function coefficients were used to examine the effect of modelling parameters on the maximum slope value.
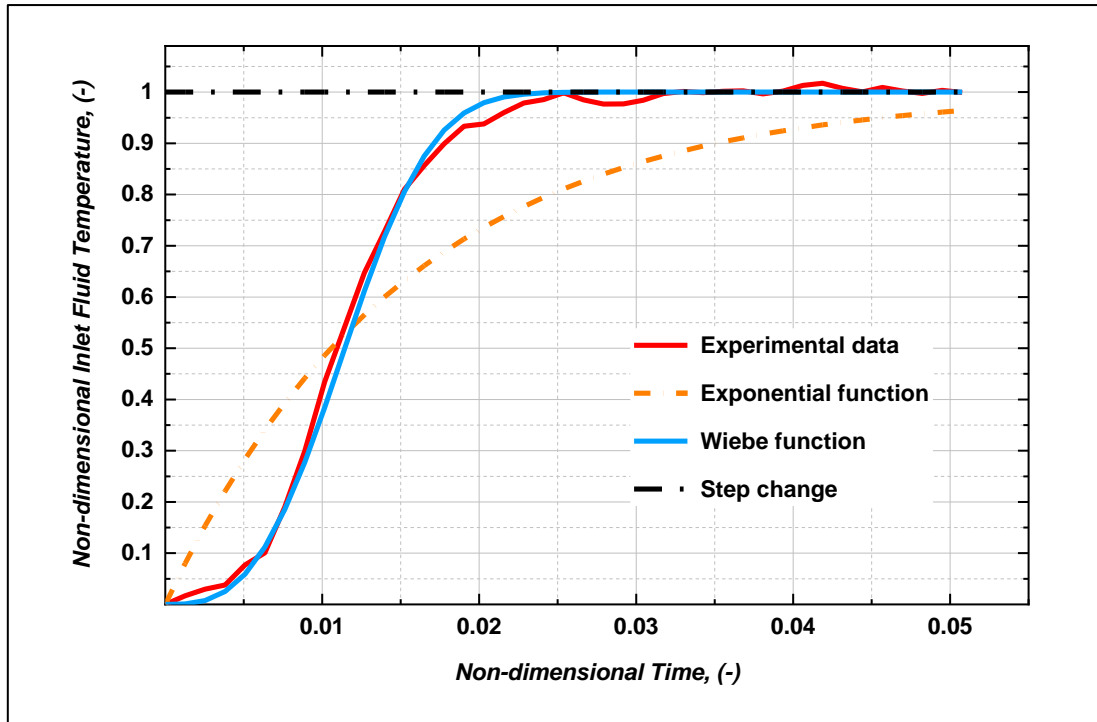
Figure 4.1 Typical sample of inlet fluid temperature curve fitness for S6 sample at 2.5m/s.

According to Equation 4.3, at constant τ_i, the time constant τ is proportional to the heat capacity of a working fluid and inversely proportional to the heat capacity of the matrix. The literature survey showed that in most investigations, the time constant $\tau > 0.1$ [13][43][158][159][201]. This might be attributed to the high experimental flow rate, small heat capacities of the tested samples, or the heating and switching methods that require a longer operational real-time. However, in the case when the exponential function was demonstrated, the maximum slope method was sensitive to the time constant $\tau < 0.1$ when $NTU_s < 5$ [190]. This sensitivity decreases with the increase in the NTU_s value. To investigate this impact on the current results, Figure 4.2 was generated for several NTU_s values and at two different time constant ratios τ, while the longitudinal conduction in the test core was ignored.
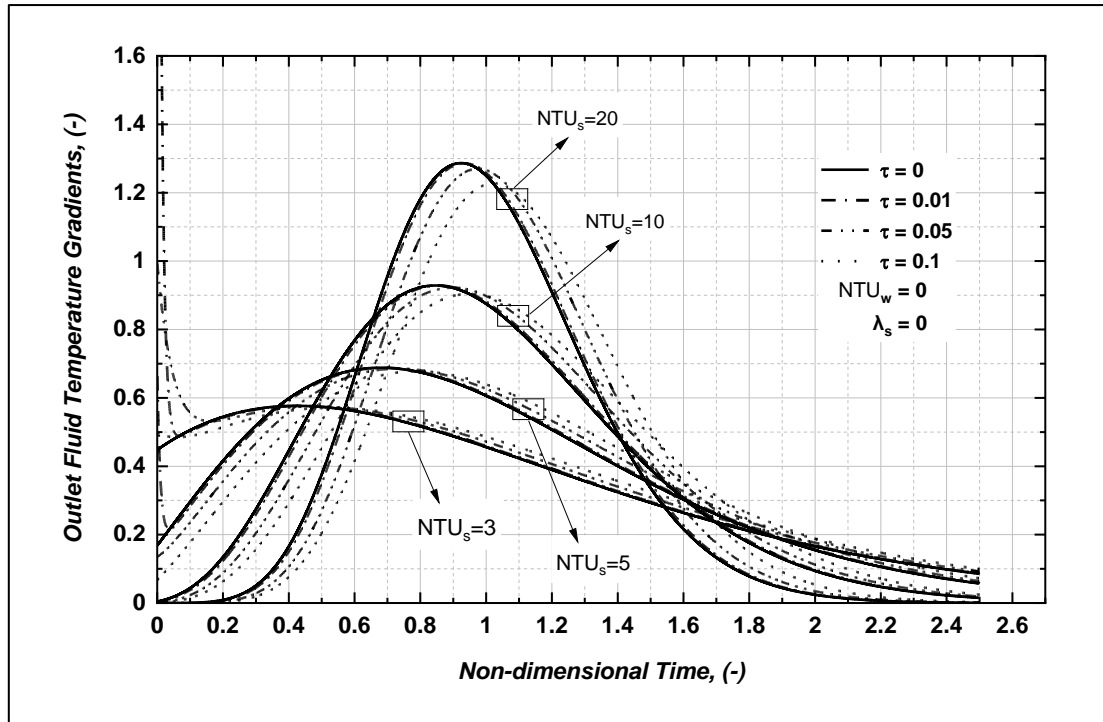
Figure 4.2 Impact of the time constant on the maximum slope value.

The graph shows that even when the Wiebe function is used, the first derivative curves are sensitive to the rapid fluid inlet temperature variation for the small NTU_s values. This impact decreases as the NTU_s value increases, in agreement with Hesheng et al.'s [190] reported data. Moreover, it can also be noticed that changing the time constant ratios over the range from 0.03 to 0.05 has an unmeasured impact on the maximum value S_{max}. Therefore, in the current work, τ has been assumed to be a constant equal to 0.04.

4.3.2 Axial conduction effect on the maximum slope value.

The effect of the axial conduction parameter λ_s on first derivative curves, corresponding to different NTU_s values, are shown in Figures 4.7 and 4.8. The first derivative curves for $\lambda_s = 0$ are presented as a solid line. The broken lines represent the slope curves at three different values of λ_s. It can be seen that the first differentiated curves of small NTU_s are less sensitive to the conduction parameter λ_s. If the NTU_s is large, the slope curves become significantly dependent upon the λ_s values.
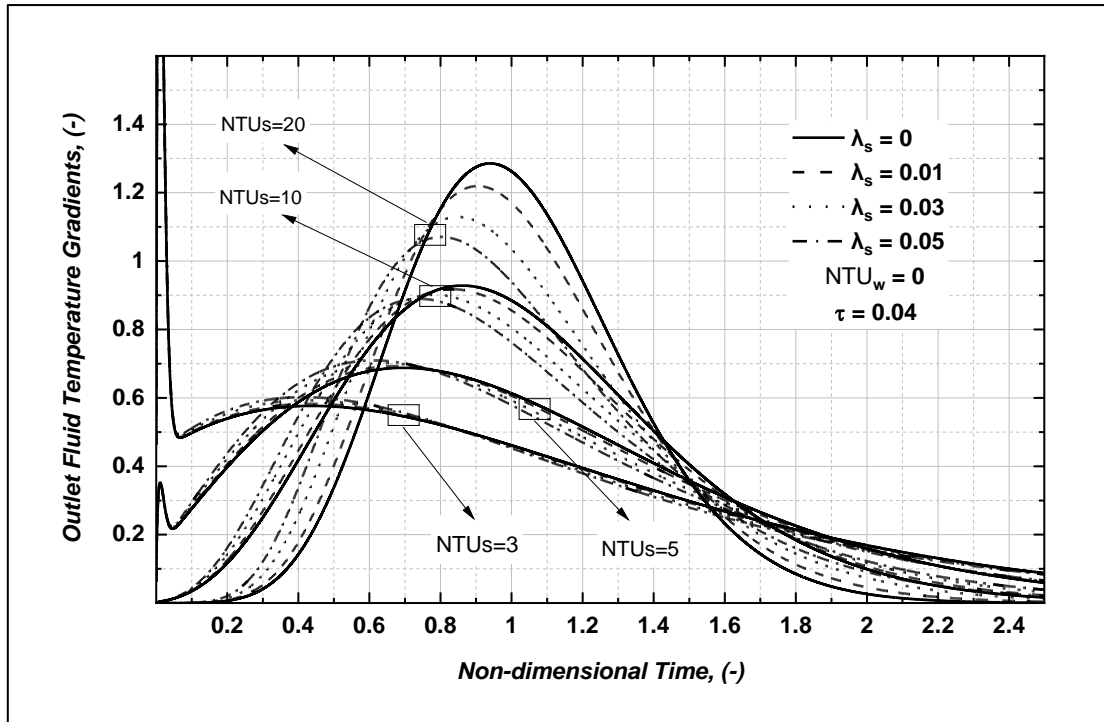
Figure 4.3 The effect of low λ_s on the magnitude S_{max} and t_{max}.

For the cases with large conduction parameters, the curves become less sensitive to the variation of the NTU_s value and differentiated curves become closer to each other, making it harder to distinguish between them for different NTU_s values.
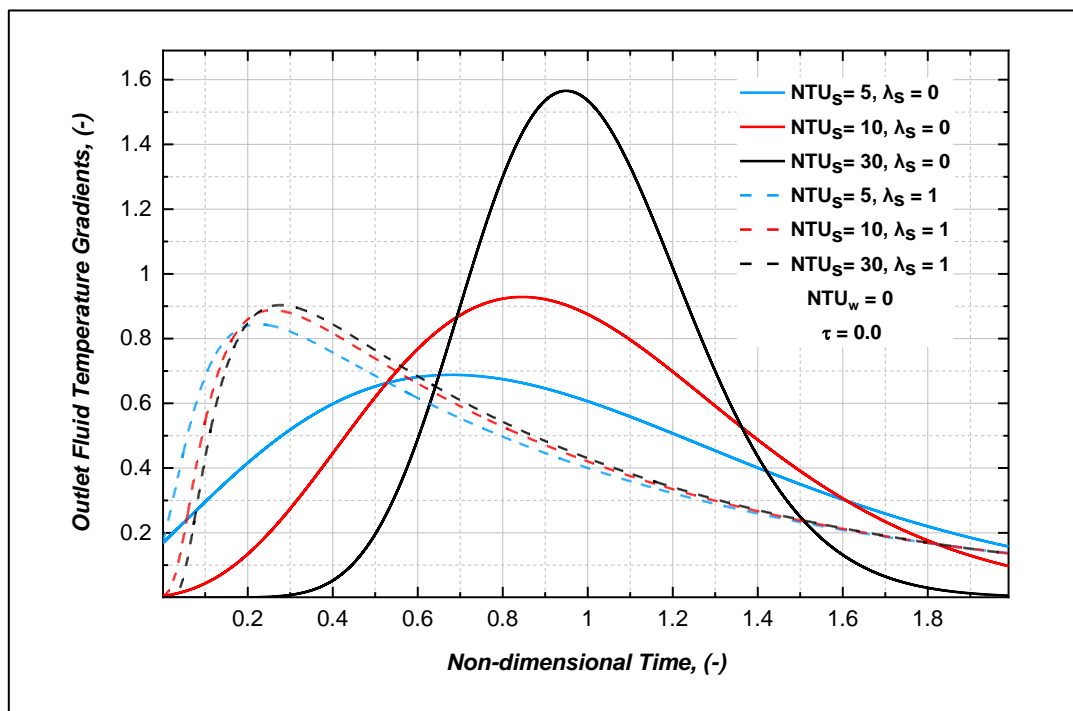
Figure 4.4 The effect of high λ_s on the magnitude S_{max} and t_{max}.

69

For an ideal temperature step change, Pucci et al. [183][196] underscored the theory of the single-blow transient technique and presented the effect of longitudinal heat conduction on the maximum slope value. They showed that this effect is dominant when the NTU_s value > 2. Furthermore, they compared their numerical results with those of Locke [195], who neglected this impact in his analysis. The comparison was presented graphically similar to that in Figure 4.5.

It can be seen that the NTU_s value of the samples, determined by the maximum-slope method, will be overestimated or underestimated if axial conduction is ignored in the single-blow model. For NTU_s values < 7.2, neglecting axial conduction results in a slight overestimation in the NTU_s values. The opposite results would be obtained if the test regenerator matrix has large NTU_s values. The error becomes more severe as the NTU_s value increases. Note that these results were presented for the case with an adiabatic side-wall, otherwise the error in the estimated NTU_s values would be more serious in the situation the heat dissipation into the side-wall is overlooked.
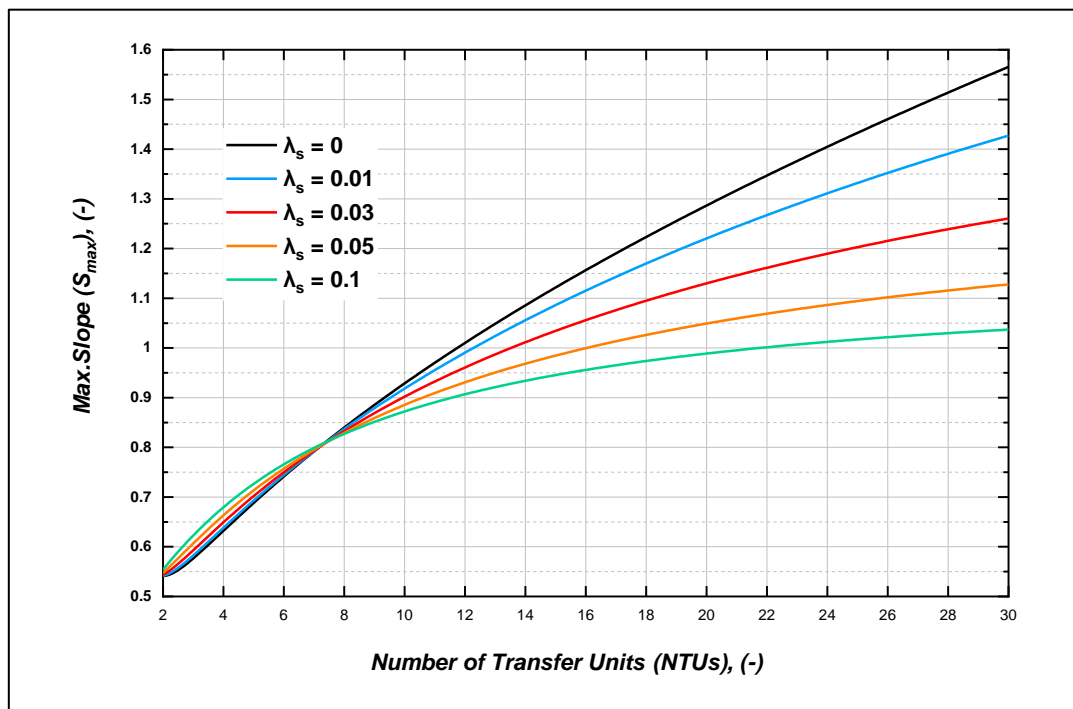
Figure 4.5 The NTU_s as a function of S_{max}.

Krishnakumar and Venkatarathnam [197] showed that variation of NTU_s can be predicted from the maximum slope alone when the axial conduction parameter is overestimated or underestimated. The error was very small at low values of NTU_s, whereas the error in the predicted NTU_s is marginal at high NTU_s values. The error in

the estimated NTU_s value, due to neglecting the axial conduction, is shown in Figure 4.6.
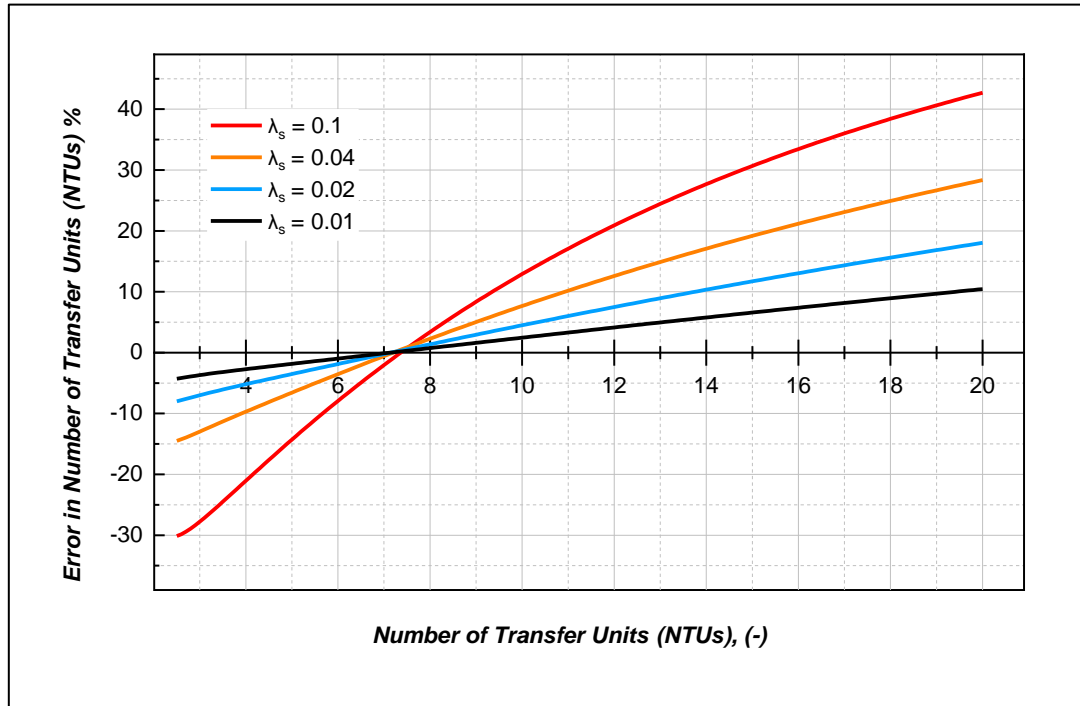
Figure 4.6 Error Error in NTU_s value estimation due to the conduction effect.

In many cases, measuring the axial conduction parameter is a difficult task, particularly in complicated geometries such as in multilayer heat regenerators. In such configurations, the axial conduction parameter depends on the contact resistance between the adjacent layers. The lower number of contact points reduces the effective thermal conductivity across the tested matrices, making it difficult to measure. Among the researchers who have used the maximum slope method, only Krishnakumar and Venkatarathnam [197] used the time t_{max} at which maximum slope occurs to estimate the NTU_s value and the longitudinal heat conduction parameter λ_s from a single experimental test. If S_{max} and t_{max} are known, the NTU_s and λ_s can be predicted from the graphical relationship between the S_{max}, t_{max} and NTU_s values in Figure 4.7.
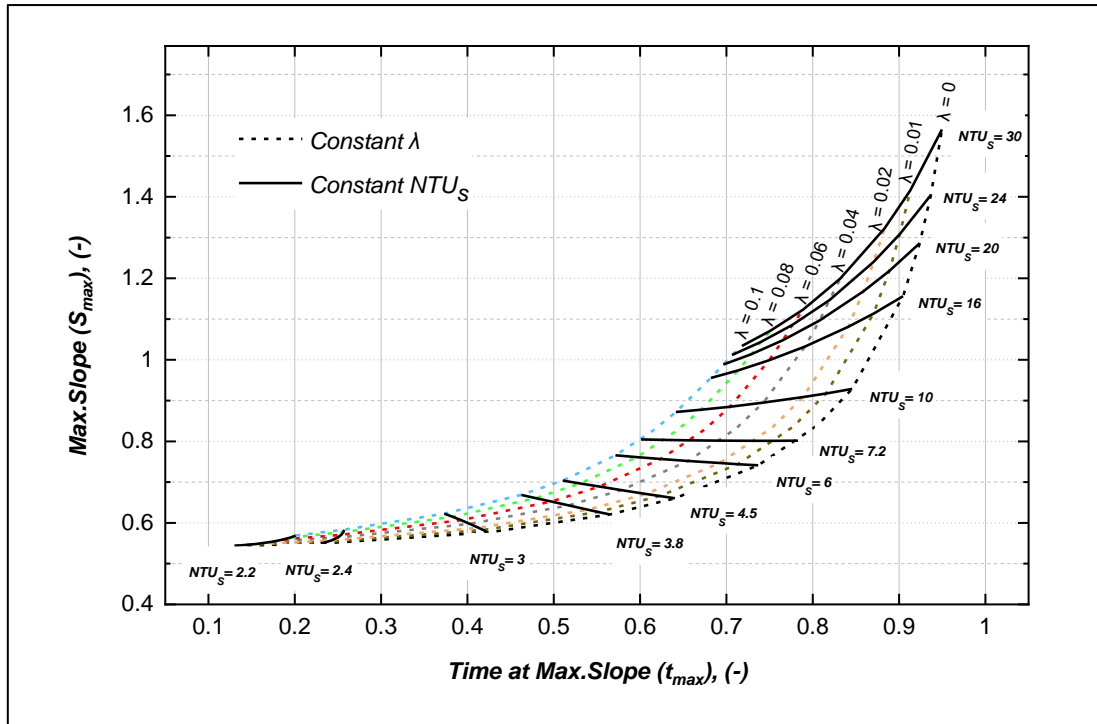
Figure 4.7 Variations of S_{max} with t_{max} for different NTU_s and λ_s values at $\tau = 0$.

This method is particularly useful for the determination of high NTU_s values but not for low NTU_s value cores. It can be noticed that at constant λ_s and low values of NTU_s, the t_{max} becomes inefficient to accurately obtain the NTU_s and λ_s. In the current study, the tested samples were made of stacks of metallic layers. This resulted in lower effective thermal conductivities across the sample parallel to the flow direction. Furthermore, the samples were relatively small and had lower NTU_s values < 20. The solution of the single-blow model has been used to estimate the longitudinal heat conduction parameter λ_s of the semi-homogenous matrices. Values of the conduction parameter λ_s were always < 0.01. at the lowest flow rates. Based on this, the impact was neglected in the current research.

4.3.3 Non-adiabatic wall effect on the maximum slope value.

The wall modelling parameters NTU_w and R_{tc} were seen to have a measurable impact on the maximum gradient [13][55][158][159]. It is worth noting that increasing NTU_w leads to an increase in the heat transfer surface area between the side-wall and the fluid, while increasing R_{tc} means the side-wall has less mass so less energy can be stored in the wall. For a constant R_{tc} equal to 3, the impact of the NTU_w values on the gradient curves are illustrated in Figure 3.12. As can be seen, increasing the NTU_w results in a decrease in the maximum slope value.
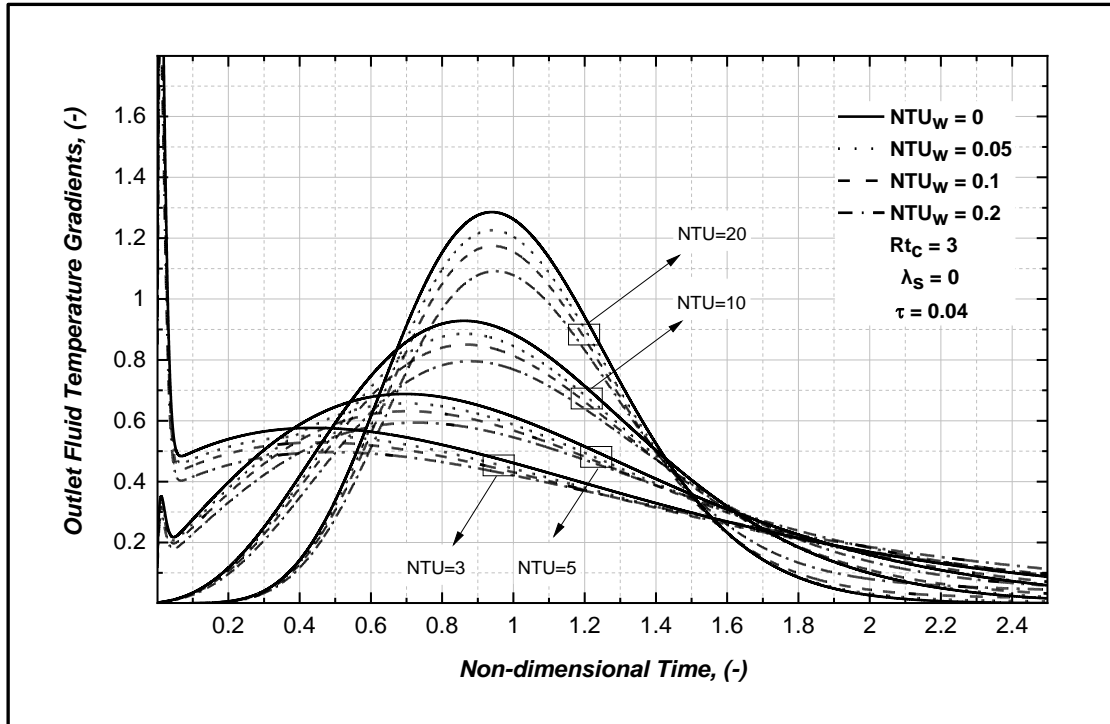
Figure 4.8 Effect of NTU_w value on the gradient curves.

However, the unique relationship between the maximum slope and NTU_s value still exists, but only for a fixed NTU_w value. If the NTU_w value is known, the NTU_s can be determined directly from the relationship between the maximum slope and the NTU_s values at that NTU_w value; if not, the maximum slope value could correspond to more than one pair of NTU_s and NTU_w values, as shown in Figure 4.9. For example, assuming S_{max} is equal to 0.9 and NTU_w is equal to 0.2, and if the side-wall effect is neglected, the NTU_s can be underestimated by 28% error.
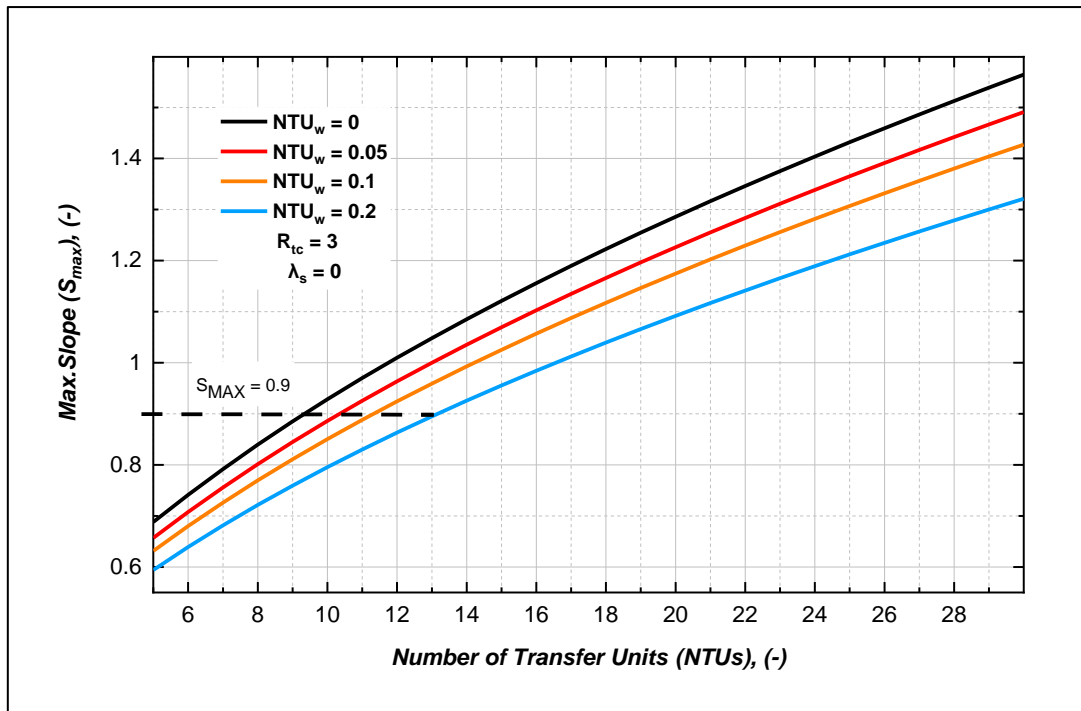
Figure 4.9 Relationship between the maximum slope and NTU_s values for different NTU_w values.

For a constant NTU_w, reducing the mass of the side-wall has an impact on the gradient curves, as shown in Figure 4.10. It is noticeable that the variation of R_{tc} has a quantifiable impact on the gradient curves when the NTU_w is large.
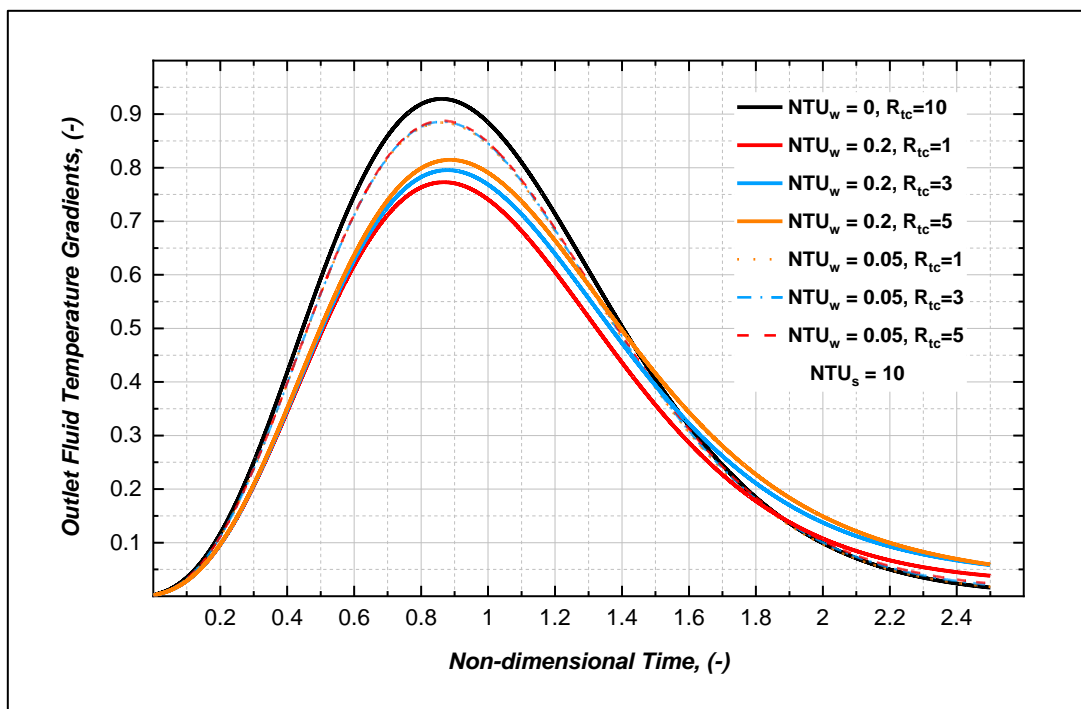
Figure 4.10 Effect of R_{tc} variation on the gradient curves for different NTU_w values.

Moreover, Figure 4.11 shows that the NTU_s may be underestimated if the effect of R_{tc} is neglected. The error increases as the heat transfer surface area or the heat capacity of the side-wall increases. For instance, when the maximum slope value $S_{max} = 1$, $NTU_w = 0.2$, and $R_{tc} = 1$, there is an approximately 34% possible error.
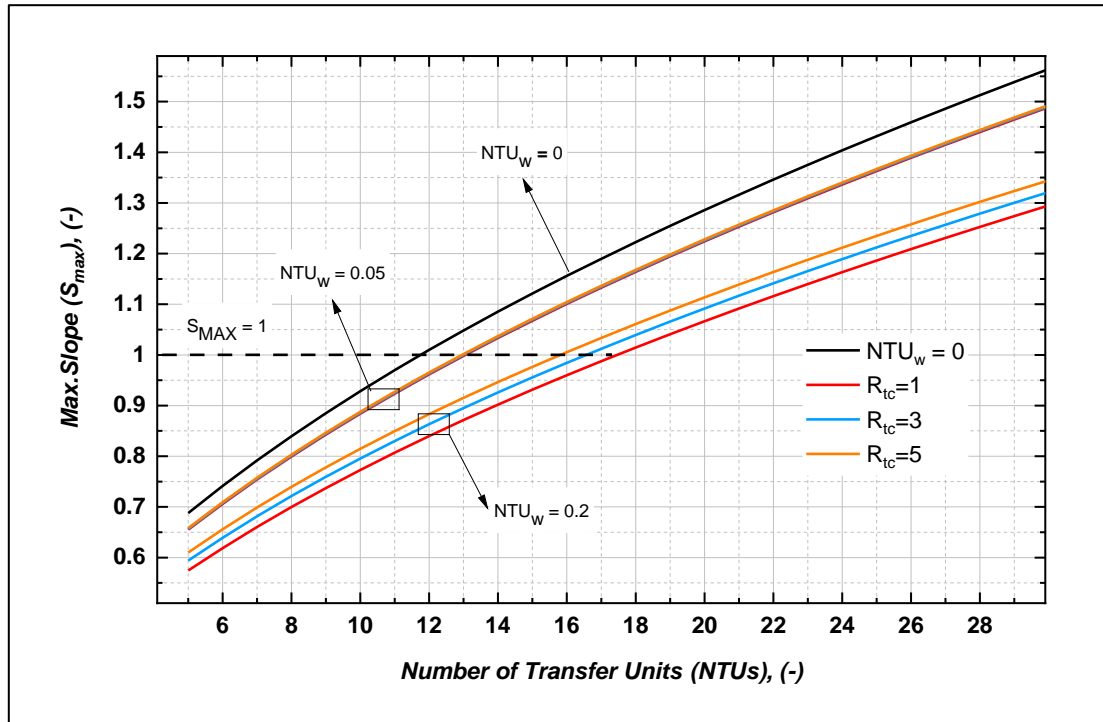
Figure 4.11 Impact of R_{tc} on the maximum slope value at different NTU_w values.

4.4 Summary

The single-blow transient technique has been used to evaluate the thermal performance of heat exchangers. An advanced single-blow transient testing model was solved numerically using a finite-difference procedure. Numerical results were obtained from the solution for different operating conditions. To improve the accuracy and applicability of the testing method, two reduction methods: direct matching and maximum slope were chosen to determine the number of transfer units ($NTUs$). The accuracy of this experiment depends also on the validity of the model of the experiment. Hence, a comprehensive study was carried out to investigate the influence of modelling parameters on the predicted data. This included the inlet fluid temperature variation with time, the axial conduction in the flow direction and the impact of the non-adiabatic side wall. A new limitation of the maximum slope method was found dependent on finite inlet fluid temperature step change. The numerical results indicated that the assumption of no longitudinal conduction across the sample

75

may be valid when the samples and effective thermal conductivity are small. The results showed also that neglecting the impact of the sidewall heat transfer may cause a considerable error in the prediction of $NTUs$. This error is a particular issue if the side wall has a large heat capacity or high surface area in contact with the matrix was the case with aluminium foams used in this study.

CHAPTER 5. Experimental Apparatus and Methods

This study aims to compare several types of structures as regenerators, with a minimum level of uncertainty when the single blow transient technique is used. The existing literature reports that using the maximum slope reduction method for testing small samples allows significant room for error. Unfortunately, testing large samples was not possible in this study due to the limitations of the testing system and the limited availability of the metal foams. The flow system's restrictions are associated with the suction unit, which drives the air through the sample. The current suction unit cannot provide a high flow rate due to a high-pressure drop across the sample. This issue could be addressed by using a large centrifugal pump; however, the testing cost would be higher and a large pump could also cause a higher noise level or have an impact on flow expansion. Because of this, the samples were designed and assembled to meet the system's best working conditions, while simultaneously achieving the goals of the study.

5.1 Sample design, manufacture, and assembling.

In order to be able to draw conclusions from the experimental work, it was necessary to create samples that were similar in some way due to the huge number of material variables. Initial proposals were constant: heat transfer surface area; $NTUs$ value, mass, pressure drop or volume. In the time available it was not possible to perform preliminary experiments on a set of samples and then modify them to give the desired property. For example, create a sample, measure its $NTUs$ and then modify that sample to provide a specified $NTUs$. Also, some of the parameters, notably the surface area could not be determined with great accuracy. The construction of the samples was more time consuming than originally predicted. Great care was taken to ensure that the samples remained in the same form throughout the experiment program. Samples of different thicknesses would have been much harder to fit into the different rigs. Keeping the volume constant significantly simplified the experiments.

Based on this fact, the only available options are to produce composite samples either based on a constant weight or a constant volume. Both options are heavily influenced by the weight and volume of the aluminium foam samples: these samples

are much lighter than the stainless steel wire screen samples at a constant volume. Therefore, producing wire mesh samples with a similar weight to the aluminium foam samples means fewer wire mesh layers are used. The result would produce samples with a very low NTU_s value. Hence, the only remaining option is to assemble composite samples based on a constant volume.

5.1.1 Production of wire mesh samples

Despite the availability of many different sized wire mesh sheets, only a few different types can be used in the current study. Using fine wire mesh layers causes high-pressure drops across the samples. The pressure drop increases with a decrease in pore size, as will be shown in the Results chapter. Using a large mesh size is not the best option as the heat transfer area is small, and this results in low NTU_s values. Consequently, four moderate sizes of woven wire mesh were selected to be tested in this study. They were specified based on the number of openings per linear inch of screen (10, 20, 30,40 PPI). All of them were made of 304 stainless steel and obtained from Inoxia [207]. The preparation process of the wire mesh samples is shown in Figure 5.1. The sheets were first cut into 60 mm wide strips, as presented in Figure 5.1. A. The strips were then folded into a square shape and loaded between 2 mm square plastic sheets to reduce cutting deformation at the edges (Figure 5.1. B). After that, the folded pieces were punched out using a Norton Fly Press with a 6-ton capacity (Figure 5.1. C). The punch created 51.5mm diameter circle screens, shown in Figure 5.1. D.
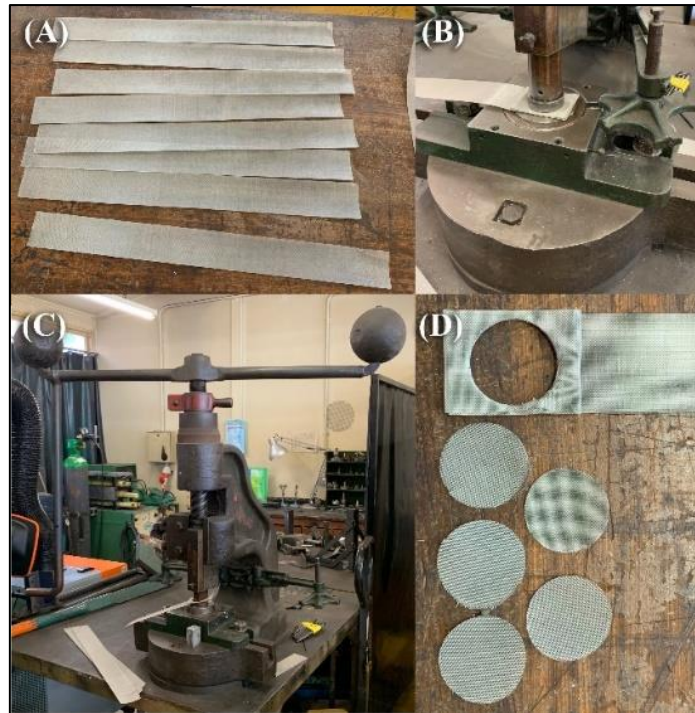
Figure 5.1 Equipment used for wire mesh samples production.

It was challenging to achieve a uniform circle using the punch. A side cutter was used to solve the problem by trimming off the excess wire from the circular mesh screen edge. After that, the wire mesh screens were stacked together to create a cylindrical shape. A stainless steel wire of 0.3mm diameter was used to fix the wire mesh screens together. The stacked layers were then ground on the pedestal grinding machine to remove the serrated edges to achieve a final diameter of 51.1mm. The wire mesh screen samples tested in this study are illustrated in Figure 5.2. The physical properties of the tested wire mesh screens samples are listed in Table 5.1.
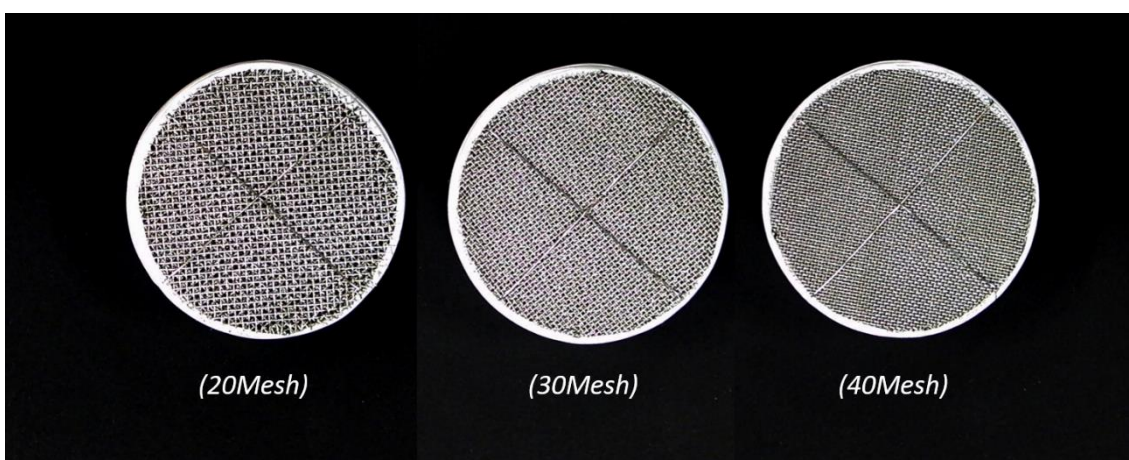
Figure 5.2 An image of the wire mesh screen samples that were tested in this study.

Table 5.1 The physical properties of wire mesh screens samples.

Pore size (mm)	Sample type	Number of layers	Weight (gr)	Thickness (mm)	Wire size (mm)	Volume (mm³)
0.915	20 Mesh	40	91.9	24.75	0.36	50758
0.567	30 Mesh	50	109.5	24.8	0.28	50860
0.411	40 Mesh	66	118	25.05	0.224	51373

5.1.2 Production of Metal Foam and Slicing Samples

Six metal foam samples inherited from previous work [37] were used in this study. They were retested and then combined with wire mesh layers in order to investigate their performance as regenerators. The samples were made of pure aluminium using a replication manufacturing technique [36]. The samples were selected based on the similarity of porosities and differences in size and shape of the pores. The categorization of pore size and pore shape is illustrated in 00. The size and shape of the salt grains used in the manufacturing process determined the pore size and shape of the samples. Pore shape is further subdivided as irregular - i.e. crushed and spherical pore shapes, whereas pore size can be sorted, based on the pore diameters: small 1-1.18 mm, medium 1.4-1.7 mm and large 2-2.36 mm pore sizes.
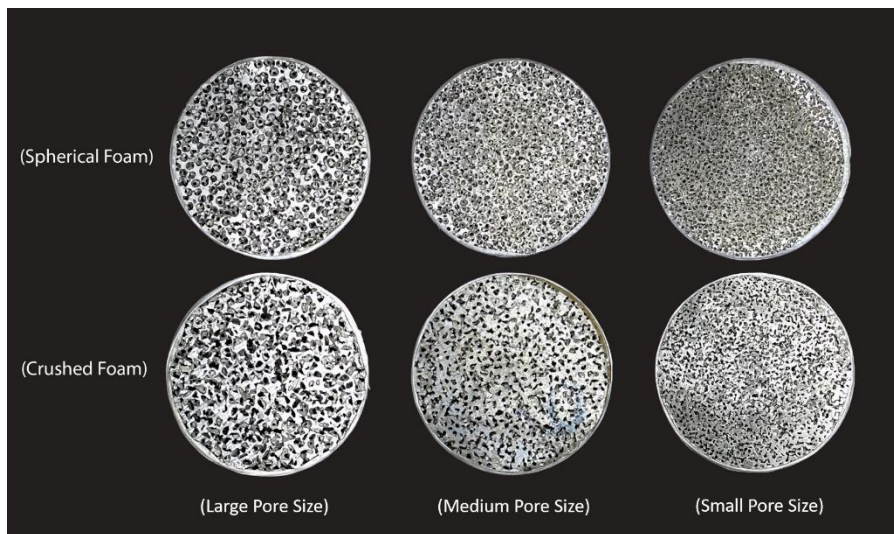
Figure 5.3 Aluminium foam samples tested in this study.

The samples were first re-tested to evaluate their hydraulic and thermal performance as regenerators. To maintain the correct orientation and order, the samples were first marked and then sliced into three equal pieces. Slicing was performed using EDM (electrical discharge machining) to prevent the ligaments from being distorted. In addition, this cutting method minimizes the amount of material removed in the cutting process. The slicing was conducted by Erodatools Ltd [208]. A

0.25 mm wire size diameter made of brass was used. Each sample length was reduced by 0.75 mm. The effect of slicing was examined before the sliced samples in the hybrid structure were used. The physical properties of the tested metal foam samples are listed in Tables 5.2 and 5.3.

Table 5.2 The physical properties of the original aluminium foam samples.

Pore Size (mm)	Sample type	Sample name	Weight (gr)	Thickness (mm)	Diameter (mm)	Volume (mm³)
1.09	Crushed	S4	50.1	24.34	51.1	50191
	Spherical	S6	41.5	24.85	50.85	50466
1.55	Crushed	M5	49.4	23.68	51.29	48907
	Spherical	M10	43.8	25.36	51.18	52172
2.18	Crushed	L5	49.4	23.17	51.17	47648
	Spherical	L10	41.4	24.54	51.16	50446

Table 5.3 The physical properties of the sliced aluminium foam samples.

Pore Size (mm)	Sample Type	Sample name	Weight (gr)	Thickness (mm)	Diameter (mm)	Volume (mm³)
1.09	Crushed	Sliced S4	47.9	23.54	51.1	48277
	Spherical	Sliced S6	36.1	24.05	50.85	48841
1.55	Crushed	Sliced M5	42.3	22.88	51.29	47273
	Spherical	Sliced M10	36.3	24.56	51.18	50526
2.18	Crushed	Sliced L5	41	22.37	51.17	46003
	Spherical	Sliced L10	34.1	23.74	51.16	48801

5.1.3 Sample assembling

The multi-layered samples should have a perfect cylindrical shape to seal the airflow path between the sample and the sample holder. The seal prevents any bypass between the samples and the sample holder and ensures that all the measured air passes through the sample. Moreover, it has the benefit of insulation as it minimizes the wall-side effect during the thermal tests. The cylindrical shape was achieved by utilizing a small jig, shown in Figure 5.4, to aid the alignment of the sample layers. The jig was made of PVC with a 52 mm internal diameter and was 35mm long. The sheets were first stacked into the jig in random orientation. Then, a stainless steel wire of 0.3mm in diameter was used to tighten the layers and create a rigid structure. The final process was to wrap PTFE tape (Polytetrafluoroethylene) around the outside of the multi-layered samples.
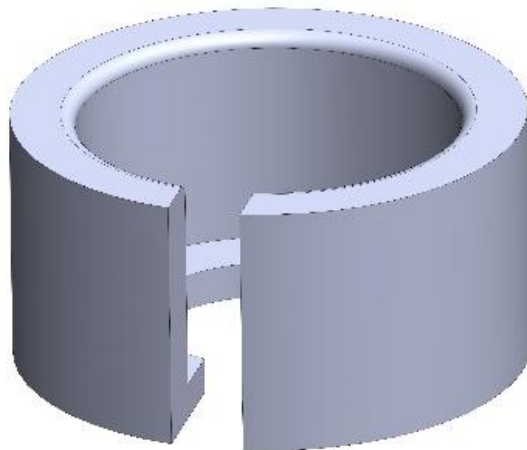
Figure 5.4 A PVC assembling jig.

Thirty-six hybrid samples were produced in total from the combination of the six samples of aluminium metal foams and the three samples of 304L stainless steel woven screens. They were assembled to cover a wide range of heterogeneous structures with a high variety of structural parameters (pore size and moderate porosity). The physical properties of the tested metal foam samples are listed in Tables 5.4 and 5.5.

Table 5.4 Geometrical parameters of heterogeneous porous media made replicated aluminium foams with irregular pores and stainless steel mesh layers.

Foam type	Sample name	Number of mesh layers	Total weight (gr)	Thickness (mm)	Total volume (mm³)
Crushed-S4	1 S4/ 2 Me40	44	86.00	25.35	51988.78
	2 S4/ 1 Me40	22	66.10	24.28	49794.38
	1 S4/ 2 Me30	35	88.00	25.18	51629.89
	2 S4/ 1 Me30	20	69.00	25.55	52398.95
	1 S4/ 2 Me20	28	78.00	25.30	51886.24
	2 S4/ 1 Me20	14	60.00	24.58	50399.38
Crushed-M5	1 M5/ 2 Me40	44	87.00	25.03	51704.62
	2 M5/ 1 Me40	22	62.10	23.99	49566.19
	1 M5/ 2 Me30	35	81.50	24.63	50878.17
	2 M5/ 1 Me30	20	65.60	25.05	51756.27
	1 M5/ 2 Me20	28	75.00	24.88	51394.70
	2 M5/ 1 Me20	14	58.00	24.03	49638.50
Crushed-L5	1 L5/ 2 Me40	44	82.00	24.58	50596.83
	2 L5/ 1 Me40	22	52.00	23.67	48723.26
	1 L5/ 2 Me30	35	79.50	24.90	51265.97
	2 L5/ 1 Me30	20	60.60	24.18	49773.28

| | 1 L5/ 2 Me20 | 28 | 70.00 | 24.90 | 51265.97 |
| | 2 L5/ 1 Me20 | 14 | 54.00 | 23.78 | 48949.73 |

Table 5.5 Geometrical parameters of heterogeneous porous media made replicated aluminium foams with irregular pores and stainless steel mesh layers.

Foam type	Sample name	Number of mesh layers	Total weight (gr)	Thickness (mm)	Total volume (mm³)
Spherical-S6	1 S6/ 2 Me40	44	88.10	25.25	51278.25
	2 S6/ 1 Me40	22	59.30	24.38	49501.28
	1 S6/ 2 Me30	35	83.90	24.81	50384.69
	2 S6/ 1 Me30	20	62.80	26.15	53105.99
	1 S6/ 2 Me20	28	75.60	25.14	51044.70
	2 S6/ 1 Me20	14	56.20	24.55	49856.67
Spherical-M10	1 M10/ 2 Me40	44	85.50	25.15	51740.24
	2 M10/ 1 Me40	22	57.00	25.03	51483.08
	1 M10/ 2 Me30	35	83.00	25.21	51853.39
	2 M10/ 1 Me30	20	61.00	25.75	52974.60
	1 M10/ 2 Me20	28	72.00	25.29	52017.97
	2 M10/ 1 Me20	14	53.00	25.15	51729.95
Spherical-L10	1 L10/ 2 Me40	44	82.80	25.03	51523.33
	2 L10/ 1 Me40	22	54.10	24.28	49979.17
	1 L10/ 2 Me30	35	82.30	24.63	50699.78
	2 L10/ 1 Me30	20	59.60	25.67	52851.30
	1 L10/ 2 Me20	28	68.30	25.35	52192.46
	2 L10/ 1 Me20	14	50.60	24.40	50236.53

5.2 Designing and manufacturing the sample's holder.

Once the multi-layered samples were wrapped, they were inserted between the two circular rings of the test section. Four M3.5 x 50mm countersunk screws and nuts were then used to hold the sample and the holder rings together. The sample holder, shown in Figure 5.5, was designed and manufactured to mount multi-layered samples. Two key aspects were taken into consideration when the sample holder was developed and produced. First, it should be made of a material with good machinability so the end product would have good surface finishing. Second, it should have low thermal properties, to minimise the impact on the thermal examinations. Acetal plastic was seen to have these properties. An Acetal rod, supplied by Direct Plastics Ltd [181], was used to fabricate the sample holder. According to the manufacturer, this type of plastic has a specific heat capacity of 1.4 J/g.K, and thermal conductivity of 0.39 W/K.m. The two circular rings of the test section had an outside diameter of 70 x 50 mm long. It was designed to accommodate a cylindrical specimen of up to 52 mm

diameter by 35 mm in length. The circular test sample holder rings had O-ring grooves machined on the external diameter to create a seal between the test section and the sample holder. Three-millimetre Nitrile O-rings were used to seal the gap between the sample holder and the test section.
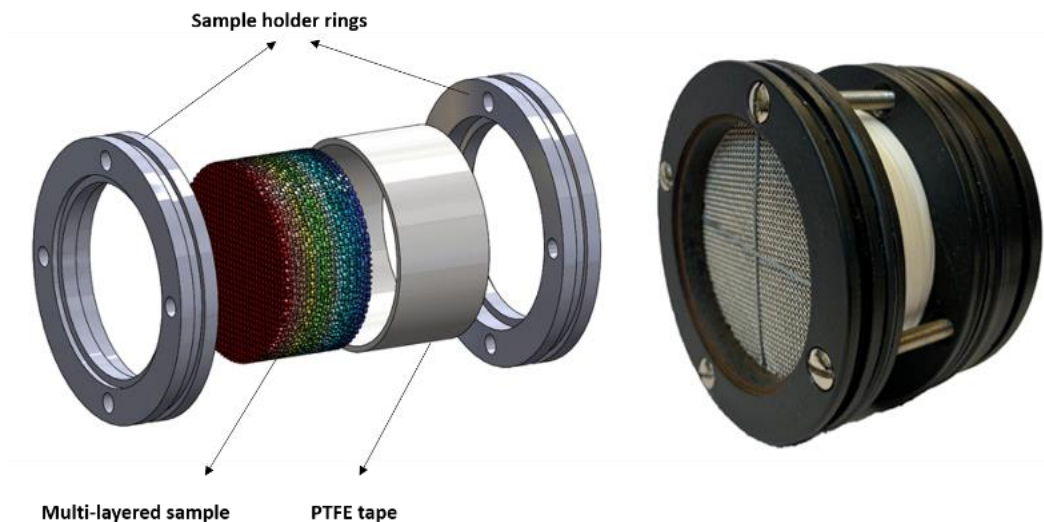
Figure 5.5 The sample holder, including porous bed layers.

Previous analytical researchers [17][75][209] have mentioned the compression effect on wire mesh structure (compactness factor). As the compactness factor increases, the porosity of the wire mesh layer structure decreases. As a result, the pressure drop through the layers may increase. Therefore, the influence of the compression value on the tested samples was worthy of experimental examination. The samples were compressed together in the holder by tightening up the four M4 screws using a low range torque wrench (Hazet-5108-2 CT). This torque wrench was used to tighten the screws between 0 and 2.5 Nm. Applying a torque force of more than 2.5 Nm on the hybrid samples caused damage to the foam integrity. However, it was found that varying the torque within this range had no measurable impact on either the hydraulic or the thermal performance. For similar testing conditions, a 2.5 Nm torque was applied for all the samples before they were inserted into the test section. The test section, shown in Figure 5.6, is a cylindrical block of PVC plastic (diameter 160 mm by 60 mm long), bored out to accept the test section holder with a sufficient clearance to allow the compression of the Nitrile O-rings.
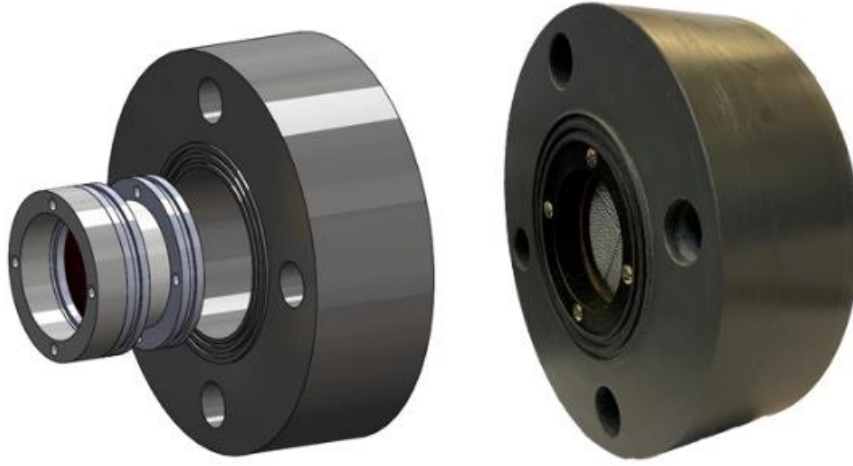
Figure 5.6 cylindrical PVC test section.

5.3 Volumetric porosity

One of the microstructure parameters used to characterise the porous media is volumetric porosity ϵ. It describes the void volume available for the fluid flow through the solid matrix structure. It is defined as [68][210][128][113].

$$\epsilon = 1 - \frac{V_m}{V_S}$$

5.1

Where V_m is the solid phase volume and V_S is the regenerator total volume. The volumetric porosity of porous media can be measured by a great variety of methods. The volumes can be obtained experimentally from basic measurements. For the semi-homogeneous foam samples, the samples were weighed and divided by the aluminium density to determine the solid phase volume. According to the supplier, the density of the aluminium was equal to 2681 kg/m3. The values of the total volume of samples were obtained from the direct measurement of the tested samples. For the packed woven wire mesh screens, plain, square and have equal openings size and wires diameter, the porosity can be obtained by the expression given by Chang [150][137] where n, d_w, P_t, D are the number of screen layers, diameter of the wire, screen transverse pitch and diameter of the sample respectively.

$$\epsilon = 1 - \frac{\pi n d_w^2}{2 P_t D} \left(1 + \frac{d_w^2}{P_t^2}\right)^{0.5}$$

5.2

Almost the same technique used to determine the porosity of each semi-homogeneous samples were implemented to identify the porosities of the hybrid regenerators. The aluminium foam slices were measured for their weight and volume

after being sliced. The aluminium density was used to identify the aluminium solid volume in the heterogeneous regenerator. The total volume of the hybrid samples was measured and used to determine the wire mesh screen volumes. According to the manufacturer, the 304 stainless steel has a density equal to 8,000 Kg/m³; this was utilised to calculate the solid volume of the mesh screens. By applying Equation 5.3, the porosity of the heterogeneous samples was determined.

$$\epsilon = 1 - \frac{(V_{SF} + V_{SM})}{V_S} \qquad\qquad 5.3$$

Figure 5.7 shows the variation of porosity for the different materials used. The graph demonstrates the porosity of wire mesh samples combined with crushed type metal foam layers. It can be seen that wire mesh screens have higher porosity than aluminium metal foams. Replacing the wire mesh screens with one or two slices of aluminium foam results in a steady decrease in porosity. A similar trend was observed when the wire meshes were combined with spherical type metal foam layers. An insignificant difference in porosity between the two combinations was calculated.
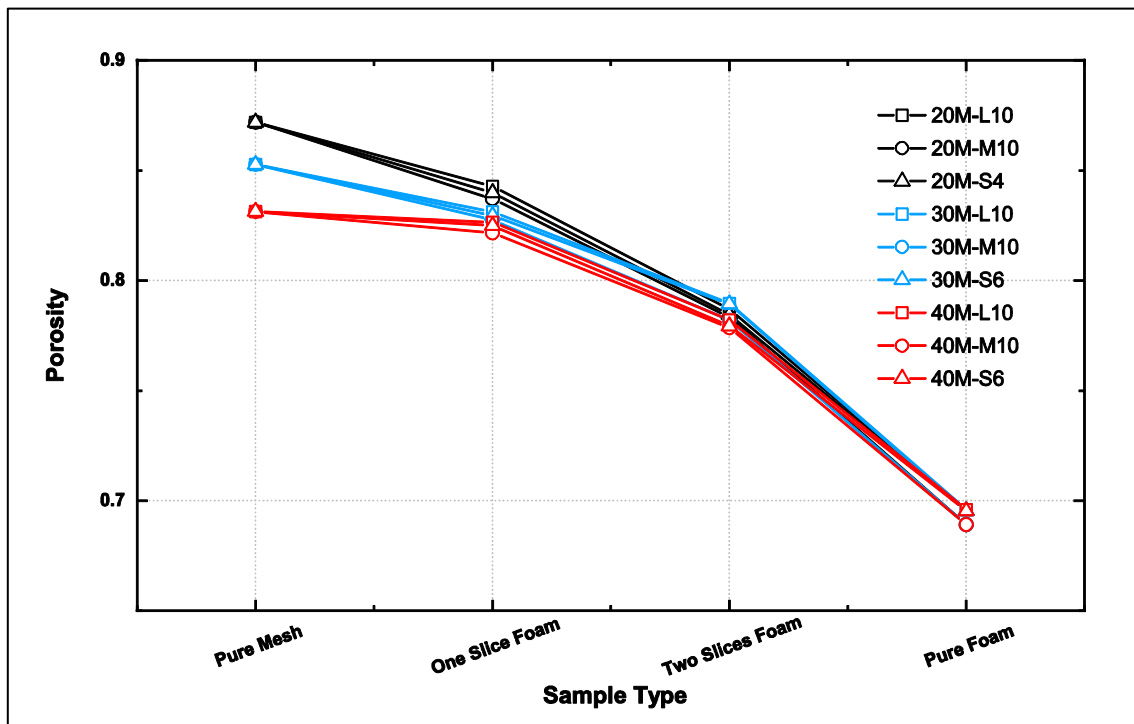
Figure 5.7 Porosity variation with different structures made of mesh screens and crushed foam layers.

5.4 Heat and mass transfer in porous media

After knowing the number of transfer units within each sample, the heat transfer coefficient h_s may be obtained using Equation 1.4 [197].

$$h_s = NTU_s \dot{m}_f c_f / A_{HT}$$ 5.4

The determination of the heat transfer surface area in porous media is a challenge due to the complexity of the internal structure. This challenge becomes more complicated when the sample pore shapes are not identical [211]. The definition of the heat transfer area of the semi-homogeneous screen-packed matrix is a function of the porosity of the wire mesh screens ϵ, thickness L, cross sectional area A_{cs} of the matrices, and the net wire diameter d_w [13][55][137][171]. It is given as:

$$A_{HT} = 4(1 - \epsilon)A_{cs}L/d_w$$ 5.5

For the semi-homogeneous metal foam samples, the shape of the pores in all samples was assumed to be spherical. This assumption is based on the fact that the salt particles used to produce the pores in the metal foam samples were also spherical in shape. Therefore, one can calculate the number of spherical pores N in each sample, then calculate the total heat transfer surface area of spheres. The number of pores was obtained from the volumetric porosity of the samples. First, the void volume V_V was calculated using the multiplication of the total volume of the sample by the porosity. The void volume represents the total volume of pores inside the matrices. Therefore, for the average pore size d_P of each foam, the category was used with the void volume to determine the number of pores in each sample. The number of pores was then used to estimate the total heat transfer surface area of the samples.

$$V_V = V_S \epsilon$$ 5.6

$$N = \frac{6V_V}{\pi d_P^3}$$ 5.7

$$A_{HT} = N\pi d_P^2$$ 5.8

This method is equivalent to the use of the specific surface area A_{Sp} to determine the heat transfer surface area of a packed bed of spheres. According to a

previous study [18], the heat transfer surface area is the subject of the total matrix volumes by specific surface area and can be expressed as:

$$A_{TH} = A_{sp} V_s \qquad 5.9$$

The specific surface area for a bed of uniform spheres having an average sphere diameter d_s can be expressed as [36]:

$$A_{sp} = 6(1 - \epsilon)/d_s \qquad 5.10$$

As this equation was derived to calculate the specific surface area of spheres, the term "$1 - \epsilon$" should be replaced by the term "ϵ" to obtain the specific surface area of the pores and the final form of the equation can be written as:

$$A_{sp} = 6\epsilon/d_p \qquad 5.11$$

The heat transfer surface area of the heterogeneous regenerators was calculated based on the physical properties of each material and the contribution of the heat transfer surface area of mesh layers and foam slices in the heterogeneous regenerators. The total heat transfer surface area of the hybrid samples was considered as the summation of the solid-gas contact area of both classes of media used to perform the samples. Figure 5.8 shows the variation of the heat transfer surface area against porous structures made of wire mesh screens and layers of crushed foams. As can be seen, the heat transfer surface area varies with pore size and the combination of mesh screens and foam layers. For pure structures (mesh screens or foam layers), decreasing the pore size leads to an increase in the heat transfer surface area. Wire mesh screens have a smaller pore size compared to metal foam samples but they provided very similar heat transfer surface areas. The heat transfer surface area of pure wire meshes decreases gradually because of the replacement of mesh screens with layers of metal foam.
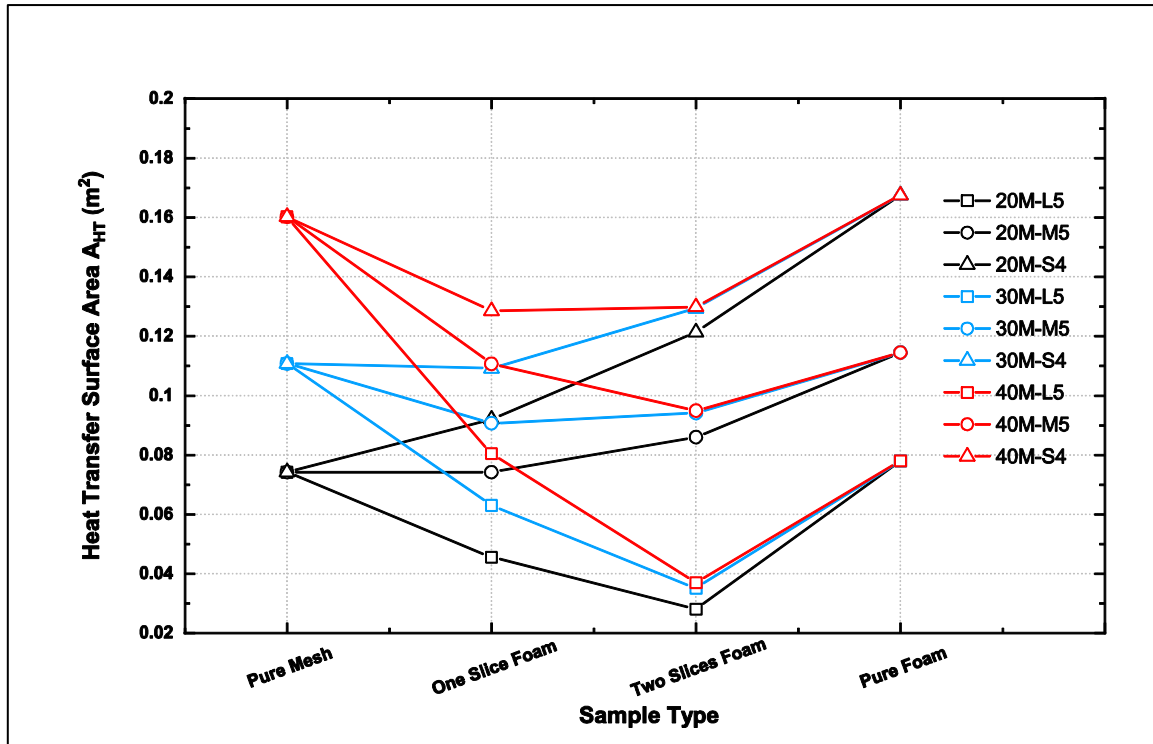
Figure 5.8 Variation of heat transfer surface area with different structures made of mesh screens and crushed foam layers.

This graph demonstrates the change in heat transfer surface area due to the replacement of wire mesh screens with crushed pore metal foam layers. A similar trend was noticed in the combination between wire mesh screens and the spherical metal foam layers. An insignificant difference in heat transfer surface area was calculated between the two combinations.

5.5 Determination of heat capacity for hybrid regenerators

One key advantage of a compound material is that it presents the possibility of combining certain properties from two or more types of materials to create a novel material with several new properties. Material property such as heat capacity is one of the most effective characteristics influencing the thermal performance of regenerators. To absorb a large amount of energy available, the regenerator needs maximum heat capacity. Aluminium has a high specific heat capacity compared to stainless steel. However, due to the mass density difference, the stainless steel samples in this study had higher heat capacity compared to the foam samples. Combining wire mesh screens and aluminium slices of foam led to a change in the heat capacity value. This change depends on the proportion of the material involved in the regenerators. The best possible estimate for the heat capacity of the heterogeneous regenerators can

be made using the rule of mixture. If the thermal energy required to increase the temperature one degree in each portion is known, the summation of energies can be assumed to be the heat capacity of the heterogeneous medium. The amounts of energy each sample can absorb produce a one-degree temperature increase, which is shown in Figure 5.9.
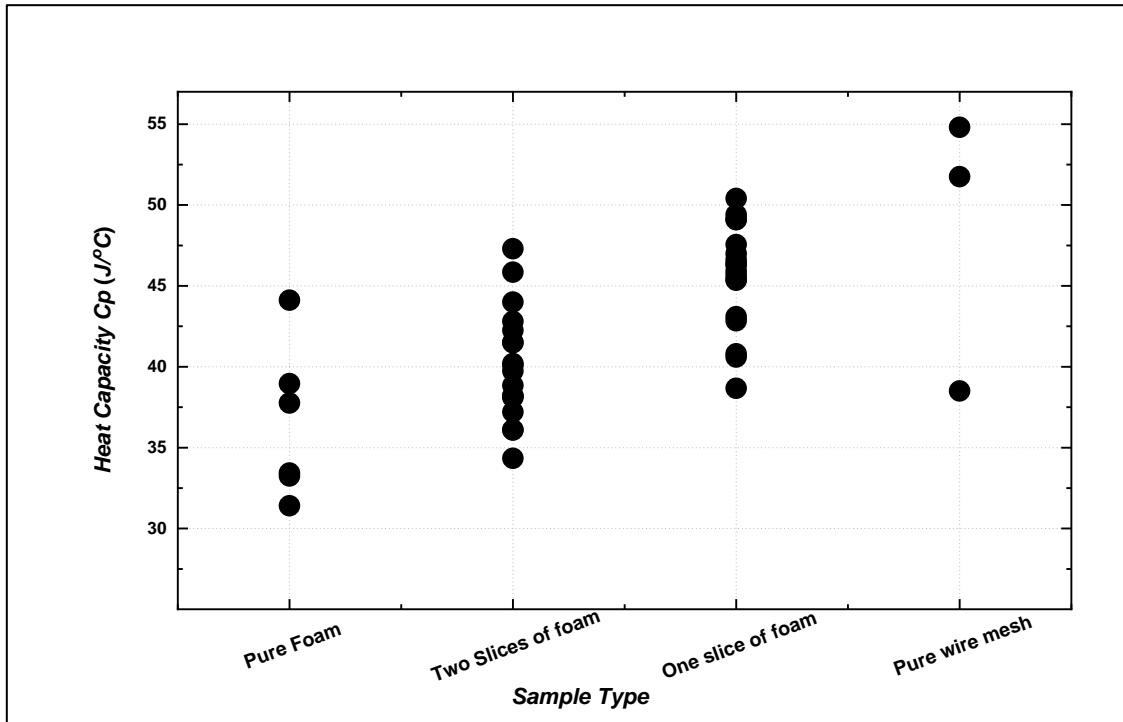
Figure 5.9 Heat capacity of the tested samples.

The total heat transfer surface area, porosity and the heat capacities of the tested samples are listed in Tables 5.6 to 5.10.

Table 5.6 Properties of wire mesh screens samples.

Sample name	Total heat transfer area (m^2)	Porosity (%)	Heat capacity (J/ ^oC)
20 Mesh	0.0742	77.97	38.5
30 Mesh	0.1108	74.01	51.8
40 Mesh	0.1602	72.29	54.8

Table 5.7 Properties of the original aluminium foam samples.

Sample name	Total heat transfer area (m^2)	Porosity (%)	Heat capacity (J/ ^oC)
S4	0.1732	63.03	46.1
S6	0.1932	69.54	38.2
M5	0.1185	62.59	45.5
M10	0.1392	68.91	40.3
L5	0.0808	61.6	45.5
L10	0.0966	69.6	38.1

90

Table 5.8 Properties of the sliced aluminium foam samples.

Sample name	Total heat transfer area (m^2)	Porosity (%)	Heat capacity (J/ ^{o}C)
Sliced S4	0.1675	63.03	44.1
Sliced S6	0.187	69.54	33.2
Sliced M5	0.1145	62.59	38.9
Sliced M10	0.1348	68.91	33.4
Sliced L5	0.078	61.6	37.8
Sliced L10	0.0935	69.6	31.4

Table 5.9 Properties of heterogeneous porous media made replicated aluminium foams with irregular pores and stainless steel mesh layers.

Sample name	Total heat transfer area (m^2)	Porosity (%)	Heat capacity (J/ ^{o}C)
1 S4/ 2 Me40	0.1285	80.71	49.4
2 S4/ 1 Me40	0.1299	74	45.9
1 S4/ 2 Me30	0.1092	81.23	50.4
2 S4/ 1 Me30	0.1294	74.89	47.3
1 S4/ 2 Me20	0.0921	82.24	45.4
2 S4/ 1 Me20	0.1213	74.65	42.8
1 M5/ 2 Me40	0.1107	80.67	49.1
2 M5/ 1 Me40	0.095	73.96	42.3
1 M5/ 2 Me30	0.0907	81.12	46.4
2 M5/ 1 Me30	0.0941	74.7	44.0
1 M5/ 2 Me20	0.0743	82.17	43.1
2 M5/ 1 Me20	0.0861	74.39	40.2
1 L5/ 2 Me40	0.0805	80.42	46.6
2 L5/ 1 Me40	0.037	73.59	37.2
1 L5/ 2 Me30	0.0631	81.12	45.4
2 L5/ 1 Me30	0.0352	73.9	41.5
1 L5/ 2 Me20	0.0456	82.09	40.6
2 L5/ 1 Me20	0.0281	74.1	38.2

Table 5.10 Properties of heterogeneous porous media made replicated aluminium foams with irregular pores and stainless steel mesh layers.

Sample name	Total heat transfer area (m^2)	Porosity (%)	Heat capacity (J/ ^{o}C)
1 S6/ 2 Me40	0.1338	82.49	49.1
2 S6/ 1 Me40	0.1422	77.95	39.7
1 S6/ 2 Me30	0.1141	82.96	46.9
2 S6/ 1 Me30	0.1427	78.93	41.5
1 S6/ 2 Me20	0.0981	83.99	42.8
2 S6/ 1 Me20	0.1339	78.45	38.2
1 M10/ 2 Me40	0.1156	82.17	47.6

2 M10/ 1 Me40	0.1073	77.86	38.1
1 M10/ 2 Me30	0.0976	82.75	46.3
2 M10/ 1 Me30	0.1058	78.2	40.1
1 M10/ 2 Me20	0.0808	83.71	40.8
2 M10/ 1 Me20	0.0983	78.33	36.1
1 L10/ 2 Me40	0.0825	82.66	45.9
2 L10/ 1 Me40	0.0402	78.22	36.1
1 L10/ 2 Me30	0.0628	83.13	45.7
2 L10/ 1 Me30	0.04	78.97	38.8
1 L10/ 2 Me20	0.0475	84.27	38.7
2 L10/ 1 Me20	0.0316	78.69	34.3

5.6 Pressure drop experimental apparatus and data logging

A blow-through pressure drop test rig is shown in Figure 5.10. It was designed and manufactured to test the porous matrices in both creeping laminar flow and turbulent flow. It consists of an open circuit cylindrical wind tunnel made of a 2-inch ABS plastic pipe with an internal diameter of 52.9 mm. A laboratory compressor was used to provide the system with compressed air at high pressure (about eight bar) and mass flow rate up to 0.02 kg/s. Once the air was released from the source, it flowed through a regulator to trap and remove any moisture or any micron particles before being stored in a plenum reservoir. The plenum reservoir has the advantage of damping the fluctuations caused by pressure pulses. Two-needle valves were connected to the plenum reservoir and used to control and fine-tune the air passing to the system. One valve was to allow the air to pass through a Roxspur flowmeter (FFLM0035 0.8% of reading + ±0.2% span) and measure the creeping flowrate in the range from 0.5 LPM to 50 LPM. The other valve directed the flow toward a precision mass flow meter (Emerson Micro Motion ±0.50%), which was used to measure a high mass flow rate (up to 0.025 kg/s).

The discharge points of both flowmeters were connected to the wind tunnel entrance using plastic tubing with a 12 mm internal diameter. A honeycomb air straightener was fitted at the wind tunnel opening to condition the upcoming air and minimize the entrance impact of the pipe. The air velocity profile was fully developed before reaching the test section in both laminar and turbulent regimes. The laminar flow required a longer pipe than that for the turbulent flow to become fully developed (138 of the pipe diameter and 30 of the pipe diameter, respectively). Thus, the pipe length was determined based on the laminar flow condition using Le/D =0.06 Re [212].

The air then flowed across the test section. The test section, shown in Figure 5.6, was secured between two standard BS 63 mm ABS flanges and held together with four M16 x 140 mm nuts and bolts. The gap between the test section and the flanges was sealed with 3 mm thick rubber gaskets.

Two pressure taps were located upstream and downstream of the test section. These were created using 6 mm push-in fittings and connected to differential pressure measuring instruments by a flexible PVC pipe. Two differential pressure transmitters measured the pressure drop across the tested sample, depending on the mass flow rate and pressure difference. A Furness Controls transmitter (332-4W with accuracy ±0.25% of reading + ±0.2 of span) with a measuring range from 0 to 50Pa was utilised for low flowrates. For high flowrates, an Omega transmitter (DPGM409DIFF - 350HDWU with accuracy ±0.25% of reading + ±0.08% of span) with a variability of 0.35 KPa was used.

The passing air was discharged to the atmosphere through a 750 mm long ABS pipe at the end of the test section. After the initial build of the rig, it was checked for leakage. This was achieved by closing off the end of the discharge pipe. The system was pressurised at 0.3 bar for 24 hours. The joints and fittings on the rig were checked for leaks using a Rocol Leak detector. No leaks were detected. It was observed that as the mass flow rate increased, the back-pressure within the system built up. For safety reasons, the back-pressure was monitored on the visual display. The air properties were measured using a static transducer (Omega - PXM409-350HGV with 0.08% accuracy), and a thermocouple (Omega 1.5mm OD, sheathed) sensor, installed in front of the test section.

ITEM NO.	PART NUMBER
1	ABS_PIPE
2	TEST_SECTION
3	6mm_PUSH FITTING
4	Differential-Pressure_Transducer
5	Thermal_Couple
6	Static_Pressure_Transducer
7	Compressed_Air_Regulator
8	Needle_Valve
9	Air_Cylinder_Tank
10	12mm_PVC_Pipe
11	Mass_Flow_Meter

DETAIL A

DETAIL C

DETAIL D
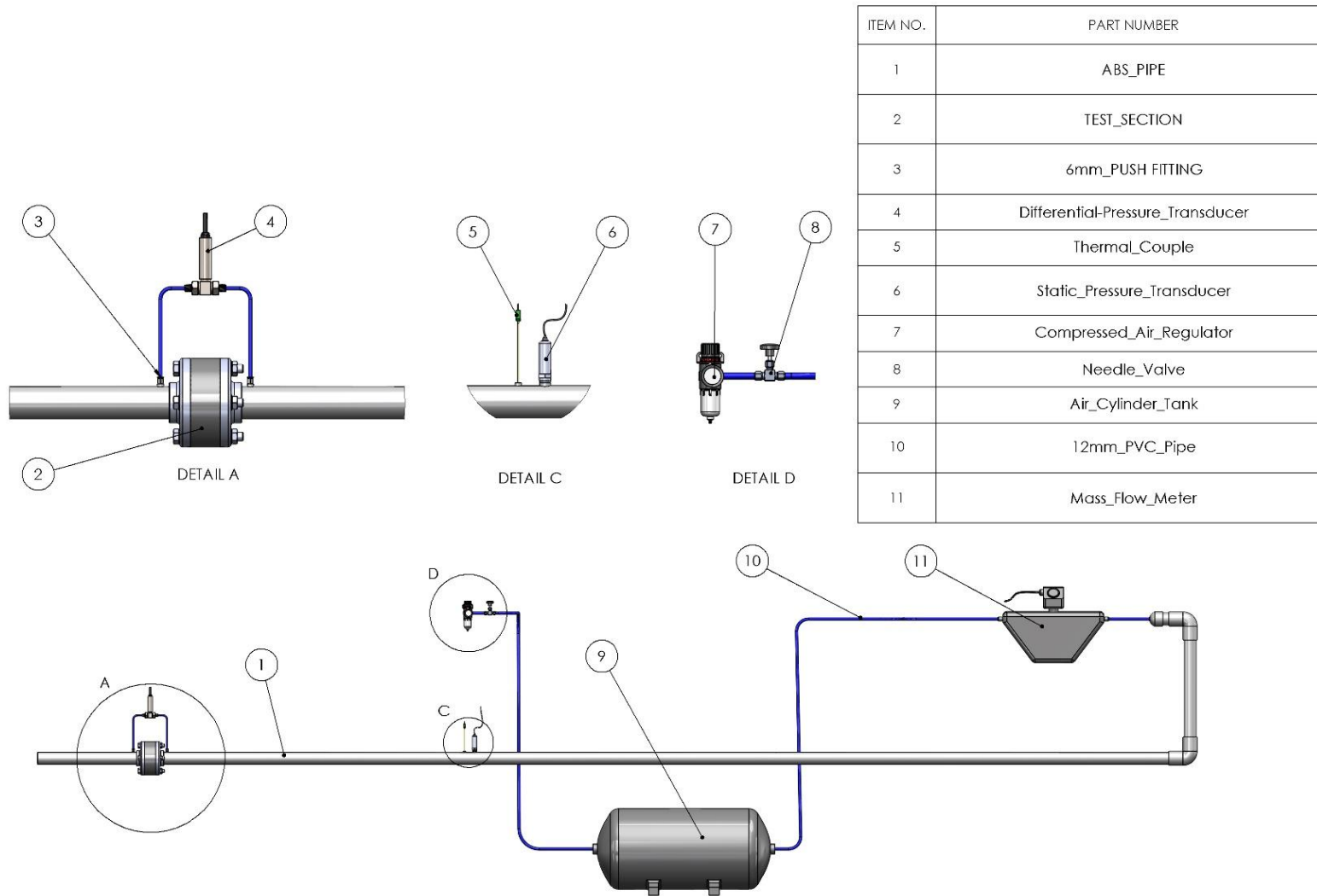
Figure 5.10 Design drawing of the test rig for measuring pressure drop.

94

Experimental data was captured and logged by a National Instruments compact DAQ data acquisition system, consisting of a voltage/current module (NI 9207, 16-Ch voltage/current, 24-bit, 500 S/s with accuracy 0.1% of reading + ±0.02% of span) and a thermocouple C Series module (NI 9212, 24-Bit, 8-Ch, 95 S/s with accuracy ± 0.05 Co using K-type thermocouple). The modules were connected to a compact DAC chassis (cDAQ-9174 four slot USB) [213].

5.6.1 Pressure drop testing procedure

Once the specimen and the sample holder had been inserted into the test section, the bolts and nuts were tightened up to 6 N/m. The test started at a high flow rate and decreased in steps to the lowest measured flow under steady-state conditions, for each run. LabVIEW code (version 17.0.1f3) was constructed to process, monitor, and log the signals received from the data acquisition system. The control valve was first adjusted to the desired mass flow rate and left for three minutes to reach a steady state. The data points were logged at a 100 Hz sample rate, for twenty seconds from each sensor. The readings received were then simultaneously averaged. The static pressure and temperature were subsequently utilised to obtain the upcoming air densities. By knowing the mass flow rate and the cross-sectional pipe area, the superficial air velocity was determined.

5.7 Heat transfer experimental apparatus

The experimental heat transfer equipment shown in Figure 5.11 was first designed and manufactured by Barari [214] and later used to measure the heat transfer performance of regenerators by Abuserwal [37] and Luna [36]. It was constructed to meet the requirements of the transient single blow technique. In the current study, the apparatus was refurbished, developed, and equipped with new instrumentation to improve the accuracy of measurements and reduce the time consumption of testing. It is an open circuit wind tunnel consisting of a closed-loop heating system, an orifice plate, the detour section, test section (Figure 5.11, Detail A), suction unit and data acquisition unit.

In the single blow technique, it is essential to maintain the airflow temperature at the matrix entrance. This was achieved by establishing the heating system (Figure 5.11, Detail F). The heating system was established and consisted of an Omega inline

heater (AHF-14240), a proportional integral derivative (PID) controller, an On/Off solid-state relay (SSR), and a thermocouple (Omega - 0.5mm OD, sheathed). The suction unit withdrew air through the inline heater. The 240 V heater was able to achieve a temperature of 15°C above the ambient air temperature. The heater power was regulated through a (Solid State Relay) SSR - On/Off electronic switch. The SSR was synchronized with the PID controller, built within Lab-view software. The cycle started from the PID, which manages the operation time and passes a signal to the DAQ then to SSR. The thermocouple was installed downstream to close the circuit and give temperature feedback to the PID controller. The heating system was upgraded by replacing the PID controller with an Omega PID Controller (CN32PT-440 - Platinum Series, 1/32 DIN, 90 to 240 Vac), which has high accuracy and fast response. After passing through the heater, the hot air went through an airflow straightener. The straightener was made of ten fine stainless steel wire mesh screens to stabilise the airflow and reduce the turbulence caused by the internal heater fins. Next, the air flowed through a cylindrical ABS pipe towards a flange-typed orifice flow-meter (Figure 5.11, Detail E). The orifice flow-meter was designed and manufactured according to ISO standards [BS EN ISO 5167-2:2003] [215] to measure the fluid flow in the turbulent regime.

To ensure the velocity profile was fully developed reaching the orifice plate, the upcoming flow pipe length had to be 30 times longer than the pipe diameter $Le/D = 4.4 Re1/6$ [212]. The locations of the pressure taps in front of and after the orifice plate were specified by BS EN ISO 5167-2:2003 [215]. A new differential pressure transducer (Omega - PX 409 with ±0.5% accuracy) was connected to the flanged orifice plate to measure the pressure drop over the orifice plate. The orifice plate and differential pressure transducer were recalibrated against an Emerson Micro Motion flowmeter to determine the discharge coefficient C, (see Appendix 2).

ITEM NO.	PART NUMBER
1	Wooden_Box
2	Silencer
3	Test_Section
4	8mm Push fitting
5	Actuator
6	Three_way_Valve
7	Thermal_Couple
8	Gate_Valve
9	Pressure_Tapping
10	Orifice_Plate
11	Thermal_Couple
12	Static_Pressure_Transducer
13	Air_Strainer
14	240v_Heater
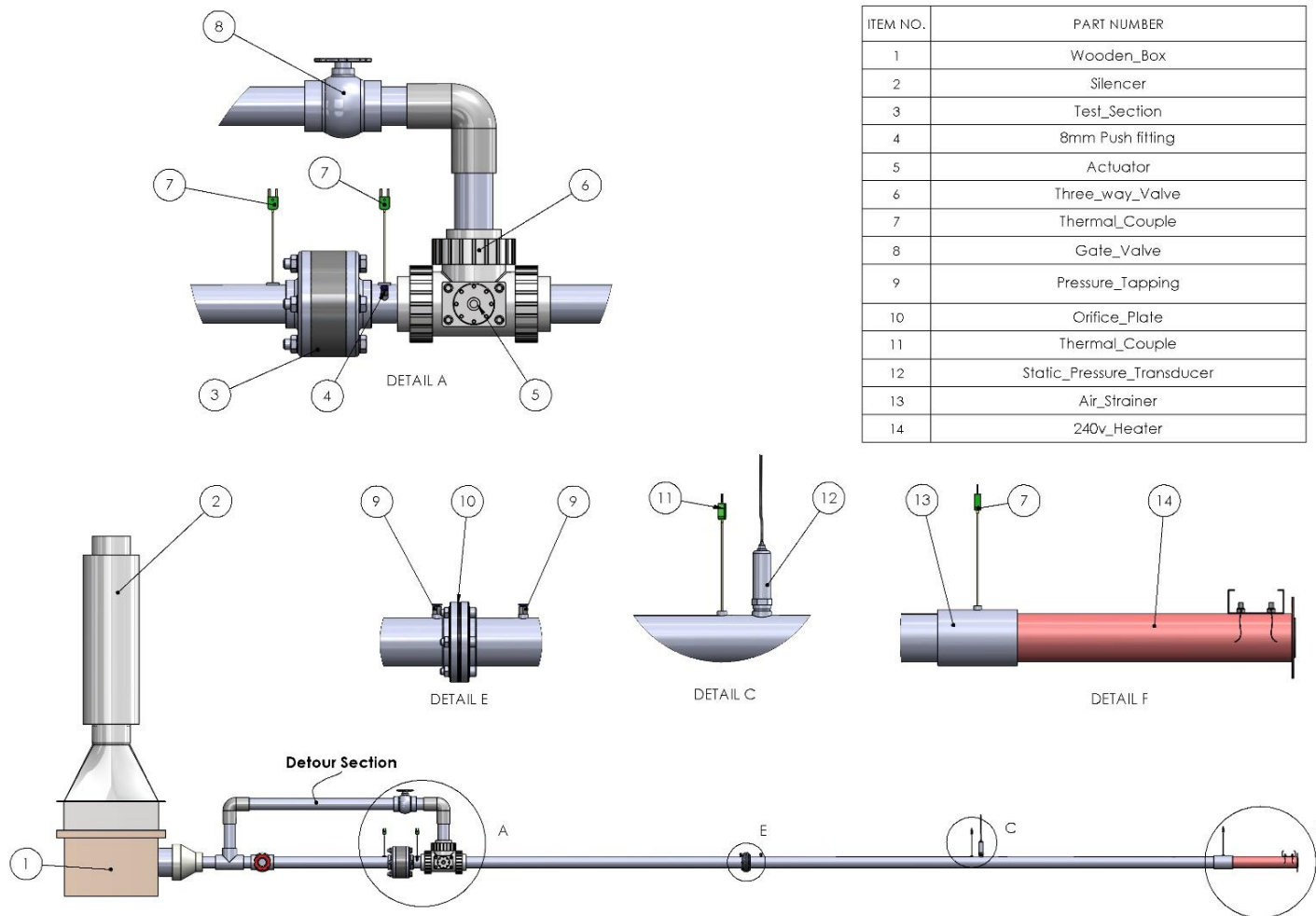
Figure 5.11 Represents the design drawing of the thermal experiment rig.

97

Instead of using the ambient conditions to measure the air properties entering the orifice plate in the prior studies, a new static pressure transducer (Omega - PXM409 with ±0.08% accuracy) and a thermocouple (Omega - 1.5mm OD, sheathed) were installed to measure the pressure and temperature in front of the orifice plate. The discharge coefficient of the orifice plate was determined to be 0.632, with a maximum inaccuracy of ± 0.3%.

After the orifice plate, the hot air entered the test section part of the rig. The essential requirement of the single-blow technique is to achieve a step-change in the fluid temperature at the tested sample entrance. A three-way ball valve (Figure 5.11.6) with a double-acting rotary vane actuator (Norgren M-60284-90) was used to divert the airflow direction towards either the test section or the detour section within 0.15 seconds.

The rotary actuator was powered by a pneumatic solenoid valve connected to a compressed air cylinder set to eight bar. It was found that the ball valve was defective due to wear and tear from use in previous projects. Scars on the ball surface area caused high friction between the ball and the internal surface of the valve. The rotary actuator required ten bars to generate enough torque to overcome the friction resistance inside the valve. According to the actuator datasheet, the maximum operating pressure should not exceed eight bar. Therefore, the three-way valve was replaced by a new three-way valve to prevent any damage to the actuator.

As the air was diverted from the detour section to the test section, it experienced a sudden change in flow resistance. This caused a sharp reduction in the air velocity. In such a scenario, the PID controller is unable to adapt to that change in such a short time, which leads to fluctuation in the fluid inlet temperature. This problem was solved using a dummy resistance on the detour section. A gate valve on the detour section (Figure 5.11.8) provided similar flow resistance as previously experienced by the porous part in the test section. The old test section was replaced with the new test section described in Section 5.2. The replacement was necessary for two reasons: firstly, to be able to accommodate the sample holder described in Section 5.2; and secondly, to reduce the cost and time of the experiment. The old test section was made of two ABS flanges stacked back-to-back, as shown in Figure 5.12, and placed between the other two ABS flanges.
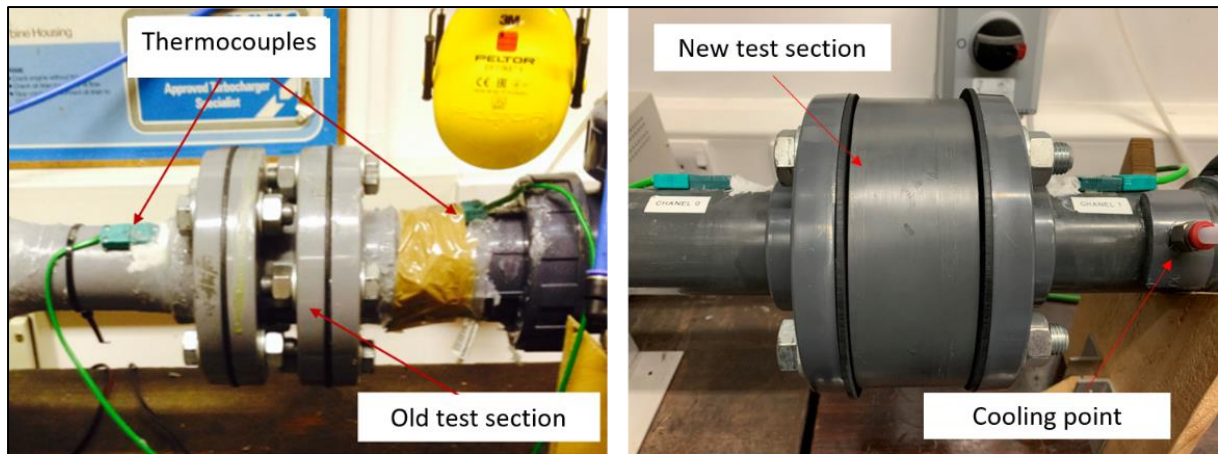
Figure 5.12 Improvement of the test section.

The flanges were fastened together by eight M16x140mm nuts and bolts. Two fine diameter thermocouples (Omega 0.01mm OD, unsheathed) were also connected under the flanges to measure the inlet and outlet air temperatures. There was a problem with the misalignment of the flanges and the different tightening forces in the connecting bolts. When the flanges are not assembled in parallel or when high torque is applied on the bolts, high internal stress transmits to the flange structure. This can cause cracking or damage to the flanges. In such a case, the flanges and thermocouples must be changed, which increases cost and time consumption. The problem was resolved by reducing the flanges and using one block test section. The number of bolts was reduced to four. After the new test section had been used, no damage in the flanges was experienced. Further, instead of sealing the gap between the flanges and the connection pipes with silicone, Nitrile O-rings were used to prevent leakage and give movement flexibility to the test section.

The cooling mechanism posed another technical issue for the previous researchers. It had been necessary to open the inlet flange in the test section to allow the ambient air to be sucked through the tested sample. In addition, a moist rag had been used to accelerate the cooling operation [37]. Because the gap between the flanges was tiny, the coolant was prevented from flowing smoothly toward the testing sample. Thus, it was necessary to wait for more than 20 minutes to complete each run. This problem was resolved by providing the system with air having a temperature at ambient temperature and about 15oC lower than the heated air. This has been achieved by using an (8mm-OD) plastic tube fitted right in front of the test section and just after the three-way valve (Figure 5.11.4). The other end of the plastic tube was connected to the lab compressed air regulator using a ball valve. The ball valve

controlled the air allowed to flow through the test section to cool it sufficiently in a short time. As a result, it was possible to complete the cooling process in two minutes as a maximum time.

A sealed wooden box fitted with two 1 KW centrifugal fans was fastened to the end of the experimental thermal rig to provide the sufficient flow rate needed for the test. The airflow velocity was tuned manually by adjusting the fan speed using an eight Amp Variac speed controller (240V variable transformer). The centrifugal fans generated high noise levels (over 100 dB) due to the high-pressure drop. Therefore, a silencer was designed and manufactured in this study at South Yorkshire Ducting Supplies Ltd [24] to eliminate the problem by aiming to keep the noise levels lower than 75dB. The silencer was installed on top of the wooden box (Figure 5.11.2). The set-up was also provided with a new National Instruments Compact DAQ data acquisition system, which was used to interpret the information received from all the sensors fixed on the experimental set-up. A VI code was built with LabVIEW software (version 17.0.1f3) to monitor and log data in real-time. This rig was also pressurized to 0.3 bars and held for 24 hours to ensure no leak occurred from the valves and pipes or joints.

The thermal testing procedure is given in (appendix 3). In both pressure drop and thermal tests, the signal from all sensors was averaged and calibrated to give a mass flow rate, differential pressure drop, static pressure, and inlet as well as outlet temperatures.

5.8 Summary

This chapter described the procedures used to manufacture and assemble the hybrid porous media including sample holder design and performing the experiments. As the hybrid samples consisted of different types of porous media, the techniques employed to determine the volumetric porosity and the heat capacity were reported. Finally, the flow and thermal experiments have been documented.

CHAPTER 6. Pressure Drop Results and Discussion

6.1 Pressure drop measurement results

Porous media consist of a complex network of paths that cause a pressure drop when fluid flows through them. To evaluate the performance of porous media, accurate pressure drop measurements are needed. In this study, pressure drop measurements were conducted over a range of velocities between 0.01 to 6 ms^{-1}. Each sample was tested three times. The logged data was then analysed and compared against models available in the literature to identify the hydraulic characteristics of each sample. The arithmetic mean values were registered as the hydraulic characteristics of the specimen. The pressures and temperatures at the inlet of the test section were measured to obtain the working air density. By knowing the mass flow rate and the cross-section area of the testing channel, the velocity could be calculated. An example of three tests is shown in Figure 6.1. A slight variation at high flow velocity was noticed: this may be due to the transition in the flow from post laminar to turbulent, or to the high uncertainty of instrumentation after reaching the working condition limits.
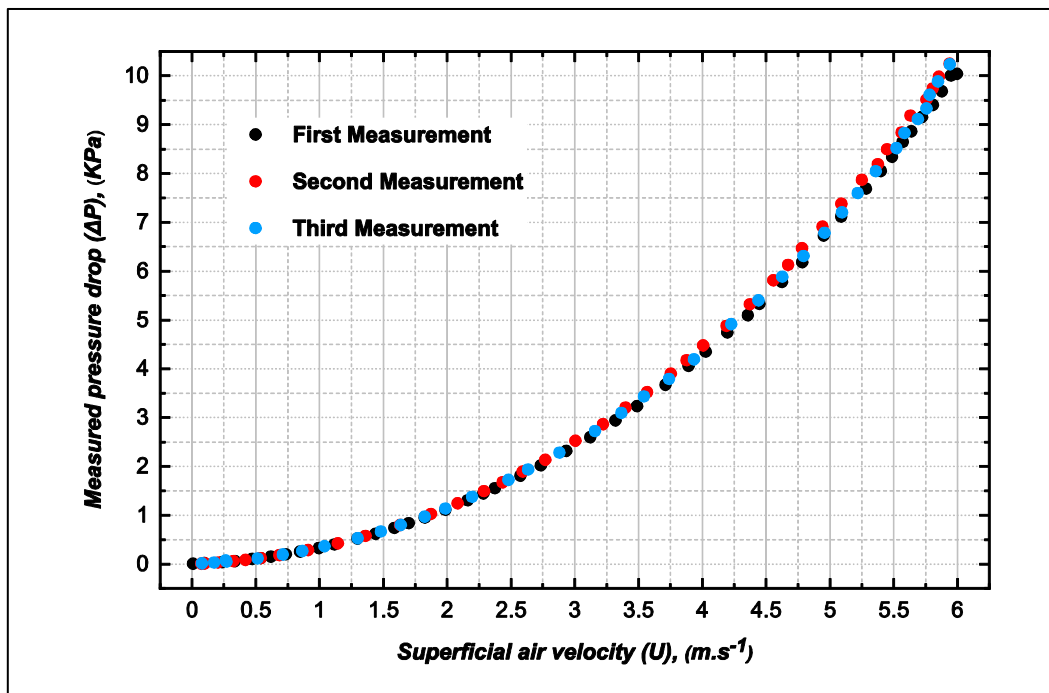
Figure 6.1 Typical values of pressure measurements.

The most common way to depict experimental pressure drop results is to plot the hydrostatic pressure gradient $\frac{-\Delta p}{L}$ against the fluid velocity as an independent variable [87][92][93][94][95][115]. This can provide an immediate sense of the magnitude of the pressure drop across the sample. The measured pressure drop data can be divided into two categories: Darcy regime data, in which the Darcy permeability can be determined and Non-Darcy regime data where the Forchheimer permeability, inertia and the form drag coefficients are identified. The results of original samples (foam before slicing and screen packed beds) in the Darcy regime and Forchheimer regimes are presented in Figures 6.2 and 6.3, respectively. The measured pressure drop data indicates that the pressure gradient increases with the frontal air velocity and decreases with the pore size. It is worth noting that the pressure drop in the crushed pore shape samples varies with the average pore sizes and porosities while in the spherical samples it depends on pore size change only, as the spherical samples have almost equal porosity. It was also noticed that, at low velocities, the experimental pressure-drop data for nine samples is overlapped. Different structures can generate similar pressure drops at constant air velocity.
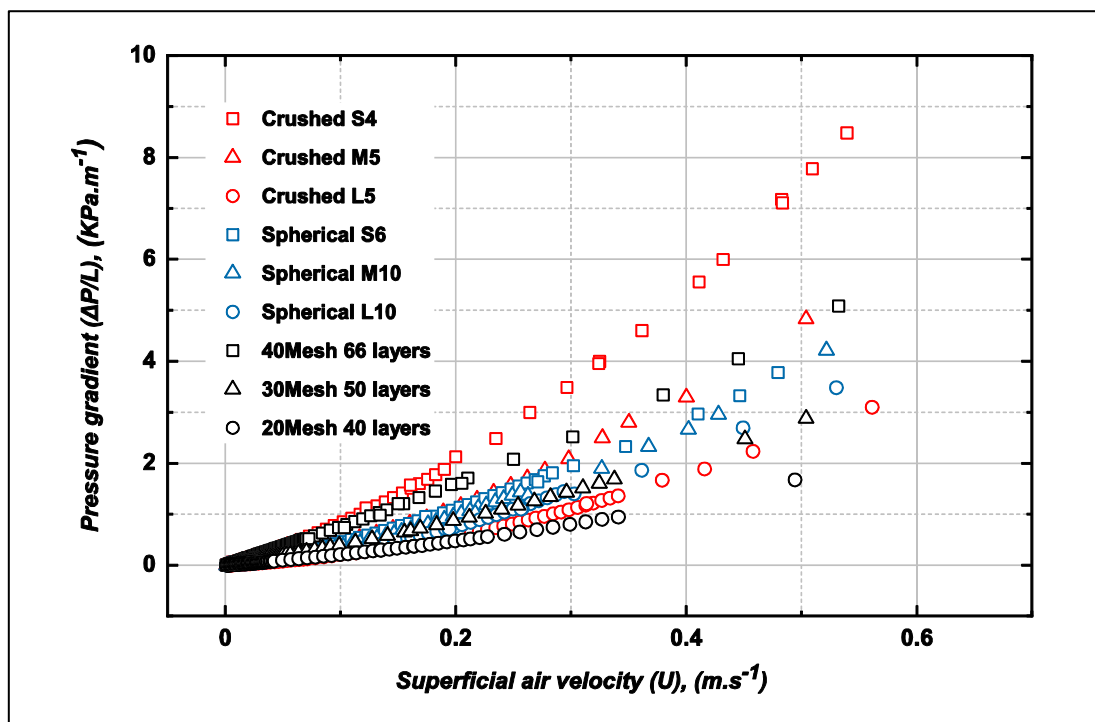
Figure 6.2 Measured pressure gradient versus frontal air velocity (semi-homogeneous samples).

At high velocities, the contribution of inertia force becomes more significant in the pressure drop. Decreasing the pore size at constant porosity provides more surface area, thus, additional friction resistance is added. There are notable differences in pressure drops between the screen packed beds and the replicated metal foam samples. The replicated metal foam samples have lower porosity and a larger solid surface area, which cause high-pressure drops. The pressure drops in the spherical metal foam samples do not appear to be systematic, though the tested samples have a very similar porosity. This is likely because of the irregularity in the interstitial flow properties or the microstructure defects reported by the manufacturer [37].
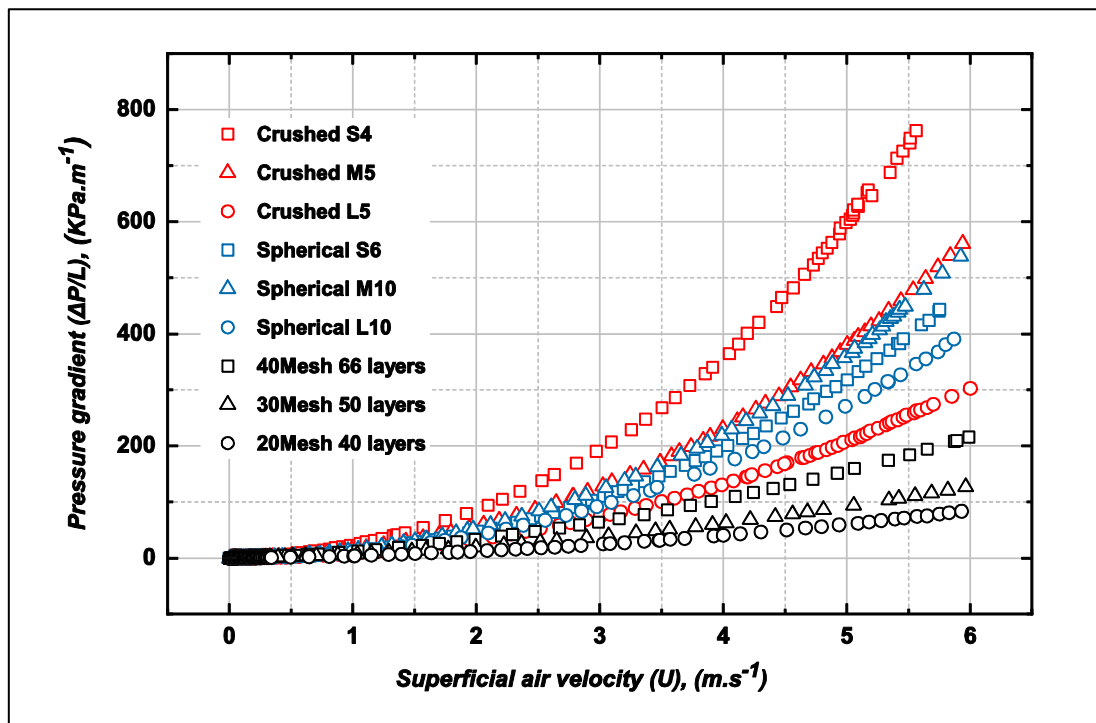
Figure 6.3 Measured pressure gradient versus frontal air velocity (Semi-homogeneous samples).

The main goal of this research was to evaluate the hydrothermal performance of heterogeneous porous materials. To achieve this goal, the original metal foam samples were cut into three slices of equal thickness. The metal foam samples were retested to investigate the slicing impact on the performance of metal foams. A comparison between the pressure drop gradients of the sliced samples and the original samples is shown in Figures 6.4 and 6.5. Oun and Kennedy [103] investigated the pressure-drop behaviour associated with airflow through a stack of open-cell Inconel porous layers. Their results showed that there is an average 10 % increase in

pressure drop due to the misalignment of the discs, generating a discontinuity in the porous structure at lower air velocities. As the airflow velocity increases, the entrance effect of distorted flow patterns develops across the sample, resulting in a 10–20 % increase in the pressure loss.

There is very limited data in the literature regarding the impact of slicing on metal foams since the majority of metal foams are inclined toward heat exchanger applications, which favour high thermal conductivity. As explained previously, two types of foams materials vary in pore shape (crushed and spherical pore shape) and ligament thickness and size. The experimental measurements in both Darcy and Forchheimer regimes showed that the pressure gradient increases once the samples have been sliced. The small pore size samples induced higher pressure compared with medium and large pore size samples. Crushed pore foam samples showed higher sensitivity to the slicing effect than that in the spherical pore shape samples.
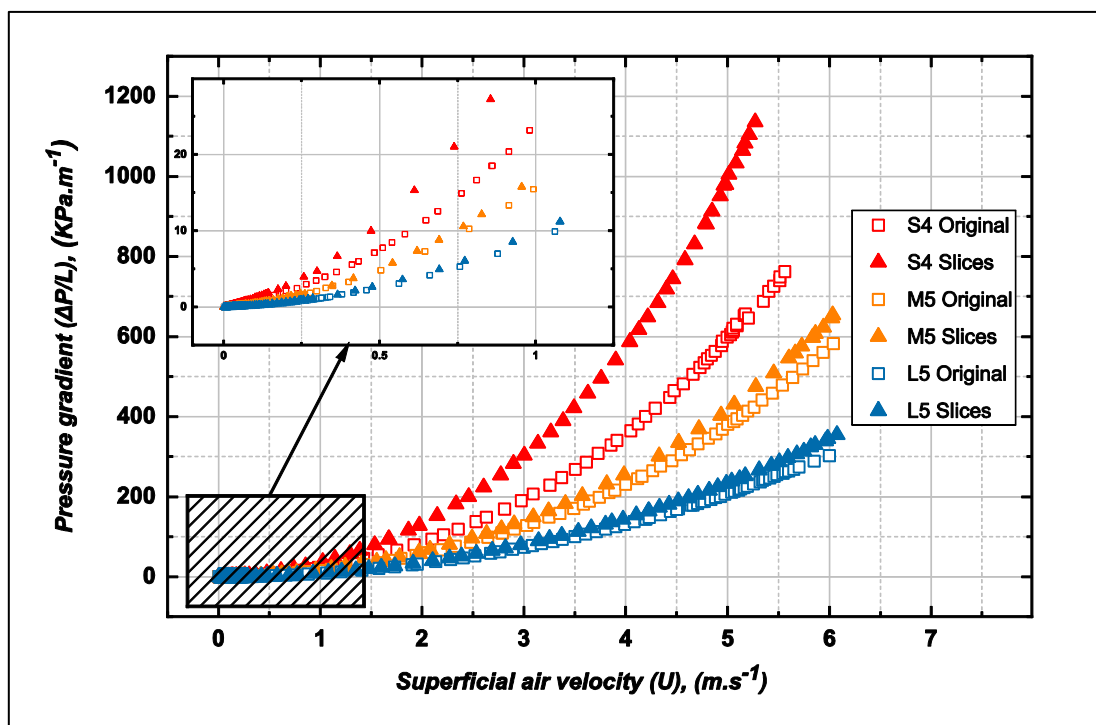
Figure 6.4 The effect of slicing on the pressure drop gradient (Crushed metal foams).
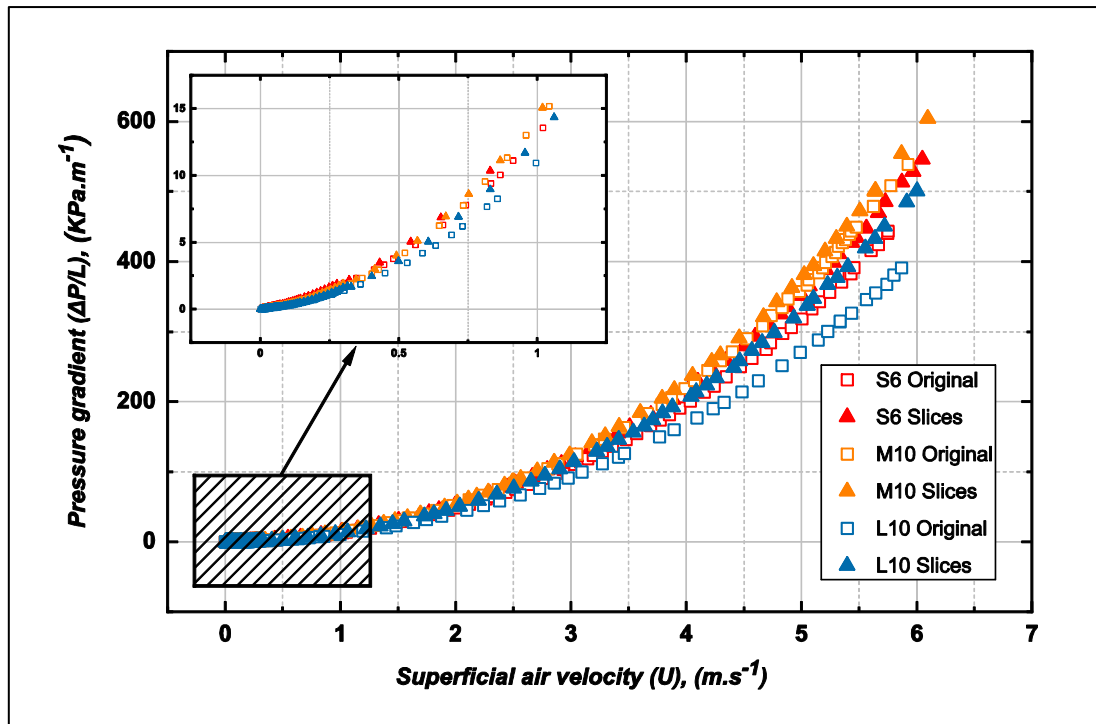
Figure 6.5 The effect of slicing on the pressure drop gradient (Spherical foams).

Usually, the flow through a porous medium is driven by a macroscopic pressure gradient $\frac{\Delta p}{L}$, where L is a macroscopic length scale. Moreover, it is classically considered that a porous medium can be represented to an equivalent homogeneous medium [138][216]. In such a scenario, the pressure drop is assumed to be linearly proportional to the thickness of the bed. This allows the pressure drop to be a function of velocity only. However, this might not be true for fluid flow across heterogeneous porous media made of two different materials. Varying the structure in the flow direction causes a change in the pressure drop distribution. Measuring this change is a difficult task, and requires static pressure measurements along the tested sample. The samples are generally small and conducting such measurements cannot be easily achieved. Therefore, this change was neglected under the assumption that the pressure drop difference would be much smaller than the effective pressure drop across the whole sample. Based on this assumption, the pressure drop gradients of the hybrid samples were obtained. Shown in Figures 6.6 to 6.11 are the measured pressure gradients for the heterogeneous samples plotted against the superficial air velocity in the Darcy regime. By reason of comparison, the measured pressure gradients for the semi-homogenous samples are also added to the graphs.
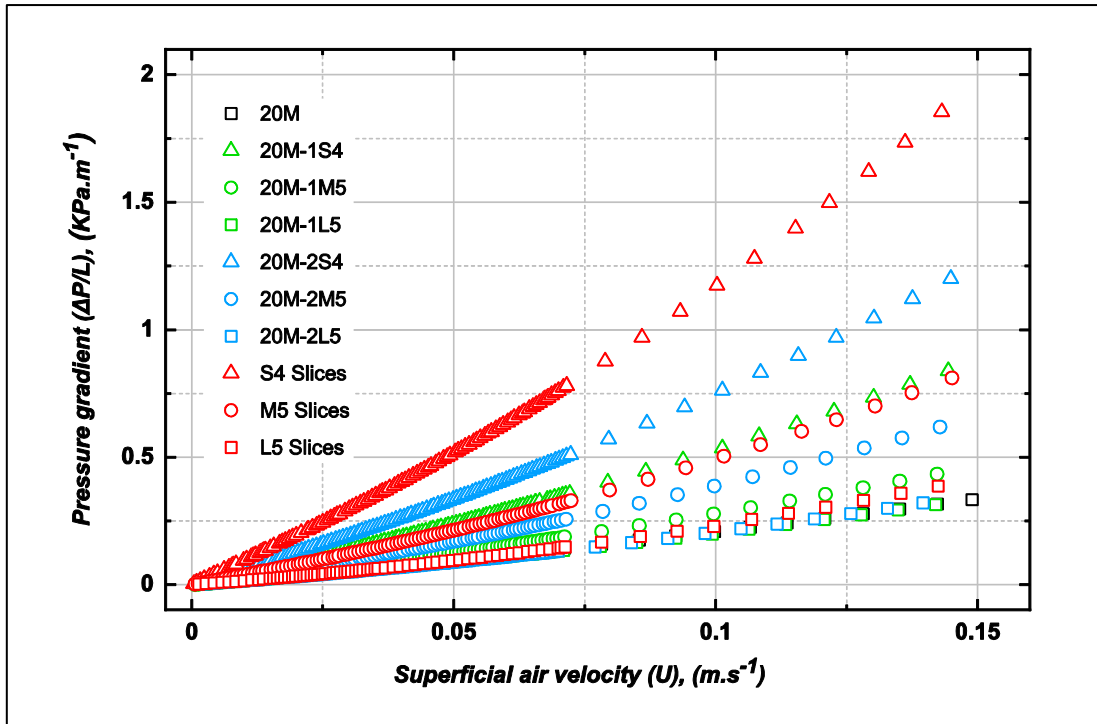
Figure 6.6 Pressure drop gradient vs superficial air velocity in Darcy flow (Crushed with 20 Mesh).
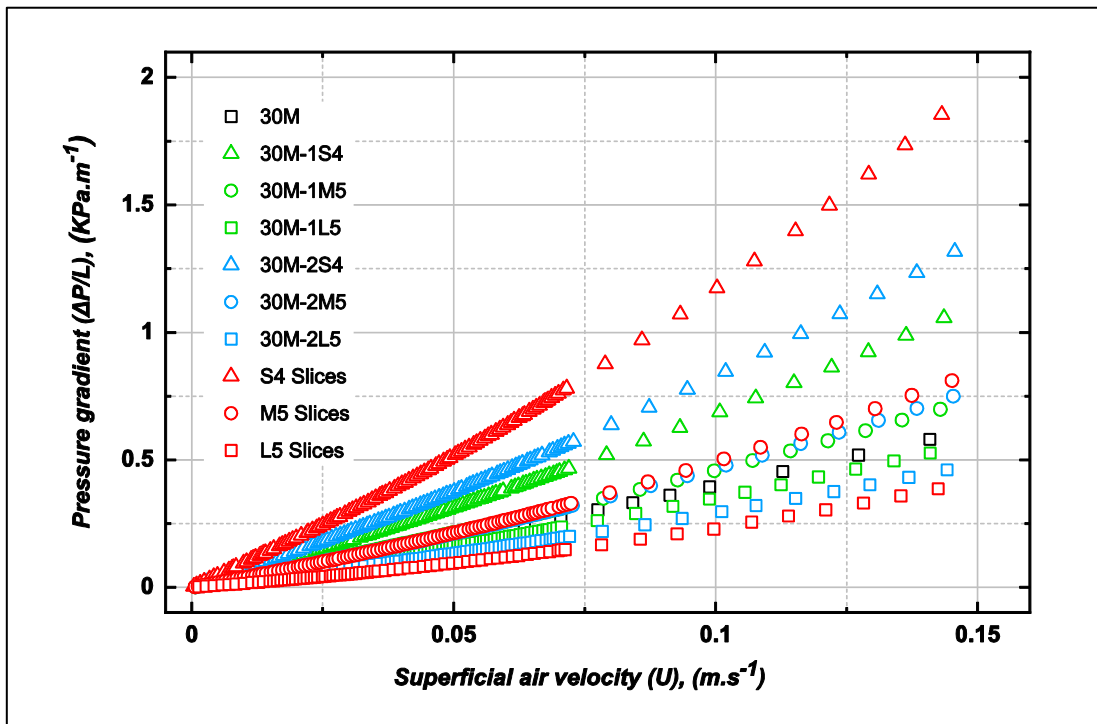
Figure 6.7 Pressure drop gradient vs superficial air velocity in Darcy flow (Crushed with 30 Mesh).
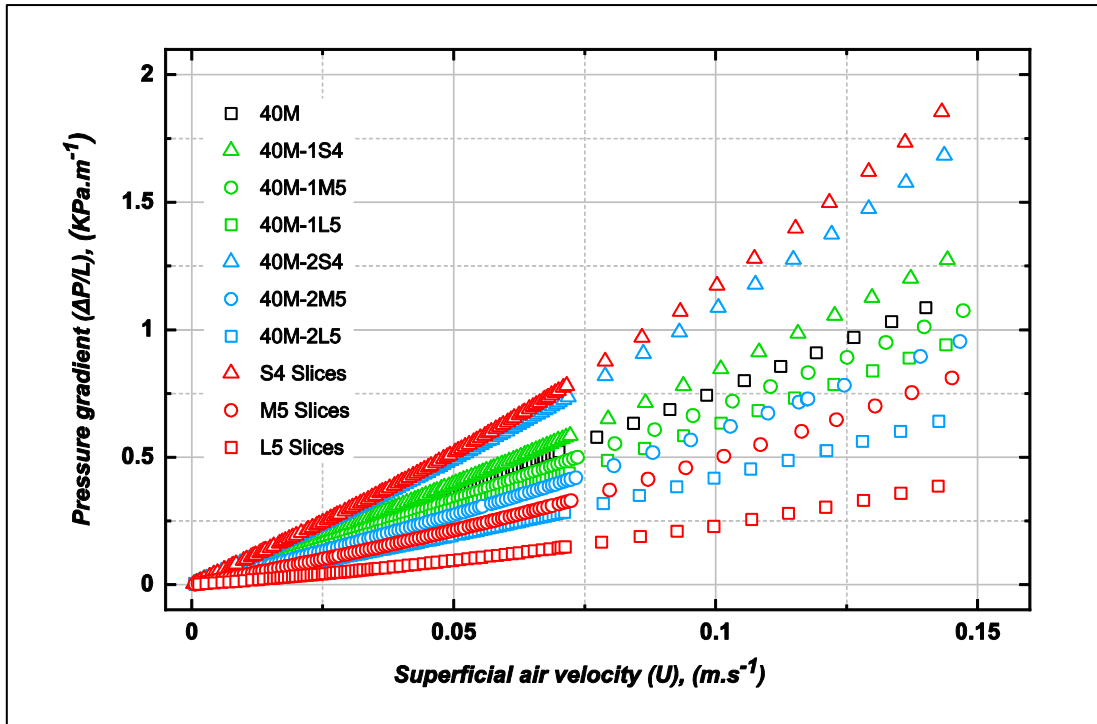
Figure 6.8 Pressure drop gradient vs superficial air velocity in Darcy flow (Crushed with 40 Mesh).
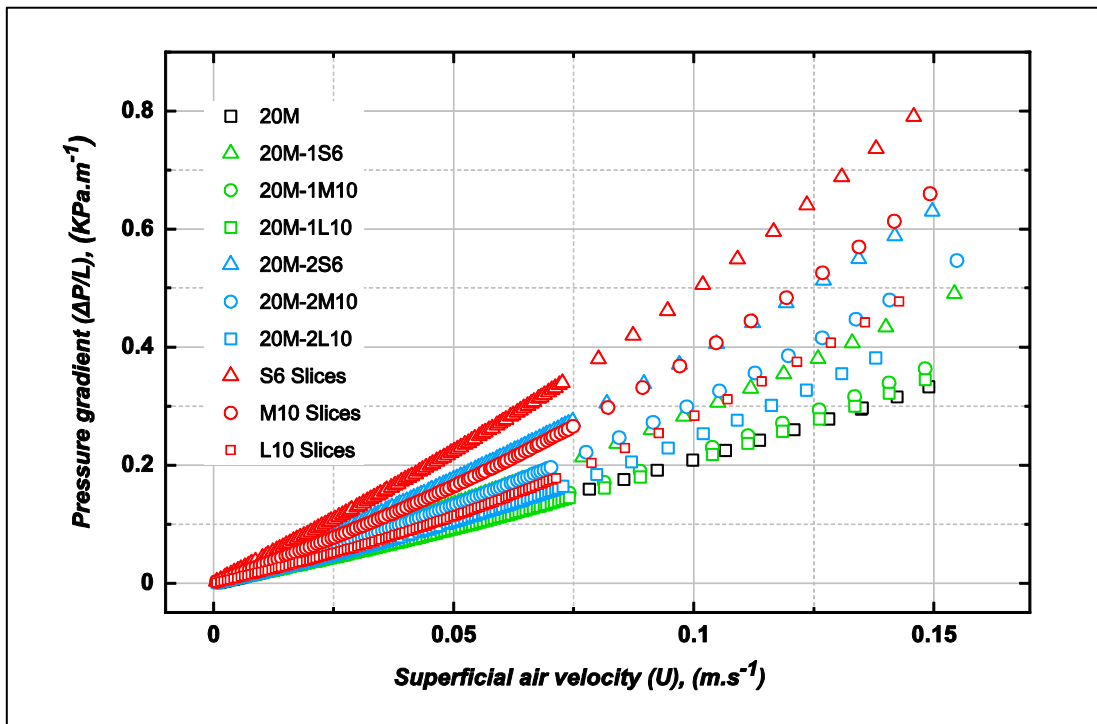
Figure 6.9 Pressure drop gradient vs superficial air velocity in Darcy flow (Spherical with 20 Mesh).
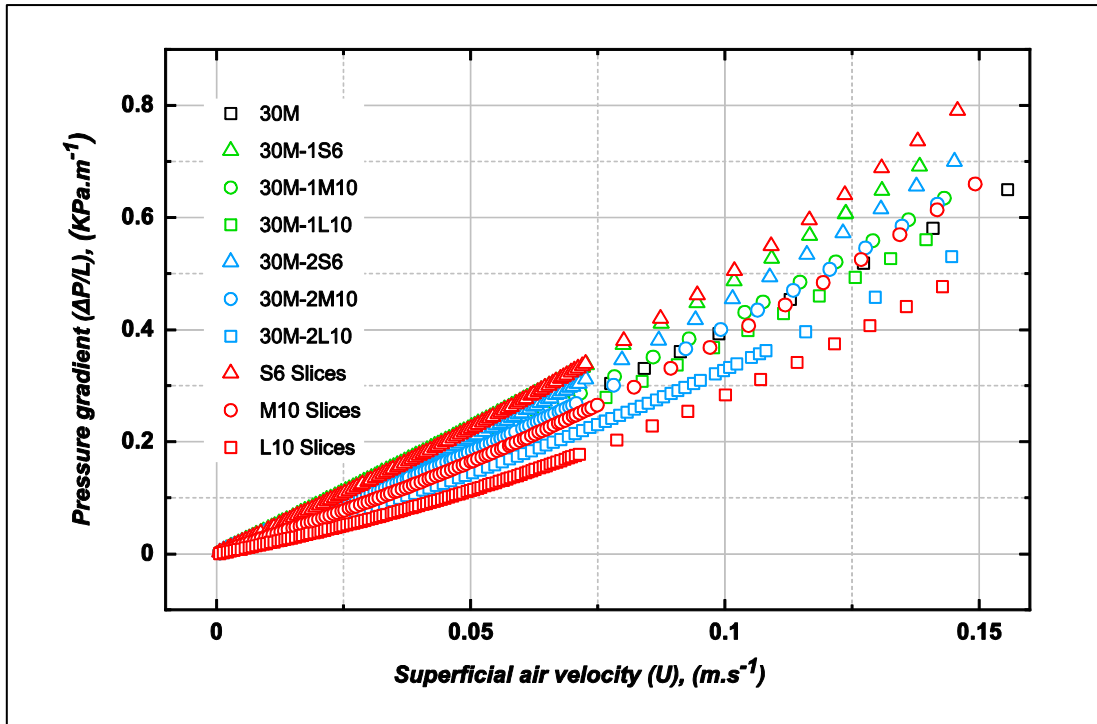
Figure 6.10 Pressure drop gradient vs superficial air velocity in Darcy flow (Spherical with 30 Mesh).
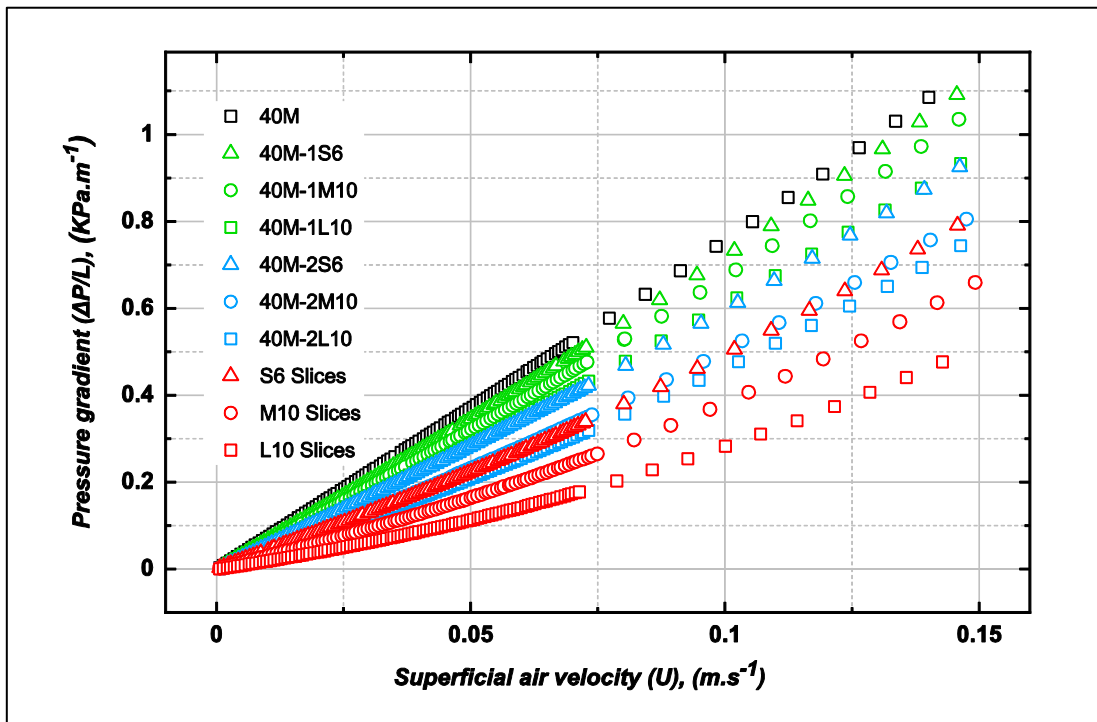
Figure 6.11 Pressure drop gradient vs superficial air velocity in Darcy flow (Spherical with 40 Mesh).

When flow velocity increases, the inertia effect reveals a non-linear relationship between the pressure gradient and the superficial air velocity. The experimental pressure gradient for the semi-homogenous and heterogeneous porous media at high flow rates are presented in Figures 6.12 to 6.17.

108
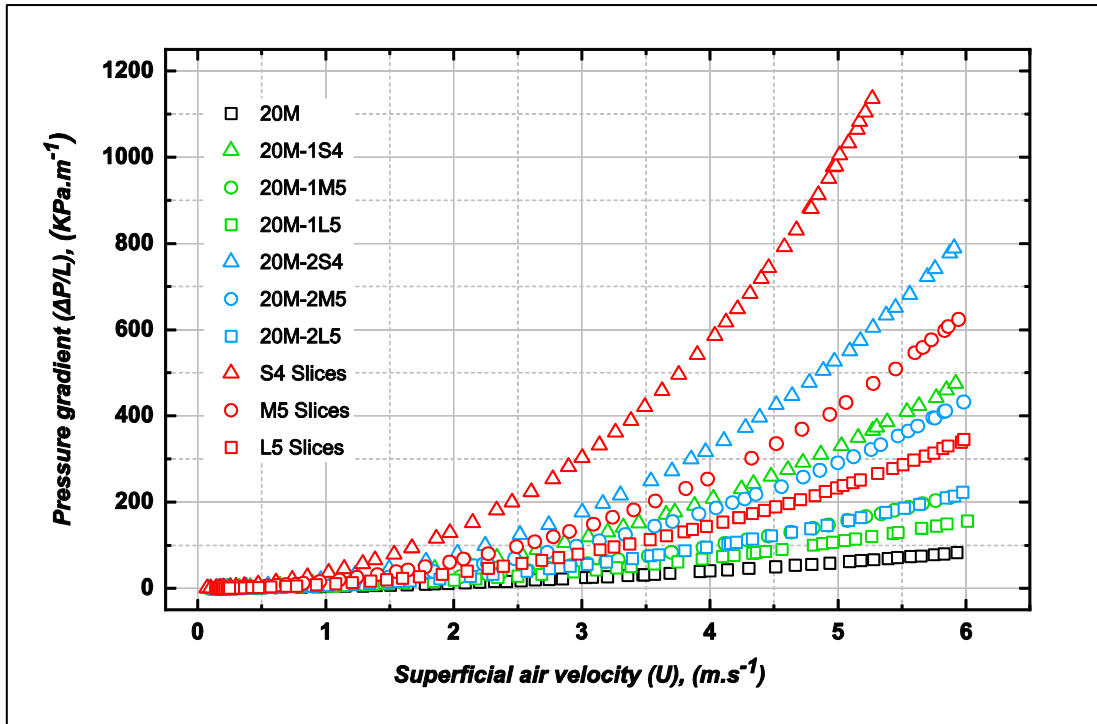
Figure 6.12 Pressure drop gradient vs superficial air velocity (Crushed with 20 Mesh).
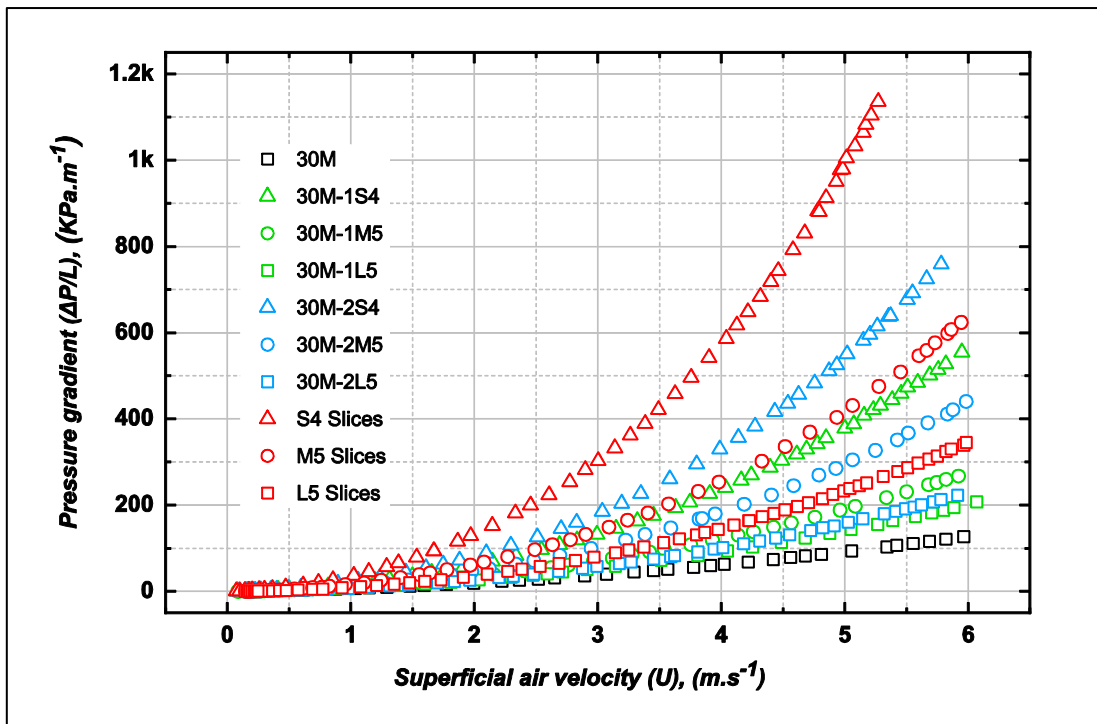
Figure 6.13 Pressure drop gradient vs superficial air velocity (Crushed with 30 Mesh).
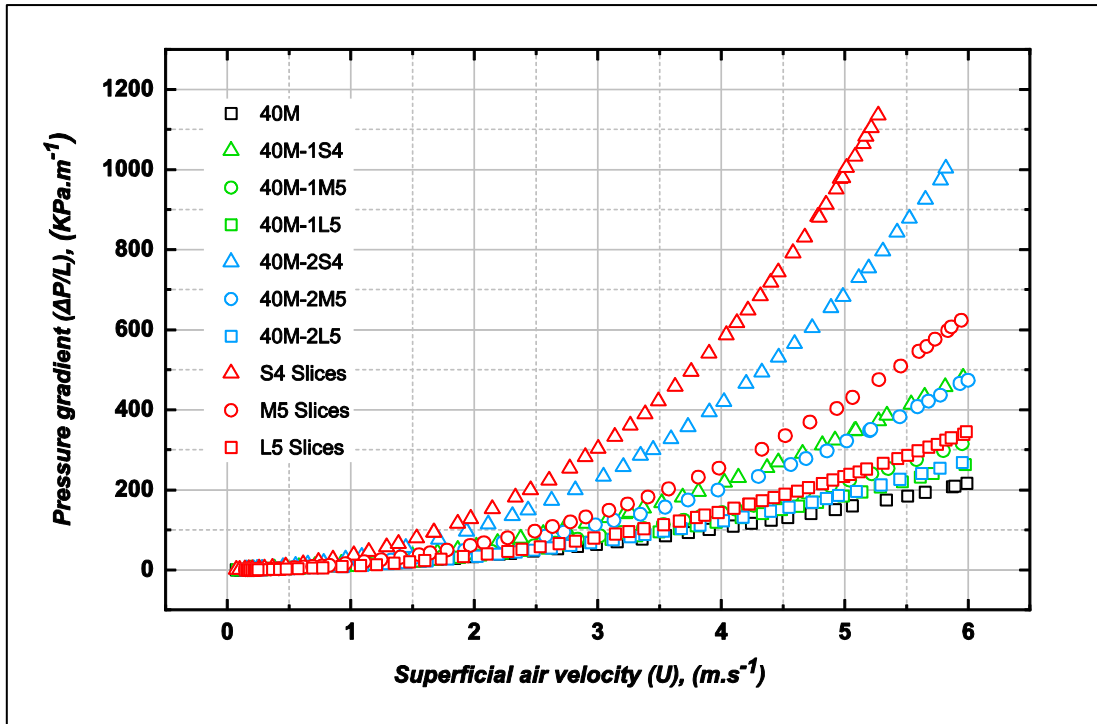
Figure 6.14 Pressure drop gradient vs superficial air velocity (Crushed with 40 Mesh).
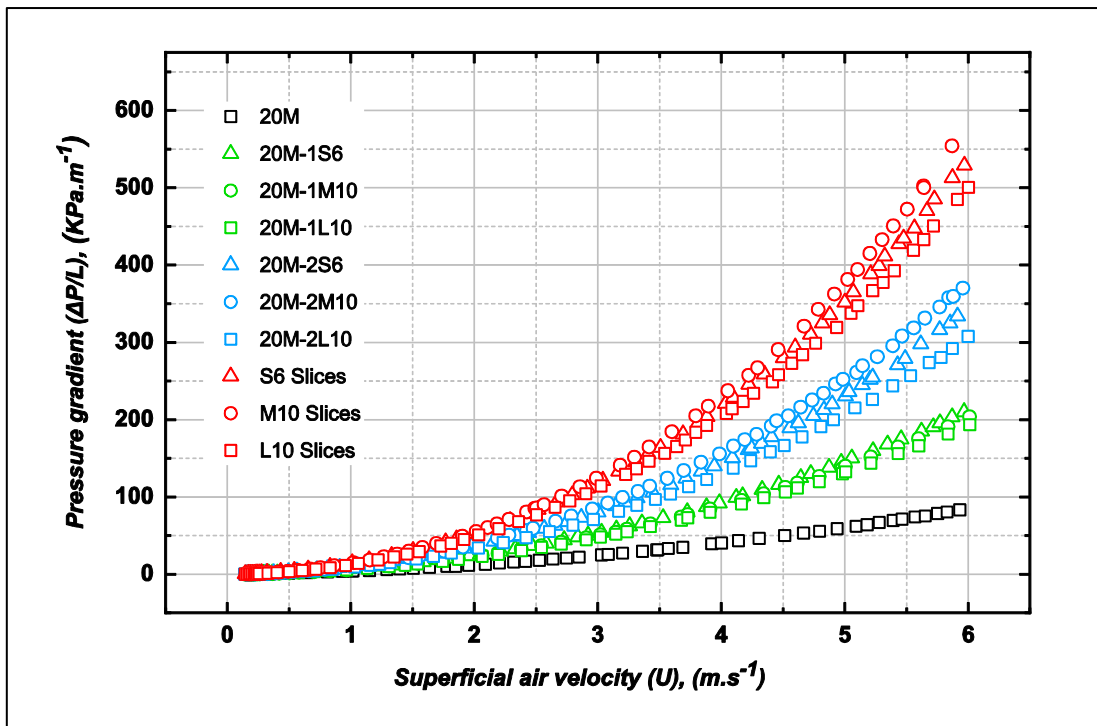
Figure 6.15 Pressure drop gradient vs superficial air velocity (Spherical with 20 Mesh).

110
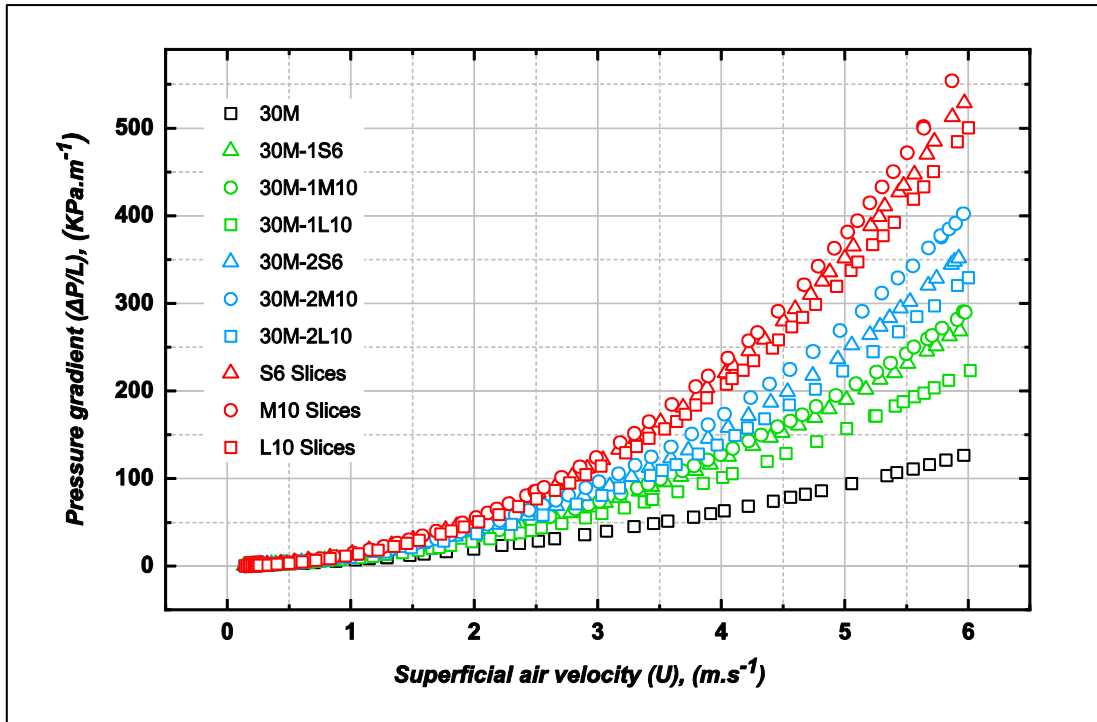
Figure 6.16 Pressure drop gradient vs superficial air velocity (Spherical with 30 Mesh).
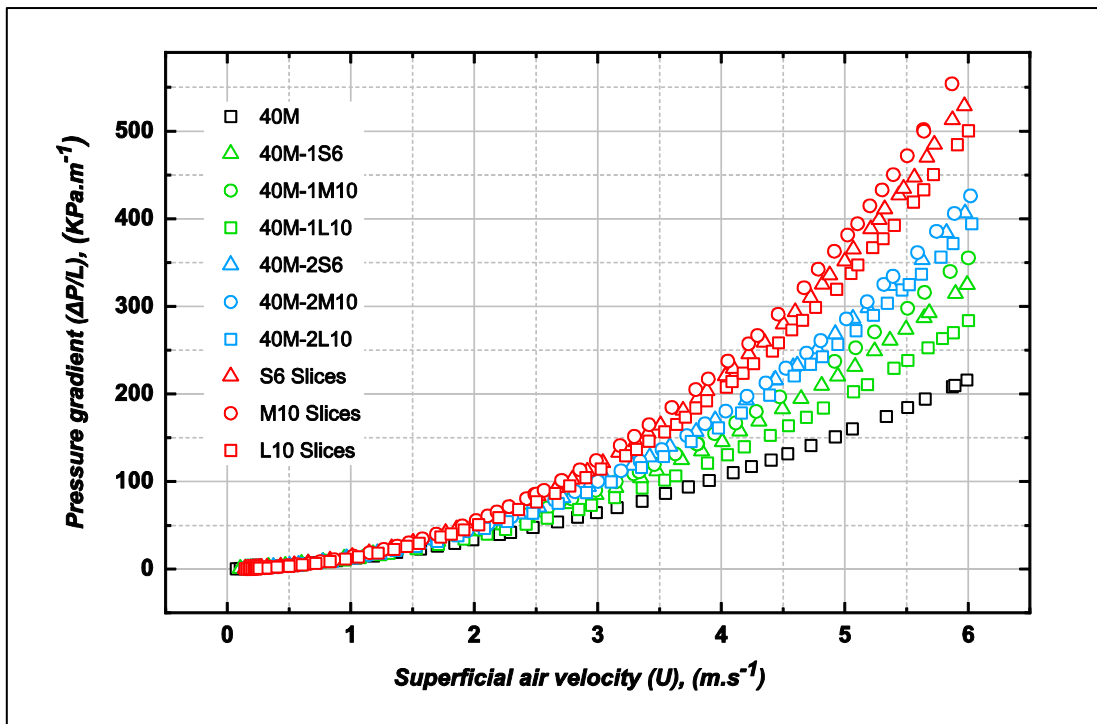
Figure 6.17 Pressure drop gradient vs superficial air velocity (Spherical with 40 Mesh).

The measured data indicated that the pressure drop behaviour across the heterogeneous structures is similar to that presented by the semi-homogeneous structures. It can be seen that the pressure drop increases with frontal air velocity in qualitative agreement with the semi-homogeneous regenerators. The reduction of

111

pore size or the porosity of media increases the pressure loss. The impact of heterogeneity on the pressure gradient depends on the type of semi-homogeneous porous media involved in the hybrid structure. The pressure drop increases with the proportion of material that has higher flow resistance. It also increases when the proportion of materials with a smaller pore size or lower porosity increases.

Understanding the pressure drops generated by porous materials is essential for accurate hydraulic parameter measurements. Hydraulic parameters such as permeability (K), inertia coefficient (F) and drag coefficient (β) are often used to characterise a given porous material. They can be determined experimentally by applying a curve fitting technique to the measured pressure drop data, then, comparing the fitting coefficients with Darcy and Forchheimer-extended Darcy equations (Equations 6.1 and 2.3) [32][93][96][101][108][133]. Note that the value of the free term c in the extended second order equation is usually neglected [84].

$$\frac{-\Delta p}{L} = \mu_f K^{-1} U \qquad\qquad 6.1$$

$$\frac{-\Delta p}{L} = \frac{\mu_f}{K} U + \beta \rho U^2 + c \qquad\qquad 6.2$$

The result referred to as the Darcy regime (the viscous regime) is often fitted using the linear regression method to determine the Darcy permeability [73]. On the other hand, two regression methods have been reported to estimate hydraulic parameters in the Forchheimer regime (the inertia regime): linear and parabolic regression [32]. Antohe et al. [68] showed that using the parabolic fit to estimate permeability and inertia coefficient may lead to a higher error in the final results compared with a linear fit. Bhattacharya et al. [32] examined the two techniques and found no significant difference between the estimated values. Both linear and parabolic fitting are common in the literature [32][63][79][93][95][133][132].

6.2 Flow regimes in porous media

Based on the present state of knowledge, there are four flow regimes in simple and complex porous media [66][217], namely: pre-Darcy, laminar (Darcy), post-laminar (Forchheimer) and turbulent flow regimes [61][65][94][116]. Flow regimes primarily depend upon a local fluid's properties and velocity as it percolates through porous media voids [61][66]. There is no agreement about the thresholds of each

regime [61][101][108][124][138]. This likely stems from using a different characteristic length to define the Reynolds number [65][66][94][115][116]. Even for the same characteristic length, comparative research has shown that the transition generally takes place earlier in packed spheres than in metal foams, except for transition to the turbulent regime which is quicker in metal foams [61]. To characterise the flow regime in porous media one can modify the extended Darcy-Forchheimer model (Equation 2.3 above) to compute the reduced pressure drop gradient $\left(\frac{-\Delta p}{LU}\right)$.

$$\frac{-\Delta p}{LU} = \frac{\mu_f}{K} + \beta \rho U \qquad 6.3$$

The reduced pressure drop gradient is then plotted against the superficial air velocity as shown in Figure 6.18. This technique has been widely utilised in the literature [61][66][92][94][95][101]. The only drawback is that one must perform experiments just beyond the transition point so the deviation of the reduced gradient can be observed [108].
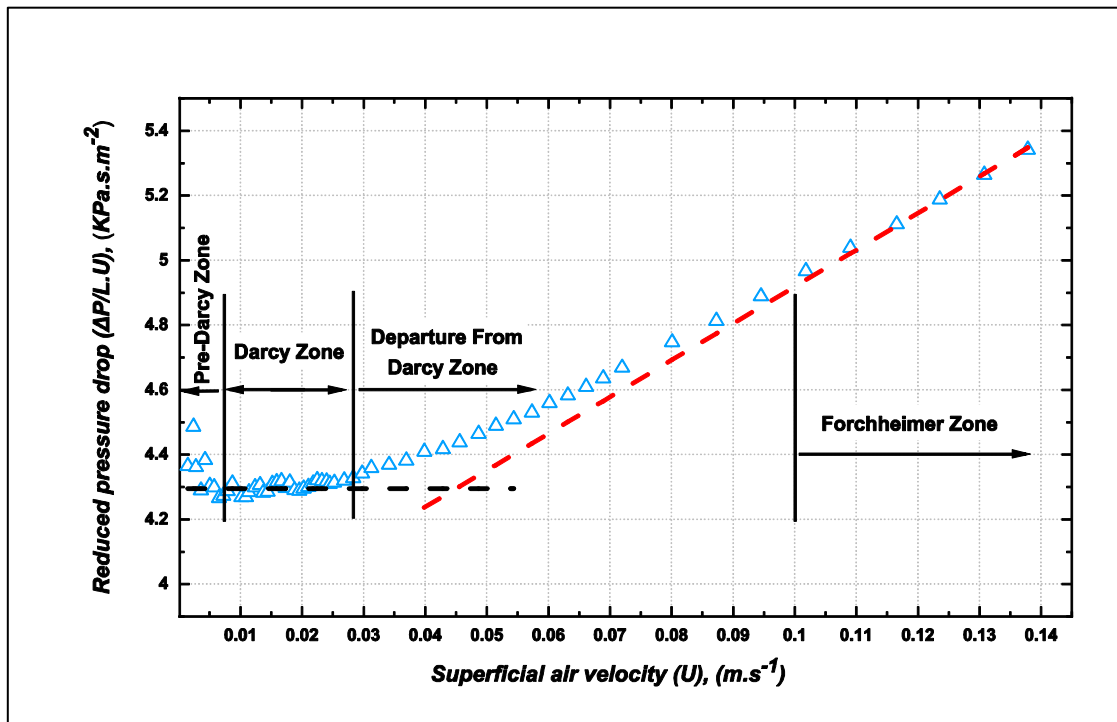
Figure 6.18 Reduced pressure drop gradient vs low superficial air velocity of three-slices S6 sample.

6.2.1 Pre-Darcy regime

It can be seen in Figure 6.18 that the pre-Darcy regime comes into existence at extremely low velocity, appearing as scattered data points. This regime is not clearly understood, and usually overlooked for two reasons: firstly, the lack of sensitive instrumentation that can measure extremely low-pressure drop and flow rate; and secondly, the small number of applications requiring such a low flow rate. However, this regime has been attributed to the non-Newtonian behaviour of fluids [66][94][115]. The streaming potential generated by the flow, particularly in fine-grained media, produces small counter-currents along the pore walls in a direction opposite to the mainstream [65][66][94][102][116]. There is no precise information about the pre-Darcy regime and the upper limitation of this regime is subjective [66][94][115]. The published data about spherical packed beds has shown that the effect of pre-Darcy increases with a decrease in particle size [66], and the Reynolds number corresponding to the upper bound is less than 10^{-5} [65]. It can be noticed that after the pre-Darcy regime there is a very short regime, where the values of the reduced pressure drop data are relatively small. This is most likely the transition zone between the pre-Darcy regime and the Darcy regime.

6.2.2 Darcy regime

The purely viscous Darcy regime can be identified by the point at which the slope of the reduced pressure drop becomes a horizontal line showing independence of velocity. Due to the slow flow and low momentum, the flow engulfs and attaches to the surfaces of the solid phase. The wakes and inertial drag are absent and the viscous drag is solely responsible for this flow regime [65][94]. The velocity distribution can be determined by the actual geometry of the internal structure [61][95][102]. The properties of the fluid are responsible for the pressure drop in this regime [61][65][66][102][116]. Reynolds numbers corresponding to the lower and upper limitations of the Darcy regime are fuzzy and strongly dependent upon the pore geometry and the flow rate [66][217]. There is not sufficient information about the boundary of the Darcy regime. However, the published data indicates that it is a relatively narrow regime [101] and its upper limitation depends on the porous medium structure [61][108], as well as the solid surface roughness [111]. The thresholds of the Darcy regime were determined by observing when the experimental data clearly

diverged from Darcy's law. An example of a departure from Darcy's Law is illustrated in Figure 6.19.
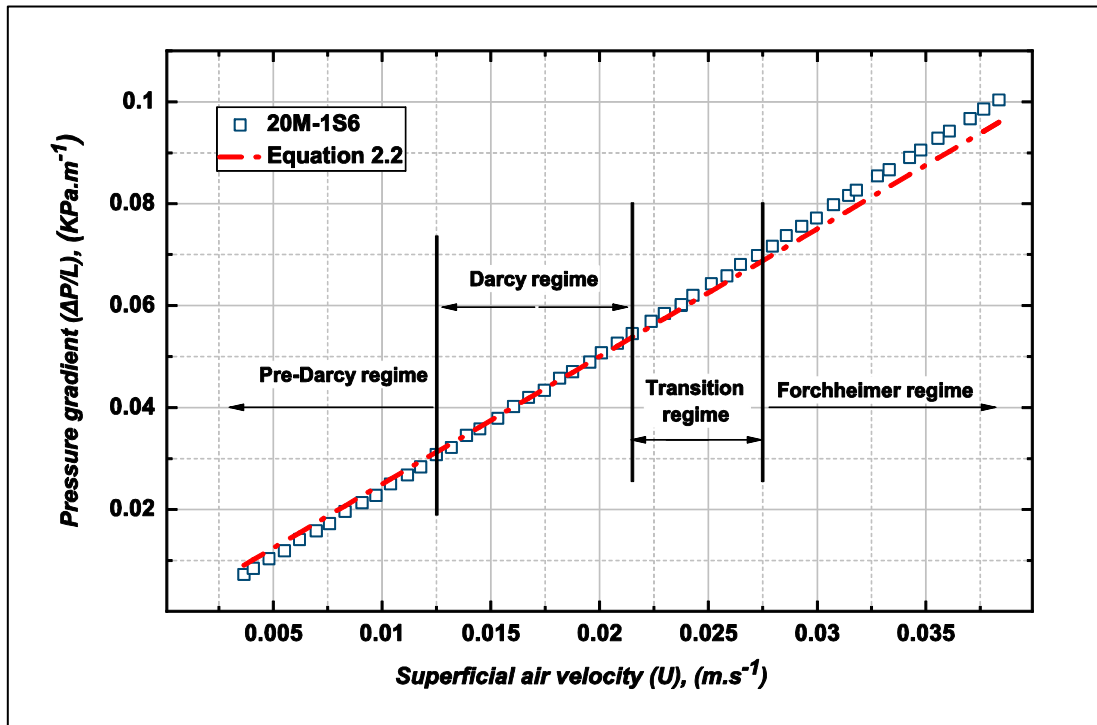
Figure 6.19 Curve fitting of measured pressure drop vs superficial air velocity in Darcy regime.

Shown in Figure 6.20 is an example of the measured data at low velocities for both the semi-homogeneous and heterogeneous porous media. The relationship between pressure drop gradients and the frontal air velocity appears to be linear, which confirms the validity of Darcy's Law for creeping flow. The permeability in the Darcy regime is linked to the internal morphology of porous media. Therefore, this study aimed to determine the Darcy permeability and utilise it as a general characteristic length that describes the flow across both the semi-homogeneous and heterogeneous structures. The least-squares straight-line regression method was performed to fit the measured pressure gradient-velocity data, as shown in Figure 6.20. The dashed line represents the predicted pressure loss using Darcy's Law, expressed in Equation 6.1. The goodness-of-fit was indicated (R2 value), and data points were added or excluded as necessary. Equation 6.1. was compared with the correlations resulting from the regression process to determine the Darcy permeability of the measured samples.
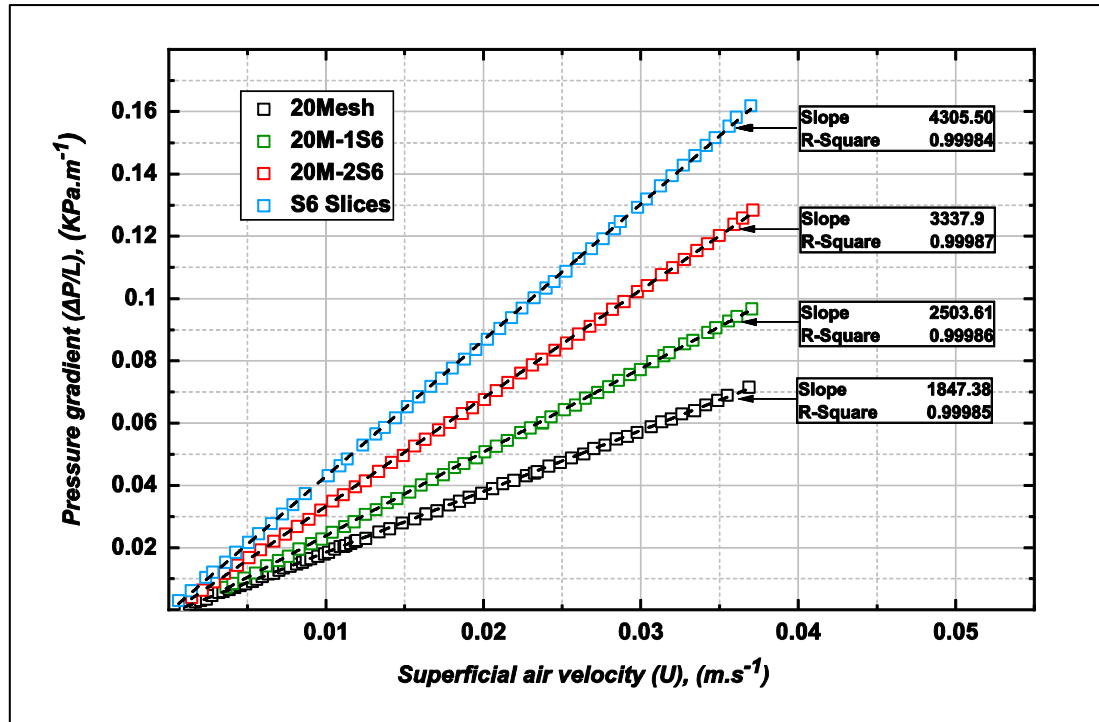
Figure 6.20 Pressure drop gradient variation vs superficial air velocity of metal foam and wire mesh samples.

The thresholds of the Darcy regime were determined by observing where the measured data diverged from the best line fit. Darcy permeabilities and the thresholds of the Darcy regime for the tested samples are tabulated in Tables 6.1 to 6.5.

Table 6.1 Darcy's permeability and regime limitations of original semi-homogeneous foam samples.

Sample	ε	PPI	Average pore size (mm)	Permeability K X10^{-9} (m^2)	Darcy's Regime limitations
Crushed S4	0.6303	15-20	1.09	2.51	$0.023 < Re_k < 0.094$
Crushed M5	0.6259	10-15	1.55	5.07	$0.040 < Re_k < 0.169$
Crushed L5	0.616	5-10	2.18	13.58	$0.036 < Re_k < 0.150$
Spherical S6	0.6954	15-20	1.09	4.57	$0.256 < Re_k < 0.384$
Spherical M10	0.6891	10-15	1.55	6.19	$0.014 < Re_k < 0.306$
Spherical L10	0.696	5-10	2.18	9.98	$0.064 < Re_k < 0.202$

Table 6.2 Darcy's permeability and regime limitations of semi-homogeneous wire mesh samples.

Sample	ε	PPI	Pore size, (mm)	Permeability K X10^{-9} (m^2)	Darcy's Regime limitations
20 Mesh	0.872	20	0.915	9.85	$0.016 < Re_k < 0.218$
30Mesh	0.853	30	0.567	4.75	$0.073 < Re_k < 0.529$
40 Mesh	0.831	40	0.411	2.46	$0.024 < Re_k < 0.286$

116

Table 6.3 Darcy's permeability and regime limitations of semi-homogeneous metal foam samples.

Sample	Permeability $K \times 10^{-9}$ (m^2)	Darcy's Regime limitations	Sample	Permeability $K \times 10^{-9}$ (m^2)	Darcy's Regime limitations
S4 Slices	1.88	$0.013 < Re_k < 0.097$	S6 Slices	4.23	$0.022 < Re_k < 0.182$
M5 Slices	4.71	$0.023 < Re_k < 0.097$	M10 Slices	5.90	$0.026 < Re_k < 0.198$
L5 Slices	11.16	$0.082 < Re_k < 0.163$	L10 Slices	9.45	$0.028 < Re_k < 0.146$

Table 6.4 Darcy's permeability and regime limitations of heterogeneous samples (Crushed with Mesh).

Sample	Permeability $K \times 10^{-9}$ (m^2)	Darcy's Regime limitations	Sample	Permeability $K \times 10^{-9}$ (m^2)	Darcy's Regime limitations
20M-1S4	4.04	$0.022 < Re_k < 0.108$	20M-2S4	2.91	$0.024 < Re_k < 0.083$
20M-1M5	7.75	$0.033 < Re_k < 0.156$	20M-2M5	5.78	$0.025 < Re_k < 0.108$
20M-1L5	11.23	$0.057 < Re_k < 0.125$	20M-2L5	11.48	$0.071 < Re_k < 0.143$
30M-1S4	2.99	$0.059 < Re_k < 0.162$	30M-2S4	2.55	$0.022 < Re_k < 0.121$
30M-1M5	4.43	$0.016 < Re_k < 0.109$	30M-2M5	4.58	$0.039 < Re_k < 0.146$
30M-1L5	5.86	$0.142 < Re_k < 0.208$	30M-2L5	7.22	$0.032 < Re_k < 0.140$
40M-1S4	2.37	$0.016 < Re_k < 0.095$	40M-2S4	1.96	$0.017 < Re_k < 0.072$
40M-1M5	2.79	$0.025 < Re_k < 0.141$	40M-2M5	3.59	$0.020 < Re_k < 0.067$
40M-1L5	3.14	$0.032 < Re_k < 0.119$	40M-2L5	4.91	$0.027 < Re_k < 0.139$

Table 6.5 Darcy's permeability and regime limitations of heterogeneous samples (Spherical with Mesh).

Sample	Permeability $K \times 10^{-9}$ (m^2)	Darcy's Regime limitations	Sample	Permeability $K \times 10^{-9}$ (m^2)	Darcy's Regime limitations
20M-1S6	4.04	$0.022 < Re_k < 0.108$	20M-2S6	2.91	$0.024 < Re_k < 0.083$
20M-1M10	7.75	$0.033 < Re_k < 0.156$	20M-2M10	5.78	$0.025 < Re_k < 0.108$
20M-1L10	11.23	$0.057 < Re_k < 0.125$	20M-2L10	11.48	$0.071 < Re_k < 0.143$
30M-1S6	2.99	$0.059 < Re_k < 0.162$	30M-2S6	2.55	$0.022 < Re_k < 0.121$
30M-1M10	4.43	$0.016 < Re_k < 0.109$	30M-2M10	4.58	$0.039 < Re_k < 0.146$
30M-1L10	5.86	$0.142 < Re_k < 0.208$	30M-2L10	7.22	$0.032 < Re_k < 0.140$
40M-1S6	2.37	$0.016 < Re_k < 0.095$	40M-2S6	1.96	$0.017 < Re_k < 0.072$
40M-1M10	2.79	$0.025 < Re_k < 0.141$	40M-2M10	3.59	$0.020 < Re_k < 0.067$
40M-1L10	3.14	$0.032 < Re_k < 0.119$	40M-2L10	4.91	$0.027 < Re_k < 0.139$

6.2.3 Forchheimer regime

Increasing the frontal air velocity means the momentum transfer inside the medium is excessive and this perturbs the Darcy flow [94][101]. Consequently, the flow transits from the Darcy to Forchheimer regimes. Although it is generally accepted that this deviation is due to the prominent role of inertial forces, the physical explanation of the deviation is still unknown [86]. Some researchers have attributed this transition to the high local fluid velocity caused by the non-homogeneity of the porous media [66][218] or the macro-roughness of the pores [86]. Others think the

interstitial pore space curvature [219], the formation of the boundary layer [220], or the streamline patterns [221] may be responsible. However, there is agreement that the pressure drop gradient is a second order of the velocity and the viscous effect exists simultaneously with the inertial effect in this regime [66]. The empirical model proposed by Forchheimer (Equation 2.3) was seen as sufficient to describe the pressure-drop-frontal air velocity relationship in both semi-homogeneous and heterogeneous structures. Second-order polynomial regression was applied for all the tested samples at high air velocity. An example of measured data fitness is shown in Figure 6.21.
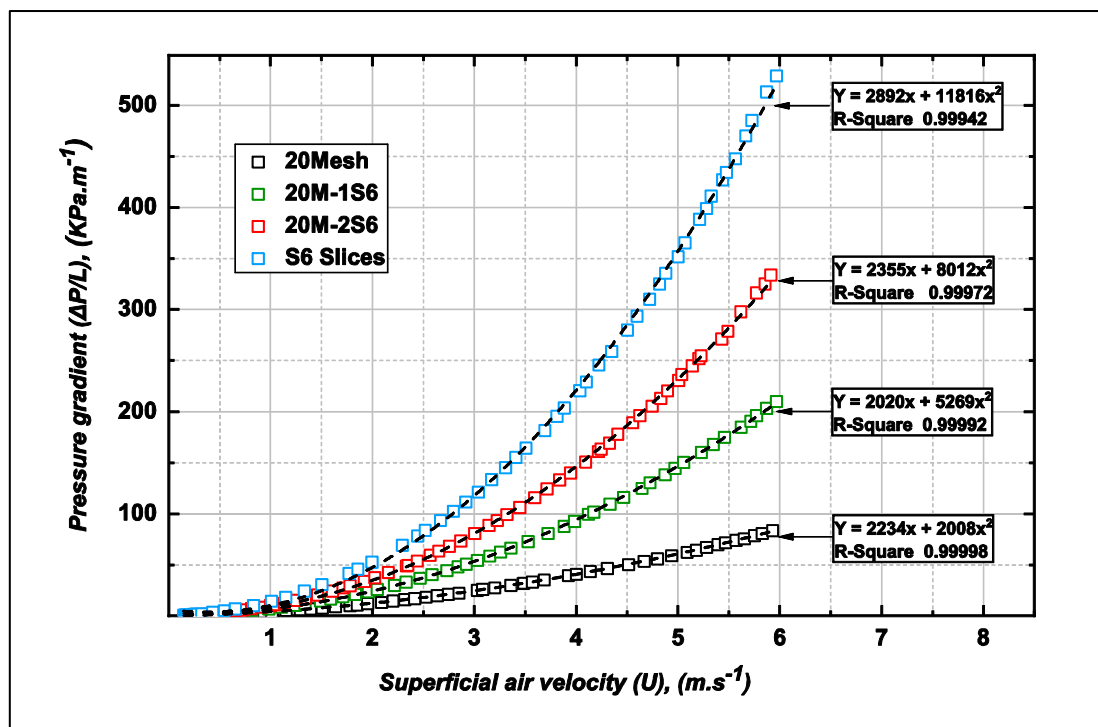
Figure 6.21 The typical quadratic relationship at the Forchhiemer flow regime.

The fitting correlations were compared with the Forchheimer correlation given in Equation 2.3 and the regression constants were used to obtain the hydraulic parameters in the Forchheimer flow regime. The contribution of the inertial forces in the total pressure drop was demonstrated by reducing the pressure gradient data and plotting the results against the superficial air velocity as shown in Figure 6.22. This contribution is discernible by ascertaining when the reduced pressure drop gradient has a positive slope at a relatively high air velocity. In Figure 6.22, it is shown where the reduced pressure drop gradient was linearly fitted and represented by the red dashed line. This presentation technique is also convenient to determine the upper and lower thresholds of this regime. There is some concern about the offset point of

this transition [102]. A comparison of flow through packed beds of uniformly sized particles and multi-sized particles showed that the inertial regime started earlier in the non-uniform beds [66]. This study showed consistency in the range of Reynolds numbers

corresponding to the upper and lower thresholds of the flow regimes. However, there was not sufficient data to verify the transition behaviour. The experimental data showed significant scatter, see Figure 6.34. This may be the result of geometric ambiguity of the internal structure such as structure defection, ligament variation or mesh stuck orientation.
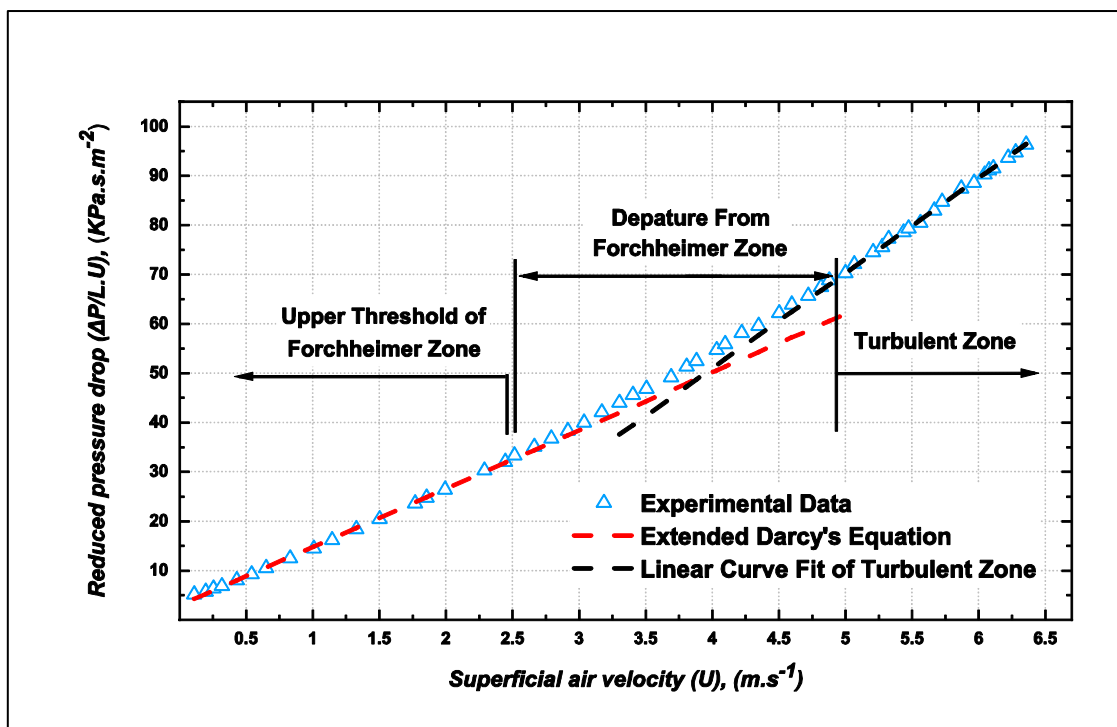
Figure 6.22 Reduced pressure drop gradient vs high superficial air velocity of three-slices S6 sample.

Beyond the Forchheimer regime, there is a short transitional zone followed by the turbulent flow regime. Unlike flow in an open pipe, the flow transition takes place gradually from the laminar to turbulent flow regimes [64][86][222]. Similar to the process for the Darcy regime, the measured data was characterised to determine the Reynolds numbers corresponding to the entrances and departure of the flow in the Forchheimer regime.

The results of the measured hydraulic parameters and the thresholds of Forchheimer flow regimes for the tested samples and those available from the open literature are tabulated in Tables 6.6 to 6.11.

Table 6.6 Hydraulic parameters and regime limitations of semi-homogeneous foam samples in the Forchheimer regime.

Sample	Permeability K X10^{-9} (m^2)	Forchheimer's Regime limitations	Inertia Coefficient (F)	Drag Coefficient $\boldsymbol{\beta}$, (m^{-1})
Crushed S4	2.91	0.165 < Rek < 7.444	0.735	13638
Crushed M5	5.70	0.543< Rek < 13.735	0.752	9955
Crushed L5	12.81	0.356< Rek < 36.781	0.694	6132
Spherical S6	9.39	0.384 < Rek < 13.124	0.869	8973
Spherical M10	11.64	0.611< Rek < 13.095	1.089	10093
Spherical L10	12.56	0.474 < Rek < 20.125	0.875	7811

Table 6.7 Hydraulic parameters and regime limitations of semi-homogeneous wire mesh samples in the Forchheimer regime.

Sample	Permeability K X10^{-9} (m^2)	Forchheimer's Regime limitations	Inertia Coefficient (F)	Drag Coefficient $\boldsymbol{\beta}$, (m^{-1})
20 Mesh	8.15	0.381 < Re$_k$ < N/D	0.146	1614
30Mesh	4.18	0.859 < Re$_k$ < N/D	0.146	2254
40 Mesh	2.48	0.452< Re$_k$ < N/D	0.188	3768

Table 6.8 Hydraulic parameters and regime limitations of semi-homogeneous metal foam samples in the Forchheimer regime.

Sample	Permeability K X10^{-9} (m^2)	Forchheimer's Regime limitations	Inertia Coefficient (F)	Drag Coefficient $\boldsymbol{\beta}$, (m^{-1})
S4 Slices	2.73	0.160< Re$_k$ < 7.882	1.164	22298
M5 Slices	6.23	0.274 < Re$_k$ < 14.293	0.887	11231
L5 Slices	12.70	0.479 < Re$_k$ < 24.167	0.745	6610
S6 Slices	6.29	0.417< Re$_k$ < 12.863	0.730	9198
M10 Slices	11.64	0.639 < Re$_k$ < 14.378	1.093	10134
L10 Slices	15.76	0.568 < Re$_k$ < 19.254	1.142	9099

Table 6.9 Hydraulic parameters and regime limitations of Forchheimer regime in heterogeneous samples (Crushed with Mesh).

Sample	Permeability $K \times 10^{-9}$ (m^2)	Forchheimer's Regime limitations	Inertia Coefficient (F)	Drag Coefficient β, (m^{-1})	Sample	Permeability $K \times 10^{-9}$ (m^2)	Forchheimer's Regime limitations	Inertia Coefficient (F)	Drag Coefficient β, (m^{-1})
20M-1S4	5.20	$0.560 < Re_k < 12.327$	0.640	8872	20M-2S4	4.65	$0.404 < Re_k < 10.204$	0.934	13695
20M-1M5	8.46	$0.636 < Re_k < 23.520$	0.400	4349	20M-2M5	7.53	$0.632 < Re_k < 14.259$	0.687	7920
20M-1L5	10.79	$0.445 < Re_k < 29.296$	0.328	3154	20M-2L5	13.11	$1.128 < Re_k < 27.890$	0.504	4406
30M-1S4	3.83	$0.399 < Re_k < 14.843$	0.583	9413	30M-2S4	3.29	$0.353 < Re_k < 10.518$	0.854	14884
30M-1M5	4.92	$0.449 < Re_k < 21.432$	0.370	5273	30M-2M5	6.48	$0.432 < Re_k < 17.571$	0.653	8108
30M-1L5	5.88	$0.550 < Re_k < 29.039$	0.301	3920	30M-2L5	7.97	$0.390 < Re_k < 21.850$	0.423	4734
40M-1S4	2.80	$0.359 < Re_k < 9.640$	0.503	9493	40M-2S4	2.43	$0.264 < Re_k < 7.064$	0.813	16506
40M-1M5	3.11	$0.514 < Re_k < 12.326$	0.335	6011	40M-2M5	3.95	$0.555 < Re_k < 10.885$	0.582	9267
40M-1L5	3.29	$0.598 < Re_k < 17.447$	0.283	4933	40M-2L5	5.24	$0.882 < Re_k < 19.896$	0.385	5312

Table 6.10 Hydraulic parameters and regime limitations of Forchheimer regime in heterogeneous samples (Spherical with Mesh).

Sample	Permeability $K \times 10^{-9}$ (m^2)	Forchheimer's Regime limitations	Inertia Coefficient (F)	Drag Coefficient β, (m^{-1})	Sample	Permeability $K \times 10^{-9}$ (m^2)	Forchheimer's Regime limitations	Inertia Coefficient (F)	Drag Coefficient β, (m^{-1})
20M-1S6	9.01	$0.600 < Re_k < 22.175$	0.401	4224	20M-2S6	7.73	$0.790 < Re_k < 13.239$	0.577	6567
20M-1M10	10.13	$0.713 < Re_k < 23.690$	0.495	4916	20M-2M10	12.86	$0.628 < Re_k < 19.809$	0.771	6803
20M-1L10	12.89	$0.727 < Re_k < 25.537$	0.445	3916	20M-2L10	11.61	$0.758 < Re_k < 23.433$	0.680	6314
30M-1S6	4.39	$0.561 < Re_k < 15.731$	0.335	5055	30M-2S6	6.18	$0.464 < Re_k < 16.396$	0.519	6605
30M-1M10	5.69	$0.507 < Re_k < 21.026$	0.422	5593	30M-2M10	6.83	$0.633 < Re_k < 17.029$	0.607	7346
30M-1L10	5.32	$0.621 < Re_k < 21.604$	0.316	4337	30M-2L10	9.60	$0.319 < Re_k < 22.744$	0.645	6580
40M-1S6	3.07	$0.506 < Re_k < 11.646$	0.332	5986	40M-2S6	5.40	$0.449 < Re_k < 15.147$	0.572	7791
40M-1M10	3.37	$0.501 < Re_k < 13.118$	0.386	6645	40M-2M10	6.24	$0.532 < Re_k < 15.770$	0.642	8124
40M-1L10	3.53	$0.523 < Re_k < 18.211$	0.320	5380	40M-2L10	6.29	$0.326 < Re_k < 17.935$	0.597	7527

Table 6.11 Darcy's and Forchhimer permeability of metallic foam samples reported in the literature.

Reference	Metallic type	ε	PPI	Pore size (mm)	Darcy Permeability $K \times 10^{-9}$ (m^2)	Forchheimer Permeability $K \times 10^{-9}$ (m^2)	Inertia Coefficient (F)	Drag Coefficient β, (m^{-1})	Darcy's Regime limitations	Forchheimer Regime limitations
Boomsma et. al [108]	Aluminium	0.921	10	6.9	NA	352.9	NA	120	$Re_k < 26.5$	NA
Boomsma et. al [108]	Aluminium	0.920	20	3.6	NA	108.9	NA	239	$Re_k < 22.3$	NA
Boomsma et. al [108]	Aluminium	0.928	40	2.3	NA	71.2	NA	362	$Re_k < 14.2$	NA
Bağcı and Dukhan [101]	Aluminium	0.885	10	NA	98.9	161.7	0.078	NA	$1.3 < Re_k < 3.9$	$6.2 < Re_k < 45.2$
Bağcı and Dukhan [61]	Aluminium	0.87	20	NA	67.7	52.9	0.094	NA	$1.2 < Re_k < 1.9$	$6.4 < Re_k < 37.5$
Bağcı and Dukhan [101]	Aluminium	0.885	40	NA	53.4	61.1	0.110	NA	$1.3 < Re_k < 2.1$	$3.6 < Re_k < 39.1$
Kouidri et al. [111]	Copper	0.93	20	1.2	5.9	6.4	0.039	NA	$4.5 < Re_k < 7.0$	$Re_k > 21$
Kouidri et al. [111]	NiFeCr	0.92	20	1.2	2.3	2.3	0.018	NA	$4.0 < Re_k < 5.4$	$8.15 < Re_k < 16.5$
Kouidri et al. 9[111]	Inconel	0.92	20	1.2	1.3	1.3	0.013	NA	$3.0 < Re_k < 3.88$	$4.00 < Re_k < 12.30$
Dukhan and Ali [223]	Aluminium	0.89	10	2.55	NA	250	NA	35	$12.5 < Re_k < 29.2$	$29.2 < Re_k$
Dukhan and Ali [223]	Aluminium	0.9	20	1.27	NA	150	NA	45	$12.5 < Re_k < 29.2$	$29.2 < Re_k$
Abuserwal [37]	stainless steel	10	0.784	2.000	29.62	NA	NA	NA	$0.72 < Re_k < 1.10$	NA
Abuserwal [37]	Aluminium alloy	15	0.878	1.400	21.1	NA	NA	NA	$0.29 < Re_k < 0.56$	NA
Abuserwal [37]	stainless steel	20	0.746	1.000	9.69	NA	NA	NA	$0.17 < Re_k < 0.45$	NA
Luna [36]	stainless steel	10	0.81	2.000	NA	16.7	NA	0.79	NA	NA
Luna [36]	stainless steel	20	0.75	1.000	NA	5.3	NA	1.90	NA	NA
Luna [36]	stainless steel	30	0.73	0.500	NA	2.66	NA	3.00	NA	NA
Luna [36]	stainless steel	200	0.75	0.075	NA	0.216	NA	15.00	NA	NA
Landrum et. al [29]	phosphor bronze	325	0.6738	0.043	NA	0.016	0.179	27500	NA	NA
Landrum et. al [29]	phosphor bronze	325	0.6702	0.043	NA	0.016	0.382	58000	NA	NA
Landrum et. al [29]	stainless steel	635	0.6312	0.020	NA	0.004	0.275	69000	NA	NA
Landrum et. al [29]	stainless steel	635	0.6304	0.020	NA	0.003	0.211	59000	NA	NA

6.3 Impact of Heterogeneity on the Hydraulic Parameters

To graphically compare the measured Darcy permeability of the tested samples, the tabulated permeabilities given in Tables 6.2 to 6.5 were plotted as a function of porosity in Figures 6.23 and 6.24. On the left of the figures are the foam samples (3 in total) and on the right are mesh samples (3 in total). The data in the middle is made up of combinations of these samples. As can be seen, the permeability increases if the porosity or the pore size increases. Higher porosity means less solid material per unit volume, hence, less obstruction in the flow direction, which explains the higher permeability in wire mesh screens compared to metal foam samples. Each group of aluminium foams has almost equal porosity, hence, the increase in Darcy permeability is mainly due to the pore diameter increase. Both pore density and porosity influence the permeability in the heterogeneous structure. The permeability decreases when a material has a small pore size.
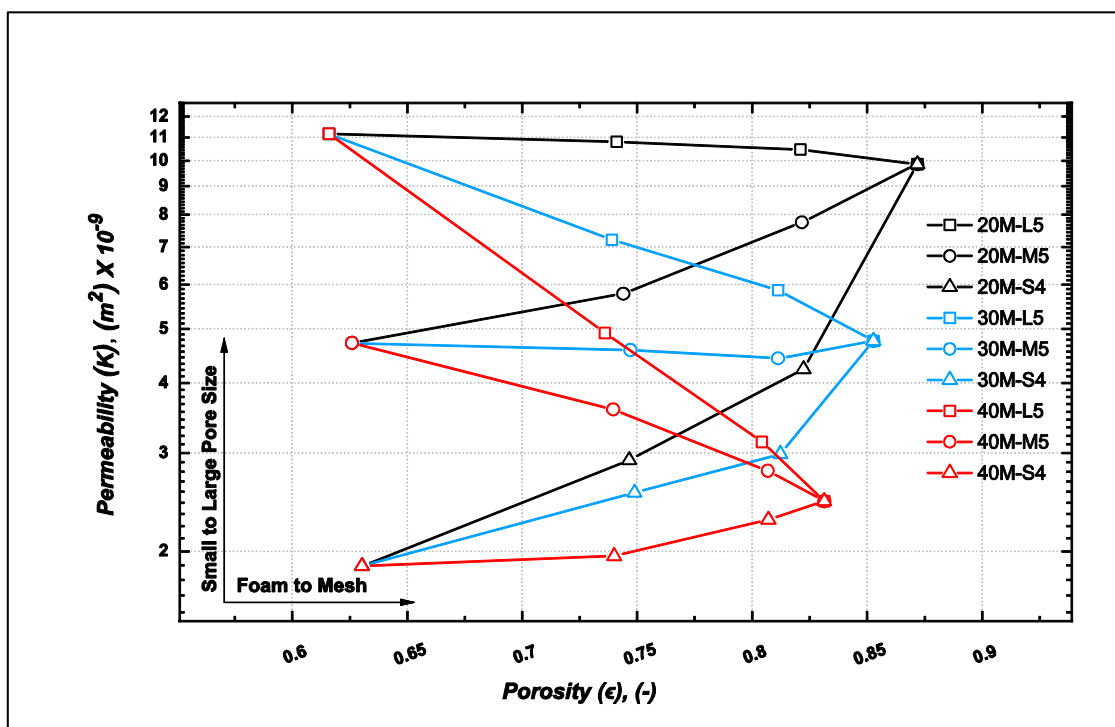
Figure 6.23 Darcy's permeability variation due to maternal portions (Crushed with Mesh).
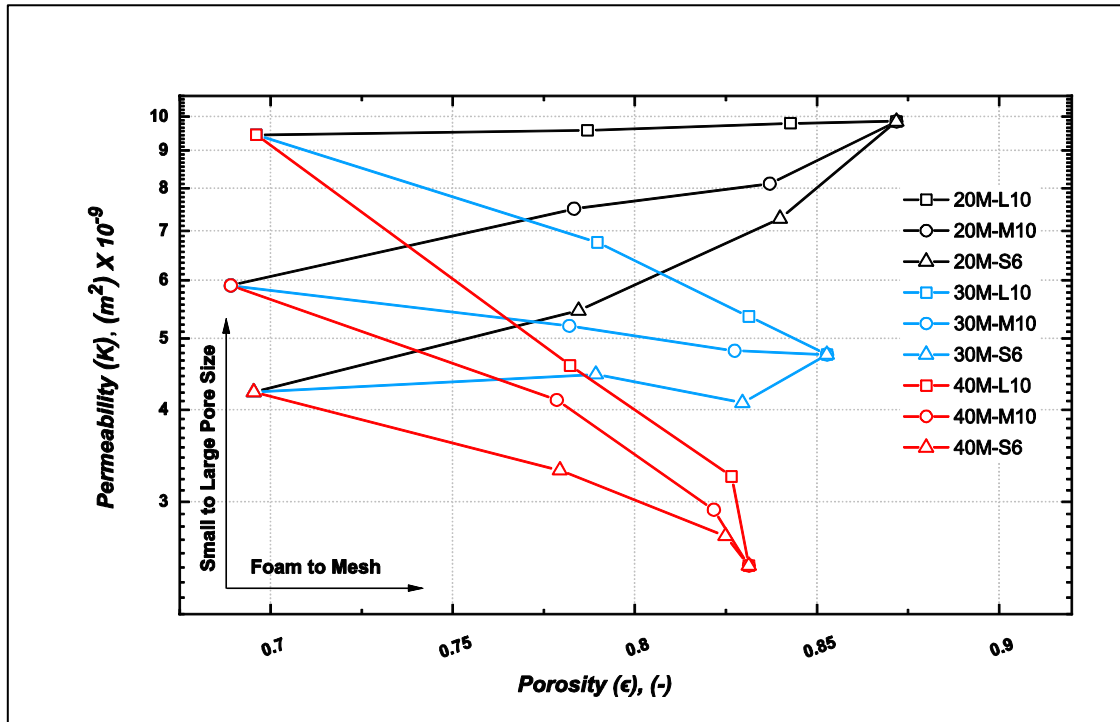
Figure 6.24 Darcy's permeability variation due to maternal portions (Spherical foam with Mesh).

Over the last two decades, a large number of investigations have been undertaken into the relationship between the structure and hydraulic parameters. The published data is not consistent, even for the same class of material. Some studies have attributed the discrepancies to the fact that various flow regimes provide different hydraulic parameters. As observed by Antohe et al. [92], Dukhan and Minjeur [93], Dukhan et al. [95], and Boomsma and Poulikakos [108], the values of the permeability in the Darcy regime and permeability in the Forchheimer regime are different. The measured permeabilities from the Darcy and Forchheimer regimes are compared in Figure 6.25. As can be seen, the same porous medium exhibits different permeabilities in different flow regimes. The permeability of metal foam which is calculated in the Forchheimer regime seems to be high compared to those obtained from the Darcy regime. This increase in permeability could be due to the ability of the flow at high velocity to sweep the boundary layers on the internal solid surfaces of the foam, allowing more space for the flow to transport. This is not the case for the packed beds of mesh screens. The results obtained from testing three different wire mesh packed beds showed that the permeability in the Forchheimer regime is lower than that in the

124

Darcy regime. This is likely due to cellular structures differences between the stochastic topology and periodic structure [14].
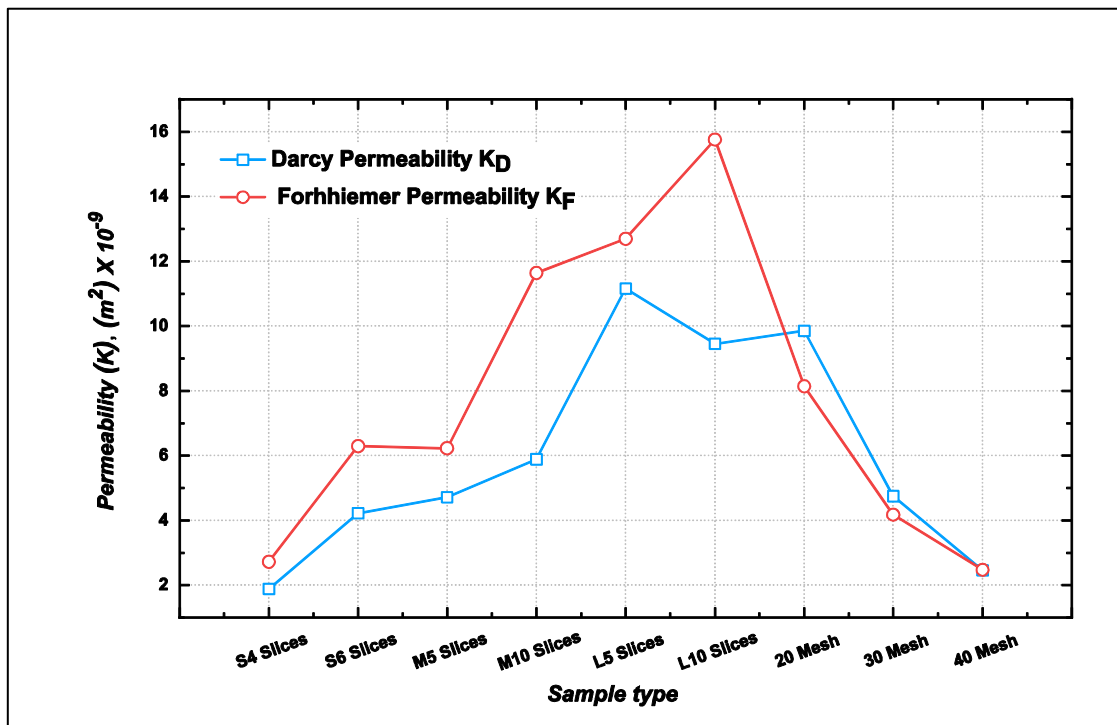
Figure 6.25 Darcy and Forchheimer permeabilities of semi-homogeneous samples.

Shown in Figures 6.26 to 6.29 are comparisons between measured Darcy and Forchheimer permeabilities of the heterogeneous structures. It was observed that the microstructure differences between the metal foams and wire mesh screens influence the difference in permeability in the heterogeneous structure. It can also be seen that the permeability difference increased with the number of slices. The heterogeneous regenerators made of wire mesh screens and irregular pore metal foams showed lower differences in permeability than those made of mesh screens and spherical pores. This is more noticeable when the hybrid structure consists of two foam slices.
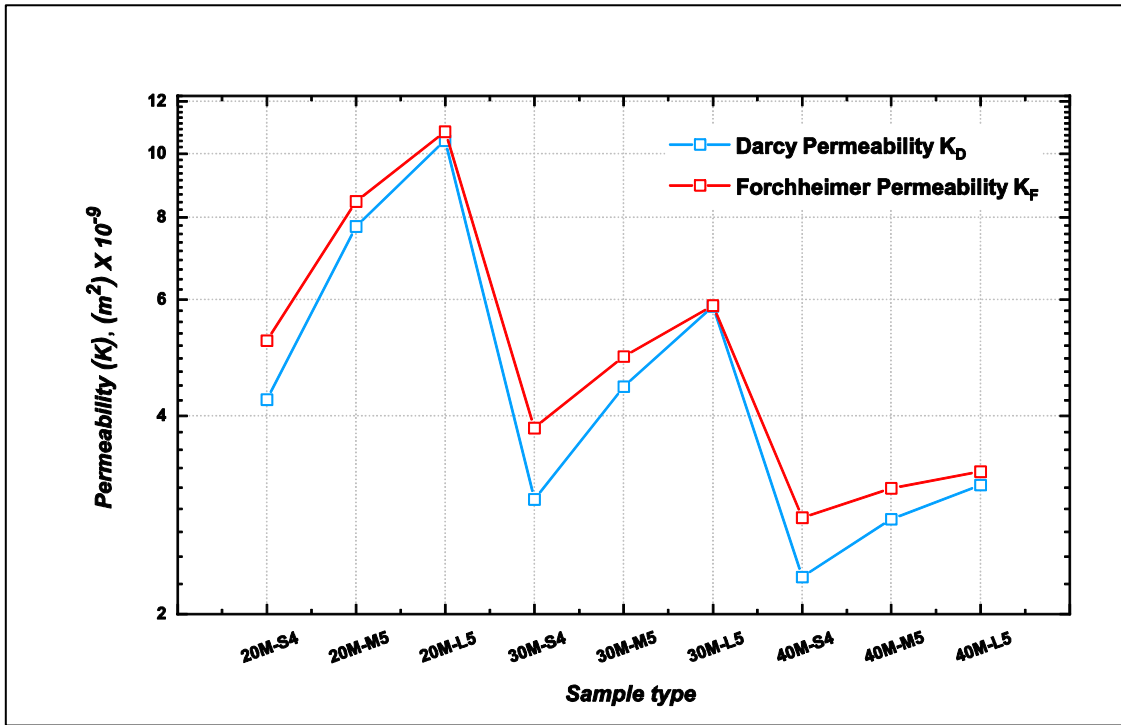
Figure 6.26 Darcy and Forchheimer permeabilities of heterogeneous samples (One slice Crushed foam with Mesh).
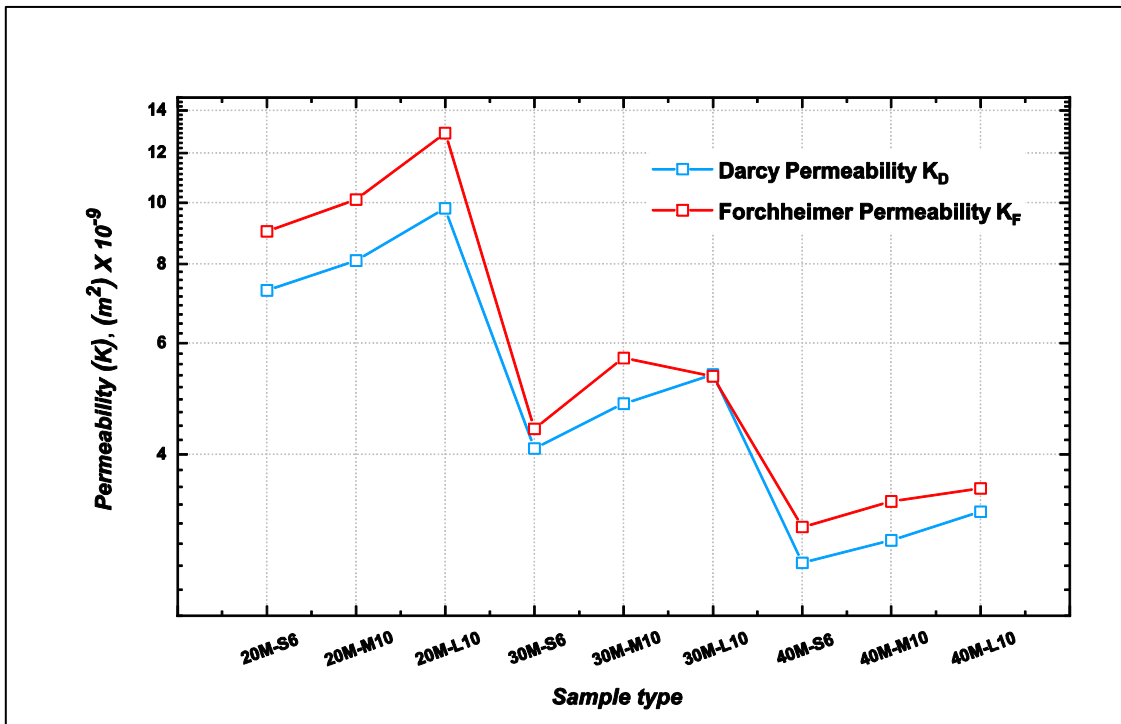
Figure 6.27 Darcy and Forchheimer permeabilities of heterogeneous samples (One slice Spherical foam with Mesh).
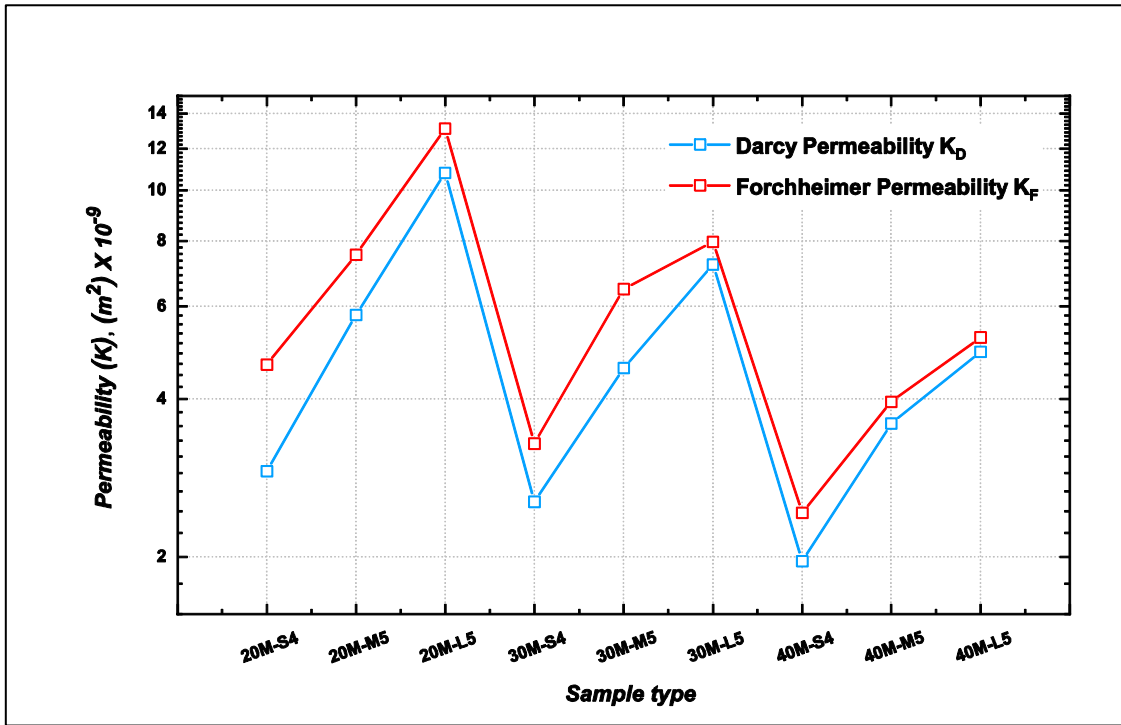
Figure 6.28 Darcy and Forchheimer permeabilities of heterogeneous samples (two slices Crushed foam with Mesh).
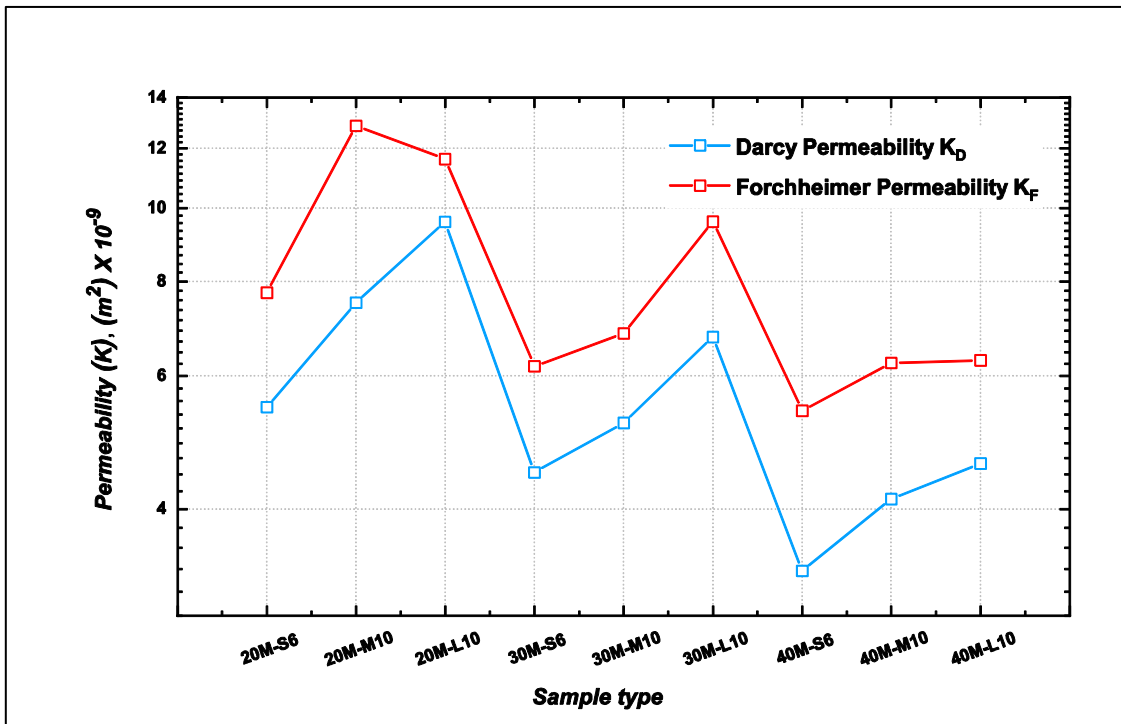
Figure 6.29 Darcy and Forchheimer permeabilities of heterogeneous samples (two slices Spherical foam with Mesh).

The inertia and drag coefficients of all the tested structures are compared, based on the pore size and the porosity, shown in Figures 6.30 to 6.33.

127
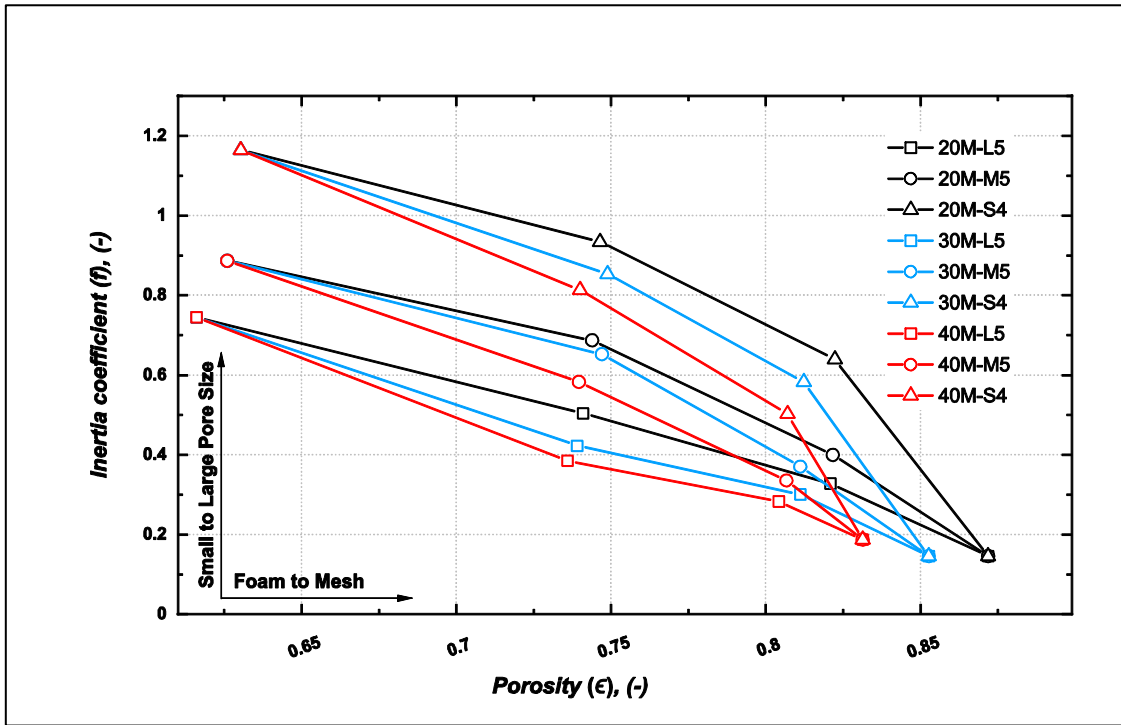
Figure 6.30 Inertia coefficient vs porosity (Crushed foam with Mesh).
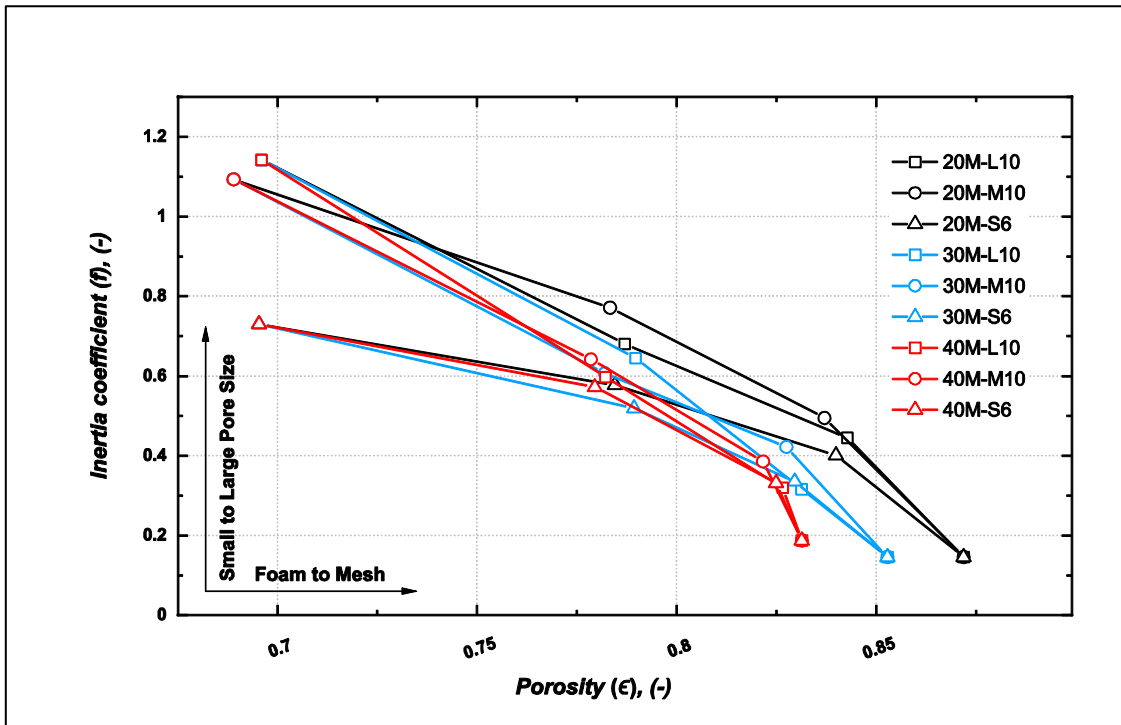
Figure 6.31 Inertia coefficient vs porosity (Spherical foam with Mesh).
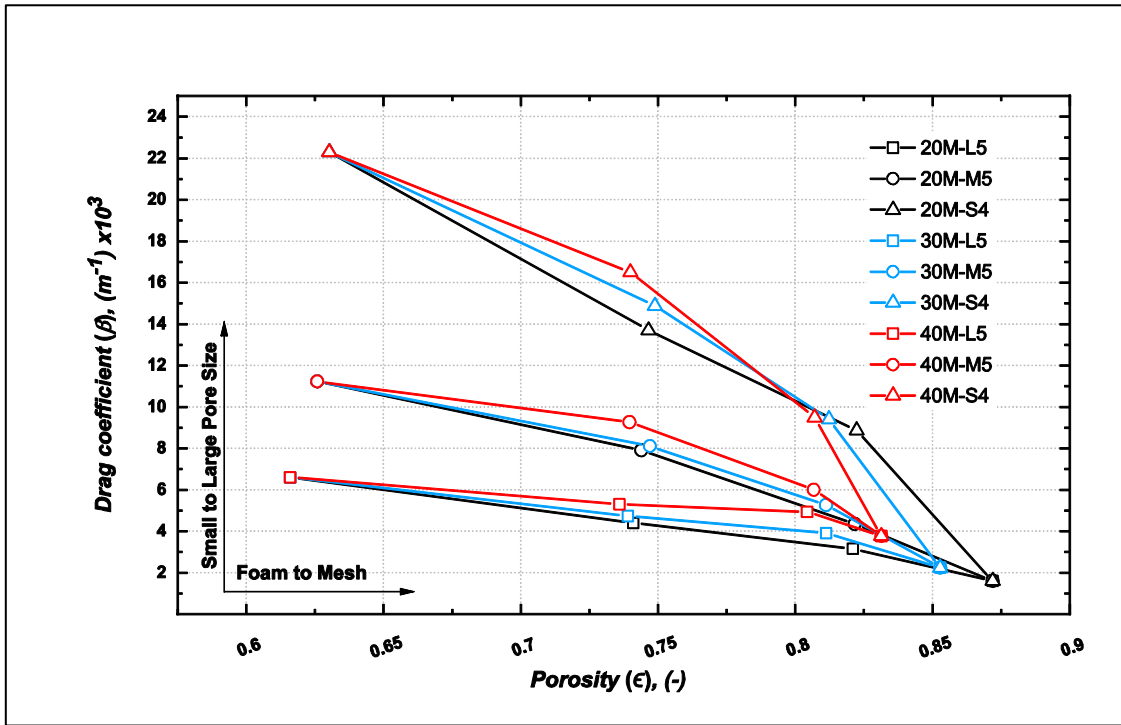
Figure 6.32 Form drag coefficient vs porosity (Crushed foam with Mesh).
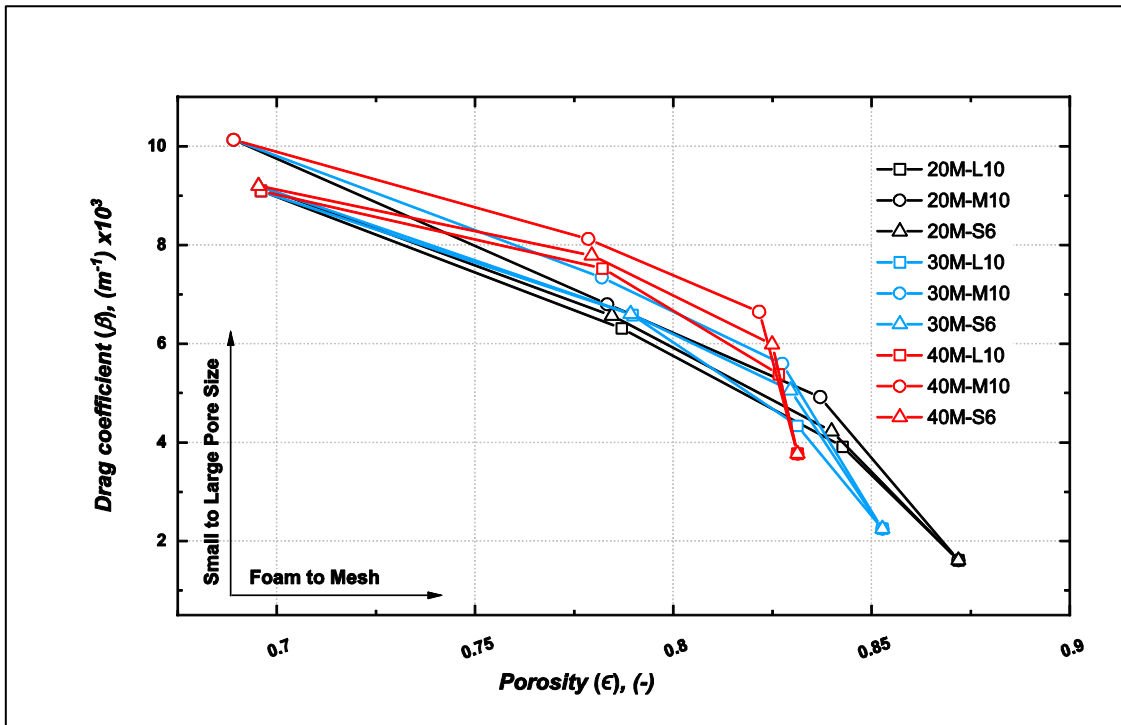
Figure 6.33 Form drag coefficient vs porosity (Spherical foam with Mesh).

Both inertia and drag coefficients decreased with increasing porosity and pore diameter. It is clear from these results that the inertia coefficient decreases with an increase in porosity and is more sensitive to porosity than the pore size. The measured inertia and drag coefficients for wire mesh packed beds are significantly lower than those for metal foam samples. This quantifies the porosity difference between the tested samples. Each group of metal foams has identical porosity but different pore sizes. Decreasing the pore diameter in metal foams increases the number of fibres forming the structure, and thus the flow resistance [32]. The microstructure differences between the metal foams and wire mesh screens influence the inertia and drag coefficients of the heterogeneous structure. It can be seen that both the inertia and drag coefficients decrease when the slices of foam are replaced with wire mesh screen layers.

The literature also shows a discrepancy in the Reynolds number responding to entrances and departures of Darcy and Forchheimer regimes [65][66][102][116]. Limited studies considering the limitations of transition zones in metal foams were found in the literature [61][101][111][223] and no attention has been paid to the limitations from weak inertia to strong inertia in screen packed beds. Although the same flow regimes have been identified in metal foam structures, the Reynolds number at which the transition occurs has not been verified. This is likely due to the influence of microstructure parameters on the transition [108]. The geometrical parameters (pore size and porosity) were found to influence both the thresholds of the flow regime and hydraulic parameters. Besides, this influence depends upon the porous media type, the flow regime, flow properties, physical features of the specimen and the materials of which it is made. Shown in Figure 6.34 are the upper and the lower thresholds of Darcy and Forchheimer regimes found for all classes of porous media tested in the current study.
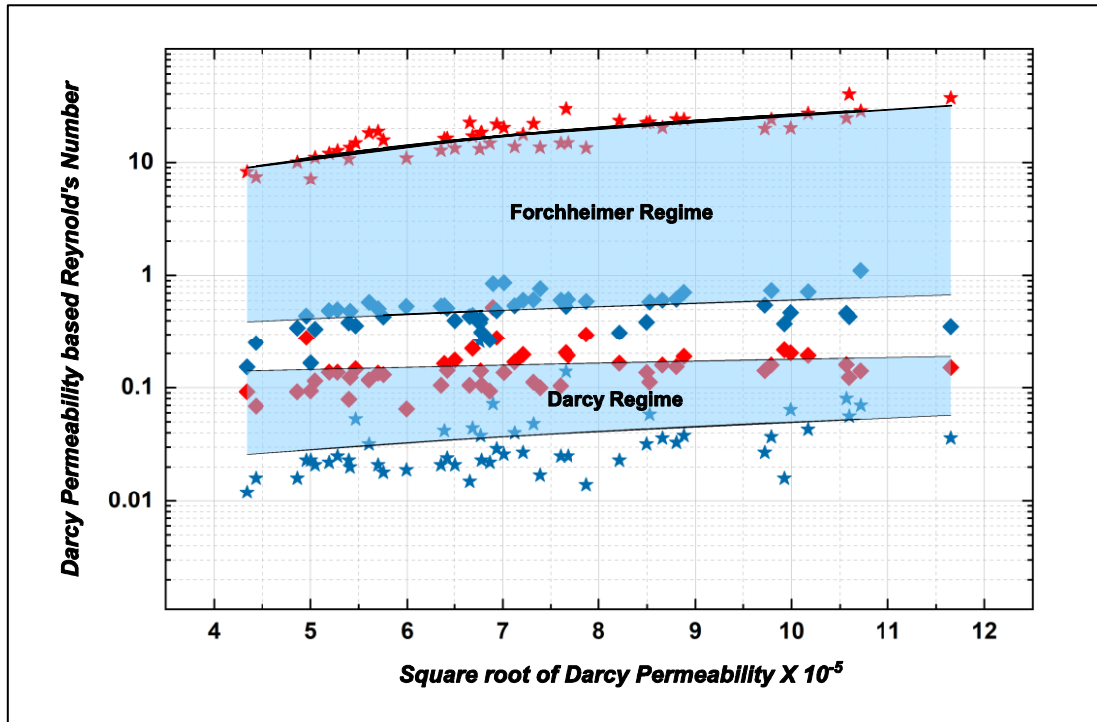
Figure 6.34 The upper and lower thresholds of Darcy and Forchheimer flow regimes,

To the knowledge of the researcher, there is no particular procedure that can be adopted to compare measured transport properties of random geometries. This may be due to variations in the morphology of different porous materials. Strictly speaking, a comparison of the different hydraulic parameters is justified only when experiments are conducted with identical combinations of geometric parameters. There is agreement that the hydraulic parameters are strongly dependent on the geometric parameters, namely, pore shape and size, porosity, alignment thicknesses and shape. However, it is accepted that all the geometric characteristics have a very slight influence on the values of the hydraulic parameters, except pore size and porosity. This may justify why previous researchers have chosen to describe the behaviour of the hydraulic parameters as a function of pore size or porosity [108][138][84][63][79]. In the present study, measured values of permeability in Tables 6.9 and 6.10 were compared with some of the reported data in a semi-log plot, Figure 6.35. A higher porosity or pore size means less obstruction in the flow path.

The impacts of porosity and pore size on fluid flow characteristics of aluminium foams were demonstrated by Boomsma et. al [108], Hunt and Tien [175], and Phanikumar and Mahajan [224]. Several samples with pore sizes ranging between

0.69mm and 6.9mm, and porosity between 0.87 and 0.99, were tested. Liu et al. [128] and Luna [36], on the other hand, tested woven wire mesh structures with a porosity between 0.37 to 0.81 and pore size from 0.067mm to 2mm. The results showed that porosity and pore size have a substantial impact on the magnitude of permeability, which increases with both the porosity and pore size of media.
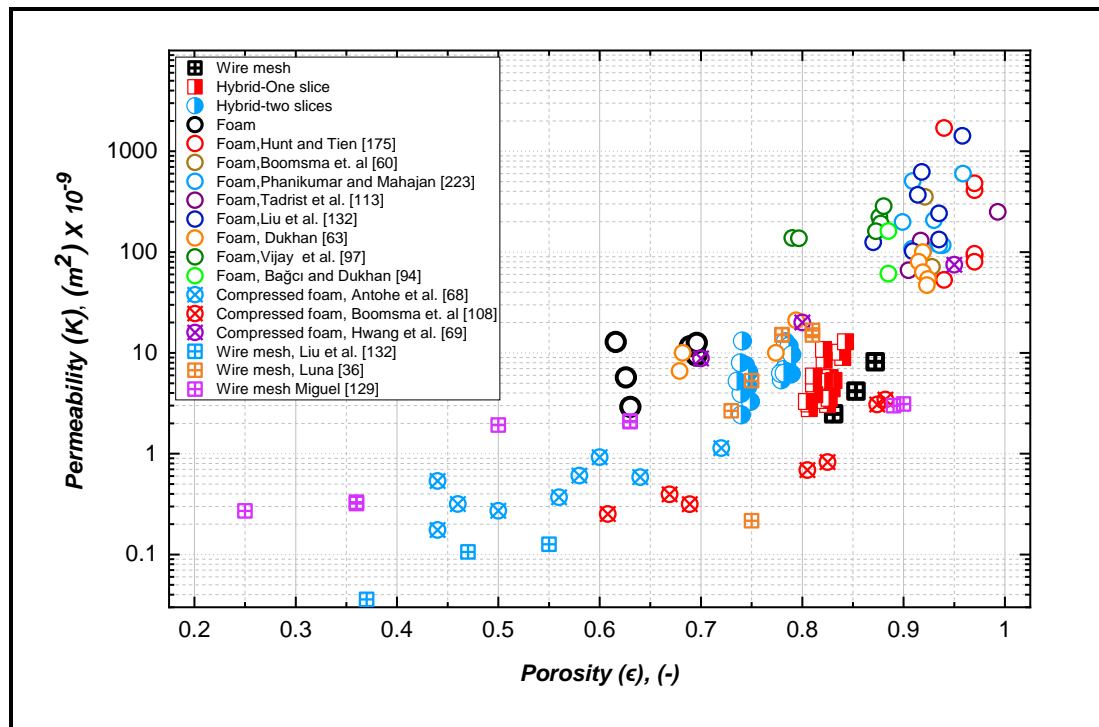
Figure 6.35 Permeability versus porosity.

The impact of the geometric characteristics on the inertia and the form drag coefficients in porous media have been also examined by many investigators [32][225][134][128]. For modern porous media (foams) and traditional porous media (packed beds), the inertia and drag coefficients were shown to decrease with porosity and/or pore size. The review also reveals that the impact of structure on the inertia coefficients was mostly discussed for high porosity metal foams and few experimental studies have considered the flow properties of wire mesh screen packed beds [24][36][128][129].

Liu et al [128] tested very fine sintered multi-layer woven wire mesh structures. The tested samples had the same wire diameter (0.14 mm), while porosity was maintained between 37% and 55%. Their results also showed that the porosity has an insignificant impact on friction factors and the inertia coefficient decreased with the

porosity of the medium. Miguel [129] identified the airflow characteristics of 14 woven porous screen samples with regular and irregular mesh geometries and different wire shapes. He concluded that the shape of wire and mesh geometry have a negligible influence on the inertia and form drag coefficient. However, the reduction of those coefficients was found to be strongly dependent on screen porosity. The literature survey showed that the published data regarding flow resistance across wire meshes is rather scarce and outdated. Also, most of the recent studies are based on numerical simulations [11][21][226][136] or focus on the flow resistance behaviour as a function of Reynolds number [20][79][80][83][139][227] but not the hydraulic parameters. According to Bhattacharya et al. [32] who experimentally investigated the impact of the structural parameters (porosity and pore size) on inertia coefficients in metallic foams, the inertia coefficients are more sensitive to changes in porosity than the pore size. Other studies also showed inertia coefficients are strongly affected by tortuous irregularly-shaped flow passages. They found the shape and size of tortuous passages vary based on the manufacturing method and the materials used [38][58] and the geometric idealisation is a problem as it does not accurately represent the structure of metal foam [63].

Figures 6.36 and 6.37 are plots of the measured inertia and form drag coefficients and previously published data for foams and screens packed beds versus the porosity. The results agree qualitatively with the literature. The measured data demonstrates that the inertia coefficients decrease with porosity.
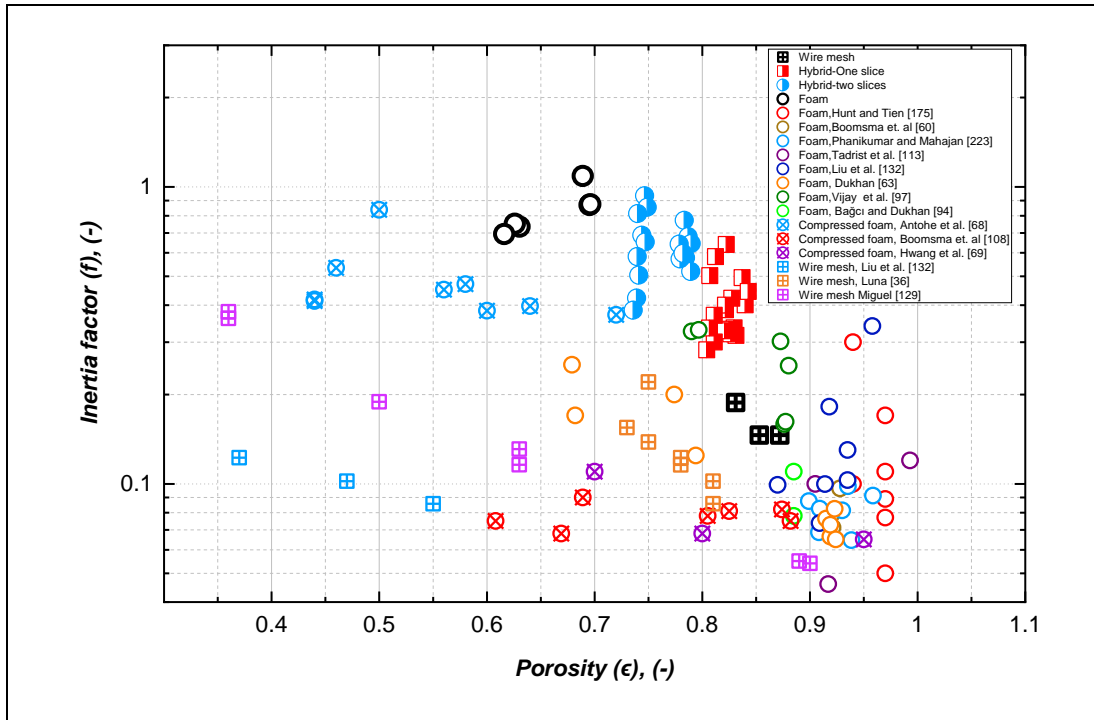
Figure 6.36 Inertia coefficient versus porosity.
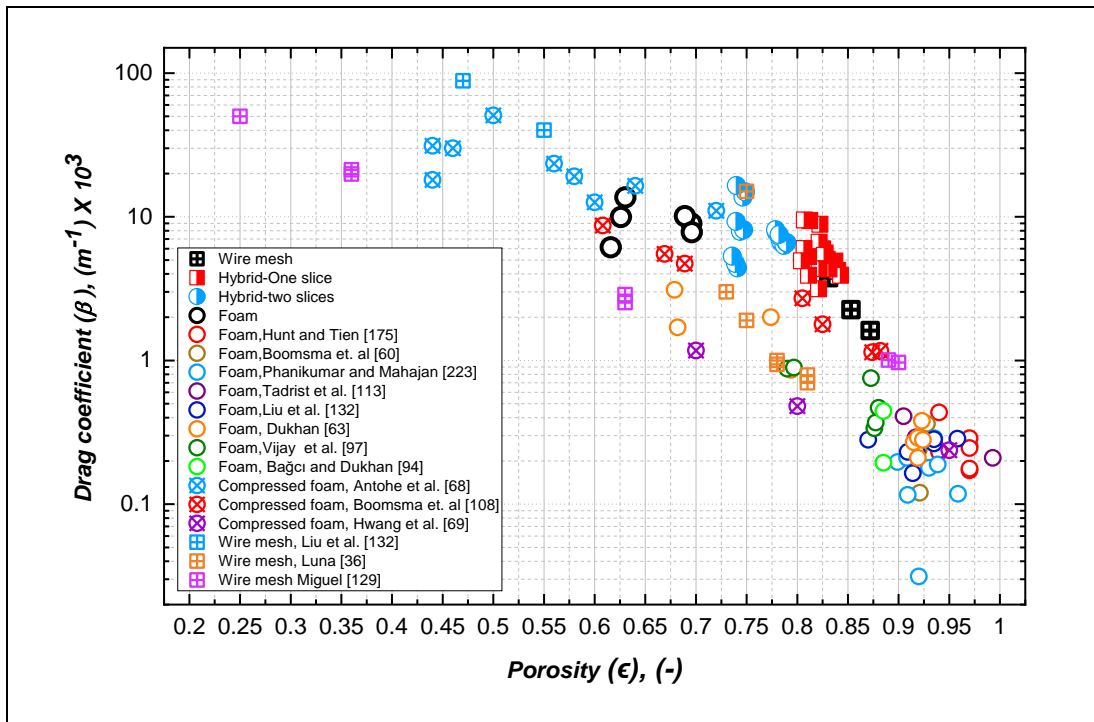
Figure 6.37 Form drag coefficient versus porosity.

6.4   Friction factor results

The pressure drop in the dimensionless form may provide more description of the flow resistance and further confirm flow regime boundaries. As was shown earlier, there are several modified forms to calculate the fanning friction factor and Reynolds number from the measured data. The current data correlated in non-dimensional form using the friction factor based on the square root of permeability (measured in the Darcy regime) and the Reynolds number based on the same characteristic length. Figure 6.38 shows an example of the friction factor behaviour versus Reynolds number at several flow regimes.
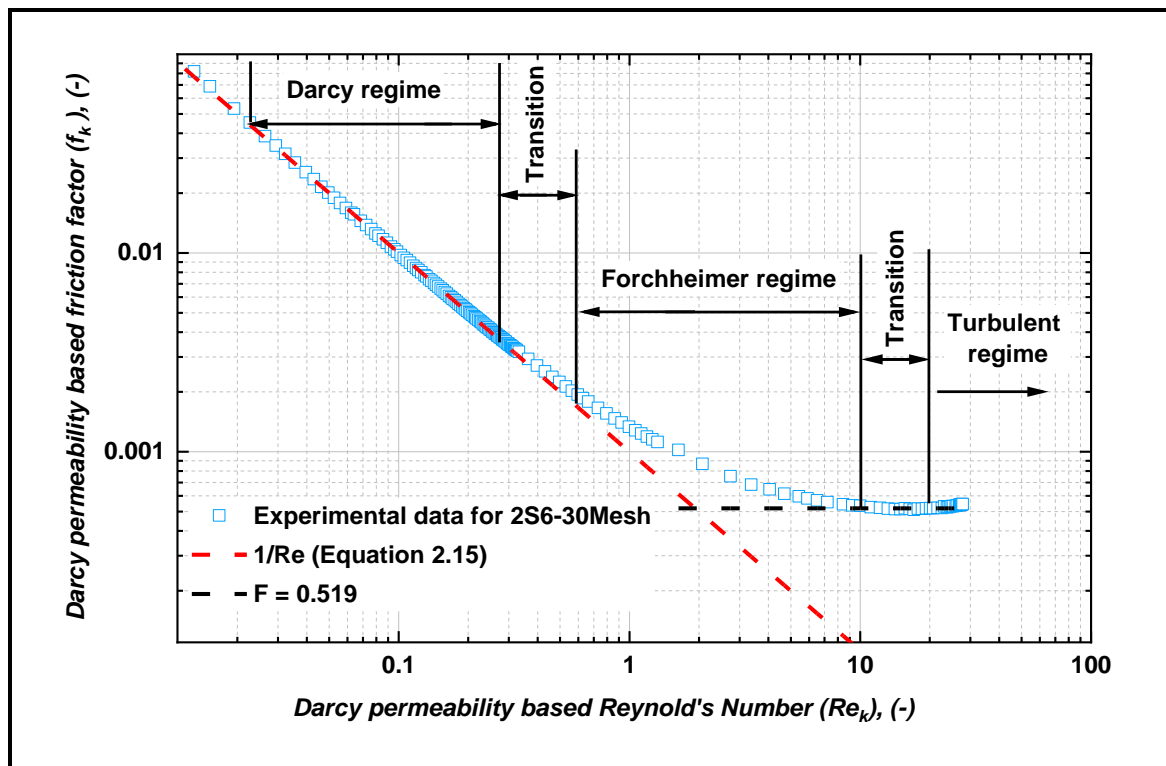
Figure 6.38 Friction factor vs Reynolds number.

According to Dukhan et al. [61], the frictional factor in metal foams decreases with the Reynolds number. At high Reynolds numbers, corresponding to the turbulent flow regime, the friction factor tends to an inertia coefficient. The authors noticed that the friction factor decreased with the porosity and pore size of the metal foams. Tian et al. [14] experimentally investigated the effects of topology of cellular metals including mesh screens and metal foams upon fluid flow. Their results showed that the friction factor of wire screens is not simply a function of porosity as metal foam materials and packed beds, but also a function of orientation (open area ratio). Xu et al. [11] performed both experimental and numerical studies on fluid flow through

135

metallic wire mesh structures. The results revealed that at Reynolds number <2000, the friction factor is independent of the Reynolds number and the flow resistance is dominated by form drag. Beavers et al. [100], Paek et al. [74], Hamaguchi et al. [228], Vafai et al. [141] and Kececioglu and Jiang [116] all used the square root of the Darcy permeability $\sqrt{K}$ as a characteristic dimension, the friction factor is expressed as:

$$f_{\sqrt{K}} = \frac{1}{Re_{\sqrt{K}}} + B \qquad 6.4$$

Flow regimes can be identified by comparing the experimental data to Equation 6.4. The friction factor behaviour for the semi-homogeneous sample in the present study is shown in Figure 6.39. The linear curve plotted in the graph is for the term $1/Re_{\sqrt{K}}$. It represents the flow resistance in the Darcy regime and serves as a reference line.
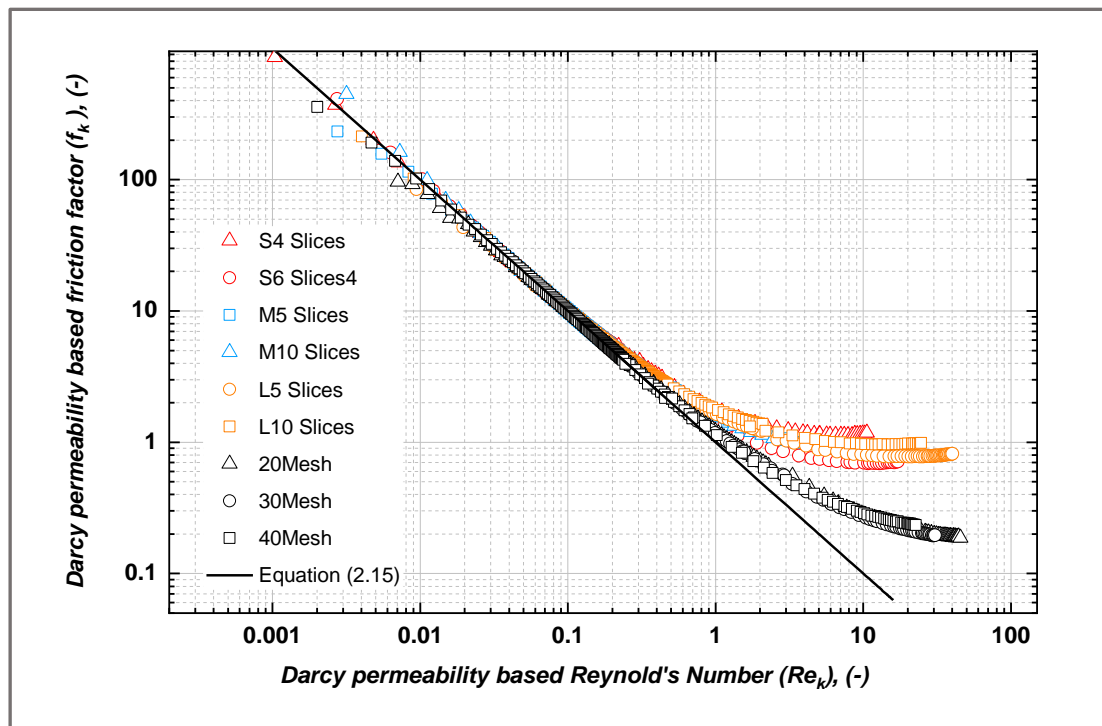
Figure 6.39 Friction factor vs Reynold's number (for Semi-homogeneous samples).

The results for the heterogeneous regenerators are shown in Figures 6.40 to 6.45.
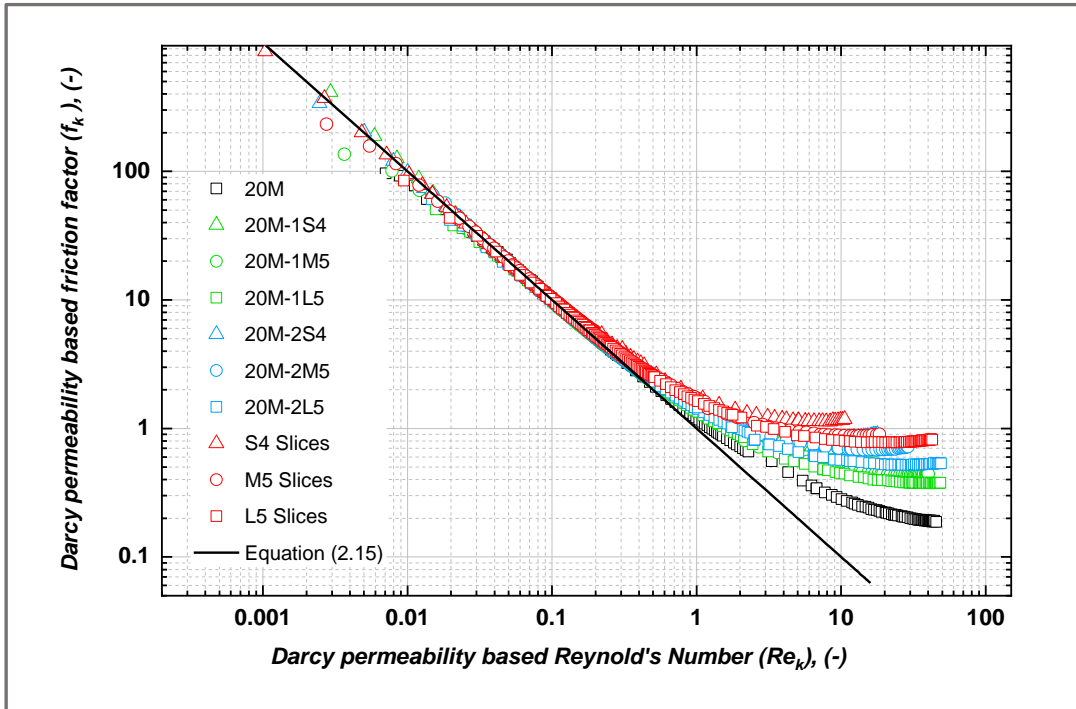
Figure 6.40 Friction factor vs Reynold's number (for Crushed with 20 Mesh).
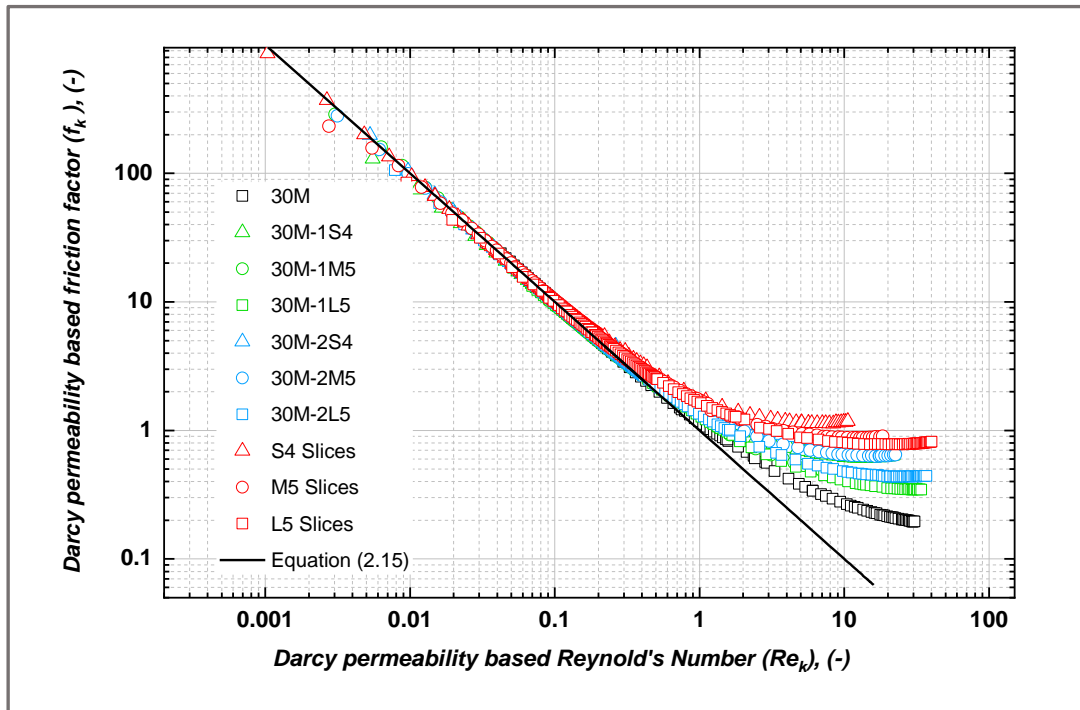
Figure 6.41 Friction factor vs Reynold's number (for Crushed with 30 Mesh).
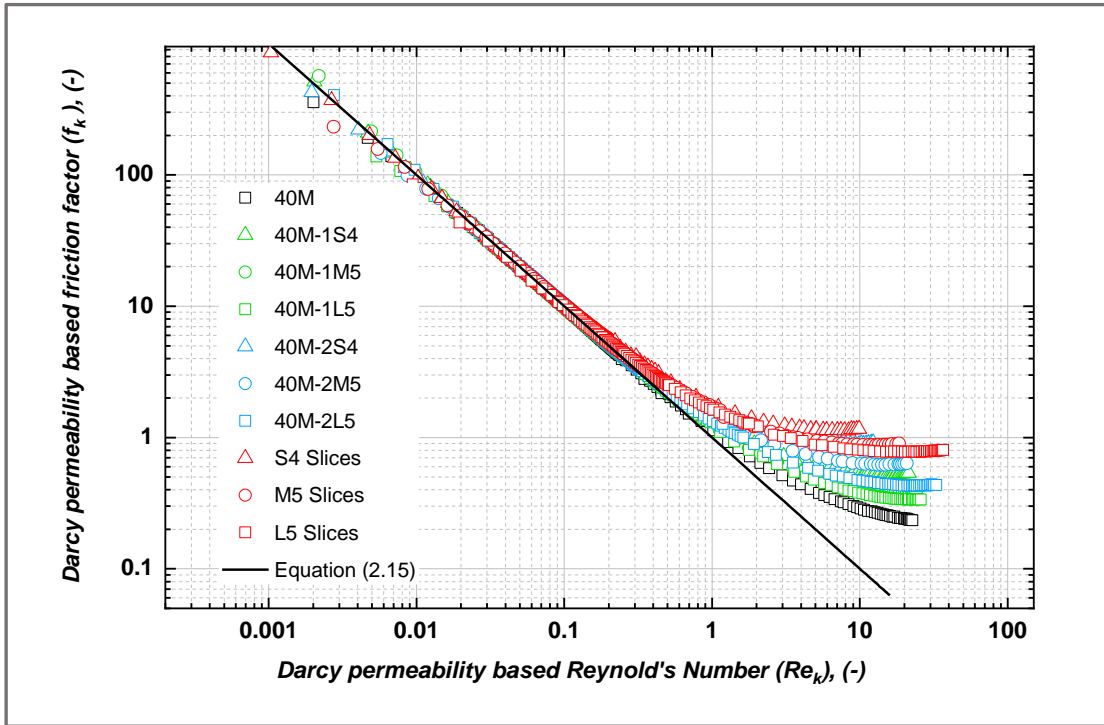
Figure 6.42 Friction factor vs Reynold's number (for Crushed with 40 Mesh).
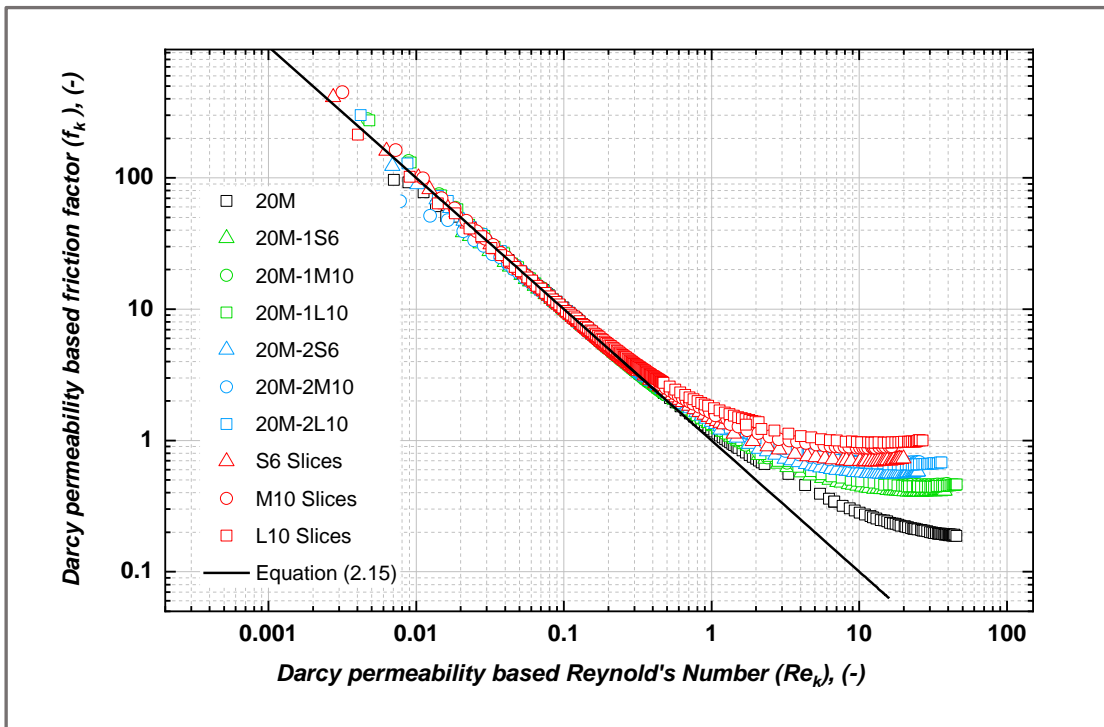
Figure 6.43 Friction factor vs Reynold's number (for Spherical with 20 Mesh).
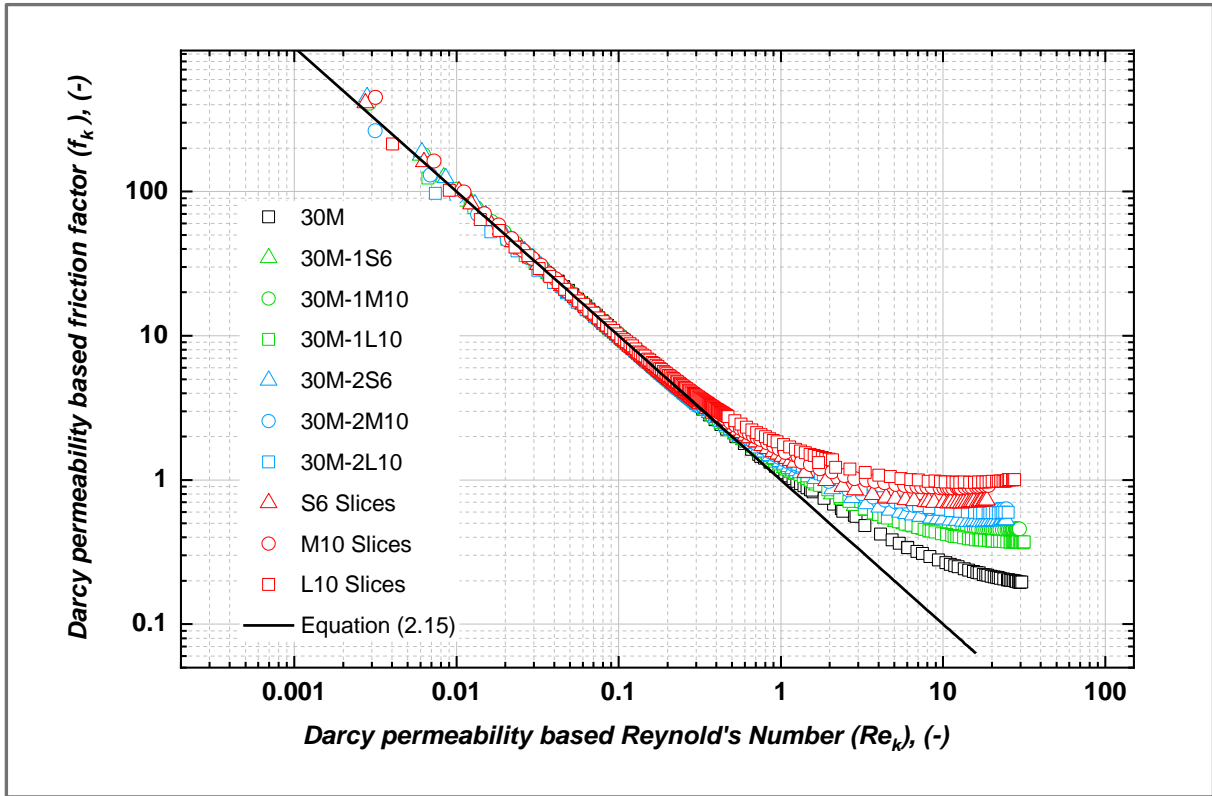
Figure 6.44 Friction factor vs Reynold's number (for Spherical with 30 Mesh).
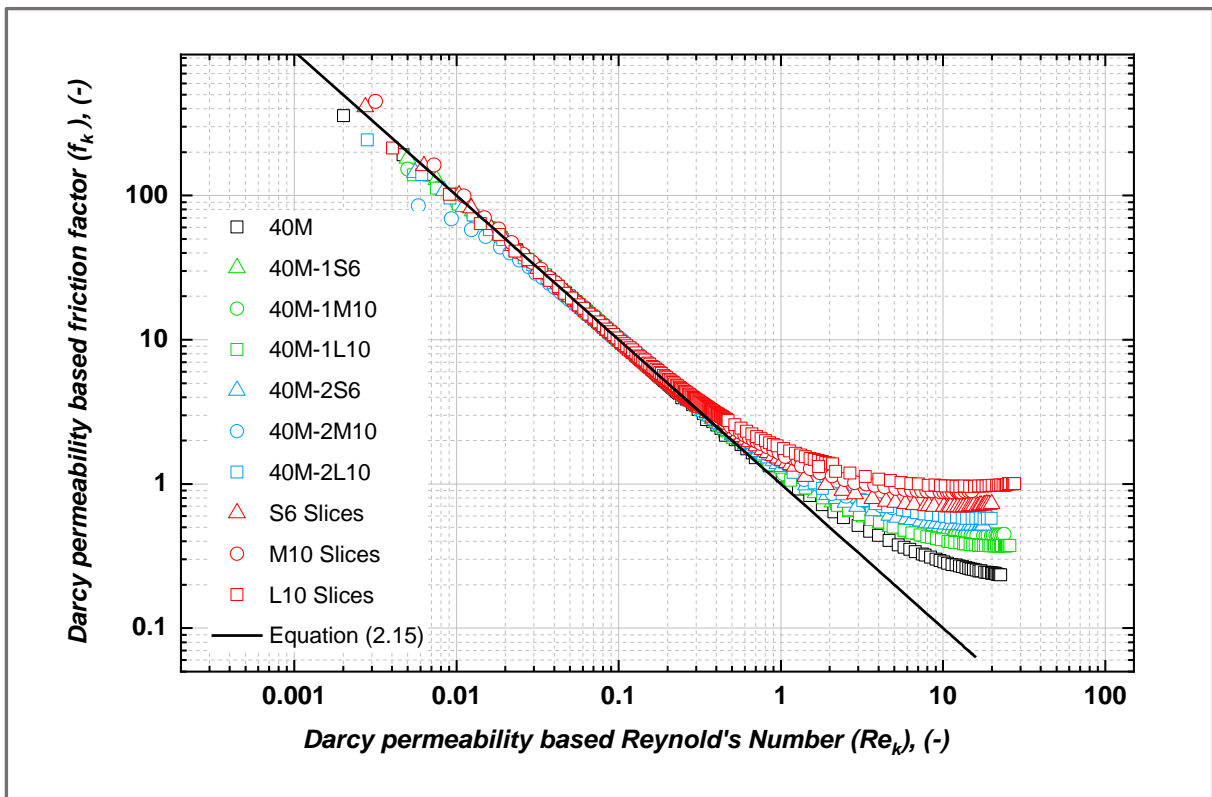
Figure 6.45 Friction factor vs Reynold's number (for Spherical with 40 Mesh).

139

The presentation of the experimental data showed a good agreement with this relationship in all tested samples in the Darcy regime ($f_{\sqrt{K}} = 1/Re_{\sqrt{K}}$). What merits attention is the gradual convergence of the friction factor and when the friction factor has an asymptotic value at a high Reynolds number. It was observed that the friction factor in the same samples increases slightly when $Re_{\sqrt{K}} > 10$. According to Dukhan et al. [61] and Mancin et al. [133], at high Reynolds numbers, the friction factor tends to the inertia coefficient. Therefore, this behaviour is most likely due to the compressibility effect at high flow rates. The compressibility effect can be accounted for by a term added to the pressure gradient [138]. However, this data lies beyond the scope of the current research and the turbulent regime was ignored.

The inertia constant has been considered a universal constant by many researchers. For example, it was equal to 0.074 for Beavers et al. [100], equal to 0.105 for Paek et al. [74], equal to 0.076 for Hamaguchi et al. [228] and equal to 0.057 for Vafai et al. [141]. Mancin et al. [133] compared their experimental results obtained from the testing of aluminium foams with those obtained from these four models and others available in the literature. They found that none of these models seems to estimate experimental pressure drop with an acceptable level of accuracy. They attributed this to the difference in the morphological parameters between the tested samples. Figure 6.46 illustrates the comparisons between the experimental results and those obtained from the four aforementioned models. As it appears, none of them is suitable for any of the tested samples and the models underestimate the friction factor at high flow rates.
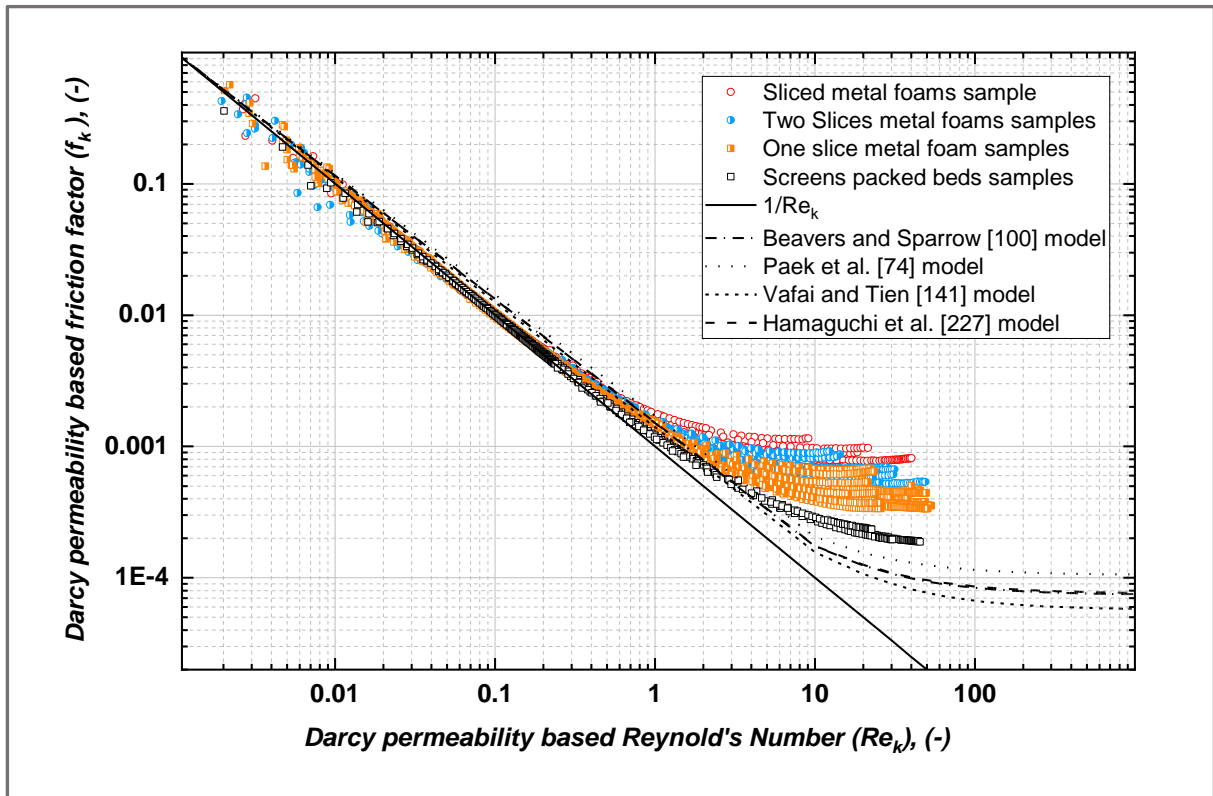
Figure 6.46 Friction factor vs Reynolds number for the tested samples.

6.5 Summary

This chapter discusses the flow test results in terms of pressure drop and hydraulic parameters at different flow regimes. The impact of porosity, pore size and heterogeneity on the fluid flow was demonstrated. The influence of those physical parameters on both the pressure drop and flow regimes has been clarified. Based on the measured pressure drop of this study, it is noted that the increase in pore size decreases the pressure drop. The Forchheimer-extended Darcy flow model is invoked for computing the permeability and inertia coefficient of the matrices. The results showed that samples with sample pore size show low permeability and high inertia coefficients. The experimental data has also been represented in non-dimensional form as a Fanning friction factor and Reynolds number relationship. The square root of Darcy permeability was used to characterize those dimensionless numbers. Based on the measured data, the friction factor of the three woven metal screens (plain square type) is less than that of foam matrixes. The flow resistance increases as the

141

percentage of foam materials increases in hybrid matrixes. Several expressions presented in the literature were tested to describe the flow resistance in laminar and post-laminar regimes. As it appears, no one was suitable for all of the tests to describe all types of porous media. This may be since every model defines its specific geometrical parameters. Generalizing correlation requires taking into account all geometrical parameters.

CHAPTER 7. Thermal Data Processing and Results

Once the pressure drop tests had been completed, the samples were each tested three times for their thermal behaviour. The measurements were taken at six different airflow velocities from ≈ 1.3 m. s^{-1} to 6 m. s^{-1}. The inlet and outlet temperatures were the same before the three-way valve was opened. Once the valve was opened, the inlet and outlet fluid temperatures started varying until reaching a new equilibrium position. The fluid inlet temperature increased sharply, achieving a step-change in less than 0.3 seconds, depending on the heat capacity and the flow rate. The outlet temperature increased gradually as the hot air passed through the sample until it reached the steady-state, hopefully, equal to the fluid inlet temperature. An example of typical transient temperature data obtained from testing the 2S6-30Mesh sample at (5.5 m. s^{-1}) is illustrated in Figure 7.1.
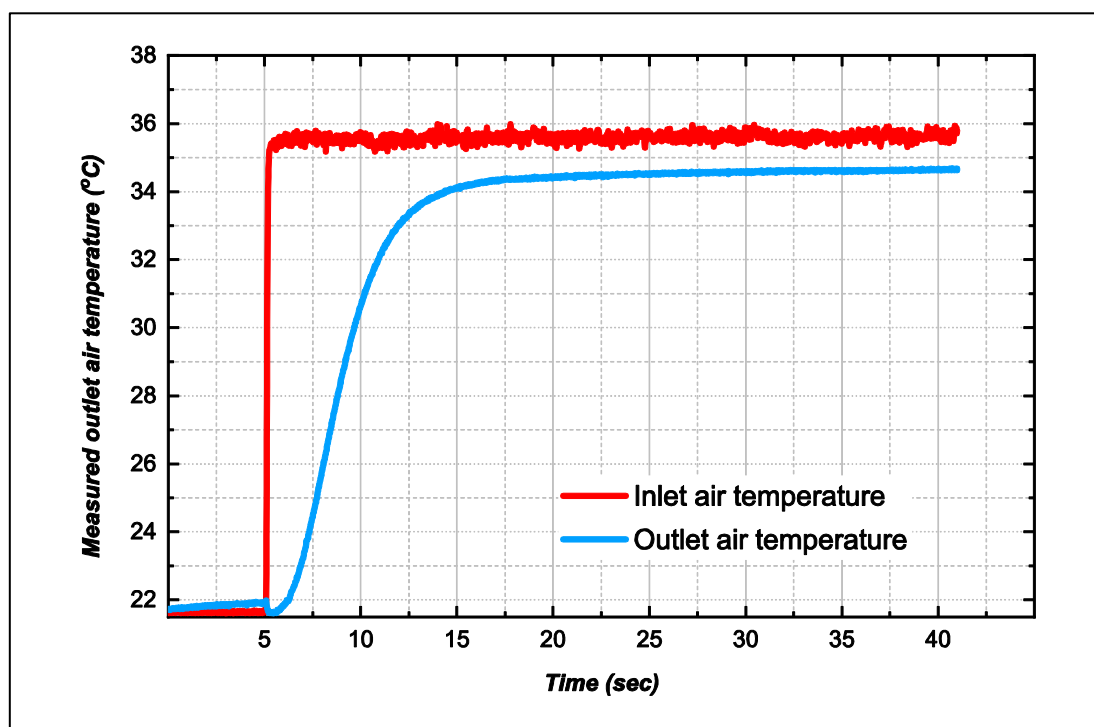
Figure 7.1 Typical transient temperature curves from testing 2S6-30Mesh sample at 5.5 m/s.

It was noticed that once the cooling line was switched off, a small rise occurred in the outlet temperature before the valve was opened. There is a T-junction located at the end of the detour (See Figure 5.11). As the hot air passed through the detour section, the temperature of the T-junction increased. Because of the short distance between the T-junction and the downstream thermocouple, the thermocouple sensed

the higher temperature of the T-junction once the cooling air was stopped. Moreover, once the three-way valve opened, the cooled air that has been captured between the sample and the three-way valve flows toward the thermocouple, resulting in returning the temperature to the initial state. This only occurred when the system was in operation for an extended period.

It can be seen that there is a difference between the inlet and outlet temperatures after the step change. This difference was due to the heat loss through the side-wall. It depended on the contact between the tested sample and the sample holder. Although the circumference of the tested sample was insulated, some energy was still lost through the sample holder. Compared to the wire mesh screens, the metal foam slices have a sizeable surface area in contact with the sample holder, making the difference more measurable. However, this impact was minimal when the sample was assembled from wire mesh screens only, as the mesh had contact with the side-wall, not the surface.

7.1 Temperatures and time non-dimensionalisation.

In each run, the average values of the differential pressure drop across the orifice plate, the static pressure, and the temperature of the flowing air before the orifice plate were recorded and used to calculate the mass flow rate flows into the system. As mentioned in Section 12, the test section including the tested sample was in the thermal equilibrium state and the initial temperature before and after the samples were recorded. Therefore, the recorded temperatures were averaged and considered as the initial temperature $T_0^\star$ for the system. The maximum air temperature $T_{f\,max}^\star$ was obtained from averaging inlet fluid temperatures once it had reached the steady-state (after opening the three-way valve). Equation 2.9 was then applied to bring the actual temperatures to dimensionless forms. The system time constant τ_{sys} was determined in each run. Equation 3.15 was then utilised to calculate the non-dimensional time. An example of dimensionless data obtained from re-testing the 2S6-30Mesh sample three times is shown in Figure 7.2.
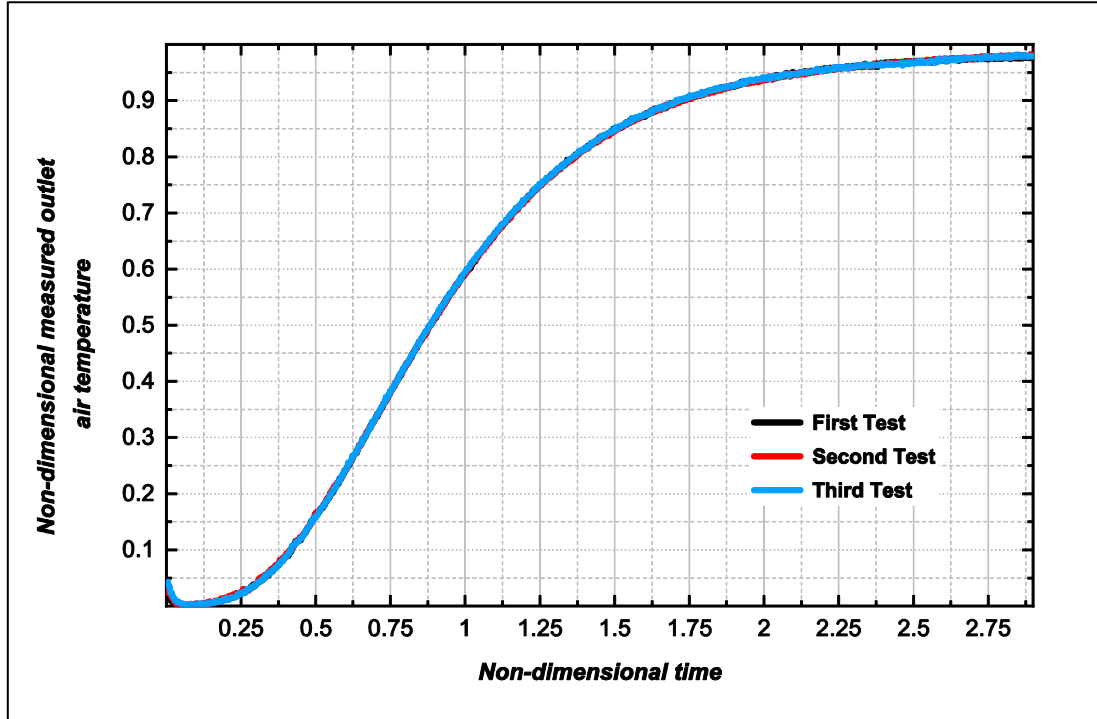
Figure 7.2 Three thermal test runs for sample 2S6-30Mesh at 5.5 m/s in non-dimensional form.

7.2 Differentiation of outlet temperature curves.

Prediction of the NTU_s involved finding the inflection point in the first differentiation of the outlet temperature curve (maximum slope value). The first derivative was approximated numerically, using the central difference scheme, Equation 7.1. The derivative approximations at endpoints were computed using the forward difference scheme, Equation 7.2. The derivative process was implemented in Matlab software using the (*diff*) function.

$$\frac{dT}{dt} = \frac{(T_{i+1} - T_{i-1})}{2\Delta t}$$

7.1

$$\frac{dT}{dt} = \frac{(T_{i+1} - T_i)}{\Delta t}$$

7.2

Although the temperature module, which is used for logging the thermal data, was designed to omit the unwanted voltages, the logged data demonstrated significant noise. This was likely a result of turbulence and airflow circulation or due to the signal interference between the thermocouples and other electrical equipment. However, even moderate noise would amplify significantly once the first derivation was

145

calculated. An example of the differentiation of experimental data is presented in Figure 7.3.
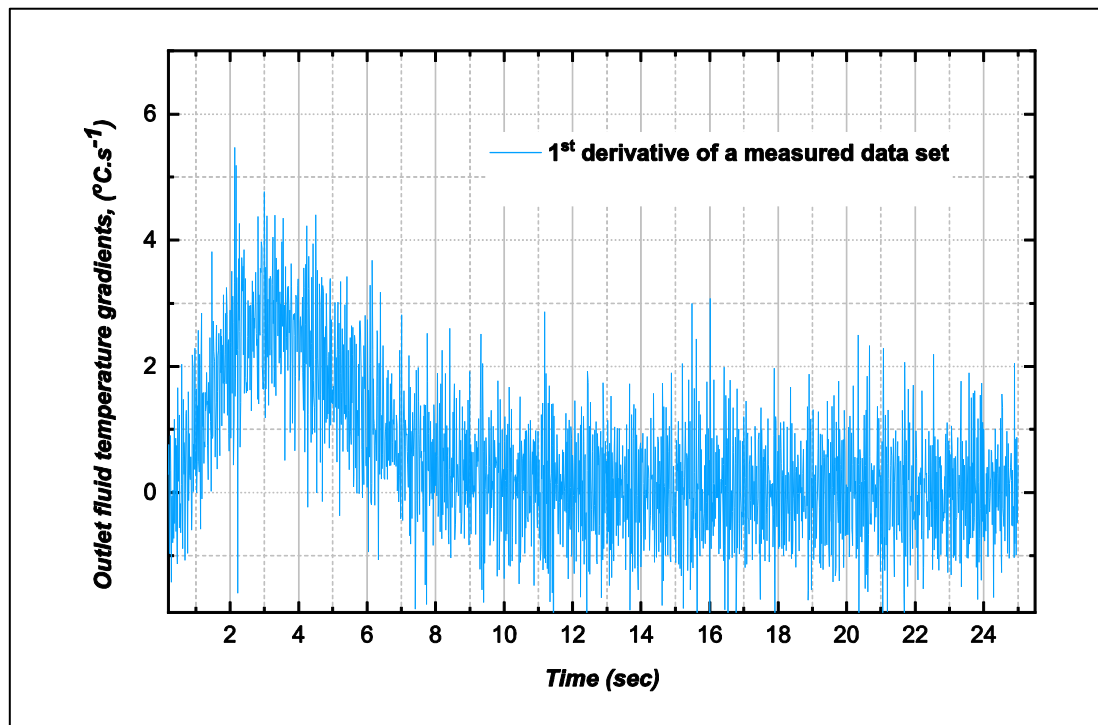
Figure 7.3 An example of the 1st derivative of the outlet temperature curve for the S6 sample at 2.5 m/s.

7.3 Data smoothing process

A smoothing process was performed on the experimental data using two different methods: the moving average and the Shape Language Modeling tool (*SLM*). The moving average filter was first employed to remove outlier points from the experimental data; the *SLM* was then used to improve the smoothness. The moving average filter is a denoising digital filter, which works by identifying unwanted out-of-range points and replacing each point with an average of its neighbours. The intensity of points per window (data weighting) is a crucial function of the smoothing mechanism. As the number of data points increases in the window, better fitness can be achieved. However, this might result in a lag behind the original data, and care must be taken to identify the most appropriate number of points. In the present study, forty points per window were seen to provide good smoothing without any distortion to the original experimental data.

This smoothing step was conducted in the Diadem signal-processing program, designed by National Instruments. In the second step, the shape language modelling (*SLM*) technique developed by John D'Errico [229] was used in fitting piecewise regressions to these data sets. The *SLM* approach is based on least-squares splines, subjected to simple constraints. Knot points (breakpoints) can be provided by the user or determined automatically to specify where there is a slope discontinuity and a need for fitting another spline. If there are any cut-off points in the slope of the measured data, the function works to create a sequential piecewise regression to predict missing values. This technique was implemented in the *MATLAB* optimisation toolbox. As can be seen in Figure 7.4, this tool works very well as it respects quantification of experimental error when compared to the change in an outlet temperature gradient.
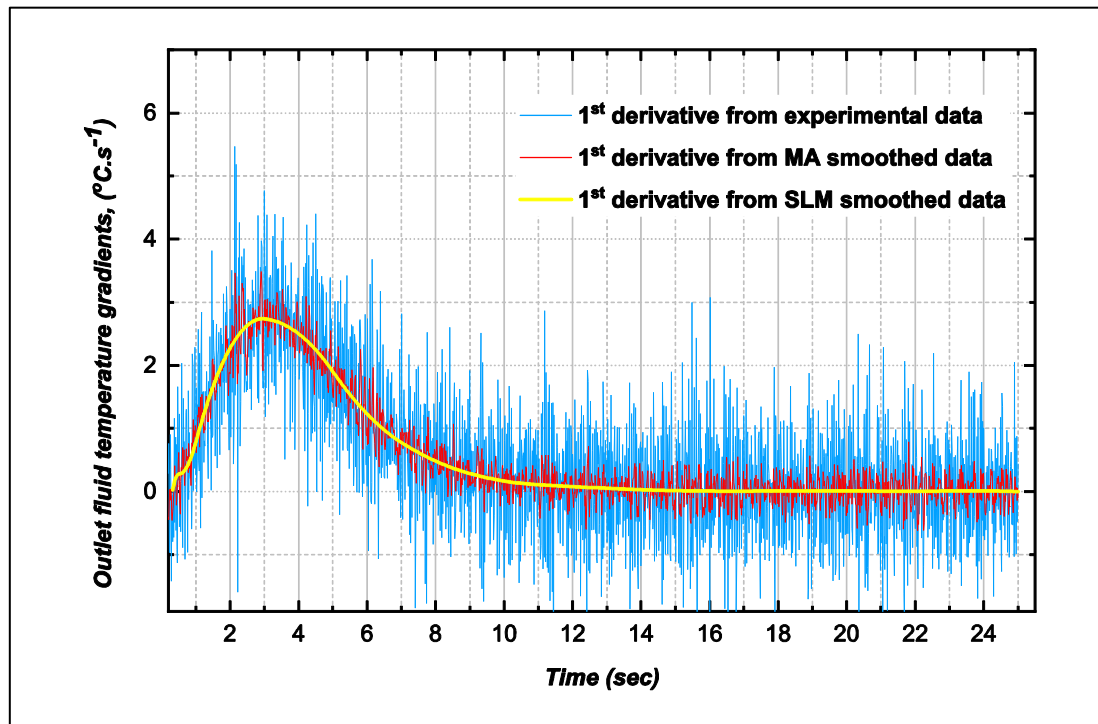
Figure 7.4 Experimental data after being smoothed by a series of smoothing techniques.

To evaluate the goodness of fitness, the residual values and the R-square were graphically and numerically measured. The residuals are usually used to investigate the strength of fitness of models or any regression methods. The residual's values are defined as the distance between the measured data and the fitted data at each point. Numerically, it is calculated as the difference between the measured and predicted data. It can be expressed mathematically as:

$$Residual\ (R) = \left(T_{measured} - T_{predicted}\right) \qquad\qquad 7.3$$

Graphically, it shows whether the errors have identical distributions (zero mean value and same variance across the time). Figure 7.5 presents an example of the distribution of the error obtained from the measured data in the current study.
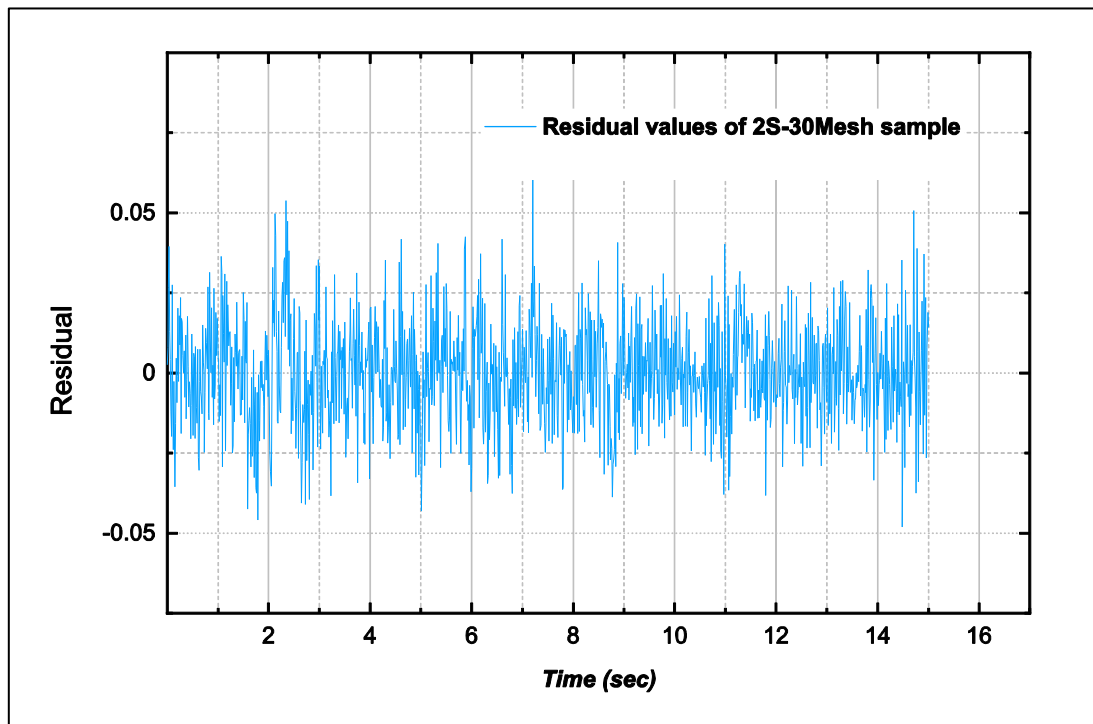
Figure 7.5 Residuals error of measured data obtained from the 2S6-30Mesh sample.

On the other hand, the coefficient of determination (*R-squared value*) is an indicator often used to investigate whether the regression model or method explains the variation of the dependent variable or not. It varies between "0" and "1", in which zero R-squared value means the regression model or method does not explain the variation of the dependent variable, and an R-squared of value one indicates perfect fitting results. At least two out of three variations are required to determine the R-squared value [230]. The definitions of the three variations are illustrated in Figure 7.6.
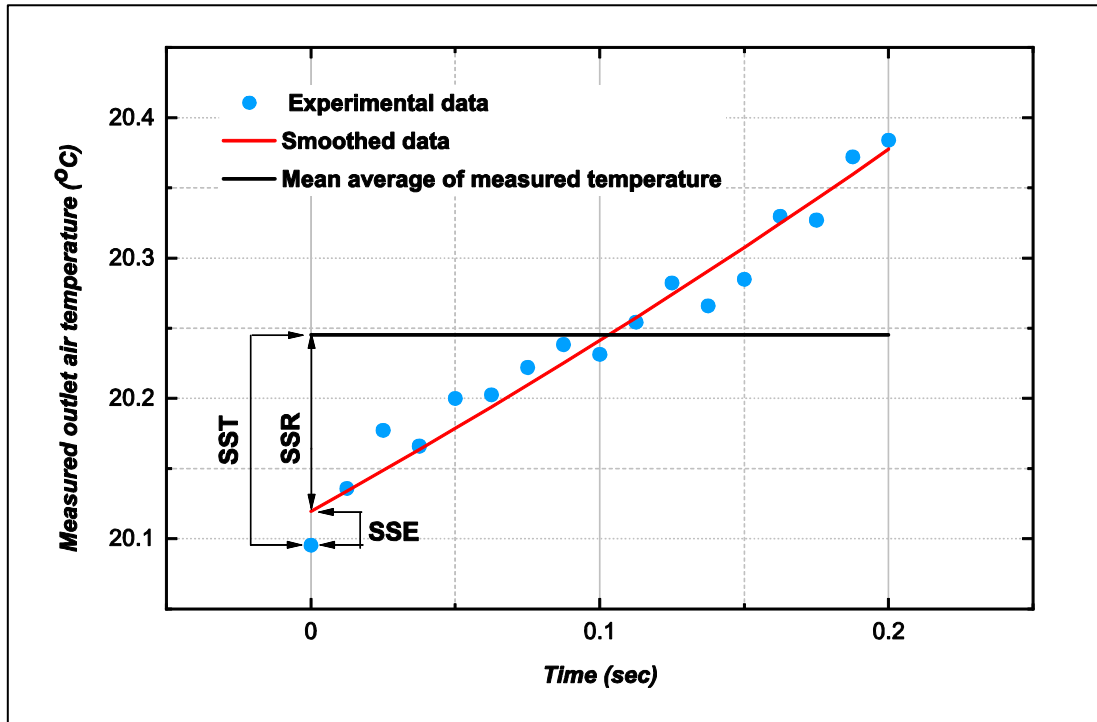
Figure 7.6 An example of a fitted curve showing the definitions of SST, SST and SSE terms.

The first variation is the sum of squares error SSE or the 'unexplained variation' as it is sometimes called. This sum is used to show the variation in the measured data which the regression model cannot explain. It is calculated from the sum of square values of the residuals:

$$SSE = \sum \left(T_{measured} - T_{predicted} \right)^2 \qquad 7.4$$

The second variation is called the sum of squares total SST. This term measures the variation in the actual data compared with the mean value. In other words, it is the sum of the squared difference between the measured temperature and the mean temperature of a selected sample. Numerically, it is calculated as:

$$SST = \sum \left(T_{measured} - T_{mean} \right)^2 \qquad 7.5$$

And finally, the explained variation or the sum of squares due to regression SSR, which shows how well the regression model fits the measured data. It is calculated by the squared difference between the predicted and the mean values as:

149

$$SSR = \sum \left(T_{predicted} - T_{mean}\right)^2 \qquad\qquad 7.6$$

Given these values, the R-squared value can be calculated as:

$$R^2 = \frac{SSR}{SST} = 1 - \frac{SSE}{SST} \qquad\qquad 7.7$$

The R-squared value was used to investigate the goodness of fitness in some parts of the fitted data, as will be demonstrated. For the heterogeneous sample 2S6-30Mesh in Figure 7.6, the R-square value was equal to 0.96.

7.4 Determination of the number of transfer units for the samples

A high maximum gradient implies a high number of transfer units NTU_s. The values of NTU_s have been estimated using the hybrid matching method explained in Section 3.3.2.6. The numerical model has been utilised to predict the solution for each run. The direct matching method was initially used to predict the number of transfer units of the regenerators and the side-wall, followed by the maximum slope method to confirm the predicted values. An example of the direct matching process is shown in Figure 7.7. Initial values were applied to the numerical model to predict the solution at those values. For instance, the initial values were 6.5 and 0.12 for NTU_s and NTU_w respectively, to predict the outlet temperature curve from testing the 2S-40Mesh sample at six m.s-1. When the matching was not achieved, the values were modified iteratively until satisfactory matching was enabled.

To endorse the predicted values, the first derivative curves for the experimental and the predictive data were calculated and compared, as shown in Figure 7.8. The maximum slope values were confirmed to be equal with insignificant error.
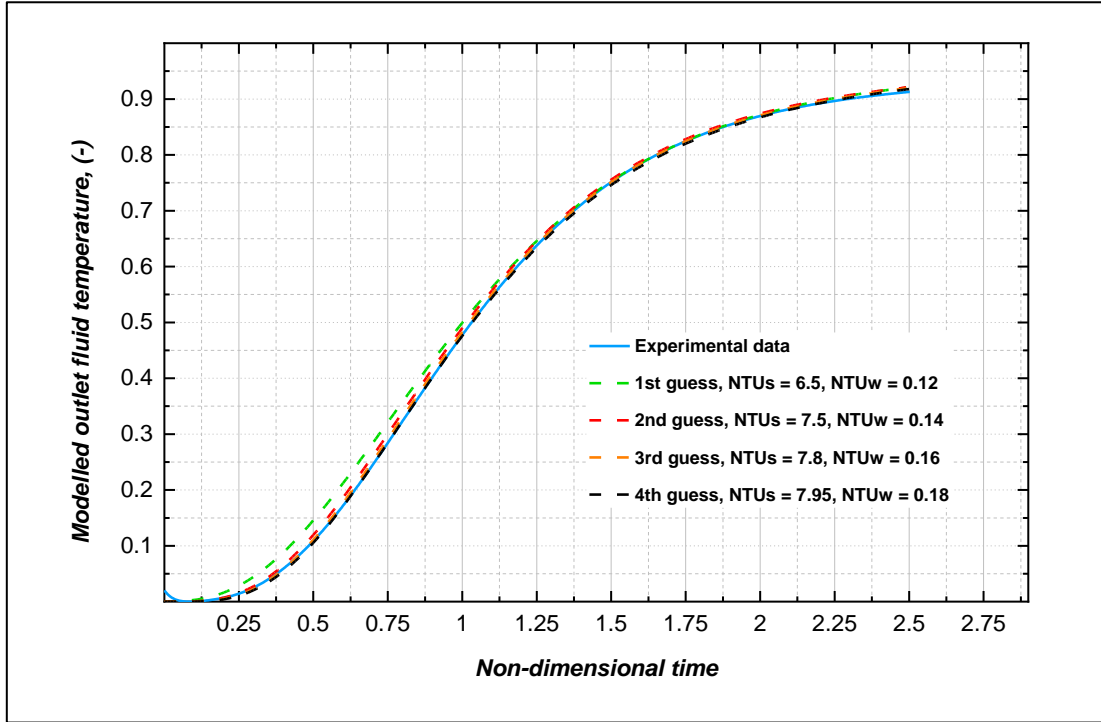
Figure 7.7 The trials of the matching technique.
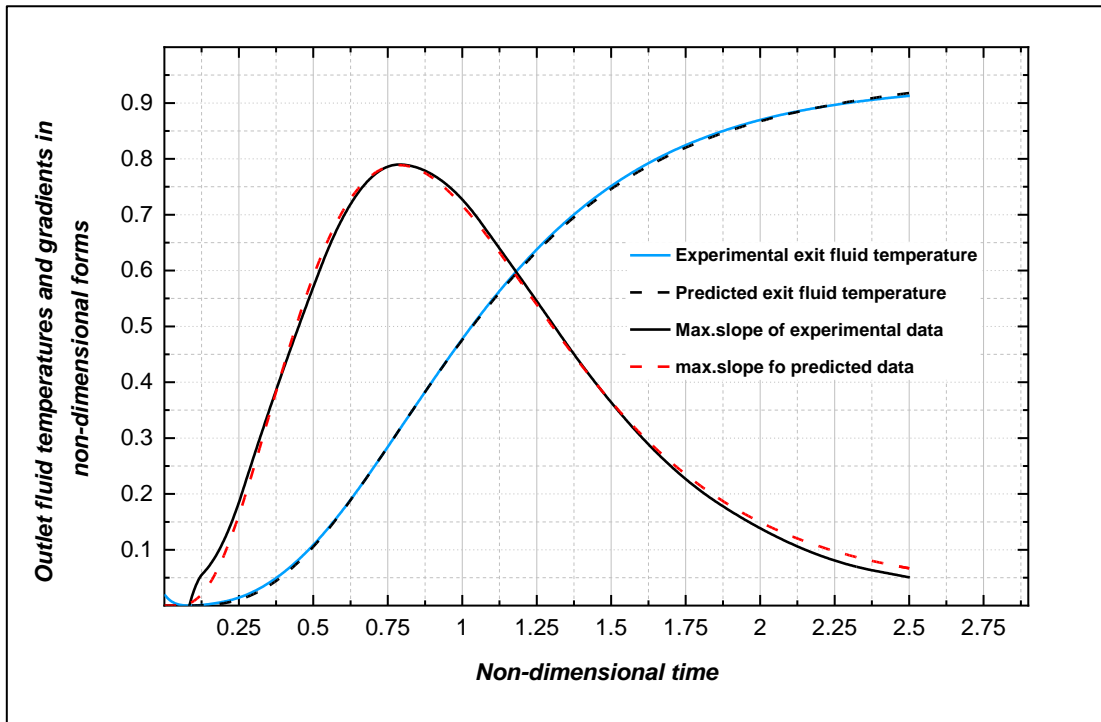
Figure 7.8 Final fit of exit fluid temperature by maximum slope method.

7.5 Impact of slicing on the thermal performance of metal foams.

This study was carried out based on the assumption that the effective thermal conductivities of the samples were close to zero. This meant the axial conduction could be omitted in the experimental data analysis. This assumption was made based on the fact that there are poor contacts between the adjacent layers and the axial conduction parallel to the flow direction has a negligible impact. Abuserwal [37] developed experimental equipment to measure the effective thermal conductivity in replicated aluminium foams with relatively low porosity. As a part of his study, he measured the effective thermal conductivity of aluminium metal foams which had been equally sliced. He reported that slicing led to air gaps between the slices, and the effective thermal conductivity was found to be 92% lower than that of the same original samples. Luan [36] attempted to measure the effective thermal conductivity across regenerative packed beds, fabricated from stainless steel wire mesh screens. He reported that the effective thermal conductivity was less than 0.1 W/m.K. In the current work, the replicated samples were sliced into three slices to produce hybrid structures. To determine the impact of slicing on the thermal performance of regenerators the sliced samples were retested and compared with their pre-slicing performance. The numerical solution was employed to estimate the effective thermal conductivities of the multi-layered pure samples. The results confirmed the outcome of the previous researchers [37][36].

It was expected that the reduction of the effective thermal conductivity would lead to an enhancement in the thermal performance of the regenerators. However, the parametric study in this research showed that this fact is true only for a large number of NTU_s values ($NTU_s > 7.2$). Consider two metal foam samples, as demonstrated in Figure 7.9; one has a lower NTU_s value (lower than 7.2) and the other a higher NTU_s value (larger then 7.2). The maximum slope values mapped to these NTU_s values are represented in red when the samples have high effective thermal conductivity and in blue when they have zero effective thermal conductivity. It can be seen that slicing metal foam samples with low NTU_s values would result in lower thermal performance; this is in contrast to when the sample has a large NTU_s value, when the slicing tends to improve the thermal performance of the samples.
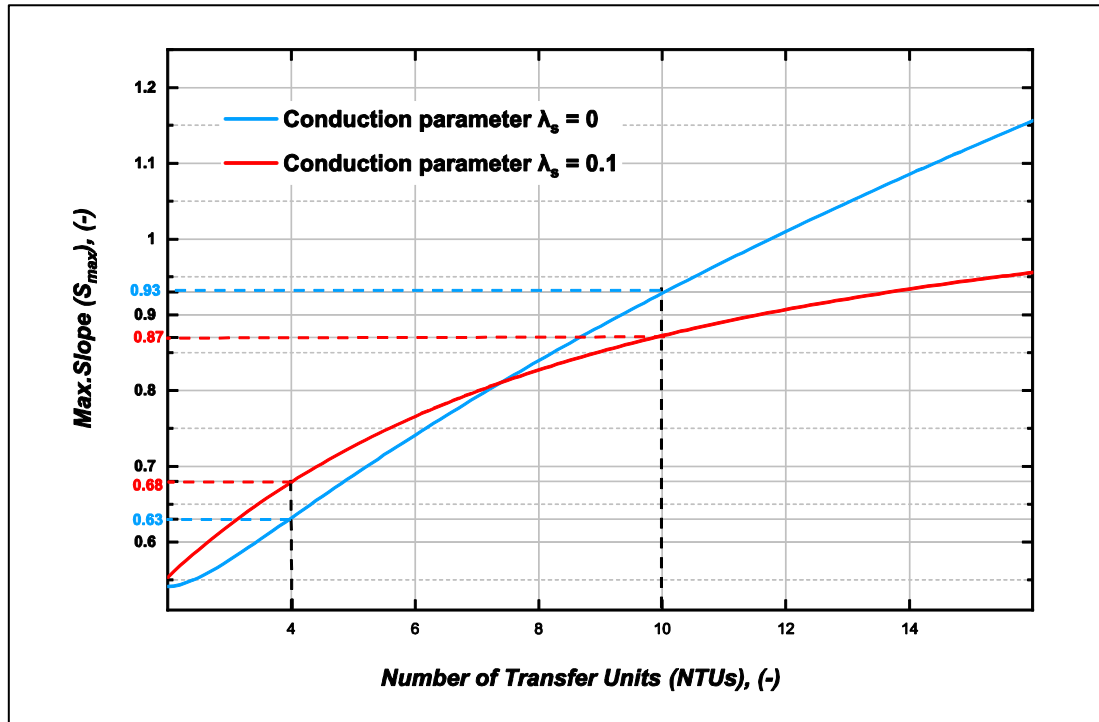
Figure 7.9 Effect of conduction parameter on the prediction of $NTUs$ values.

Slicing the samples cannot be achieved without some loss of the solid material. Although wire *EDM* machining can cut through metals with minimum mass removal, this was not the case with the light samples used in the present study. Most of the tested foam samples each had a weight lower than 50g. The slicing process caused a six-gram mass reduction in the original samples (almost 12% of the weight of the original sample). According to Equation 4.1, the maximum slope value decreases as the weight of the sample decreases. This may be attributed to the reduction in sample weight causing a decrease in the heat capacity and the heat transfer surface area of the tested sample. The influence of the mass loss on the outlet temperature gradient is illustrated in Figure 7.10. It was found that a five-gram mass reduction causes a decrease in the maximum slope value from 0.8 to almost 0.7, which is about a 26% decrease in the NTU_s value if the axial conduction and the side-wall effect impacts are neglected.

153
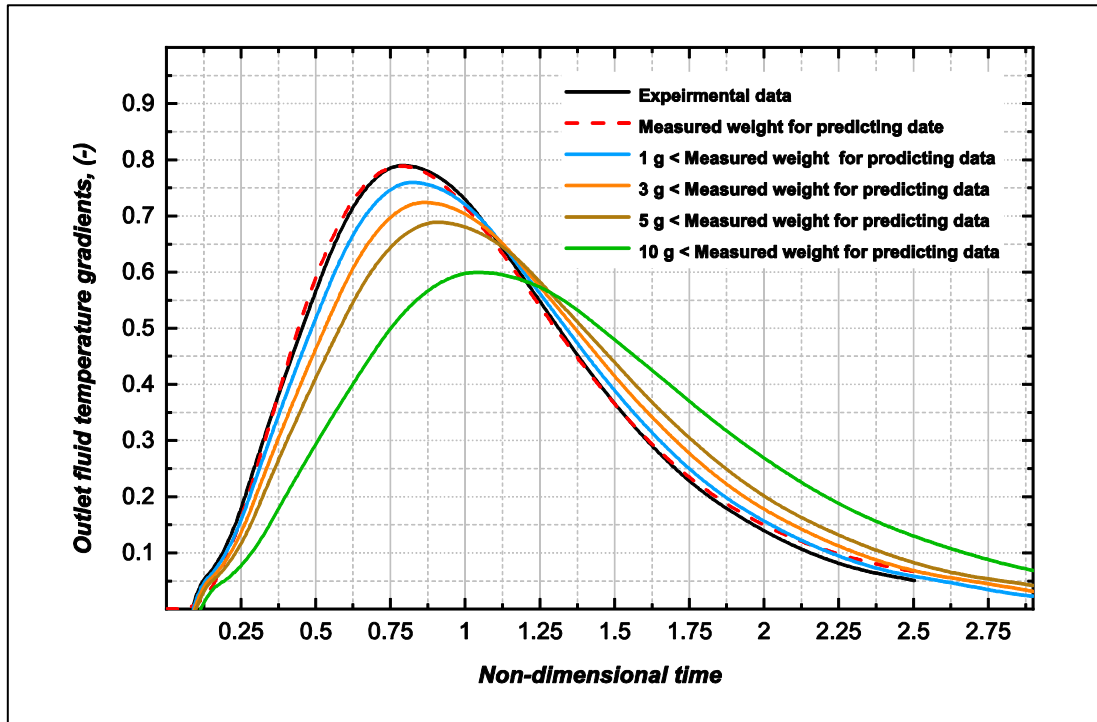
Figure 7.10 Effect of mass reduction on the maximum slope value.

7.6 Number of transfer units (NTU_s)

One of the outcomes from the previous data processing was to obtain the number of the transfer units NTU_s, at six different flow rates for each regenerator. The number of the transfer can be used as an indicative parameter usually used to compare the thermal performance of several structures and determine the optimal regenerator. The number depends on the heat capacity of the working fluid and the thermal resistance between the regenerator solid surface [231]. A typical efficient regenerator requires a dense material with a high heat capacity and a large heat transfer surface area [5][42]. High heat capacity can be achieved by decreasing the porosity, while a large heat transfer surface area may be obtained from increasing the pore density. The predicted NTU_s values are plotted non-dimensionally against the Darcy Reynold's number, which is expressed in Equation 2.11. The impact of slicing on the NTU_s values is illustrated in Figure 7.11. The sliced samples had lower NTU_s values compared with the original samples. This is most likely due to the impact of the material loss during the slicing operation, reduction in the heat transfer surface area, and the influence of thermal conductivity reduction.

154
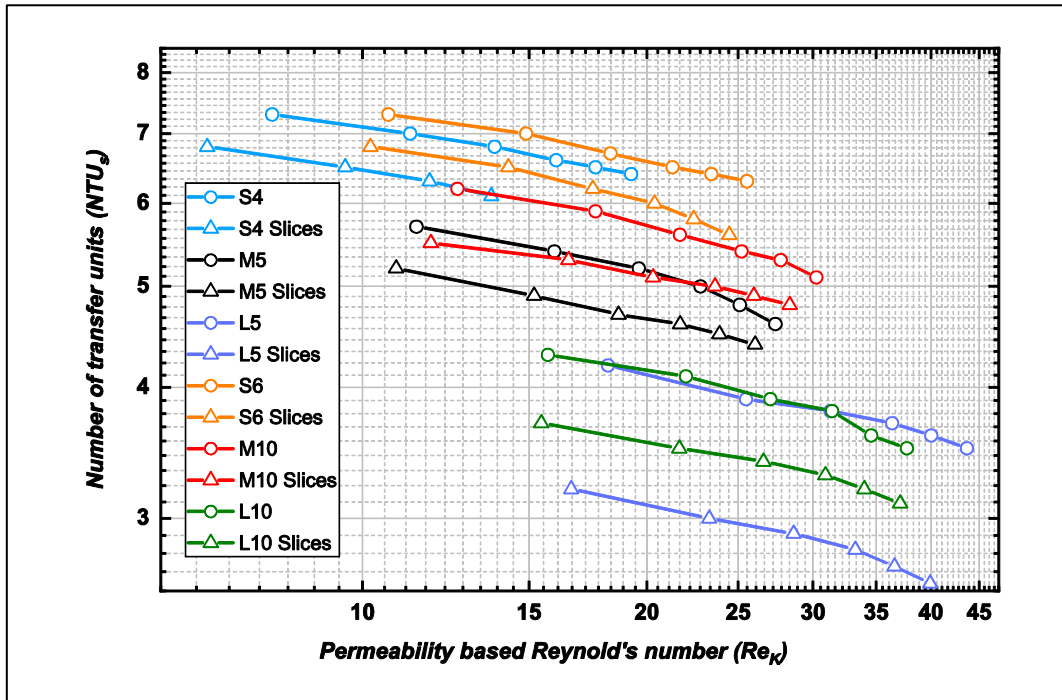
Figure 7.11 Effect of thermal conductivity on NTU_s for the samples.

The values of NTU_s for the sliced samples are plotted with the NTU_s values of the wire mesh screens sample against Darcy permeability, based on Reynold's number in Figure 7.12.
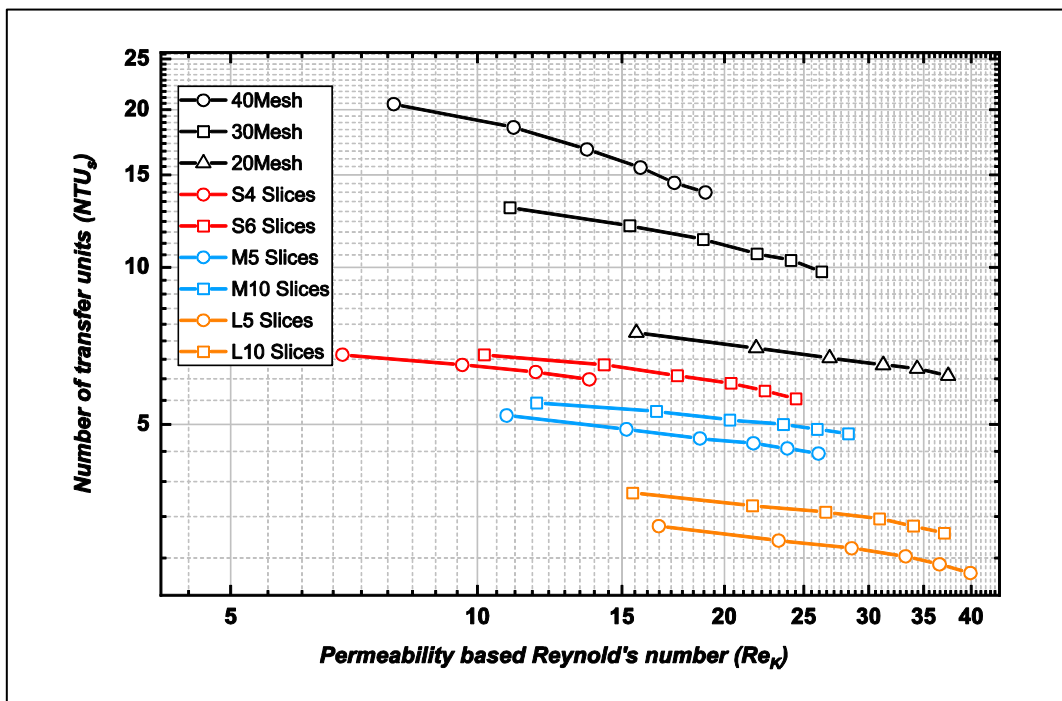
Figure 7.12 Comparison between NTU_s values of wire meshes and metal foam.

155

As can be noticed, the wire mesh screens samples have a higher NTU_s values than all the metal foam samples. Since the wire mesh samples have a slightly lower heat transfer surface area than the foam samples, the increase in the NTU_s values are more likely due to the increase in the heat transfer coefficients. Figure 7.12 indicates that the number of transfer units in both classes of media decreases inversely with the Darcy based Reynold's number. Considering only one class of media (mesh screens or foams), a decrease in either porosity or pore size leads to an increase in the solid phase or the heat transfer surface area. Consequently, the NTU_s value increases [36][159].

Metallic foam samples are made of the same materials and have almost the same porosities. The smallest average pore size samples have higher values of NTU_s than those of the medium and large. This increase is most likely due to the increase either in the heat transfer surface area or the heat transfer coefficient. The same trend has been noticed in the wire mesh screen samples. The 40Mesh sample showed the highest NTU_s value, while the 20Mesh sample has the closest NTU_s value to the metal foam samples. However the variation in NTU_s value in the mesh samples is not only due to the pore size difference but also the porosity difference.

The impact of heterogeneity on the NTU_s is shown in Figures 7.13 to 7.18. Each graph shows NTU_s values of several hybrid media made of one size of mesh layers and the sliced metal foams. The NTU_s values of pure wire mesh regenerators are presented in black while the NTU_s values for the pure aluminium foams are presented as a group in red. Heterogeneous regenerators were plotted based on slicing; one slice or two slices. The one-slice samples are indicated in green, whereas the two-slice structures are in blue.
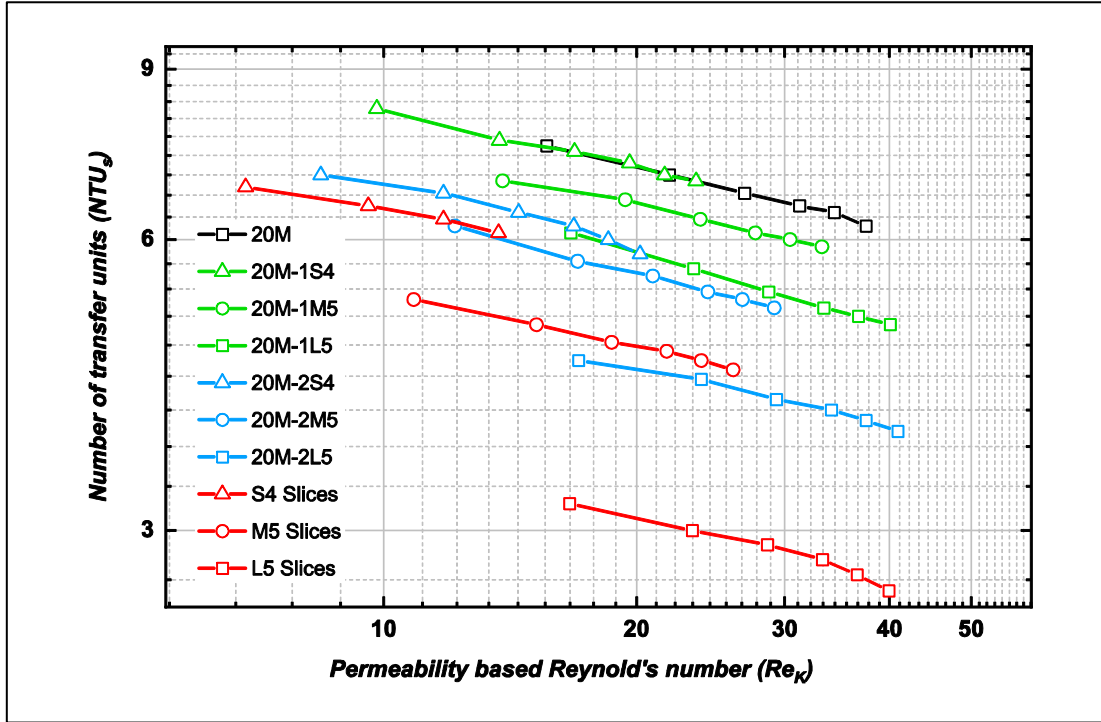
Figure 7.13 NTU_s variation vs Reynold's number based permeability (Crushed foam with 20Mesh).
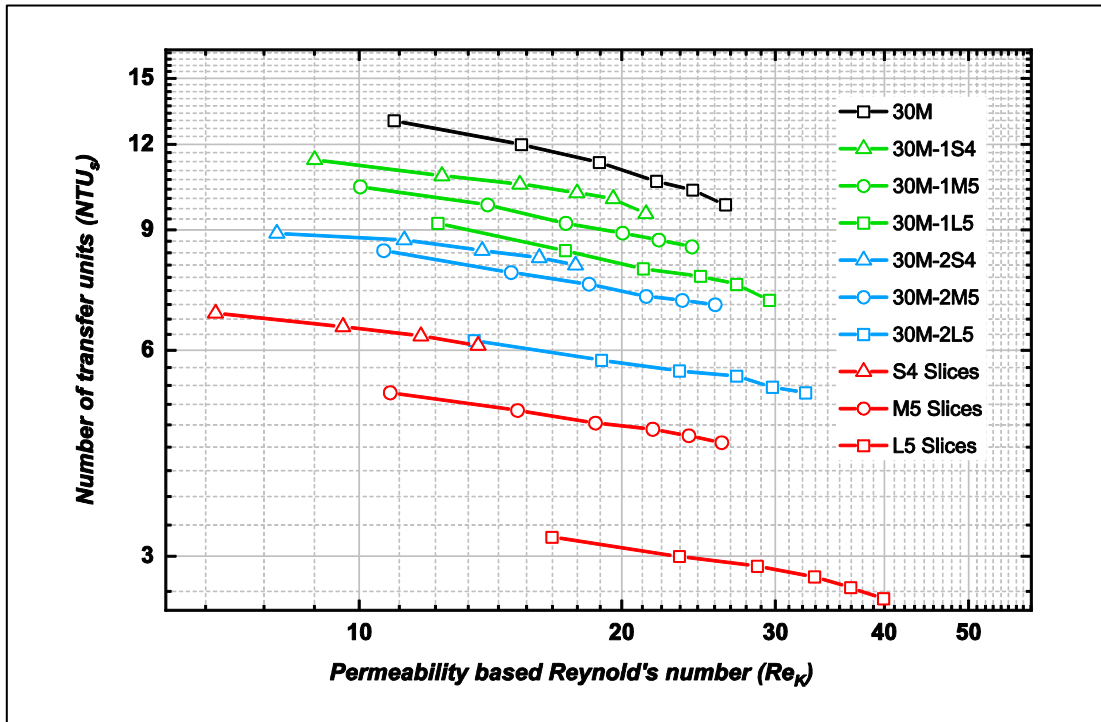
Figure 7.14 NTU_s variation vs Reynold's number based permeability (Crushed foam with 30Mesh).
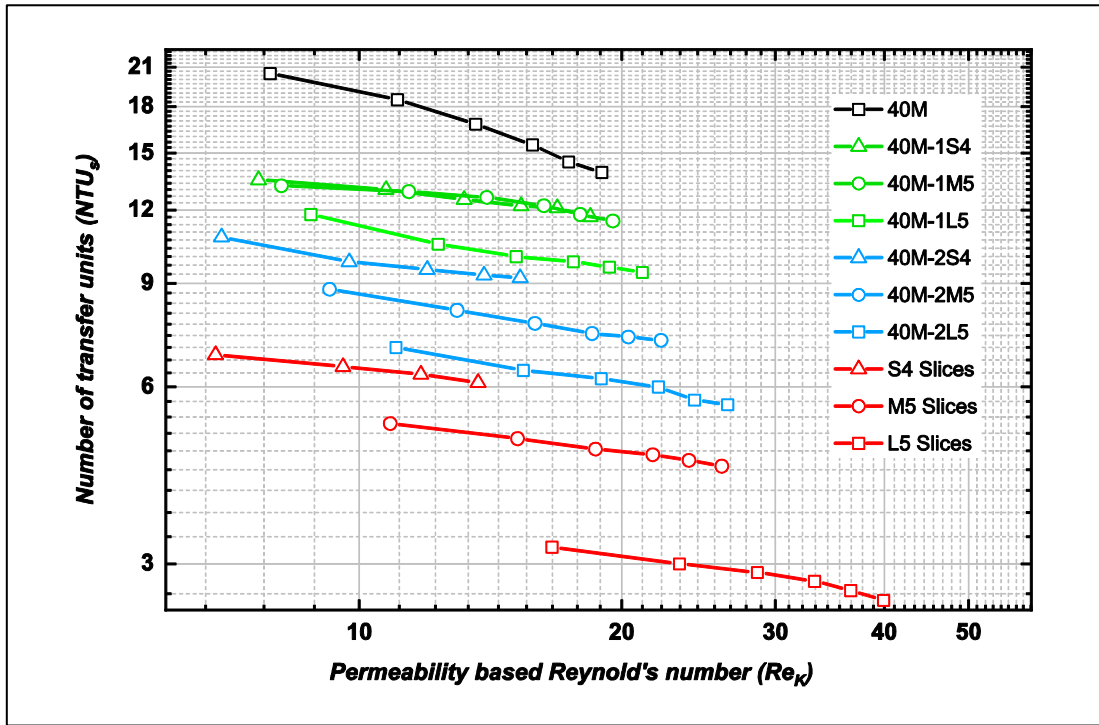
Figure 7.15 NTU_s variation vs Reynold's number based permeability (Crushed foam with 40Mesh).
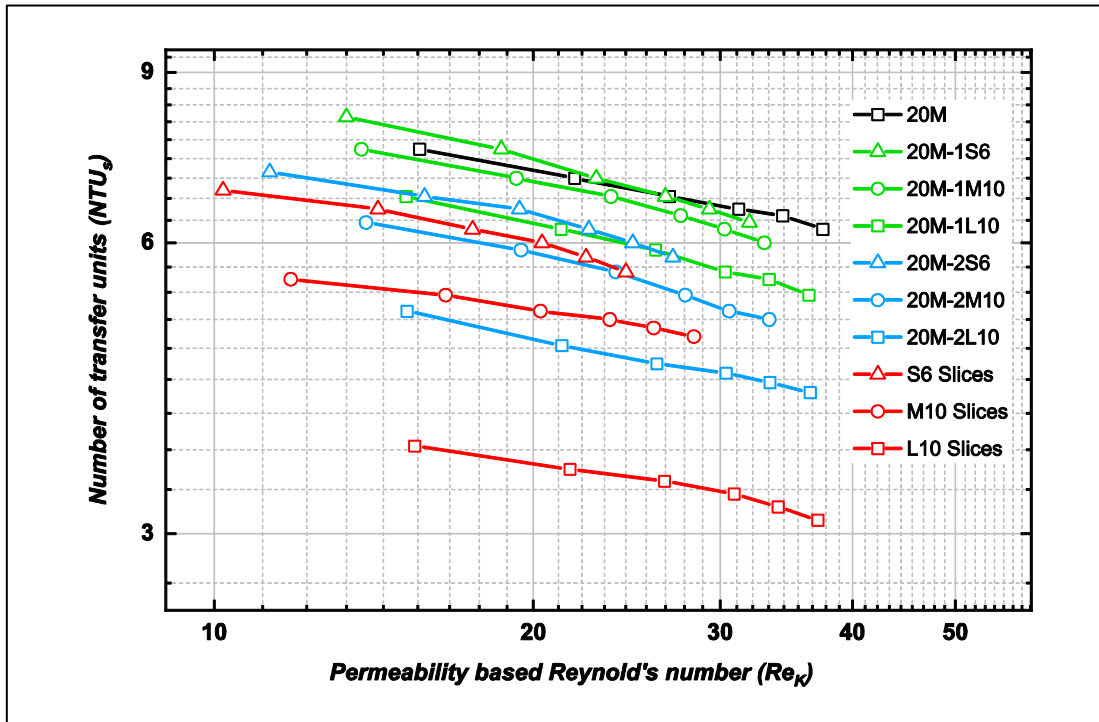
Figure 7.16 NTU_s variation vs Reynold's number based permeability (Spherical foam with 20Mesh).
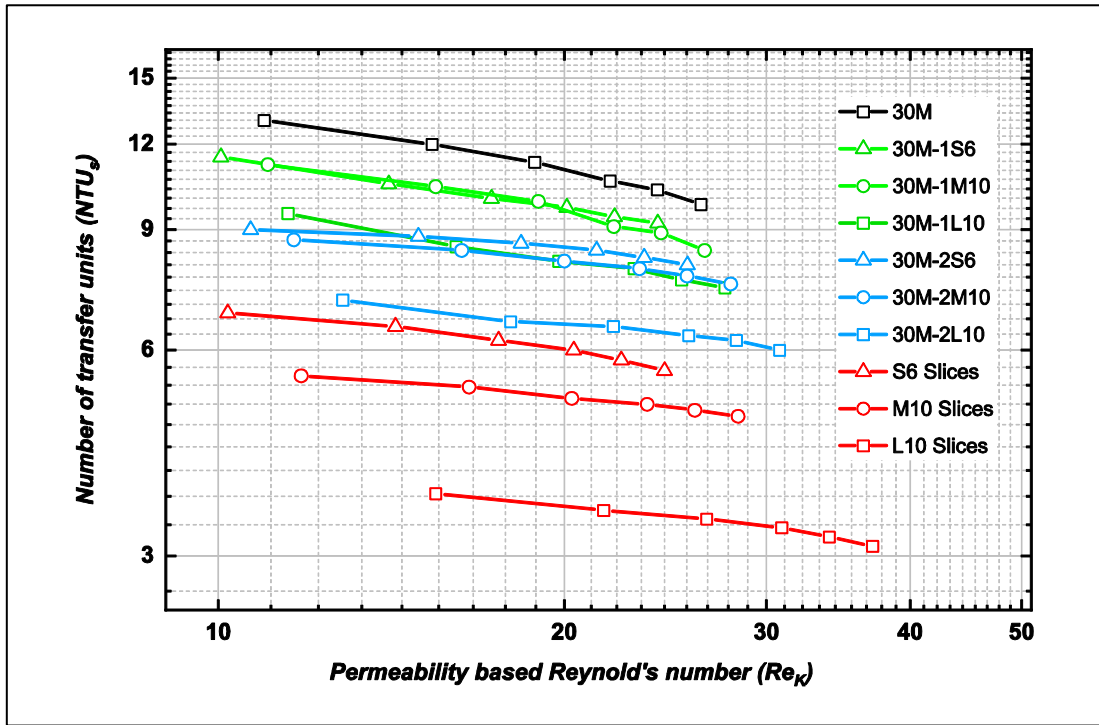
Figure 7.17 NTU_s variation vs Reynold's number based permeability (Spherical foam with 30Mesh).
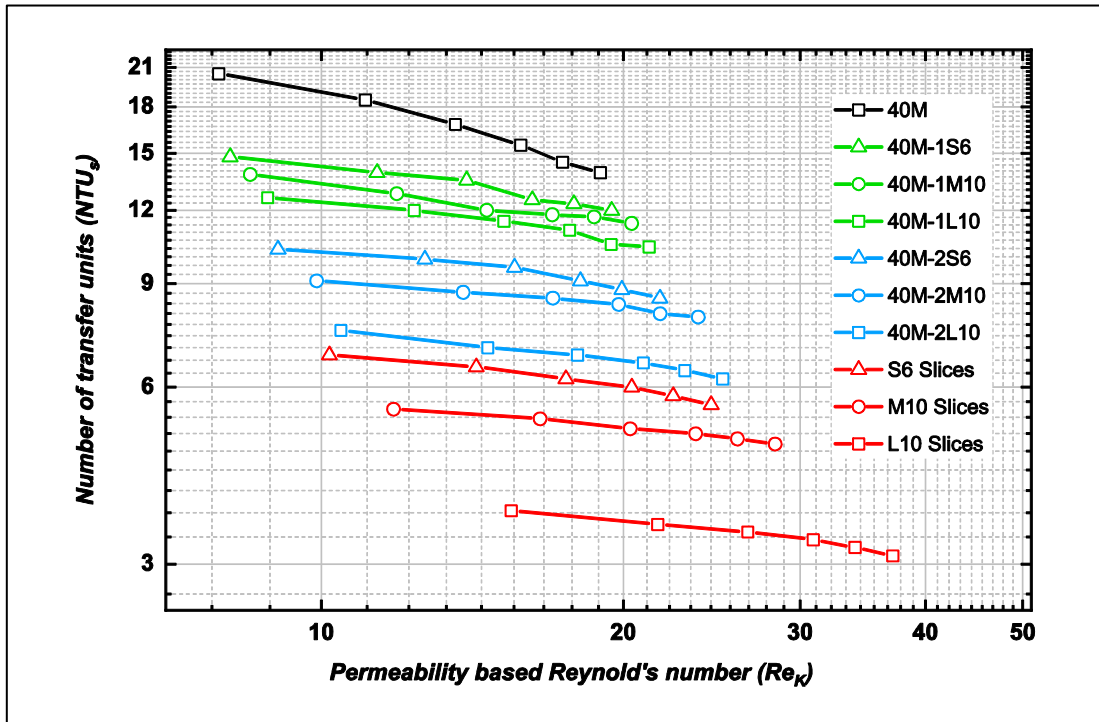
Figure 7.18 NTU_s variation vs Reynold's number based permeability (Spherical foam with 40Mesh).

159

The NTU_s values of the heterogeneous regenerators depend upon the contribution of mesh and foam in their structures. Hybrid samples assembled using fine wire mesh screens and small pore size aluminium layers have larger NTU_s values. This may be due to the increase in the heat transfer area. However, increasing pore density provokes pressure drops and increases flow resistance across the porous matrices. Seen in Figure 7.19, has been generated to discern and summarise the difference between the tested regenerators in terms of the number of the transfer units NTU_s at zero Reynold's number and the Darcy permeability.

The values of NTU_s at zero Reynold's number were obtained from applying linear regression fitting to the plotted data in Figures 7.13 to 7.18. The black group in the graph represents the zero number NTU_s values versus the Darcy permeability of wire mesh screens and metal foam samples, while the zero number NTU_s values against Darcy permeability of the heterogeneous regenerators are shown based on the number of slices (one slice in blue and two slices in red).
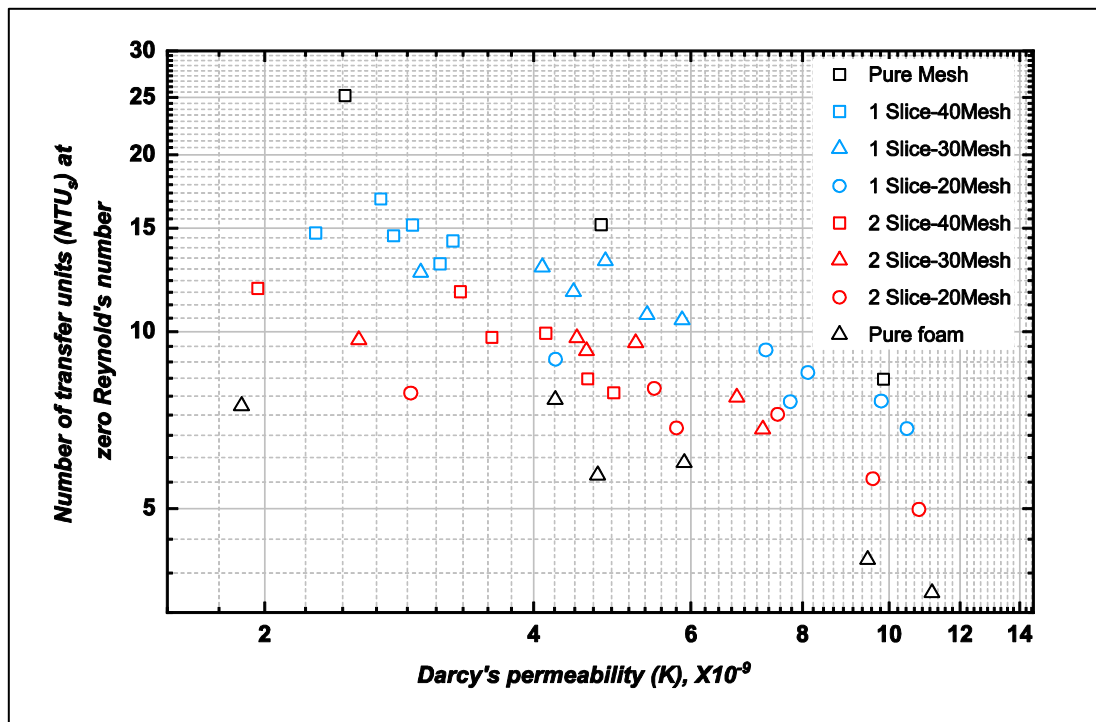
Figure 7.19 NTU_s variation vs Reynold's number based permeability.

The results show that change in the combination of mesh screens and foam layers results in a new structure with a different NTU_s value and Darcy permeability. This means it possible to obtain a similar NTU_s value with the same flow resistance

160

from several combinations of metal foam layers foam and mesh screens. For high performance in heat regenerating, the heat storage material should have a large value of NTU_s and minimal resistance to the flow [231]. As can be seen, fine wire meshes could provide a large NTU_s value, but they are much heavier than metal foams. Metal foams are much lighter but they provide lower thermal performance. It is worth noting that the change of material types in hybrid regenerators results in changes in the heat transfer surface areas A_{HT}, as well as the volumetric heat transfer coefficients h_v.

7.7 Volumetric heat transfer coefficient

The volumetric heat transfer coefficient has also been computed in this work to assess the thermal performance of the tested regenerators. This parameter has been frequently quoted in the literature for the thermal performance of regenerators, especially when measuring the specific area of porous materials is difficult [166]. It was computed using the following definition:

$$h_v = \frac{NTU_s \dot{m}_f c_p}{V_s}$$

7.8

Where NTU_s is the number of transfer units, $\dot{m}_f c_p$ is the heat capacity of air and V_s is the average volume of the regenerator. The literature review showed that the volumetric heat transfer coefficient depends on the pore diameter and the effective porosity of the matrices [7][137][147]. Decreasing the pore size of metallic foam led to an increase in the heat transfer coefficient [38][147][166]. The thermal performance of wire meshes was found to increase with a decrease in the pore size [36][137][157]. For metal foams, decreasing the pore size or the porosity was shown to result in an increase in the heat transfer surface area and the interstitial velocity. Subsequently, the convective heat transfer coefficient and the volumetric heat transfer coefficients were observed to increase [69][147][161]. The volumetric heat transfer coefficients of the semi-homogeneous regenerators are illustrated in Figure 7.20. The effect of the pore size on the volumetric heat transfer can be seen clearly in both the wire mesh samples and metal foam groups.
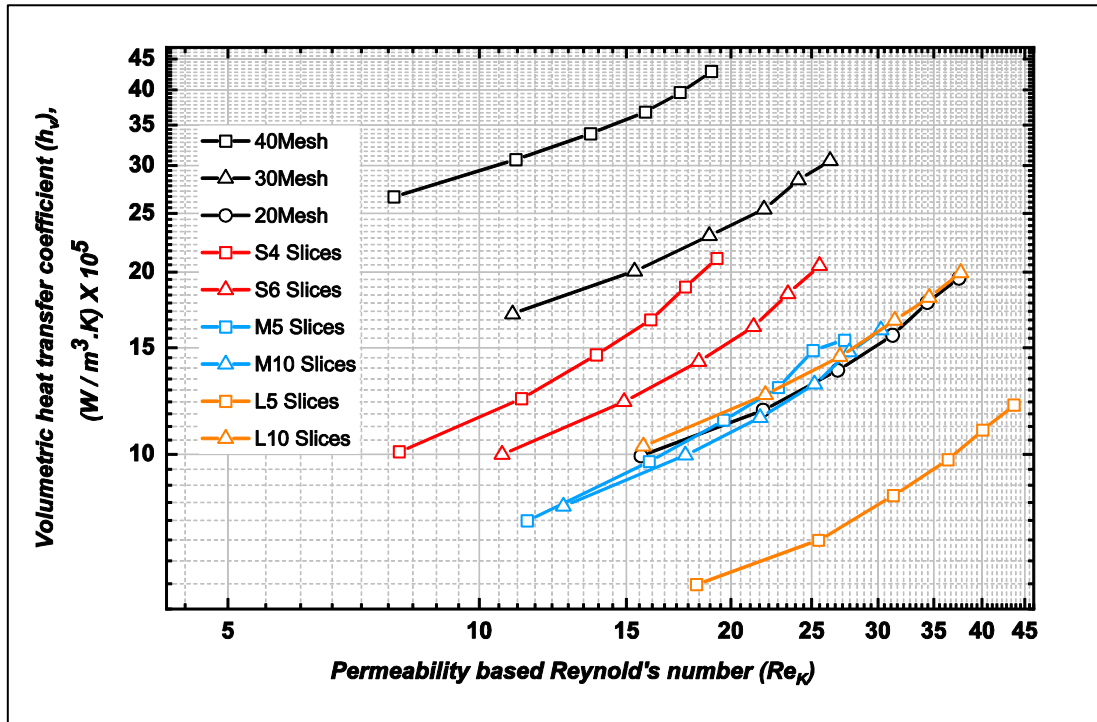
Figure 7.20 Volumetric heat transfer coefficient vs Reynold's number based permeability (Semi-homogeneous samples).

When the number of pores was halved in both classes of porous media, the volumetric heat transfer coefficients were 2 to 3 times higher at the same Reynold's number. Each group of materials (spherical foams, crushed foams, and mesh screen packed beds) has a relatively similar porosity. Hence, the increase of the heat transfer coefficients is more likely due to the increase in the heat transfer surface area that is associated with the change in the density of the pores.

Figures 7.21 to 7.26 illustrate the volumetric heat transfer coefficients for the heterogeneous regenerators. As can be seen, the volumetric heat transfer coefficient is predominantly governed by the contribution of wire meshes and foams in structures. As was demonstrated in Sections 5.3 and 5.4, changing the proportion of materials used in a heterogeneous structure results in a change in both the porosity and the heat transfer surface area. It has been shown that replacing one-third or two-thirds of the volume of the mesh screen packed beds with metal foams leads to a decrease in both the porosity and the heat transfer surface area of the heterogeneous structure. The change of the heat transfer surface area is determined by the pore sizes of materials utilised to build the heterogeneous structure.
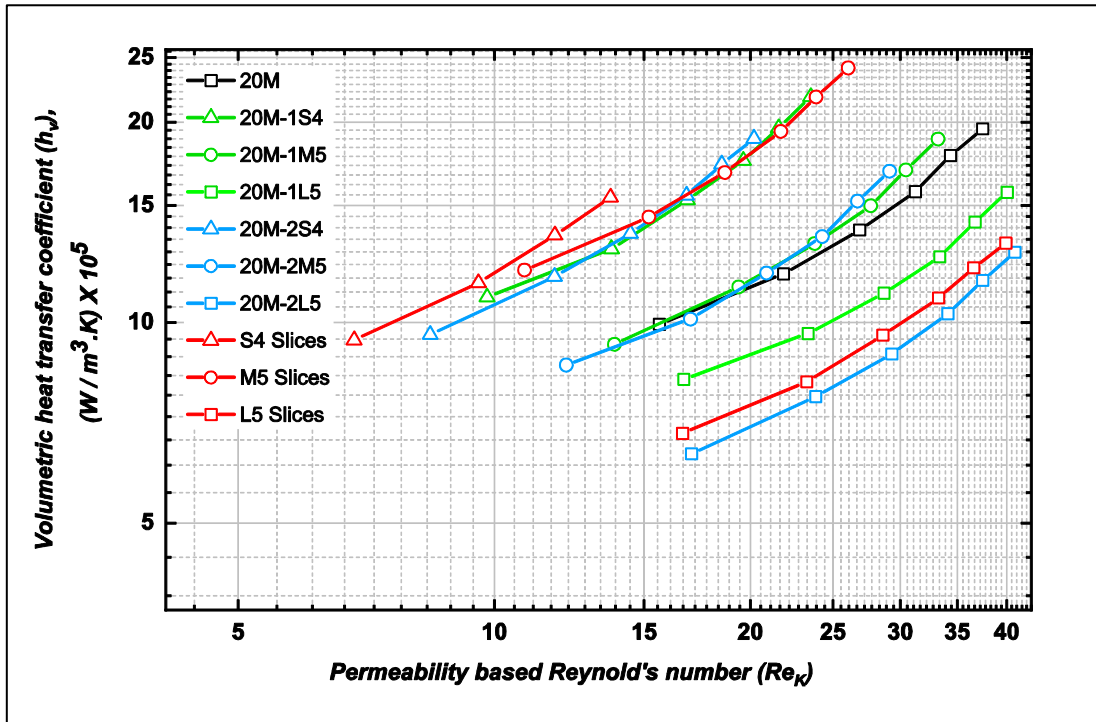
Figure 7.21 Volumetric heat transfer coefficient vs Reynold's number based permeability (Crushed foam with 20Mesh).
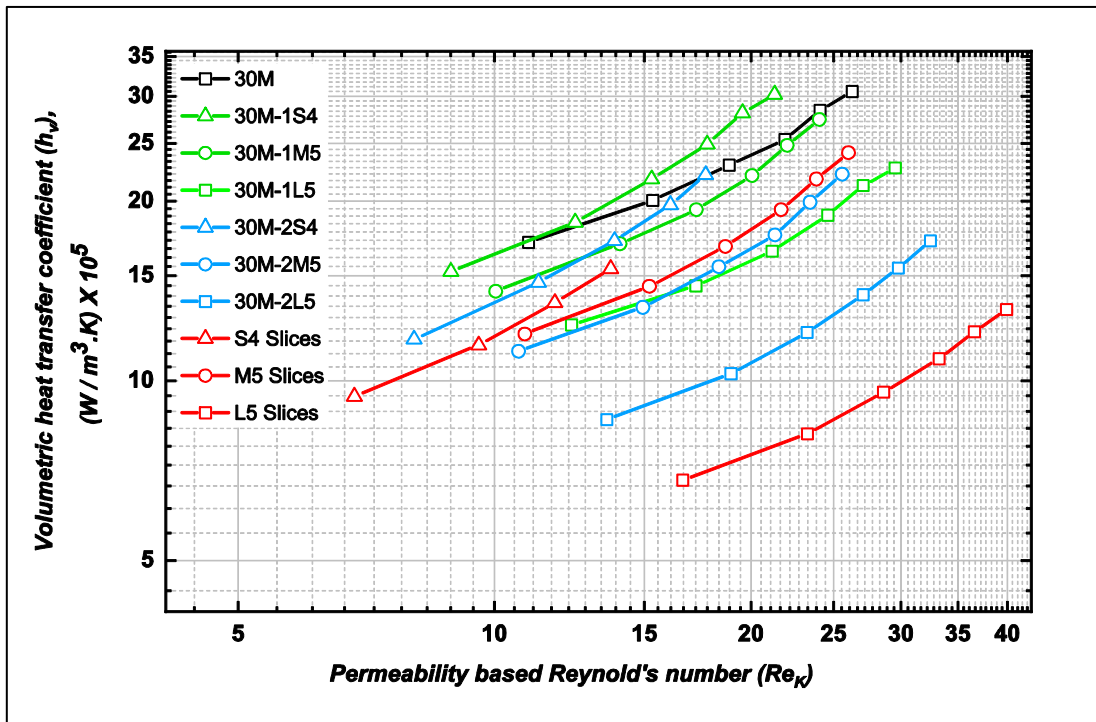
Figure 7.22 Volumetric heat transfer coefficient vs Reynold's number based permeability (Crushed foam with 30Mesh).
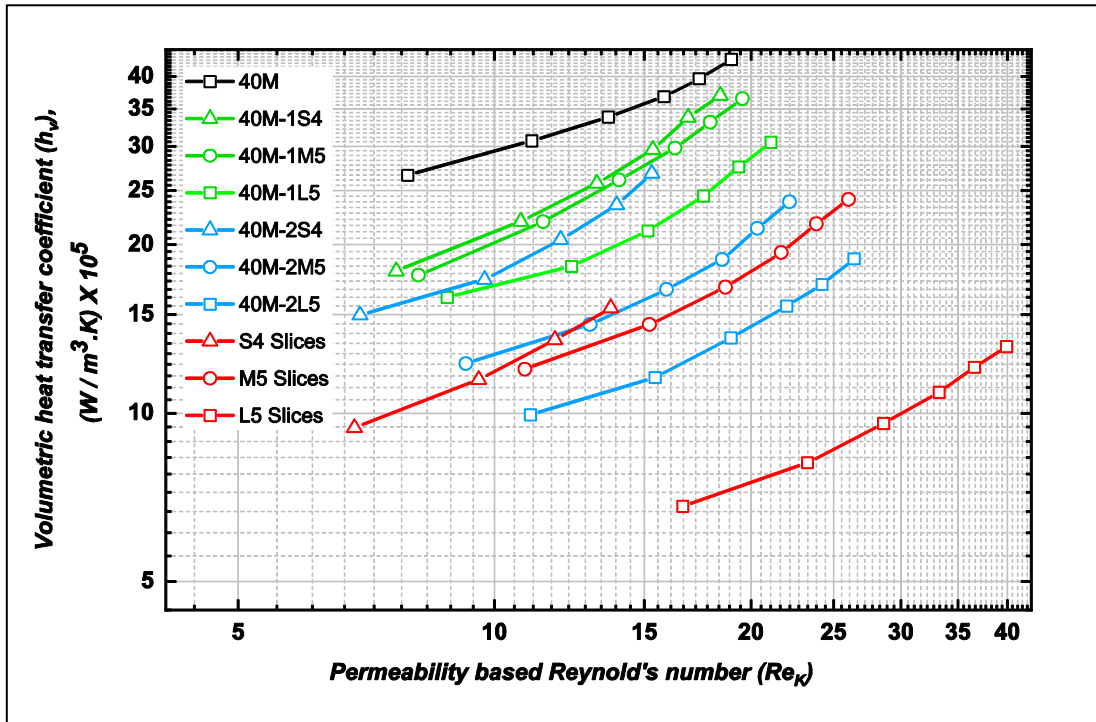
Figure 7.23 Volumetric heat transfer coefficient vs Reynold's number based permeability (Crushed foam with 40Mesh).
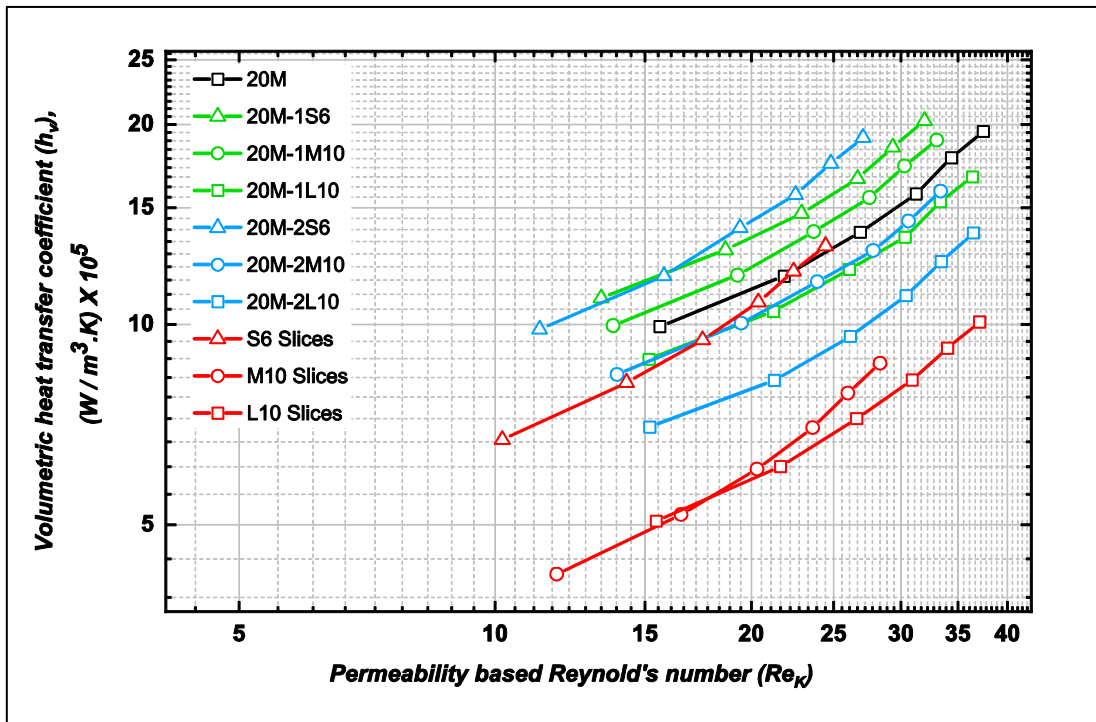
Figure 7.24 Volumetric heat transfer coefficient vs Reynold's number based permeability (Spherical foam with 20Mesh).

164
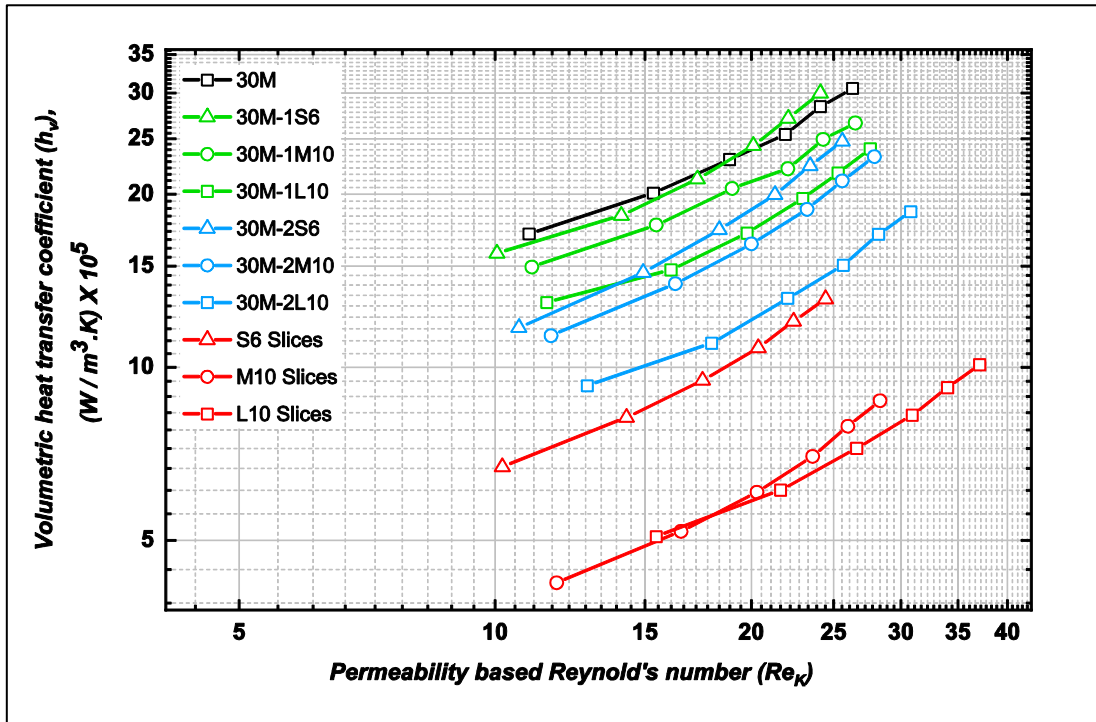
Figure 7.25 Volumetric heat transfer coefficient vs Reynold's number based permeability (Spherical foam with 30Mesh).
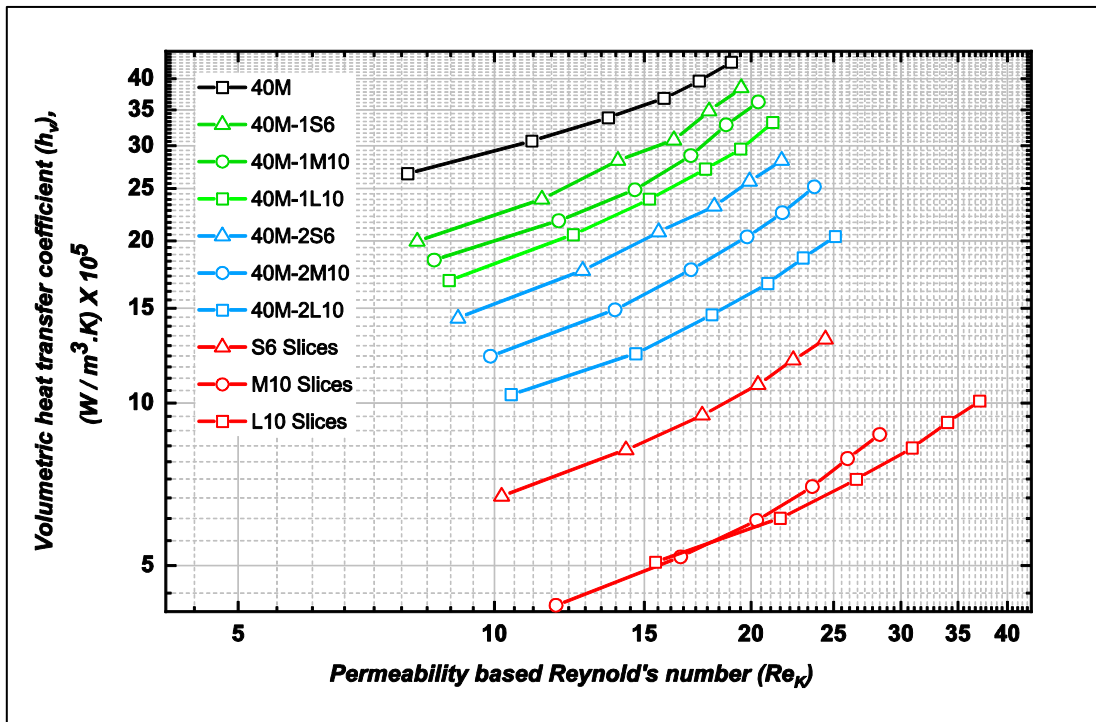
Figure 7.26 Volumetric heat transfer coefficient vs Reynold's number based permeability (Spherical foam with 40Mesh).

The general trend observed in the present study is that the volumetric heat transfer coefficient in wire meshes increases when a part of the mesh structure is replaced by metal foams. At constant volume, reducing the wire mesh contribution or increasing the metal foam contribution results in a further decrease in the volumetric heat transfer. This was not the scenario when a part of the 20Mesh sample was replaced with foam layers. Unclear behaviour was noticed when the 20Mesh screens were replaced with different types of metal foam. It can also be noticed from the figures that decreasing the pore size of wire mesh or the metal foam layers provides additional resistance which describes the reduction of the permeability based on Reynold's number.

The volumetric heat transfer coefficients between open metallic cellular materials and air have been measured by many investigators. Younis et al. [7] examined samples of ceramic foams with pore sizes ranging from 0.83mm to 2.5mm and porosity between 0.83 and 0.87. They found that at fixed porosity the h_v increases with an increase in PPI. Similar behaviour was observed in Vijya et al.'s [87] results. Hwang et al. [69] and Vijay et al. [87] investigated the impact of pore diameter on the h_v. They showed that the pore diameter effect is more predominant than the porosity effect on the convective heat transfer [87]. The effect of porosity and pore size on the wire mesh can be noticed from the tested samples by Hamaguchi et al. [140]. Figure 7.27 presents a comparison between the present work results and those obtained from the open literature for different tested macrostructure porous media. This figure shows that there is good agreement between the volumetric heat transfer coefficients h_v obtained from the present work and those for open metallic porous media reported in the literature. It can be seen that the metal foam samples show similar h_v values as those published by Younis et al. [7]. A satisfactory validation can be observed between the current mesh packed bed results in this study and those published by Hamaguchi et al. [140].
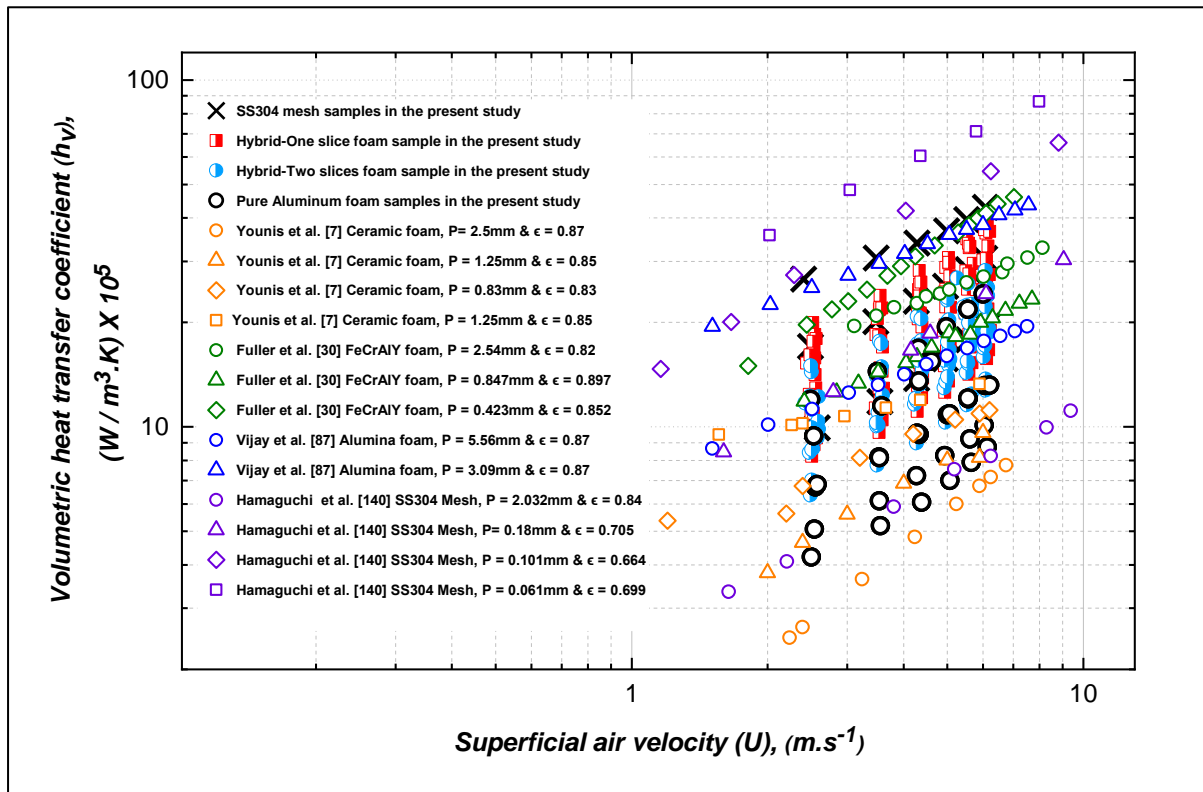
Figure 7.27 Volumetric heat transfer coefficient versus frontal velocity.

Due to the shortage of data available for comparison with the heterogeneous porous media, the experimental results were compared with those predicted for semi-homogenous structures. By comparing the results with the available experimental data, it was found that the results are in the same range of data published by Fuller et al. [30] for sintered FeCrAlY foams. The tested samples were subjected to forced air convection whilst steady-state measurements were taken. The samples had hollow cell struts, cell sizes ranged from 1-3 mm and porosity between 0.875-0.954. As a part of the study, the results for FeCrA1Y foam were compared with those for copper foam with a similar range of pore sizes but which were tested under the transient technique. A contradiction in the results due to transverse temperature distribution across the sample or across the material itself was reported. Fuller et al [30] concluded that the heat transfer coefficient in the FeCrAlY foam is mainly governed by the porosity, but in the copper, it is governed by both the porosity and the pore size. They recommended that extra care must be taken when comparing for predictive purposes. They expressed that a discrepancy may arise due to the material type, the thermal conductivity or the measurement method.

7.8 Volumetric Nusselt number

The volumetric convective heat transfer coefficient is usually presented in non-dimensional form as a volumetric Nusselt number [18][166][69][164]. Also, the volumetric Nusselt number is often presented as a function of Reynold's number [7][13] [18][153] or Reynold's and Prandtl numbers [5][161][175] for the comparison of volumetric Nusselt numbers. However, as has been discussed in the prior chapters, one of the main problems of porous media is the absence of a general characteristic length that can be used to identify the dimensionless constants, such as the friction factor, Reynold's number and Nusselt number. However, Darcy permeability has been expressed as a useful parameter for the characterisation of foam in porous media. It has been cited as the characteristic length by many researchers [66][78][94][101][102][111][161]. In the current study, the findings showed that Darcy's law can accurately describe the hydraulic gradient against the frontal air velocity in the viscous regime for all media tested. To simplify the comparison between the findings, the square root of Darcy permeability was used to identify the Reynold's and Nusselt numbers. Moreover, the optimal structure was determined graphically from the volumetric Nusselt /Reynold's number graphs. The Reynold's number was calculated using Equation 2.10, whereas the Nusselt number was obtained from the following expression:

$$Nu_v = \frac{h_v}{K_f} \sqrt{K}$$

7.9

Where $\sqrt{K}$ is the Darcy permeability, h_v is the volumetric heat transfer coefficient and K_f is the effective thermal conductivity of the fluid, which is air in this study. The results for the semi-homogenous samples are shown in Figure 7.28. Although metallic porous media with low porosity and small pore size are preferred for achieving high thermal performance, they cause a remarkable increase in flow resistance. To understand the comparison clearly, we should keep in mind that both the Reynold's and Nusselt numbers are functions in the square root of Darcy permeability. In addition, the measurements were taken under a similar flow rate. Subsequently, an increase in the permeability leads to a right shift in the measured data on the "X" axis (increase in Reynold's number). Additionally, increasing the

permeability or the volumetric heat transfer coefficient would cause an upside shift in the measured data (upside shift on the "Y" axis means an increase in the volumetric Nusselt number and vice versa).
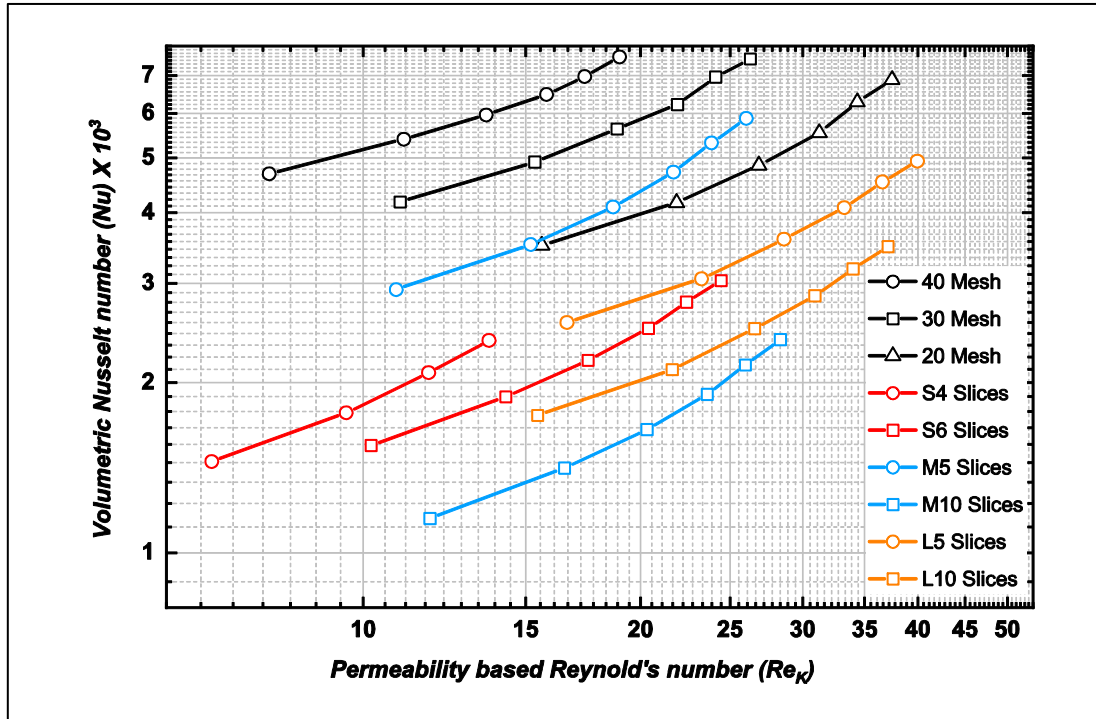
Figure 7.28 Volumetric Nusselt number vs Reynold's number based Permeability (semi-homogeneous samples).

It is clear from the graph that the wire mesh samples have higher Nusselt numbers at any given Reynold's number compared with the metal foam samples. The three samples provide almost the same Nusselt numbers but with different flow resistances represented by the change in Reynold's numbers. The increase in the thermal performance of the wire mesh samples compared with metal foams might be due to the difference in the interaction between the local structure of the media and the fluid passing through them. In general, the results showed that decreasing the mesh size or porosity led to a decrease in the Darcy permeability indicating higher flow resistance. Amongst the metal foam samples, the M5 sample showed the highest thermal performance, but a higher resistance compared with the large pore foam samples. The large pore foam samples present similar flow resistance as that generated by the 20mesh sample. However, their thermal performance is lower than the 20Mesh sample, in particular the L10 sliced sample. Figures 7.29 to 7.34 present the volumetric Nusselt number for the heterogeneous structures.
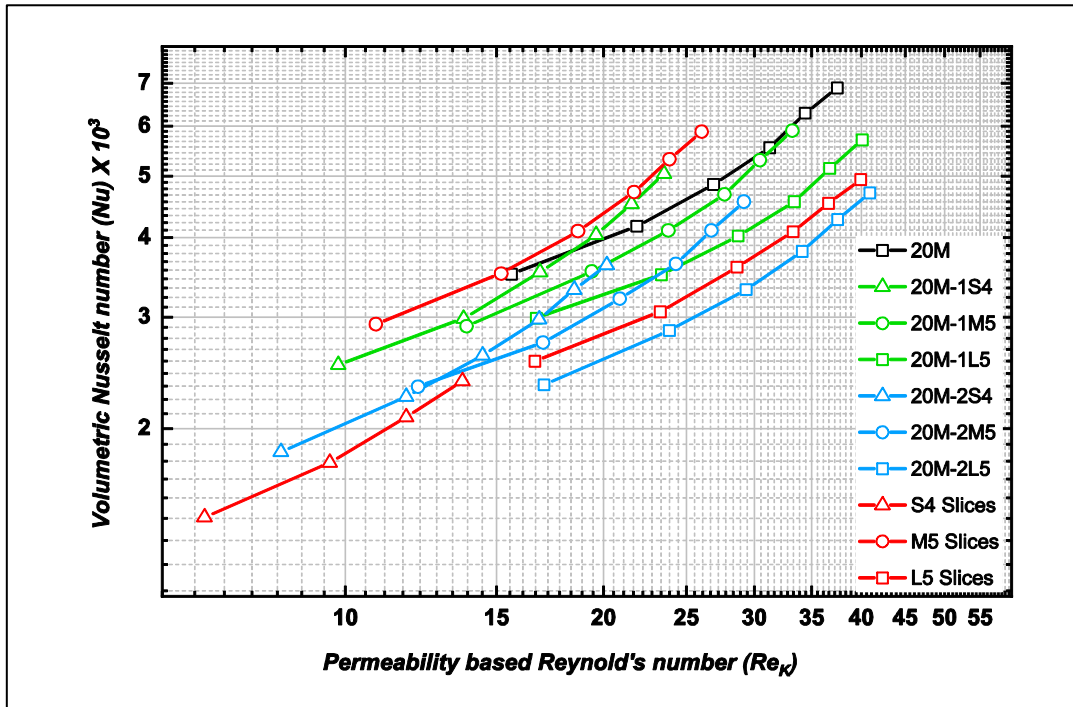
Figure 7.29 Volumetric Nusselt number vs Reynold's number based Permeability (Crushed foam with 20Mesh).
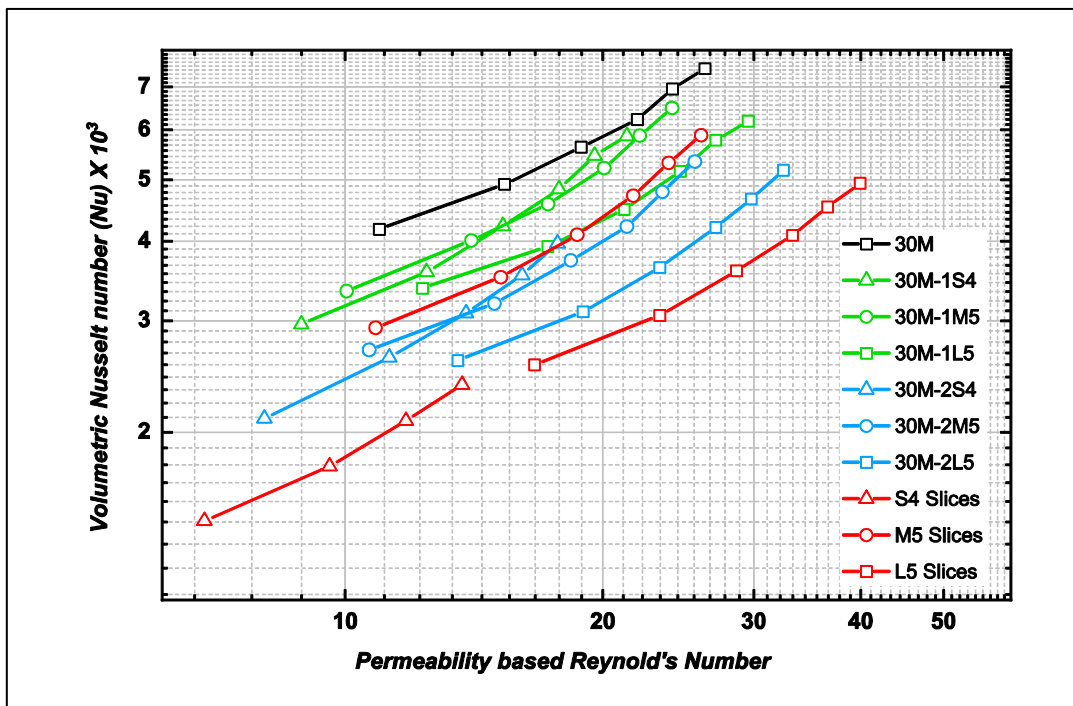
Figure 7.30 Volumetric Nusselt number vs Reynold's number based permeability (Crushed foam with 30Mesh).

170
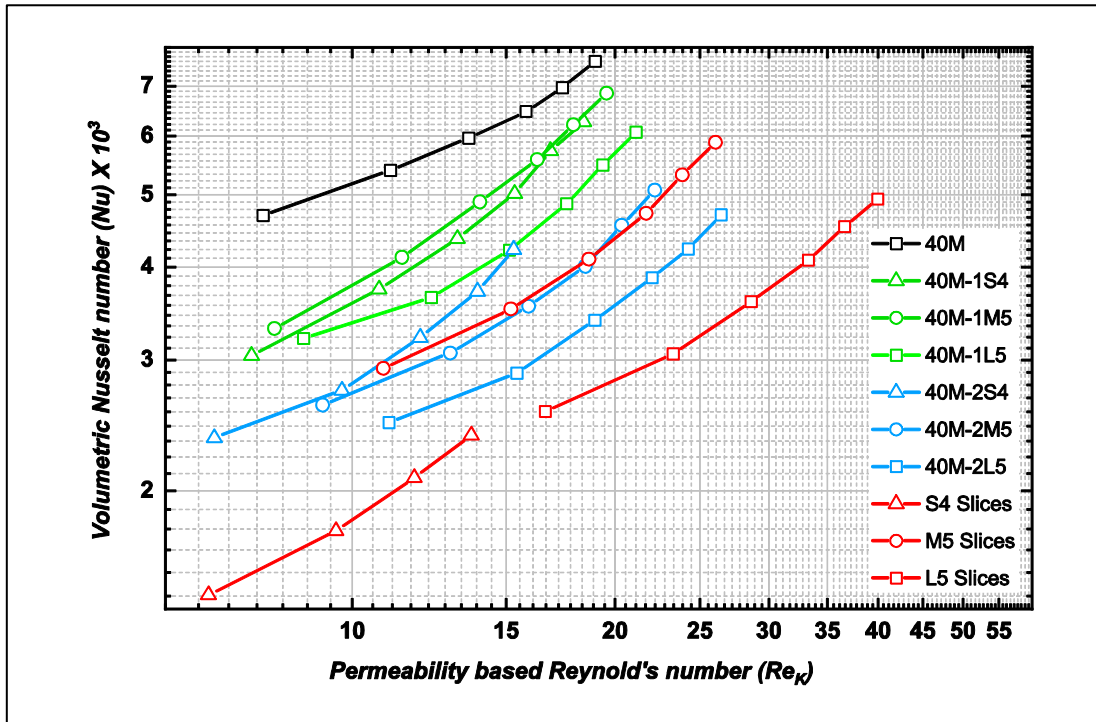
Figure 7.31 Volumetric Nusselt number vs Reynold's number based permeability (Crushed foam with 40Mesh).
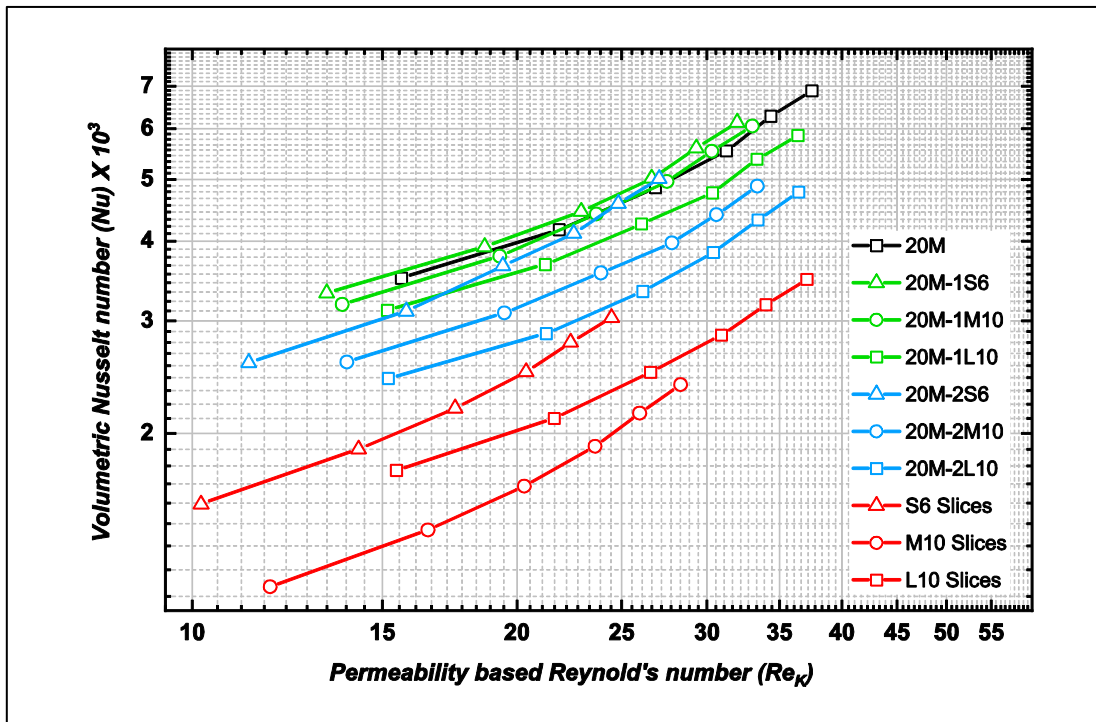
Figure 7.32 Volumetric Nusselt number vs Reynold's number based permeability (Spherical foam with 20Mesh).

171
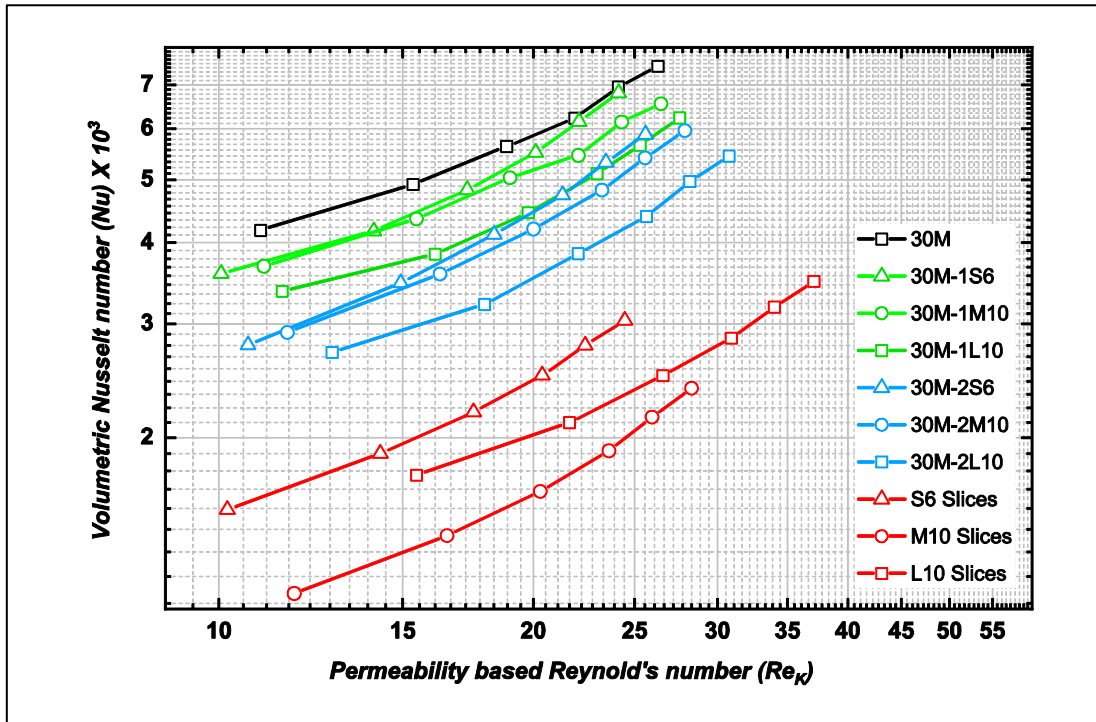
Figure 7.33 Volumetric Nusselt number vs Reynold's number based permeability (Spherical foam with 30Mesh).
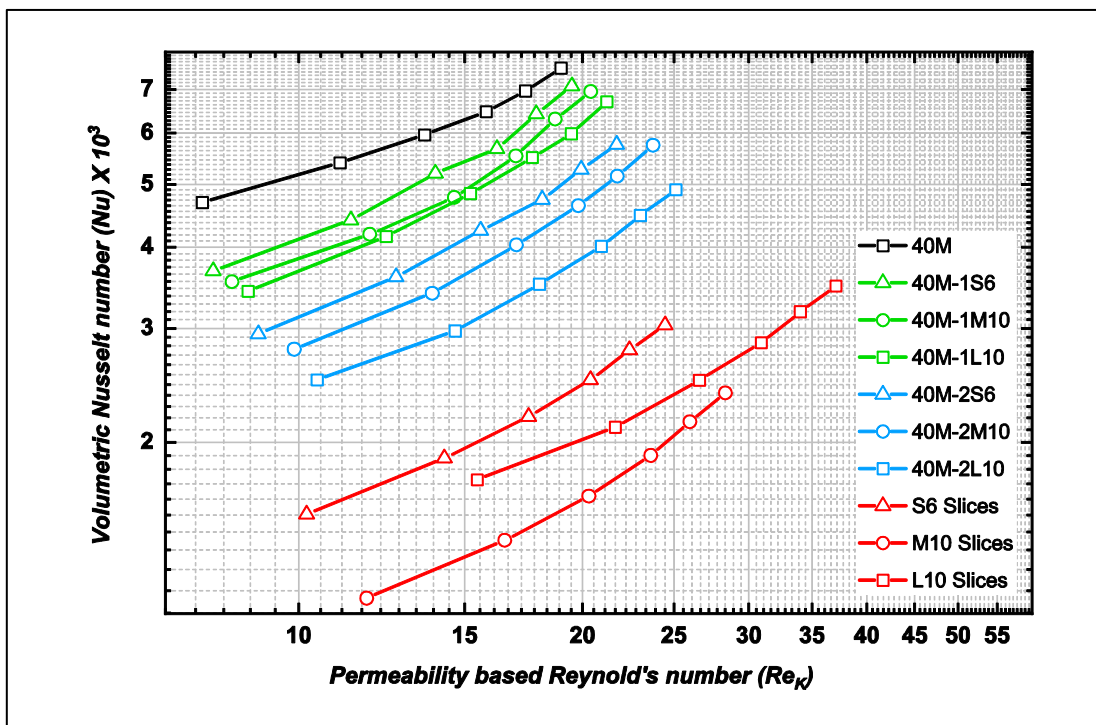
**Figure 7.34 Volumetric Nusselt number vs Reynold's number based permeability (Spherical foam with 40Mesh).**

It appears from the graphs that the combination between the metal foams layers leads to enhancement in the thermal performance of the metal foam samples. This enhancement is governed by the contribution of the original materials in heterogeneous structures. For ideal performance, the regenerator results should be located in the upper right-hand corner of the graphs, which indicates a high volumetric Nusselt number and high Reynold's number due to an increase in Darcy permeability. The heterogeneous structure results show that replacing the foam layers with the mesh screens leads to improvement in the thermal performance of the heterogeneous structure. The improvement increases with the number of mesh layers and the reduction of the mesh size.

Looking at the change in the heat transfer surface area with structure in Figures 5.7 and 5.8, one can observe that, at constant volume, replacing one-third of the wire mesh screen structures with metal foam layers decreases both the porosity and the heat transfer surface area. Decreasing the porosity results in lower permeability and high flow resistance. On the other hand, reducing the heat transfer surface area leads to lower thermal performance. However, by looking at Figure 5.8, it can be noticed that the difference in the heat transfer surface area between the tested samples is insignificant. Therefore, the variation in the thermal parameters must be attributed to some other factors linked to the difference in the cell morphology.

The hydrothermal performance of the heterogeneous porous structure has been characterised based on the flow resistance in the weak laminar flow in which the inertia forces impact has not been counted. In real-life applications, inertia loss should be considered especially at significant flow rates. The results revealed that the inertia coefficients of wire mesh screen samples are much lower than those of the metal foam samples. Therefore, the hydrothermal performance of the wire mesh samples can be considered much better than the metal foams in this study. Nevertheless, there is a remarkable difference between the hydrothermal performance of the wire mesh samples. It has been noticed that the thermal performance of the wire mesh screens increases with a decrease in the mesh size; however, the flow resistance increases.

Figure 7.35 illustrates the hydrothermal performance for the tested samples at relatively high velocity (5 m. s^{-1}). Notice that the wire mesh screens samples provide a similar thermal performance or higher than the metal foam samples. The thermal

performance of the wire mesh screens samples increases linearly with the reduction of pore size, however, the penalty is an increase in the required pumping power. Metal foam samples show thermal performance in the order of that in 20Mesh sample but with high flow resistance. The hydrothermal performance of the heterogeneous samples tends to vary linearly with structure type. Considering the samples' weight, thermal performance, and pressure loss, the 20Mesh sample offered good thermal performance for an acceptable flow-friction power compared with the other two wire mesh samples. Moreover, it is 20% lighter than the other two candidates, which makes it the optimal structure among the tested samples in the current study.
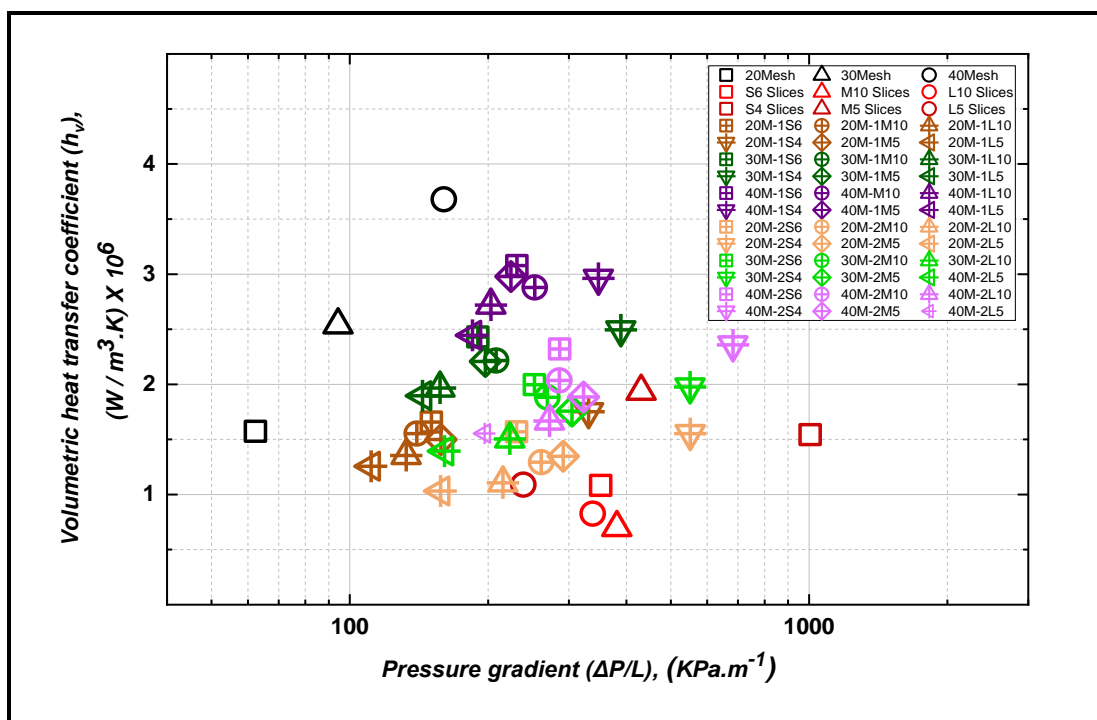
Figure 7.35 Volumetric heat transfer coefficient vs pressure gradient.

Luna [36] performed experiments on a previous version of the experimental rigs described here. He did measurements on a number of different types of porous media including mesh, felts, replicated porous metal foams. In order to compare the performance of this diverse range of materials, he characterised the thermal performance of the porous media using the Stanton number, Colburn (j) factor and Reynolds number. The Stanton number is a dimensionless number that indicates the ratio of heat transferred to a fluid relative to the thermal capacity of the fluid [23][113].

$$St = \frac{h}{\rho u c_p}$$ 7.10

It can also be written in terms of other dimensionless groups [232] as:

$$St = \frac{Nu}{RePr}$$ 7.11

The corresponding Colburn factor (j) which characterizes the heat transfer performance can be calculated from the Stanton number using the following expression [156][232].

$$j = St * Pr^{\frac{2}{3}}$$ 7.12

with the Prandtl number, Pr and the Reynolds number Re, (based on the channel diameter). However, neither the $NTUs\ vs\ Re$ nor $j\ vs\ Re$ representations gave a single relationship for all the tested samples.

In convective heat transfer applications, the loss associated with the desired heat transfer is pressure drop. Here the pressure drop was characterised in terms of the permeability based friction factor, see (Equation 2.13). The Friction factor varied with velocity however it achieved a constant value in the Forcheimer regime where the heat transfer measurements were predominantly performed.

The plot of the Colburn and against friction coefficient is shown in Figure 7.36. The friction factor spans from 0.1 (low-pressure drop) to 1.1 (highest pressure drop) so roughly varies by an order of magnitude. The Colburn factor is plotted on the y axis varies from 100 (lowest heat transfer) to 600 (highest heat transfer). The four types of samples tested can seem to be grouped together but span a range of both friction coefficient and Colburn factor.
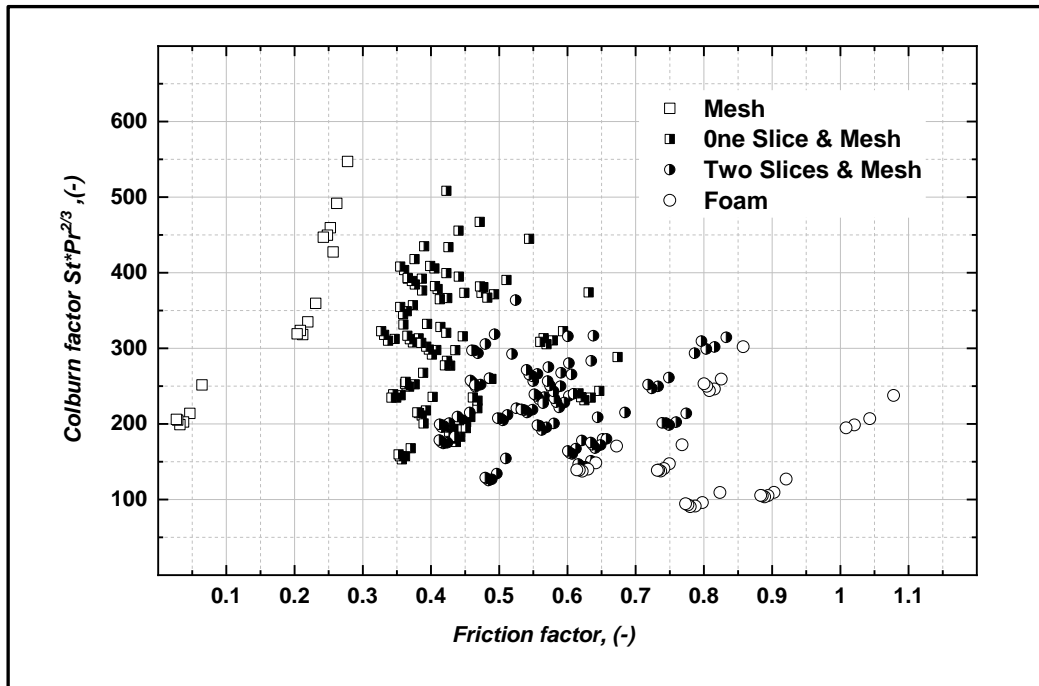
Figure 7.36 Colburn factor plotted against friction coefficient for the samples investigated in this study. Data for measurements performed in the Forcheimer.
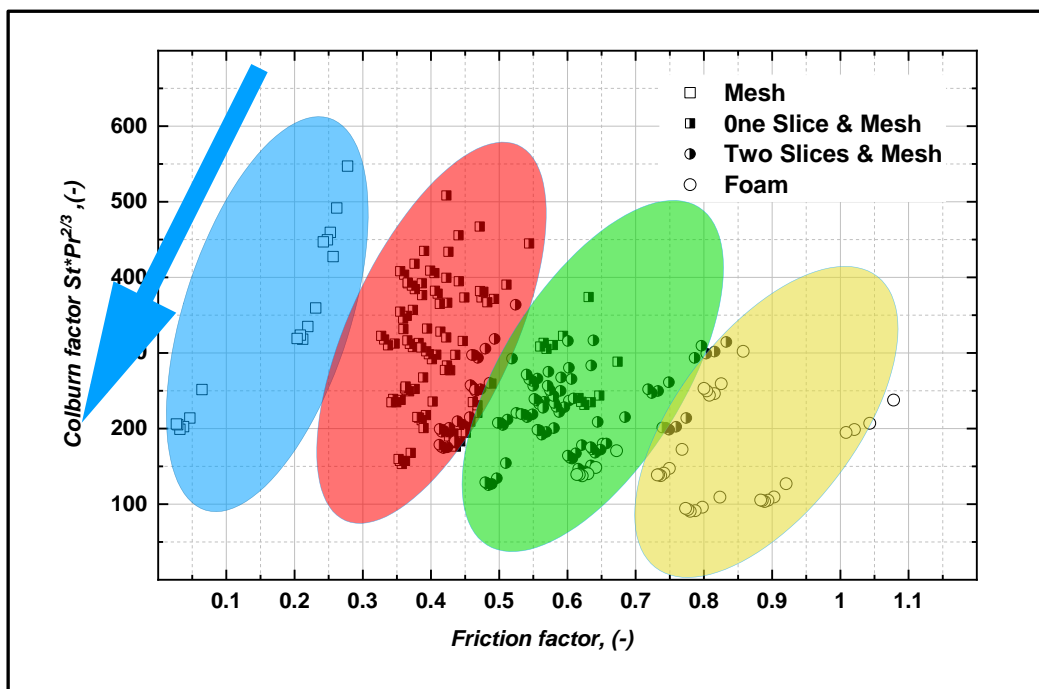
Figure 7.37 An annotated version of Figure 7.36. Oval colours: yellow – foam, green – two slices & mesh, red – one slice and mesh, blue – mesh.

An annotated version of Figure 7.36 is shown in Figure 7.37. Coloured ovals have been used to identify the 4 major groups of materials. It can be seen that whilst they cover a similar range of thermal performance they separate in terms of friction factor and hence pressure drop. The spread in the Colburn number appears to relate

to the 'pore size' of the media with materials having large pore sizes in each group having a lower Stanton number than those with large pore size, the differences in fraction factor were less significant (within a group). Pore sizes for the largest and smallest mesh and foam samples are shown in Figure 7.37. The large blue arrow indicates increasing pore size. An objective of this treatment was that it might be possible to summarise the results from this study with a mathematic expression. However, the strong dependence of heat transfer on pore size meant this was not feasible. There was no overlap in the spacing between the wires in the mesh (largest value 0.9 mm) and the smallest foam pore size (1.1 mm). A mesh spacing and pore are not really identical spaces. Definition of the pore size becomes even more problematic in the hybrid samples. In heat transfer terms the one slice and mesh samples are clearly more related to the mesh and the two slice and mesh samples closer to the foam.

Some observations may be drawn from this treatment. The pressure drop of foam may be reduced if partly replaced with some mesh, with no detriment to the thermal performance. The foam samples used here do not improve either the pressure drop or heat transfer performance of the mesh. Thus it might be possible to improve the performance of some porous media with partial substitution.

7.9 summary

This chapter presented the methods and techniques used to evaluate the samples thermal performance. The measured outlet temperature curves were non-dimensionalised to predict the thermal parameters of the tested samples. The dimensionless experimental outlet temperature profiles and the numerical modelled ones are compared to estimate the number of transfer units of each tested sample. To understand the impact of the effective thermal conductivity on the predicted $NTUs$, the $NTUs$ values of the foam samples before and after slicing were compared. A slight decrease was noticed which may be due to the reduction in the heat transfer surface area. The volumetric heat transfer coefficients, the Nusselt and Colburn numbers were also obtained for each sample. This chapter also assessed the impact of the geometrical parameters on those parameters. The performance results were discussed as well, conclusions were drawn about the relative performance of different

porous structures and the metals from which they are made. The woven metal screens samples show high thermal performance compared with metal foam samples. Samples with small pore sizes provide high heat transfer coefficients due to the large heat transfer surface area. The performance of the metal foams was enhanced as a part of the sample being replaced by woven mesh layers. The general trend was that the thermal performance increased as the portion of mesh increased in the hybrid samples. There was no clear correlation that can be derived from the current study due to the large variation in the geometrical parameters.

CHAPTER 8. Conclusions and recommendations

8.1 Conclusions

This study experimentally investigated the hydraulic and thermal performance of heterogeneous regenerators made of woven stainless stain mesh screens and aluminium foams.

8.1.1 Experiments

- Thirty-six heterogeneous regenerators were investigated for their hydraulic and thermal performance using dry air. The regenerators were constructed such that they all had the same volume. Each heterogeneous regenerator consisted of one or two slices of aluminium foam representing respectively one-third or two-thirds of the total regenerator's volume whilst the rest of the structure was constructed from square woven mesh screens. To understand the impact of the combination of two different types of media on the flow and thermal performance, the results were compared to semi-homogeneous regenerators constructed from square woven mesh screens or slices of aluminium foam only.

- The hydraulic and thermal characteristics of various types of regenerative materials were measured under steady and unsteady state conditions respectively. Two test rigs were designed and built to achieve the aims and objectives of this study and the following conclusions were drawn.

8.1.2 Steady-state pressure drop measurements and hydraulic parameters

1- The pressure drop increased with the frontal air velocity. Four flow regimes were observed in all the samples: Pre-Darcy, Darcy, Forchheimer and turbulent flow regimes.

2- The pressure drop was found to increase with decreasing pore size. Generally, metal foams induced higher pressure drops compared with packed beds of screens.

3- The pressure drop across the multiple metal foams increased after the original sample was sliced. The increase of the pressure drop depended on the pore size.

4- The pressure drop across the heterogeneous regenerators was found to be dependent on porous materials that made up the heterogeneous matrix. Heterogeneous regenerators made of small pore or low porosity material presented higher pressure loss.

5- Darcy permeability, Forchheimer permeability, inertia factor and drag form coefficient were determined at two flow regimes: Darcy regime and Forchheimer regime. The permeabilities were found to increase with increasing the pore size while inertia factor and drag form coefficient decreased, in agreement with the published data. The mesh wire packed beds had higher permeabilities and lower inertia and drag coefficients in comparison with metal foams.

6- Darcy and Forchheimer permeabilities, inertia factor and drag form coefficient of the heterogeneous regenerators were found to depend on the proportion and the physical features of porous materials employed in the construction. Permeability increased and inertia coefficients decreased with increasing the proportion of material that has higher permeability and lower inertia coefficients.

7- Forchheimer permeability differed from Darcy permeability. Forchheimer permeability was found to be higher in semi-homogeneous metal foam structures, but an opposite trend was observed in the mesh wire packed beds. The difference depends on the pore size.

8- The Forchheimer permeability of the heterogeneous regenerators was slightly higher than Darcy permeability. The difference became considerable when two slices of spherical metal foams were used to fabricate the heterogeneous regenerators.

9- The square root of the permeability, measured in the Darcy regime, was used as a representative dimension for defining Reynolds number and friction factor. Flow regimes (from pre-Darcy to turbulent) were identified, along with transitions from one to another observing the deviation from the slopes of all series of experimental data. The critical values of Reynolds numbers at which the flow transition from pre-Darcy to the regime were found to be between 0.02 and 0.1 while the flow transition from Darcy regime to quadratic Forchheimer regime was found to be from 0.3 to 11.

10- The results showed that the friction factor of both the semi-homogeneous and heterogeneous matrix materials decreased with an increase of Reynolds number. At the Darcy flow regime, the relationship between the friction factor and the Reynold number is equal to 1/Rek. The experimental results at high Reynolds number were compared and none of the existed models seemed to accurately describe the friction factor.

8.1.3 Heat transfer measurement and thermal parameters

1- The heat transfer performance of semi-homogeneous and heterogeneous regenerators was investigated using the single blow technique. The number of the transfer unit, mean volumetric heat transfer coefficient and volumetric Darcy permeability based Nusselt number were estimated by solving an advanced single blow model that considered the inlet temperature variation, non-adiabatic side-wall and the axial conduction in the solid as well as in the side-wall.

2- Several reduction methods were revised and the hybrid reduction method consisting of the direct matching technique and the maximum gradient scheme was implemented to predict the number of transfer units NTU_s of the tested regenerators.

3- A parametric study was performed to understand the influence of modelling parameters such as NTU_s, NTU_w, R_{tc} and inlet air response on the predicted outlet temperature and the maximum gradient.

4- The Wiebe function was found to be accurate to describe the fluid inlet time-temperature variation. This study showed that the dimensionless time required by the fluid inlet temperature to reach the steady-state conditions introduced a new limitation for the maximum gradient scheme.

5- The heat transfer performance was first evaluated using the NTU_s value. The NTU_s decreased with the increase of Reynolds number or flow rate. The metal foams were sliced and the NTU_s value was found to decrease in comparison with the NTU_s values of the original samples.

6- The pore size was found to have a significant influence on the thermal performance of the regenerator. Decreasing of pore size or the mesh number means larger heat transfer surface area increasing NTU_s. Mesh wire screens samples showed always

higher NTU_s than all the metal foam samples due to the increase in the convective heat transfer coefficient.

7- The NTU_s values of the heterogeneous regenerators varied with the contribution of the wire meshes and metal foams layers in their structures. With increasing the fine mesh layers the NTU_s values increased. Plotting the NTU_s values at zero Reynolds number versus Darcy permeability revealed that similar NTU_s can be obtained from several combinations of mesh and foam layers but with different Darcy permeability values.

8- The volumetric heat transfer coefficients were calculated and plotted against Darcy permeability based Reynolds number. The results showed that the volumetric heat transfer coefficients increased with Reynolds number, pore size, and mesh number. 20Mesh sample provided a similar volumetric heat transfer coefficient in the same order as that for small and medium pore size foam samples, with lower flow resistance.

9- The volumetric heat transfer coefficient of the heterogeneous regenerators varied based on the combined materials. The combination of one layer of metal foams with 20Mesh or 30Mesh provided a similar volumetric heat transfer coefficient which can be considered as an improvement in the hybrid sample weight, however, the flow resistance increased.

10- Volumetric Nusselt number based on the square root of Darcy permeability was calculated and found to increase with Reynolds number. In general, the volumetric Nusselt number of mesh wire screen samples was higher compared with the sliced metal foam samples. Medium sliced foam samples provided similar volumetric Nusselt numbers in almost the same order as of the 20Mesh sample, however, with extra pressure drop penalty.

11- Volumetric Nusselt number based on the square root of Darcy permeability for the heterogeneous regenerators was found to increase gradually from pure metal foam samples to pure mesh samples receipting the proportion of each material type in the heterogeneous structures.

12- The results consistently show that the wire mesh samples perform better as regenerators; however, the replicated porous metals have the advantage of being tailored to a wide array of specifications, being able to reproduce behaviours of the

meshes with almost half of the weight. Among all the regenerators investigated, the 20Mesh sample appears the best hydrothermal performance at a constant flow rate because it produces a satisfactorily high heat transfer and is accompanied by a moderate pressure drop.

13- The measured thermal and pressure drops were compared using Colburn numbers and friction factors. This demonstrated that there was more impact on the pressure drop (The addition of foam resulted in increased pressure drop) between the different types of sample than on heat transfer. The variation in thermal performance was found to be linked to the pore size. However, there is no single definition of pore size that links the void space in such disparate types of a sample as mesh and foams meaning correlations could not be found.

8.2 Future work

This work is unique as the heterogeneous materials and no available data in the available literature. This study has opened the door for a new class of porous media which may bring about advantages that can overweight their mother materials. However, extensive work can be done to deeply understand the interaction between these materials and the working fluid in many real-life applications. Here are some shortcomings which can be covered in the future.

1- Defection was reported about the geometrical properties of the replicated metal foam samples for whom the picked samples have been picked up. This may have a certain contribution to the uncertainty of current results. Generally, it means more heterogeneous structures should be tested and compared with the results achieved in the current work.

2- The pore size and shape was found to have a remarkable influence on the hydraulic structure parameters. Less attention was paid to the porosity effect in the current investigation as the porosity of the selected foam samples is almost similar. Therefore, further tested samples with a different wide range of geometrical features should be tested to understand the influence of those parameters on the thermo-fluid parameters in heterogeneous porous materials.

3- The permeability in the Forchheimer of mesh wire screens packed beds found to be lower than Darcy permeability. This an opposite trend in comparison with metal foam structures. This outcome is based on three tested wire mesh samples having similar volumetric size but different pore size. Thereby, extract information is required to understand this phenomenon.

4- The literature showed limited experimental data at a high fluid velocity in which the flow regime is fully developed turbulent. There is debate about the flow behaviour and parameter in this regime. The pressure drop gradient per frontal flow velocity has been shown to decrease in backed beads of spheres compared with that in the Forchheimer regime. However, it is seen to increase in metal foam, whereas no data available about the reduced gradient in wire mesh screens packed beds. Hence, one can investigate several types of structure, including the heterogeneous structure in the fully developed turbulent regime to fill this gap in the literature.

5- The literature showed the impact of metal foam slicing on the hydrostatic performance of the metal foam. The available data in the literature showed an increase in the pressure drop due to the slicing process. However, the published data has not provide any information on pore size impact after the samples being sliced. The variation of pore size can influence the magnitude of the static pressure drop across the medium. Also, the available data considered only hydraulic performance, which provides an interesting point of research.

6- The number of slices was limited to two slices of foam in this work, increasing the number of slices perhaps leads to a change in the hydraulic and thermal characteristics of the heterogeneous thermal regenerators.

7- The current study was conducted using dry air as working fluid while other fluids, gases or even moisture can be used to investigate if there is any impact due to the fluid change.

8- The wall side impact was found to influence the thermal characteristics of the regenerative heat exchanger significantly. Changing the sample's holder materials or size can provide experimental information about the wall-impact on the single-blow testing technique.

9- The porous media in nature has a non-homogeneous structure which prevents accurate heat transfer surface area and results in data scattering. Therefore, the tested samples should have been CT-scanned to determine the contact surface areas of the solid accurately and minimize the uncertainty in the obtained data.

10- The parallel effective thermal conductivity highly influences the single blow technique to the flow direction. In contrast, the steady-state depends on the thermal conductivity of the solid material normal to the flow direction. In the current work, the thermal conductivity was found to be minimal in the flow direction, but its impact on the radius direction is still an exciting topic for research.

Reference

[1]   H. Jouhara, N. Khordehgah, S. Almahmoud, B. Delpech, A. Chauhan, and S. A. Tassou, "Waste heat recovery technologies and applications," *Therm. Sci. Eng. Prog.*, vol. 6, pp. 268–289, 2018.

[2]   H. Zhu *et al.*, "Experimental and numerical investigations on the local direct leakage process of rotary regenerative air preheater," *Appl. Sci.*, vol. 10, no. 4, p. 1523, Feb. 2020.

[3]   C. Forman, I. K. Muritala, R. Pardemann, and B. Meyer, "Estimating the global waste heat potential," *Renew. Sustain. Energy Rev.*, vol. 57, pp. 1568–1579, 2016.

[4]   S. M. Sadrameli and H. R. B. Ajdari, "Mathematical modelling and simulation of thermal regenerators including solid radial conduction effects," *Appl. Therm. Eng.*, vol. 76, pp. 441–448, 2015.

[5]   W. Peng, M. Xu, X. Huai, Z. Liu, and X. Lü, "Performance evaluation of oscillating flow regenerators filled with particles, wire screens and high porosity open-cell foams," *Appl. Therm. Eng.*, vol. 112, pp. 1612–1625, 2017.

[6]   G. Wołkowycki, "Effectiveness of high temperature innovative geometry fixed ceramic matrix regenerators used in glass furnaces," *Arch. Thermodyn.*, vol. 37, no. 1, pp. 113–126, 2016.

[7]   L. B. Younis and R. Viskanta, "Experimental determination of the volumetric heat transfer coefficient between stream of air and ceramic foam," *Int. J. Heat Mass Transf.*, vol. 36, no. 6, pp. 1425–1434, 1993.

[8]   Z. Guo-Yan, T. Shan-Tung, and M. Hu-Gen, "Numerical and experimental study on the heat transfer and pressure drop of compact cross-corrugated recuperators," *J. Heat Transf. ASME*, vol. 136, no. 7, pp. 071801–1, 2014.

[9]   I. Warren, "Ljungstrom heat exchangers for waste heat recovery," *J. Heat Recover. Syst.*, vol. 2, no. 3, pp. 257–271, 1982.

[10]   K. J. Kang, "Wire-woven cellular metals: The present and future," *Prog. Mater. Sci.*, vol. 69, pp. 213–307, 2015.

[11]   J. Xu, J. Tian, T. J. Lu, and H. P. Hodson, "On the thermal performance of wire-screen meshes as heat exchanger material," *Int. J. Heat Mass Transf.*, vol. 50, no. 5–6, pp. 1141–1154, 2007.

[12]   A. A. Sertkaya, K. Altinisik, and K. Dincer, "Experimental investigation of thermal performance of aluminum finned heat exchangers and open-cell aluminum foam heat exchangers," *Exp. Therm. Fluid Sci.*, vol. 36, pp. 86–92, 2012.

[13]   P. H. Chen and Z. C. Chang, "Measurements of thermal performance of the regenerator of a cryocooler with a high number of transfer units value," *Proc. Inst. Mech. Eng. Part C J. Mech. Eng. Sci.*, vol. 210, pp. 341–352, 1996.

[14]   J. Tian *et al.*, "The effects of topology upon fluid-flow and heat-transfer within

cellular copper structures," *Int. J. Heat Mass Transf.*, vol. 47, no. 14–16, pp. 3171–3186, Jul. 2004.

[15] A. G. Evans, J. W. Hutchinson, N. A. Fleck, M. F. Ashby, and H. N. G. Wadley, "The topological design of multifunctional cellular metals," *Prog. Mater. Sci.*, vol. 46, no. 3–4, pp. 309–327, 2001.

[16] U. Bin-Nun and D. Manitakos, "Low cost and high performance screen laminate regenerator matrix," *Cryogenics (Guildf).*, vol. 44, no. 6–8, pp. 439–444, 2004.

[17] Z. Zhao, Y. Peles, and M. K. Jensen, "Properties of plain weave metallic wire mesh screens," *Int. J. Heat Mass Transf.*, vol. 57, no. 2, pp. 690–697, 2013.

[18] A. L. Avila-Marin, C. Caliot, G. Flamant, M. Alvarez de Lara, and J. Fernandez-Reche, "Numerical determination of the heat transfer coefficient for volumetric air receivers with wire meshes," *Sol. Energy*, vol. 162, pp. 317–329, 2018.

[19] W. Bussière, D. Rochette, S. Clain, P. André, and J. B. Renard, "Pressure drop measurements for woven metal mesh screens used in electrical safety switchgears," *Int. J. Heat Fluid Flow*, vol. 65, pp. 60–72, 2017.

[20] W. T. Wu, J. F. Liu, W. J. Li, and W. H. Hsieh, "Measurement and correlation of hydraulic resistance of flow through woven metal screens," *Int. J. Heat Mass Transf.*, vol. 48, no. 14, pp. 3008–3017, 2005.

[21] S. C. Costa, H. Barrutia, J. A. Esnaola, and M. Tutar, "Numerical study of the heat transfer in wound woven wire matrix of a Stirling regenerator," *Energy Convers. Manag.*, vol. 79, pp. 255–264, 2014.

[22] P. V. Trevizoli and J. R. Barbosa, "Entropy generation minimization analysis of oscillating-flow regenerators," *Int. J. Heat Mass Transf.*, vol. 87, pp. 347–358, 2015.

[23] R. Kurian, C. Balaji, and S. P. Venkateshan, "An experimental study on hydrodynamic and thermal performance of stainless steel wire mesh blocks in a vertical channel," *Exp. Therm. Fluid Sci.*, vol. 86, pp. 248–256, 2017.

[24] R. Kurian, C. Balaji, and S. P. Venkateshan, "Experimental investigation of convective heat transfer in a vertical channel with brass wire mesh blocks," *Int. J. Therm. Sci.*, vol. 99, pp. 170–179, 2016.

[25] Y. L. Haiou Sun, Shi Bu, "A high-precision method for calculating the pressure drop across wire mesh filters," *Chem. Eng. Sci.*, vol. 127, pp. 143–150, 2015.

[26] J. R. Sodré and J. A. Parise, "Friction factor determination for flow through finite wire-mesh woven-screen matrices," *J. Fluids Eng. ASME*, vol. 119, no. 4, pp. 847–851, 1997.

[27] E. Brundrett, "Prediction of pressure drop for incompressible flow through screens," *J. Fluids Eng. ASME*, vol. 115, no. 2, pp. 239–242, 1993.

[28] Y. Peng, G. Xu, X. Luo, H. W. Li, and Y. P. Liu, "Experimental study on the influence of wire diameter on the internal flow behaviour of woven metal screens," in *IOP Conference Series: Materials Science and Engineering*, 2017,

vol. 164, p. 012003.

[29] E. C. Landrum, T. J. Conrad, S. M. Ghiaasiaan, and C. S. Kirkconnell, "Hydrodynamic parameters of mesh fillers relevant to miniature regenerative cryocoolers," *Cryogenics (Guildf).*, vol. 50, no. 6–7, pp. 373–380, 2010.

[30] A. J. Fuller, T. Kim, H. P. Hodson, and T. J. Lu, "Measurement and interpretation of the heat transfer coefficients of metal foams," in *Proceedings of the Institution of Mechanical Engineers, Part C: Journal of Mechanical Engineering Science*, 2005, vol. 219, no. 2, pp. 183–191.

[31] Q. Fabrizio, A. Boschetto, L. Rovatti, and L. Santo, "Replication casting of open-cell AlSi7Mg0.3 foams," *Mater. Lett.*, vol. 65, no. 17–18, pp. 2558–2561, 2011.

[32] A. Bhattacharya, V. V. Calmidi, and R. L. Mahajan, "Thermophysical properties of high porosity metal foams," *Int. J. Heat Mass Transf.*, vol. 45, no. 5, pp. 1017–1031, 2002.

[33] W. Lu, C. Y. Zhao, and S. A. Tassou, "Thermal analysis on metal-foam filled heat exchangers. Part I: Metal-foam filled pipes," *Int. J. Heat Mass Transf.*, vol. 49, no. 15–16, pp. 2751–2761, 2006.

[34] S. Y. Kim, J. W. Paek, and B. H. Kang, "Flow and heat transfer correlations for porous fin in a plate-fin heat exchanger," *J. Heat Transf. ASME*, vol. 122, no. 3, pp. 572–578, 2000.

[35] J. Banhart, "Properties and applications of cast aluminum sponges," *Adv. Eng. Mater.*, vol. 2, no. 4, pp. 159–162, 2000.

[36] E. M. E. Luna, "Investigation of porous metals as improved efficiency regenerators," The University of Sheffield, 2016.

[37] A. F. Abuserwal, "Pressure drop and forced convective heat transfer in porous media," The University of Sheffield, 2017.

[38] A. Hamadouche, R. Nebbali, H. Benahmed, A. Kouidri, and A. Bousri, "Experimental investigation of convective heat transfer in an open-cell aluminum foams," *Exp. Therm. Fluid Sci.*, vol. 71, pp. 86–94, 2016.

[39] N. Dukhan and P. Patel, "Equivalent particle diameter and length scale for pressure drop in porous metals," *Exp. Therm. Fluid Sci.*, vol. 32, no. 5, pp. 1059–1067, 2008.

[40] G. Wołkowycki, "Experimental results on the fixed matrix regenerator effectiveness for a glass stove furnace," *Heat Transf. Eng.*, vol. 37, no. 6, pp. 591–602, 2016.

[41] D. Butrymowicz *et al.*, "Methodology of heat transfer and flow resistance measurement for matrices of rotating regenerative heat exchangers," *Chem. Process Eng.*, vol. 37, no. 3, pp. 341–358, 2016.

[42] G. Walker and V. Vasishta, "Heat-transfer and flow-friction characteristics of dense-mesh wire-screen Stirling-cycle regenerators," in *Advances in Cryogenic Engineering*, K. D. Timmerhaus, Ed. Boston, MA: Springer US, 1971, pp. 324–

332.

[43]   Z. C. Chang, M. S. Hung, P. P. Ding, and P. H. Chen, "Experimental evaluation of thermal performance of Gifford–McMahon regenerator using an improved single-blow model with radial conduction," *Int. J. Heat Mass Transf.*, vol. 42, no. 3, pp. 405–413, 1999.

[44]   J. H. Xiao, J. H. Yang, and Z. D. Tao, "Miniature double-inlet pulse tube cryocooler: Design by thermoacoustic theory compared with preliminary experimental results," in *Advances in Cryogenic Engineering*, vol. 41, P. Kittel. Plenum Press, Ed. New York: Springer, Boston, MA, 1996, pp. 1435–1441.

[45]   I. Garaway, A. Veprik, and R. Radebaugh, "Diagnostics and optimization of a miniature high frequency pulse tube cryocooler," in *AIP Conference Proceedings*, 2010, vol. 1218, pp. 167–174.

[46]   Y. K. Hou, Y. L. Ju, L. W. Yan, Y. Zhou, and J. T. Liang, "The effect of the regenerator and tube volume on the performance of high frequency miniature pulse tube refrigerators," in *AIP Conference Proceedings*, 2002, vol. 613, pp. 723–730.

[47]   Y. K. Hou, Y. L. Ju, L. W. Yan, J. T. Liang, and Y. Zhou, "Experimental study on a high frequency miniature pulse tube refrigerator with inertance tube," in *AIP Conference Proceedings*, 2002, vol. 613, pp. 731–738.

[48]   L. Y. Xiong, G. Kaiser, and A. Binneberg, "Theoretical study on a miniature Joule–Thomson & Bernoulli cryocooler," *Cryogenics (Guildf).*, vol. 44, no. 11, pp. 801–807, 2004.

[49]   X. Yang and J. N. Chung, "Size effects on miniature Stirling cycle cryocoolers," *Cryogenics (Guildf).*, vol. 45, no. 8, pp. 537–545, 2005.

[50]   H. T. Chua, X. Wang, and H. Y. Teo, "A numerical study of the hampson-type miniature Joule-Thomson cryocooler," *Int. J. Heat Mass Transf.*, vol. 49, no. 3–4, pp. 582–593, 2005.

[51]   R. Radebaugh and A. O'Gallagher, "Regenerator operation at very high frequencies for microcryocoolers," in *AIP Conference Proceedings*, 2006, vol. 823, pp. 1919–1928.

[52]   J. J. Cha, "Hydrodynamic parameters of micro porous media for steady and oscillatory flow: Application to cryocooler regenerators," Georgia Institute of Technology, 2007.

[53]   A. K. John and K. Krishnakumar, "Determination of heat transfer and flow friction characteristics of perforated plate matrix heat exchanger surfaces with various perforation shapes," in *Advances in Mechanical Engineering*, 2013, pp. 702–710.

[54]   K. H. Ko and N. K. Anand, "Use of porous baffles to enhance heat transfer in a rectangular channel," *Int. J. Heat Mass Transf.*, vol. 46, pp. 4191–4199, 2003.

[55]   P. H. Chen, Z. C. Chang, and B. J. Huang, "Effect of oversize in wire-screen matrix to the matrix-holding tube on regenerator thermal performance,"

Cryogenics (Guildf)., vol. 36, no. 5, pp. 365–372, 1996.

[56] R. Dyga and M. Płaczek, "Efficiency of heat transfer in heat exchangers with wire mesh packing," *Int. J. Heat Mass Transf.*, vol. 53, no. 23–24, pp. 5499–5508, 2010.

[57] C. Li, G. P. Peterson, and Y. Wang, "Evaporation/boiling in thin capillary wicks (I) - Wick thickness effects," *J. Heat Transf. ASME*, vol. 128, no. 12, pp. 1312–1319, 2006.

[58] D. Edouard, M. Lacroix, C. P. Huu, and F. Luck, "Pressure drop modelling on SOLID foam: State-of-the art correlation," *Chem. Eng. J.*, vol. 144, no. 2, pp. 299–311, 2008.

[59] M. Golombok, H. Jariwala, and L. C. Shirvill, "Gas-solid heat exchange in a fibrous metallic material measured by a heat regenerator technique," *Int. J. Heat Mass Transf.*, vol. 33, no. 2, pp. 243–252, 1990.

[60] K. Boomsma, D. Poulikakos, and F. Zwick, "Metal foams as compact high performance heat exchangers," *Mech. Mater.*, vol. 35, no. 12, pp. 1161–1176, 2003.

[61] N. Dukhan, Ö. Bağci, and M. Özdemir, "Metal foam hydrodynamics: Flow regimes from pre-Darcy to turbulent," *Int. J. Heat Mass Transf.*, vol. 77, pp. 114–123, 2014.

[62] C. Y. Zhao, W. Lu, and S. A. Tassou, "Thermal analysis on metal-foam filled heat exchangers. Part II: Tube heat exchangers," *Int. J. Heat Mass Transf.*, vol. 49, no. 15–16, pp. 2762–2770, 2006.

[63] N. Dukhan, "Correlations for the pressure drop for flow through metal foam," *Exp. Fluids*, vol. 41, no. 4, pp. 665–672, 2006.

[64] S. Rode, N. Midoux, M. A. Latifi, A. Storck, and E. Saatdjian, "Hydrodynamics of liquid flow in packed beds: An experimental study using electrochemical shear rate sensors," *Chem. Eng. Sci.*, vol. 49, no. 6, pp. 889–900, 1994.

[65] R. M. Fand, B. Y. K. Kim, A. C. C. Lam, and R. T. Phan, "Resistance to the flow of fluids through simple and complex porous media whose matrices are composed of randomly packed spheres," *J. Fluids Eng. ASME*, vol. 109, pp. 268–273, 1987.

[66] P. Kundu, V. Kumar, and I. M. Mishra, "Experimental and numerical investigation of fluid flow hydrodynamics in porous media: Characterization of pre-Darcy, Darcy and non-Darcy flow regimes," *Powder Technol.*, vol. 303, pp. 278–291, 2016.

[67] A. Valli, J. Hyväluoma, A. Jäsberg, A. Koponen, and J. Timonen, "Pressure drop for low Reynolds-number flows through regular and random screens," *Transp. Porous Media*, vol. 80, no. 2, pp. 193–208, 2009.

[68] B. V. Antohe, J. L. Lage, D. C. Price, and R. M. Weber, "Experimental determination of permeability and inertia coefficients of mechanically compressed aluminum porous matrices," *J. Fluids Eng. ASME*, vol. 119, no. 2,

pp. 404–412, 1997.

[69] J. J. Hwang, G. J. Hwang, R. H. Yeh, and C. H. Chao, "Measurement of interstitial convective heat transfer and frictional drag for flow across metal foams," *J. Heat Transf. ASME*, vol. 124, no. 1, pp. 120–129, 2002.

[70] Z. Xiao and Y. Zhao, "Heat transfer coefficient of porous copper with homogeneous and hybrid structures in active cooling," *J. Mater. Res.*, vol. 28, no. 17, pp. 2545–2553, 2013.

[71] Y. Conde *et al.*, "Replication processing of highly porous materials," *Adv. Eng. Mater.*, vol. 8, no. 9, pp. 795–803, 2006.

[72] R. Goodall, J. F. Despois, A. Marmottant, L. Salvo, and A. Mortensen, "The effect of preform processing on replicated aluminium foam structure and mechanical properties," *Scr. Mater.*, vol. 54, no. 12, pp. 2069–2073, 2006.

[73] J. F. Despois and A. Mortensen, "Permeability of open-pore microcellular materials," *Acta Mater.*, vol. 53, no. 5, pp. 1381–1388, 2005.

[74] J. W. Paek, B. H. Kang, S. Y. Kim, and J. M. Hyun, "Effective thermal conductivity and permeability of aluminum foam materials," *Int. J. Thermophys.*, vol. 21, no. 2, pp. 453–464, 2000.

[75] Chen Li and G. P. Peterson, "The effective thermal conductivity of wire screen," *Int. J. Heat Mass Transf.*, vol. 49, no. 21–22, pp. 4095–4105, 2006.

[76] H. Iwai, S. Kawakami, K. Suzuki, J. Tsujii, and T. Abiko, "Performance of wire springs as extended heat transfer surface for compact heat exchangers," *J. Therm. Sci. Technol.*, vol. 1, no. 2, pp. 78–89, 2006.

[77] C. A. Grattoni and R. A. Dawe, "Anisotropy in pore structure of porous media," *Powder Technol.*, vol. 85, no. 2, pp. 143–151, 1995.

[78] B. P. Muljadi, M. J. Blunt, A. Q. Raeini, and B. Bijeljic, "The impact of porous media heterogeneity on non-Darcy flow behaviour from pore-scale simulation," *Adv. Water Resour.*, vol. 95, pp. 329–340, 2016.

[79] M. Medraj, E. Baril, V. Loya, and L. P. Lefebvre, "The effect of microstructure on the permeability of metallic foams," *J. Mater. Sci.*, vol. 42, no. 12, pp. 4372–4383, 2007.

[80] A. Kołodziej, J. Łojewska, M. Jaroszyński, A. Gancarczyk, and P. Jodłowski, "Heat transfer and flow resistance for stacked wire gauzes: Experiments and modelling," *Int. J. Heat Fluid Flow*, vol. 33, no. 1, pp. 101–108, 2012.

[81] F. Azizi, "On the pressure drop of fluids through woven screen meshes," *Chem. Eng. Sci.*, vol. 207, pp. 464–478, 2019.

[82] M. Teitel, "The effect of insect-proof screens in roof openings on greenhouse microclimate," *Agric. For. Meteorol.*, vol. 110, no. 1, pp. 13–25, 2001.

[83] A. Kołodziej, M. Jaroszyński, B. Janus, T. Kleszcz, J. Łojewska, and T. Łojewski, "An experimental study of the pressure drop in fluid flows through wire gauzes," *Chem. Eng. Commun.*, vol. 196, no. 8, pp. 932–949, 2009.

[84] D. L. Valera, A. J. Álvarez, and F. D. Molina, "Aerodynamic analysis of several insect-proof screens used in greenhouses," *Spanish J. Agric. Res.*, vol. 4, no. 4, pp. 273–279, 2006.

[85] D. L. Valera, F. D. Molina, A. J. Álvarez, J. A. López, J. M. Terrés-Nicoli, and A. Madueño, "Contribution to characterisation of insect-proof screens: Experimental measurements in wind tunnel and CFD simulation," *Acta Hortic.*, vol. 691, pp. 441–448, 2005.

[86] D. Hlushkou and U. Tallarek, "Transition from creeping via viscous-inertial to turbulent flow in fixed beds," *J. Chromatogr. A*, vol. 1126, no. 1–2, pp. 70–85, 2006.

[87] D. Vijay, P. Goetze, R. Wulf, and U. Gross, "Forced convection through open cell foams based on homogenization approach: Steady state analysis," *Int. J. Therm. Sci.*, vol. 98, pp. 381–394, 2015.

[88] Z. Chai, B. Shi, J. Lu, and Z. Guo, "Non-Darcy flow in disordered porous media: A lattice Boltzmann study," *Comput. Fluids*, vol. 39, no. 10, pp. 2069–2077, 2010.

[89] C. C. Mei and J. L. Auriault, "The effect of weak inertia on flow through a porous medium," *J. Fluid Mech.*, vol. 222, pp. 647–663, 1991.

[90] A. Nazeer and D. K. Sunada, "Nonlinear flow in porous media," *J. Hydraul. Div.*, vol. 95, no. 6, pp. 1847–1858, 1969.

[91] J. C. Armour and J. N. Cannon, "Fluid flow through woven screens," *AIChE J.*, vol. 14, no. 3, pp. 415–420, 1968.

[92] J. L. Lage, B. V. Antohe, and D. A. Nield, "Two types of nonlinear pressure-drop versus flow-rate relation observed for saturated porous media," *J. Fluids Eng. ASME*, vol. 119, no. 3, pp. 700–706, 1997.

[93] N. Dukhan and C. A. Minjeur, "A two-permeability approach for assessing flow properties in metal foam," *J. Porous Mater.*, vol. 18, pp. 417–424, 2011.

[94] Ö. Bağcı, N. Dukhan, and M. Özdemir, "Flow regimes in packed beds of spheres from pre-Darcy to turbulent," *Transp. Porous Media*, vol. 104, no. 3, pp. 501–520, 2014.

[95] N. Dukhan, Ö. Bağci, and M. Özdemir, "Experimental flow in various porous media and reconciliation of Forchheimer and Ergun relations," *Exp. Therm. Fluid Sci.*, vol. 57, pp. 425–433, 2014.

[96] J. L. Lage and B. V. Antohe, "Darcy' s experiments and the deviation to nonlinear flow," *J. Fluids Eng. Trans. to ASME*, vol. 122, no. 3, pp. 619–625, 2000.

[97] S. Ergun, "Fluid flow through packed columns," *Chem. Eng. Progress.*, vol. 48, no. 2, pp. 89–94, 1952.

[98] S. Whitaker, "Flow in porous media I: A theoretical derivation of Darcy's law," *Transp. Porous Media*, vol. 1, no. 1, pp. 3–25, 1986.

[99] M. Sedghi-Asl, H. Rahimi, and R. Salehi, "Non-Darcy flow of water through a

packed column test," *Transp. Porous Media*, vol. 101, no. 2, pp. 215–227, 2014.

[100] G. S. Beavers and E. M. Sparrow, "Non-Darcy flow through fibrous porous media," *J. Appl. Mech. ASME*, vol. 36, no. 4, pp. 711–714, 1969.

[101] Ö. Bağcı and N. Dukhan, "Experimental hydrodynamics of high-porosity metal foam: Effect of pore density," *Int. J. Heat Mass Transf.*, vol. 103, pp. 879–885, 2016.

[102] A. Dybbs and R. V Edwards, "A new look at porous media fluid mechanics - Darcy to turbulent.," in *Fundamentals of Transport Phenomena in Porous Media*, 1984, pp. 199–256.

[103] H. Oun and A. Kennedy, "Tailoring the pressure-drop in multi-layered open-cell porous inconel structures," *J. Porous Mater.*, vol. 22, no. 6, pp. 1627–1633, 2015.

[104] P. Forchheimer, "Wasserbewegung durch Boden [movement of water through soil]," *Zeitschrift des Vereines Dtsch. Ingenieure*, vol. 49, pp. 1782–1788, 1901.

[105] N. Dukhan and K. Patel, "Effect of sample's length on flow properties of open-cell metal foam and pressure-drop correlations," *J. Porous Mater.*, vol. 18, no. 6, pp. 655–665, 2011.

[106] M. Teitel, "Using computational fluid dynamics simulations to determine pressure drops on woven screens," *Biosyst. Eng.*, vol. 105, no. 2, pp. 172–179, 2010.

[107] N. Dukhan and M. Ali, "Strong wall and transverse size effects on pressure drop of flow through open-cell metal foam," *Int. J. Therm. Sci.*, vol. 57, pp. 85–91, 2012.

[108] K. Boomsma and D. Poulikakos, "The effects of compression and pore size variations on the liquid flow characteristics in metal foams," *J. Fluids Eng. ASME*, vol. 124, no. 1, pp. 263–272, 2002.

[109] S. M. Hassanizadeh and W. G. Gray, "High velocity flow in porous media," *Transp. Porous Media*, vol. 2, no. 6, pp. 521–531, 1987.

[110] S. Irmay, "On the theoretical derivation of Darcy and Forchheimer formulas," *Eos, Trans. Am. Geophys. Union*, vol. 39, no. 4, pp. 702–707, 1958.

[111] A. Kouidri and B. Madani, "Experimental hydrodynamic study of flow through metallic foams: Flow regime transitions and surface roughness influence," *Mech. Mater.*, vol. 99, pp. 79–87, 2016.

[112] I. F. Macdonald, M. S. El-Sayed, K. Mow, and F. A. L. Dullien, "Fow through porous media-the Ergun equation revisited," *Ind. Eng. Chem. Fundam.*, vol. 18, no. 3, pp. 199–208, 1979.

[113] L. Tadrist, M. Miscevic, O. Rahli, and F. Topin, "About the use of fibrous materials in compact heat exchangers," *Exp. Therm. Fluid Sci.*, vol. 28, no. 2–3, pp. 193–199, 2004.

[114] B. Dietrich, "Pressure drop correlation for ceramic and metal sponges," *Chem.*

Eng. Sci., vol. 74, pp. 192–199, 2012.

[115] Z. Li, J. Wan, K. Huang, W. Chang, and Y. He, "Effects of particle diameter on flow characteristics in sand columns," *Int. J. Heat Mass Transf.*, vol. 104, pp. 533–536, 2017.

[116] I. Kececioglu and Y. Jiang, "Flow through porous media of packed spheres saturated with water," *J. Fluids Eng. ASME*, vol. 116, pp. 164–170, 1994.

[117] P. Venkataraman and P. Rama Mohan Rao, "Darcian, transitional, and turbulent flow through porous media," *J. Hydraul. Eng.*, vol. 124, no. 8, pp. 840–846, 1998.

[118] E. Skjetne and J. L. Auriault, "High-velocity laminar and turbulent flow in porous media," *Transp. Porous Media*, vol. 36, pp. 131–147, 1999.

[119] M. Teitel, "On the applicability of the Forchheimer equation in simulating flow through woven screens," *Biosyst. Eng.*, vol. 109, no. 2, pp. 130–139, 2011.

[120] Z. Li, Y. Haramura, Y. Kato, and D. Tang, "Analysis of a high performance model Stirling engine with compact porous-sheets heat exchangers," *Energy*, vol. 64, pp. 31–43, 2014.

[121] S. Mahjoob and K. Vafai, "A synthesis of fluid and thermal transport models for metal foam heat exchangers," *Int. J. Heat Mass Transf.*, vol. 51, no. 15–16, pp. 3701–3711, 2008.

[122] K. Boomsma and D. Poulikakos, "On the effective thermal conductivity of a three-dimensionally structured fluid-saturated metal foam," *Int. J. Heat Mass Transf.*, vol. 44, no. 4, pp. 827–836, 2001.

[123] S. Miwa and S. T. Revankar, "Hydrodynamic characterization of nickel metal foam, part 1: Single-phase permeability," *Transp. Porous Media*, vol. 80, no. 2, pp. 269–279, 2009.

[124] W. Zhong, X. Li, F. Liu, G. Tao, B. Lu, and T. Kagawa, "Measurement and correlation of pressure drop characteristics for air flow through sintered metal porous media," *Transp. Porous Media*, vol. 101, no. 1, pp. 53–67, 2014.

[125] L. Varshney and J. S. Saini, "Heat transfer and friction factor correlations for rectangular solar air heater duct packed with wire mesh screen matrices," *Sol. Energy*, vol. 62, no. 4, pp. 255–262, 1998.

[126] M. K. Mittal and L. Varshney, "Optimal thermohydraulic performance of a wire mesh packed solar air heater," *Sol. Energy*, vol. 80, no. 9, pp. 1112–1120, 2006.

[127] Z. Zhao and R. A. Wirtz, "Flow-through boiling of isopentane in structured-porous fins: Effects of system parameters," *J. Heat Transf. ASME*, vol. 134, no. 7, pp. 1–9, 2012.

[128] Y. Liu, G. Xu, X. Luo, H. Li, and J. Ma, "An experimental investigation on fluid flow and heat transfer characteristics of sintered woven wire mesh structures," *Appl. Therm. Eng.*, vol. 80, pp. 118–126, 2015.

[129] A. F. Miguel, "Airflow through porous screens: From theory to practical considerations," *Energy Build.*, vol. 28, no. 1, pp. 63–69, 1998.

[130] P. J. Richards and M. Robinson, "Wind loads on porous structures," *J. Wind Eng. Ind. Aerodyn.*, vol. 83, no. 1–3, pp. 455–465, 1999.

[131] J. Bear, *Dynamics of fluids in porous media*. New York: Dover Publication, INC., 1972.

[132] J. F. Liu, W. T. Wu, W. C. Chiu, and W. H. Hsieh, "Measurement and correlation of friction characteristic of flow through foam matrixes," *Exp. Therm. Fluid Sci.*, vol. 30, pp. 329–336, 2006.

[133] S. Mancin, C. Zilio, A. Cavallini, and L. Rossetto, "Pressure drop during air flow in aluminum foams," *Int. J. Heat Mass Transf.*, vol. 53, no. 15–16, pp. 3121–3130, 2010.

[134] P. Du Plessis, A. Montillet, J. Comiti, and J. Legrand, "Pressure drop prediction for flow through high porosity metallic foams," *Chem. Eng. Sci.*, vol. 49, no. 21, pp. 3545–3553, 1994.

[135] S. C. Tzeng and T. M. Jeng, "Interstitial heat transfer coefficient and dispersion conductivity in compressed metal foam heat sinks," *J. Electron. Packag. ASME*, vol. 129, no. 2, pp. 113–119, 2007.

[136] B. Kotresha and N. Gnanasekaran, "Determination of interfacial heat transfer coefficient for the flow assisted mixed convection through brass wire mesh," *Int. J. Therm. Sci.*, vol. 138, pp. 98–108, 2019.

[137] S. B. Prasad, J. S. Saini, and K. M. Singh, "Investigation of heat transfer and friction characteristics of packed bed solar air heater using wire mesh as packing material," *Sol. Energy*, vol. 83, no. 5, pp. 773–783, 2009.

[138] J. P. Bonnet, F. Topin, and L. Tadrist, "Flow laws in metal foams: Compressibility and pore size effects," *Transp. Porous Media*, vol. 73, no. 2, pp. 233–254, 2008.

[139] A. Kołodziej and J. Łojewska, "Flow resistance of wire gauzes," *AIChE J.*, vol. 55, no. 1, pp. 215–228, 2009.

[140] K. Hamaguchi, S. Takahashi, and H. Miyabe, "Heat transfer characteristics of regenerator matrix : case of packed wire gauzes," *Trans. Japan Soc. Mech. Eng. Ser. B*, vol. 49, no. 445, pp. 2001–2010, 1983.

[141] K. Vafai and C. L. Tien, "Boundary and inertia effects on convective mass transfer in porous media," *Int. J. Heat Mass Transf.*, vol. 25, no. 8, pp. 1183–1190, 1980.

[142] J. Tian, T. J. Lu, H. P. Hodson, D. T. Queheillalt, and H. N. G. Wadley, "Cross flow heat exchange of textile cellular metal core sandwich panels," *Int. J. Heat Mass Transf.*, vol. 50, no. 13–14, pp. 2521–2536, 2007.

[143] T. J. Lu, A. G. Evans, and J. W. Hutchinson, "The effects of material properties on heat dissipation in high power electronics," *J. Electron. Packag. ASME*, vol. 120, no. 3, pp. 280–289, 1998.

[144] A. L. Avila-Marin, J. Fernandez-Reche, M. Casanova, C. Caliot, and G. Flamant, "Numerical simulation of convective heat transfer for inline and stagger stacked

plain-weave wire mesh screens and comparison with a local thermal non-equilibrium model," in *AIP Conference Proceedings*, 2017, vol. 1850, no. 2017.

[145] A. L. London, J. W. Mitchell, and W. A. Sutherland, "Heat-transfer and flow-friction characteristics of crossed-rod matrices," *J. Heat Transf. ASME*, vol. 82, no. 3, pp. 199–213, Aug. 1960.

[146] K. I. Salas and A. M. Waas, "Convective heat transfer in open cell metal foams," *J. Heat Transf. ASME*, vol. 129, no. 9, pp. 1217–1229, 2007.

[147] X. lin Xia, X. Chen, C. Sun, Z. huan Li, and B. Liu, "Experiment on the convective heat transfer from airflow to skeleton in open-cell porous foams," *Int. J. Heat Mass Transf.*, vol. 106, pp. 83–90, 2017.

[148] C. Li and G. P. Peterson, "Parametric study of pool boiling on horizontal highly conductive microporous coated surfaces," *J. Heat Transf. ASME*, vol. 129, no. 11, pp. 1465–1475, 2007.

[149] A. L. London, J. W. Mitchell, and W. A. Sutherland, "Heat-transfer and flow-friction characteristics of crossed-rod matrices," *J. Heat Transfer*, vol. 82, no. 3, pp. 199–213, Aug. 1960.

[150] W. S. Chang, "Porosity and effective thermal conductivity of wire screens," *J. Heat Transf. ASME*, vol. 112, no. 1, pp. 5–9, 1990.

[151] E. Oró, J. Chiu, V. Martin, and L. F. Cabeza, "Comparative study of different numerical models of packed bed thermal energy storage systems," *Appl. Therm. Eng.*, vol. 50, no. 1, pp. 384–392, 2013.

[152] F. Darabi, "Heat and momentum transfer in packed beds," University of Leeds (Department of Chemical Engineering), 1982.

[153] S. S. Halkarni, A. Sridharan, and S. V. Prabhu, "Estimation of volumetric heat transfer coefficient in randomly packed beds of uniform sized spheres with water as working medium," *Int. J. Therm. Sci.*, vol. 110, pp. 340–355, 2016.

[154] T. E. W. Schumann, "Heat transfer: A liquid flowing through a porous prism," *J. Franklin Inst.*, vol. 208, no. 3, pp. 405–416, 1929.

[155] C. C. Chen, P. C. Huang, and H. Y. Hwang, "Enhanced forced convective cooling of heat sources by metal-foam porous layers," *Int. J. Heat Mass Transf.*, vol. 58, pp. 356–373, 2013.

[156] C. Ranganayakulu, X. Luo, and S. Kabelac, "The single-blow transient testing technique for offset and wavy fins of compact plate-fin heat exchangers," *Appl. Therm. Eng.*, vol. 111, pp. 1588–1595, 2017.

[157] P. J. Heggs and D. Burns, "Single-blow experimental prediction of heat transfer coefficients: A comparison of four commonly used techniques," *Exp. Therm. Fluid Sci.*, vol. 1, no. 3, pp. 243–251, 1988.

[158] P.-H. Chert and Z.-C. Chang, "An improved model for the single-blow measurement including the non-adiabatic side wall effect," *Int. Commun. Heat Mass Transf.*, vol. 23, no. 1, pp. 55–68, 1996.

[159] P.-H. Chen and Z.-C. Chang, "Measurements of thermal performance of cryocooler regenerators using an improved single-blow method," *Int. J. Heat Mass Transf.*, vol. 40, no. 10, pp. 2341–2349, 1997.

[160] K. K. Nielsen, K. Engelbrecht, and C. R. H. Bahl, "The influence of flow maldistribution on the performance of inhomogeneous parallel plate heat exchangers," *Int. J. Heat Mass Transf.*, vol. 60, no. 1, pp. 432–439, 2013.

[161] V. V. Calmidi and R. L. Mahajan, "Forced convection in high porosity metal foams," *J. Heat Transf. ASME*, vol. 122, no. 3, pp. 557–565, 2000.

[162] D. Geb, F. Zhou, and I. Catton, "Internal heat transfer coefficient determination in a packed bed from the transient response due to solid phase induction heating," *J. Heat Transf. ASME*, vol. 134, no. 4, pp. 1–10, 2012.

[163] V. V. Calmidi and R. L. Mahajan, "Forced convection in high porosity metal foams," *J. Heat Transf. ASME*, vol. 122, no. 3, pp. 557–565, Aug. 2000.

[164] K. Kamiuto and S. S. Yee, "Heat transfer correlations for open-cellular porous materials," *Int. Commun. Heat Mass Transf.*, vol. 32, no. 7, pp. 947–953, 2005.

[165] J. D. Jones, "Inhomogeneity of fluid flow in stirling engine regenerators," *J. Eng. Gas Turbines Power-transactions ASME*, vol. 111, no. 4, pp. 595–600, 1989.

[166] X. Fu, R. Viskanta, and J. P. Gore, "Measurement and correlation of volumetric heat transfer coefficients of cellular ceramics," *Exp. Therm. Fluid Sci.*, vol. 17, no. 4, pp. 285–293, 1998.

[167] Z. Wu, C. Caliot, G. Flamant, and Z. Wang, "Numerical simulation of convective heat transfer between air flow and ceramic foams to optimise volumetric solar air receiver performances," *Int. J. Heat Mass Transf.*, vol. 54, no. 7–8, pp. 1527–1537, 2011.

[168] K. Ichimiya, "A new method for evaluation of heat transfer between solid material and fluid in a porous medium," *J. Heat Transf. ASME*, vol. 121, no. 4, pp. 978–983, 1999.

[169] D. Y. Lee and K. Vafai, "Analytical characterization and conceptual assessment of solid and fluid temperature differentials in porous media," *Int. J. Heat Mass Transf.*, vol. 42, no. 3, pp. 423–435, 1998.

[170] S. Y. Kim, B. H. Kang, and J. H. Kim, "Forced convection from aluminum foam materials in an asymmetrically heated channel," *Int. J. Heat Mass Transf.*, vol. 44, no. 7, pp. 1451–1454, 2001.

[171] N. S. Thakur, J. S. Saini, and S. C. Solanki, "Heat transfer and friction factor correlations for packed bed solar air heater for a low porosity system," *Sol. Energy*, vol. 74, no. 4, pp. 319–329, 2003.

[172] T. Fend, B. Hoffschmidt, R. Pitz-Paal, O. Reutter, and P. Rietbrock, "Porous materials as open volumetric solar receivers: Experimental determination of thermophysical and heat transfer properties," *Energy*, vol. 29, no. 5–6, pp. 823–833, 2004.

[173] Y. S. Sim and Y. Wen-Jei, "New performance-evaluation analyses on heat transfer surfaces by single-blow technique," *Int. J. Heat Mass Transf.*, vol. 30, no. 8, pp. 1587–1594, 1987.

[174] J. Ma, P. Lv, X. Luo, Y. Liu, H. Li, and J. Wen, "Experimental investigation of flow and heat transfer characteristics in double-laminated sintered woven wire mesh," *Appl. Therm. Eng.*, vol. 95, pp. 1–9, 2016.

[175] M. L. Hunt and C. L. Tien, "Effects of thermal dispersion on forced convection in fibrous media," *Int. J. Heat Mass Transf.*, vol. 31, no. 2, pp. 301–309, 1988.

[176] B. Dietrich, "Heat transfer coefficients for solid ceramic sponges-experimental results and correlation," *Int. J. Heat Mass Transf.*, vol. 61, no. 1, pp. 627–637, 2013.

[177] G. J. Hwang, C. C. Wu, and C. H. Chao, "Investigation of non-Darcian forced convection in an asymmetrically heated sintered porous channel," *J. Heat Transf. ASME*, vol. 117, no. 3, pp. 725–732, 1995.

[178] E. Achenbach, "Heat and flow characteristics of packed beds," *Exp. Therm. Fluid Sci.*, vol. 10, no. 1, pp. 17–27, 1995.

[179] R. Chennu, "Steady state and transient analysis of compact plate-fin heat exchanger fins for generation of design data using CFD," *Int. J. Numer. Methods Heat Fluid Flow*, vol. 26, no. 2, pp. 440–460, 2016.

[180] B. S. Baclic, P. J. Heggs, and H. Z. Z. Abou Ziyan, "Differential fluid enthalpy method for predicting heat transfer coefficients in packed beds," in *Heat Transfer, Proceedings of the International Heat Transfer Conference*, 1986, vol. 5, pp. 2616–2622.

[181] J. H. Stang and J. E. Bush, "Periodic method for testing compact heat exchanger surfaces," *J. Eng. Power-transactions ASME*, vol. 96, no. 2, pp. 87–94, Apr. 1974.

[182] C.-H. Cheng and C.-S. Huang, "Extended model for single-blow transient testing method in evaluating thermal performance of heat transfer surfaces," *Int. J. Heat Mass Transf.*, vol. 21, pp. 53–63, 1994.

[183] P. F. Pucci, C. P. Howard, and C. H. Piersall, "The Single-Blow Transient Testing Technique for Compact Heat Exchanger Surfaces," *J. Eng. Power-transactions ASME*, vol. 89, no. 1, pp. 29–38, 1967.

[184] C.-H. Li and R. K. Shah, "The maximum slope of single-blow transient testing for compact heat exchanger surfaces," *J. Heat Transf. ASME*, vol. 107, no. 1, pp. 264–267, Feb. 1985.

[185] R. S. Mullisen and R. I. Loehrke, "A transient heat exchanger evaluation test for arbitrary fluid inlet temperature variation and longitudinal core conduction," *J. Heat Transf. ASME*, vol. 108, no. 2, pp. 370–376, May 1986.

[186] X. Luo, W. Roetzel, and U. Lüdersen, "Single-blow transient testing technique considering longitudinal core conduction and fluid dispersion," *Int. J. Heat Mass Transf.*, vol. 44, no. 1, pp. 121–129, 2001.

[187] C. Z.H, L. M.L, W. Y.W, and R. H.S, "A modified selected point matching technique for testing compact heat exchanger surfaces," *Int. J. Heat Mass Transf.*, vol. 27, no. 7, pp. 971–978, Jul. 1984.

[188] K. Krishnakumar, A. K. John, and G. Venkatarathnam, "A review on transient test techniques for obtaining heat transfer design data of compact heat exchanger surfaces," *Exp. Therm. Fluid Sci.*, vol. 35, no. 4, pp. 738–743, 2011.

[189] R. I. Loehrke, "Evaluating the results of the single-blow transient heat exchanger test," *Exp. Therm. Fluid Sci.*, vol. 3, no. 6, pp. 574–580, 1990.

[190] H. Ren, L. Lai, and Y. Cui, "Sensitivity analysis and numerical experiments on transient test of compact heat exchanger surfaces," *Front. Energy Power Eng. China*, vol. 2, no. 4, pp. 374–380, 2008.

[191] C. Y. Liang and W.-J. Yang, "Modified single-blow technique for performance evaluation on heat transfer surfaces," *J. Appl. Mech. ASME*, vol. 97, no. 1, pp. 16–21, Feb. 1975.

[192] H. Hausen, "Über den wärmeaustausch in regeneratoren," *Tech. Mech. und Thermodyn.*, vol. 1, no. 7, pp. 250–256, 1930.

[193] G. F. Kohlmayr, "Implementation of direct curve matching methods for transient matrix heat transfer testing," *Appl. Sci. Res.*, vol. 24, no. 1, pp. 127–148, Dec. 1971.

[194] G. F. Kohlmayr, "Extension of the Maximum Slope Method to Arbitrary Upstream Fluid Temperature Changes," *J. Heat Transf. Trans. ASME*, pp. 130–135, 1968.

[195] G. L. Locke, "Heat transfer and flow friction characteristics of porous solids," California, Stanford University. Department of Mechanical Engineering, 1950.

[196] C. P. Howard, "The single-blow problem including the effects of longitudinal conduction," in *ASME 1964 Gas Turbine Conference and Products Show*, 1964, no. 3, p. 10.

[197] K. Krishnakumar and G. Venkatarathnam, "On the use of time at maximum slope in determining the heat transfer coefficients in complex surfaces using the single blow transient test method," *Int. J. Heat Exch.*, vol. 8, no. 1, pp. 31–44, Jun. 2007.

[198] J. I. Rodriguez and A. F. Mills, "Analysis of the single-blow transient testing technique for perforated plate heat exchangers," *International Journal of Heat and Mass Transfer*, vol. 33, no. 9. pp. 1969–1976, 1990.

[199] C. C. Furnas, "Heat transfer from a gas stream to a bed of broken solids-II," *Ind. Eng. Chem.*, vol. 22, no. 7, pp. 721–731, Jul. 1930.

[200] G. F. Kohlmayr, "Exact maximum slopes for transient matrix heat-transfer testing," *Int. J. Heat Mass Transf.*, vol. 9, no. 7, pp. 671–680, Jul. 1966.

[201] G. F. Kohlmayr and D. Lombari, "A short table of maximum slopes for transient matrix heat-transfer testing," *J. Heat Transf. Trans. ASME*, vol. 92, no. 3, pp. 558–559, 1970.

[202] J. R. Mondt and D. C. Siegla, "Performance of perforated heat exchanger surfaces," *J. Eng. Power-transactions ASME*, vol. 96, no. 2, pp. 81–86, Apr. 1974.

[203] G. F. Kohlmayr, "An indirect curve matching method for transient matrix heat-transfer testing in the low Ntu-range," *Int. J. Heat Mass Transf.*, vol. 11, no. 3, pp. 567–581, Mar. 1968.

[204] S. C. Chapra and R. P. Canale, "Numerical methods for engineers," *Math. Comput. Simul.*, vol. 33, no. 3, p. 260, 1991.

[205] S. Chapra and R. Canale, *NUMERICAL METHODS FOR ENGINEERS, SEVENTH EDITION*. McGraw-Hill Science/Engineering/Math, 2015.

[206] S. Alfarawi, R. AL-Dadah, and S. Mahmoud, "Transient Investigation of Mini-Channel Regenerative Heat Exchangers: Combined Experimental and CFD Approach," *Appl. Therm. Eng.*, vol. 125, pp. 346–358, 2017.

[207] "Inoxia Ltd - Woven wire mesh, chemicals and ball milling equipment." [Online]. Available: https://www.inoxia.co.uk/. [Accessed: 18-Dec-2019].

[208] "Erodatools Ltd - Electrical discharge machining (EDM) tools." [Online]. Available: https://www.erodatoolsltd.co.uk/. [Accessed: 18-Dec-2019].

[209] J. Xu and R. A. Wirtz, "In-plane effective thermal conductivity of symmetric, diamond-weave screen laminates," *J. Electron. Packag. ASME*, vol. 127, no. 3, pp. 353–356, Sep. 2005.

[210] N. Tsolas, "Thermal spray forming of high-efficiency metal-foam heat exchangers," University of Toronto, 2010.

[211] R. Goodall, A. Marmottant, L. Salvo, and A. Mortensen, "Spherical pore replicated microcellular aluminium: Processing and influence on properties," *Mater. Sci. Eng. A*, vol. 465, no. 1–2, pp. 124–135, Sep. 2007.

[212] B. R. Munson, A. P. Rothmayer, T. H. Okiishi, and W. W. Huebsch, *Fundamentals of fluid mechanics*, 7th editio. John Wiley & Sons, Inc., 2013.

[213] "National Instruments Corporation (U.K.) Ltd." [Online]. Available: https://www.ni.com/en-gb.html. [Accessed: 18-Dec-2019].

[214] F. Barari, "Metal foam regenerators; heat transfer and pressure drop in porous metals," The University of Sheffield, 2014.

[215] B. E. I. 5167-1:2003, "Measurement of fluid flow by means of pressure differential devices inserted in circular cross-section conduits running full —Part 4: Venturi tubes," *ISO - Int. Organ. Stand.*, p. 26, 2003.

[216] M. Firdaouss, J.-L. Guermond, and P. Le Quéré, "Nonlinear corrections to Darcy's law at low Reynolds numbers," *J. Fluid Mech.*, vol. 343, pp. 331–350, Jul. 1997.

[217] E. Skjetne and J. L. Auriault, "New insights on steady, non-linear flow in porous media," *Eur. J. Mech. - B/Fluids*, vol. 18, no. 1, pp. 131–145, Jan. 1999.

[218] M. Muskat, "The flow of fluids through porous media," *J. Appl. Phys.*, vol. 8, no. 4, pp. 274–282, 1937.

[219] R. E. Hayes, A. Afacan, and B. Boulanger, "An equation of motion for an incompressible Newtonian fluid in a packed bed," *Transp. Porous Media*, vol. 18, no. 2, pp. 185–198, Feb. 1995.

[220] S. Whitaker, "The equations of motion in porous media," *Chem. Eng. Sci.*, vol. 21, no. 3, pp. 291–300, Mar. 1966.

[221] M. Panfilov and M. Fourar, "Physical splitting of nonlinear effects in high-velocity stable flow through porous media," *Adv. Water Resour.*, vol. 29, no. 1, pp. 30–41, Jan. 2006.

[222] D. Seguin, A. Montillet, and J. Comiti, "Experimental characterisation of flow regimes in various porous media—I: Limit of laminar flow regime," *Chem. Eng. Sci.*, vol. 53, no. 21, pp. 3751–3761, Nov. 1998.

[223] N. Dukhan and M. Ali, "Effect of confining wall on properties of gas flow through metal foam: an experimental study," *Transp. Porous Media*, vol. 91, no. 1, pp. 225–237, Jan. 2012.

[224] M. S. Phanikumar and R. L. Mahajan, "Non-Darcy natural convection in high porosity metal foams," *Int. J. Heat Mass Transf.*, vol. 45, no. 18, pp. 3781–3793, Aug. 2002.

[225] J. G. Fourie and J. P. Du Plessis, "Pressure drop modelling in cellular metallic foams," *Chem. Eng. Sci.*, vol. 57, no. 14, pp. 2781–2789, Jul. 2002.

[226] S. C. Costa, H. Barrutia, J. A. Esnaola, and M. Tutar, "Numerical study of the pressure drop phenomena in wound woven wire matrix of a Stirling regenerator," *Energy Convers. Manag.*, vol. 67, pp. 57–65, Mar. 2013.

[227] A. Kołodziej and J. Łojewska, "Experimental and modelling study on flow resistance of wire gauzes," *Chem. Eng. Process. Process Intensif.*, vol. 48, no. 3, pp. 816–822, Mar. 2009.

[228] K. Hamagutci, S. Takahashi, and H. Miyabe, "Flow friction and heat transfer characteristics of a regenerator matrix : Case of foamed metal," *Trans. JAPAN Soc. Mech. Eng. Ser. B*, vol. 49, no. 445, pp. 1991–2000, 1983.

[229] J. . D'Errico, "Slm-shape Language Modeling.," *MATLAB Central File Exchange*, 2017. [Online]. Available: http://www.mathworks.com/matlabcentral/fileexchange/24443. [Accessed: 11-May-2021].

[230] M. S. Lewis-Beck and A. Skalaban, "The R -squared: some straight talk," *Polit. Anal.*, vol. 2, pp. 153–171, Jan. 1990.

[231] F. Duprat and G. Lopez Lopez, "Comparison of performance of heat regenerators: Relation between heat transfer efficiency and pressure drop," *Int. J. Energy Res.*, vol. 25, no. 4, pp. 319–329, Mar. 2001.

[232] U. Brockmeier, T. Guentermann, and M. Fiebig, "Performance evaluation of a vortex generator heat transfer surface and comparison with different high

performance surfaces," *Int. J. Heat Mass Transf.*, vol. 36, no. 10, pp. 2575–2587, 1993.

Appendix 1: Advanced single-blow model for this study

➢ **Derivation of energy equations**

Assuming the solid and the fluid are initially at uniform temperature then a sudden change in the inlet air temperature occurs. One-dimensional energy balance equations can be applied on an incremental volume of length Δx and at an instant of time, as shown in Figure 10.1. The air flows at high temperatures through the matrix, hence heat is transferred to the matrix and the wall simultaneously at all positions along the flow direction.
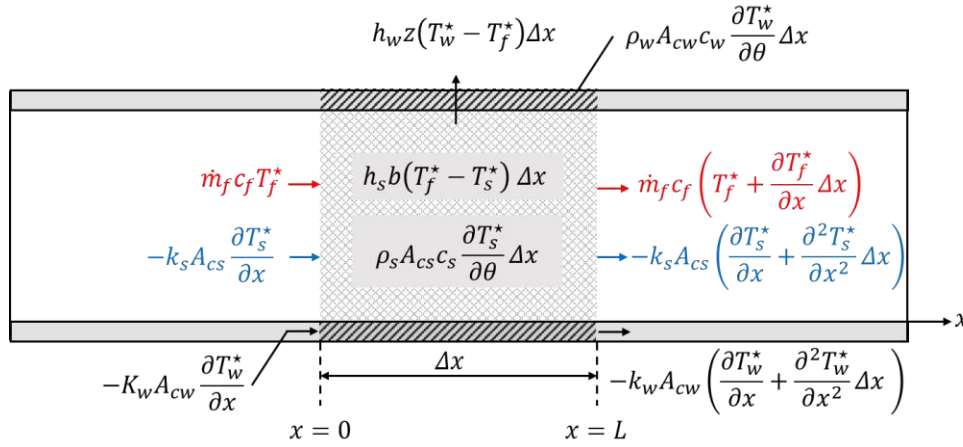
Figure 10.1 Energy balance in control volume of the complex.

Starting with the first law of thermodynamics, the energy content of the entering fluid equals the energy transferred to the wall and matrix materials and the energy in the leaving air; the single-blow system can be described by the following three partial differential equations for the fluid, the test regenerator matrix, and the side-wall, respectively:

$$\dot{m}_f c_f T_f^\star - \dot{m}_f c_f \left(T_f^\star + \frac{\partial T_f^\star}{\partial x} \Delta x \right) - h_s b \left(T_f^\star - T_s^\star \right) \Delta x - h_w z \left(T_f^\star - T_w^\star \right) \Delta x = 0 \qquad 10.1$$

$$\rho_s A_{cs} c_s \frac{\partial T_s^\star}{\partial \theta} \Delta x + h_s b \left(T_s^\star - T_f^\star \right) \Delta x + k_s A_{cs} \frac{\partial T_s^\star}{\partial x} - k_s A_{cs} \left(\frac{\partial T_s^\star}{\partial x} + \frac{\partial^2 T_s^\star}{\partial x^2} \Delta x \right) = 0 \qquad 10.2$$

$$\rho_w A_{cw} c_w \frac{\partial T_w^\star}{\partial \theta} \Delta x + h_w z \left(T_w^\star - T_f^\star \right) \Delta x + K_w A_{cw} \frac{\partial T_w^\star}{\partial x} - k_w A_{cw} \left(\frac{\partial T_w^\star}{\partial x} + \frac{\partial^2 T_w^\star}{\partial x^2} \Delta x \right) = 0 \qquad 10.3$$

The energy equations can be rearranged and rewritten as:

$$\dot{m}_f c_f \frac{\partial T_f^\star}{\partial x} \varDelta x + h_s b \left(T_f^\star - T_s^\star \right) \varDelta x + h_w z \left(T_f^\star - T_w^\star \right) \varDelta x = 0 \qquad \text{10.4}$$

$$\rho_s A_{cs} c_s \frac{\partial T_s^\star}{\partial \theta} \varDelta x + h_s b \left(T_s^\star - T_f^\star \right) \varDelta x - k_s A_{cs} \frac{\partial^2 T_s^\star}{\partial x^2} \varDelta x = 0 \qquad \text{10.5}$$

$$\rho_w A_{cw} c_w \frac{\partial T_w^\star}{\partial \theta} \varDelta x + h_w z \left(T_w^\star - T_f^\star \right) \varDelta x - k_w A_{cw} \frac{\partial^2 T_w^\star}{\partial x^2} \varDelta x = 0 \qquad \text{10.6}$$

Where

- $T_f^\star$ is fluid temperature, $T_s^\star$ is solid temperature and $T_w^\star$ is sidewall temperature.

- b and z are flow passage perimeters for the matrix and the side-wall respectively. θ is time and $\dot{m}$ is the fluid mass flow rate,

- A_c is the cross-sectional area, ρ is density, c is specific heat, k is effective thermal conductivity and h convective heat transfer coefficient. Subscripts (f), (s) and (w) indicate fluid, solid matrix and sidewall respectively.

- $\rho_s A_{cs} c_s \frac{\partial T_s^\star}{\partial \theta} \varDelta x$ is energy adsorbed by solid.

- $h_s b \left(T_f^\star - T_s^\star \right) \varDelta x$ is heat transferred to the solid by convection.

- $- k_s A_{cs} \frac{\partial^2 T_s^\star}{\partial x^2} \varDelta x$ is heat transferred in solid by conduction

- $\dot{m} c_f \frac{\partial T_f^\star}{\partial x} \varDelta x$ is heat transferred from the fluid by convection.

Note that the thermal capacitance of the fluid contained at any time within the matrix is small compared with the thermal capacitance of the matrix. That is, the fluid is normally restricted to a gas and the results to be presented will not be expected to apply for liquid fluids [196]. This also means that for the fluid, there will be no time-dependent terms in the equations and the energy accumulated by the fluid within the sample at any time can be neglected $(A_{cf} \rho_f C_f \frac{\partial T_f}{\partial \tau} \varDelta x \simeq 0)$. According to Cheng and Huang [182], the impact of this term depends upon the ratio of the heat capacity of the working fluid to the heat capacity of the matrix. For heat capacities ratios between 0.2 and 0.3, which is the range in this work, the existence of this term may lower the value

of maximum slope by 9% or less. By introducing the dimensionless variables or parameters given in Equation 10.7 to the energy equations,

$$T_w = \frac{T_w^\star - T_0^\star}{T_{f\,max}^\star - T_0^\star}, \qquad X = \frac{x^\star}{L}, \qquad t = \frac{\dot{m}c_f}{m_s c_s}\theta$$

$$NTU_s = \frac{h_s A_{HT}}{\dot{m}_f c_p}, \qquad NTU_w = \frac{h_w A_{hw}}{\dot{m}_f c_p} \qquad\qquad 10.7$$

$$\lambda_s = \frac{k_s A_{cs}}{\dot{m}_f c_p L}, \lambda_w = \frac{k_w A_{cw}}{\dot{m}_f c_p L}, \quad R_{tc} = \frac{M_s c_s}{M_w c_w}$$

> **Converting energy equations to non-dimensional form**

The derivation of the non-dimensionalisation equations can be done as:

$$\frac{\partial T_f^\star}{\partial x} = \frac{\partial T_f}{\partial (LX)} = \frac{1}{L}\frac{\partial T_f}{\partial X}$$

$$\frac{\partial T_s^\star}{\partial \theta} = \frac{\partial T_s}{\partial \left(\frac{m_s c_s}{\dot{m}c_f}t\right)} = \frac{\dot{m}c_f}{m_s c_s}\frac{\partial T_s}{\partial t}$$

$$\frac{\partial T_w^\star}{\partial \theta} = \frac{\partial T_w}{\partial \left(\frac{m_s c_s}{\dot{m}c_f}t\right)} = \frac{\dot{m}c_f}{m_s c_s}\frac{\partial T_w}{\partial t}$$

$$\frac{\partial^2 T_s^\star}{\partial x^2} = \frac{\partial}{\partial x}\left(\frac{\partial T_s}{\partial (LX)}\right) = \frac{\partial}{\partial (LX)}\left(\frac{\partial T_s}{\partial (LX)}\right) = \frac{1}{L^2}\frac{\partial^2 T_s}{\partial X^2}$$

$$\frac{\partial^2 T_w^\star}{\partial x^2} = \frac{\partial}{\partial x}\left(\frac{\partial T_w}{\partial (LX)}\right) = \frac{\partial}{\partial (LX)}\left(\frac{\partial T_w}{\partial (LX)}\right) = \frac{1}{L^2}\frac{\partial^2 T_w}{\partial X^2}$$

The dimensionless partial differential terms can be substituted into the dimensional energy equations as follows:

Into the fluid energy equation as:

$$\frac{\dot{m}_f c_f}{L}\frac{\partial T_f}{\partial X} + h_s b\left(T_f - T_s\right) + h_w z\left(T_f - T_w\right) = 0$$

$$\frac{\partial T_f}{\partial X} + \frac{h_s bL}{\dot{m}_f c_f}\left(T_f - T_s\right) + \frac{h_w zL}{\dot{m}_f c_f}\left(T_f - T_w\right) = 0$$

$$\frac{\partial T_f}{\partial X} + \frac{h_s A_{HT}}{\dot m_f c_f}\left(T_f - T_s\right) + \frac{h_w A_{HTw}}{\dot m_f c_f}\left(T_f - T_w\right) = 0$$

$$\frac{\partial T_f}{\partial X} + NTU_s\left(T_f - T_s\right) + NTU_w\left(T_f - T_w\right) = 0$$

Then, into the energy equation of the solid as:

$$\rho_s A_{cs} c_s \frac{\dot m c_f}{m_s c_s}\frac{\partial T_s}{\partial t} + h_s b\left(T_s - T_f\right) - \frac{k_s A_{cs}}{L^2}\frac{\partial^2 T_s}{\partial X^2} = 0$$

$$\frac{L\rho_s A_{cs} c_s}{m_s c_s}\frac{\partial T_s}{\partial t} + \frac{h_s b L}{\dot m c_f}\left(T_s - T_f\right) - \frac{k_s A_{cs}}{\dot m c_f L}\frac{\partial^2 T_s}{\partial X^2} = 0$$

$$\frac{\partial T_s}{\partial t} + \frac{h_s A_{TH}}{\dot m c_f}\left(T_s - T_f\right) - \frac{k_s A_{cs}}{\dot m c_f L}\frac{\partial^2 T_s}{\partial X^2} = 0$$

$$\frac{\partial T_s}{\partial t} + NTU_s\left(T_s - T_f\right) - \lambda_s \frac{\partial^2 T_s}{\partial X^2} = 0$$

And into the energy equation of sidewall as:

$$\rho_w A_{cw} c_w \frac{\dot m c_f}{m_s c_s}\frac{\partial T_w}{\partial t} + h_w z\left(T_w - T_f\right) - \frac{k_w A_{cw}}{L^2}\frac{\partial^2 T_w}{\partial X^2} = 0$$

$$\frac{L\rho_w A_{cw} c_w}{m_s c_s}\frac{\partial T_w}{\partial t} + \frac{h_w b L}{\dot m c_f}\left(T_w - T_f\right) - \frac{k_w A_{cw}}{\dot m c_f L}\frac{\partial^2 T_w}{\partial X^2} = 0$$

$$\frac{m_w c_w}{m_s c_s}\frac{\partial T_w}{\partial t} + \frac{A_{THw}}{\dot m c_f}\left(T_w - T_f\right) - \frac{k_w A_{cw}}{\dot m c_f L}\frac{\partial^2 T_w}{\partial X^2} = 0$$

$$\frac{\partial T_w}{\partial t} + R_{tc} NTU_w\left(T_w - T_f\right) - R_{tc}\lambda_s \frac{\partial^2 T_w}{\partial X^2} = 0$$

The energy equations can be expressed in dimensionless form as given in Equations 10.8-10.10.

$$\frac{\partial T_f}{\partial X} + NTU_s\left(T_f - T_s\right) + NTU_w\left(T_f - T_w\right) = 0 \qquad\qquad 10.8$$

$$\frac{\partial T_s}{\partial t} - \lambda_s \frac{\partial^2 T_s}{\partial X^2} + NTU_s\left(T_s - T_f\right) = 0 \qquad\qquad 10.9$$

$$\frac{\partial T_w}{\partial t} - R_{tc}.\lambda_w \frac{\partial^2 T_w}{\partial X^2} + NTU_w(T_w - T_f) = 0 \qquad 10.10$$

➢ **Discretisation and method of solution**

The dimensionless energy equations consist of three unknown variables: the fluid temperature T_f, solid temperature T_s, and the side-wall temperature T_w. Moreover, this model takes into consideration the longitudinal conduction in the tested sample and the side-wall, represented by second-order parabolic partial differential terms. Such a mathematical problem can only be solved numerically using the finite-difference methods (FDM) [159][187]. The temperature distribution was approximated by subjecting the energy equations to the following initial and boundary conditions.

$$t = 0 , \ T_s = T_w = 0$$
$$\left. \begin{array}{l} x = 0, T_f = f(t) \\ x = 0, \dfrac{\partial T_s}{\partial X} = 0, \dfrac{\partial T_w}{\partial X} = 0 \\ x = 1, \dfrac{\partial T_s}{\partial X} = 0, \dfrac{\partial T_w}{\partial X} = 0 \end{array} \right\} for \ t > 0 \qquad 10.11$$

The energy equations (Equations 10.8-10.10) were converted to finite-difference equations and solved numerically. First, the physical domain was divided into equal nodes in space. Knowing the initial values of $T_s \ and \ T_w$ from the initial conditions, the fluid temperature T_f at t^n can be approximated by discretising the dimensionless energy Equation 10.12 using a central difference scheme. The central difference scheme is a second-order accurate in space [183][204].
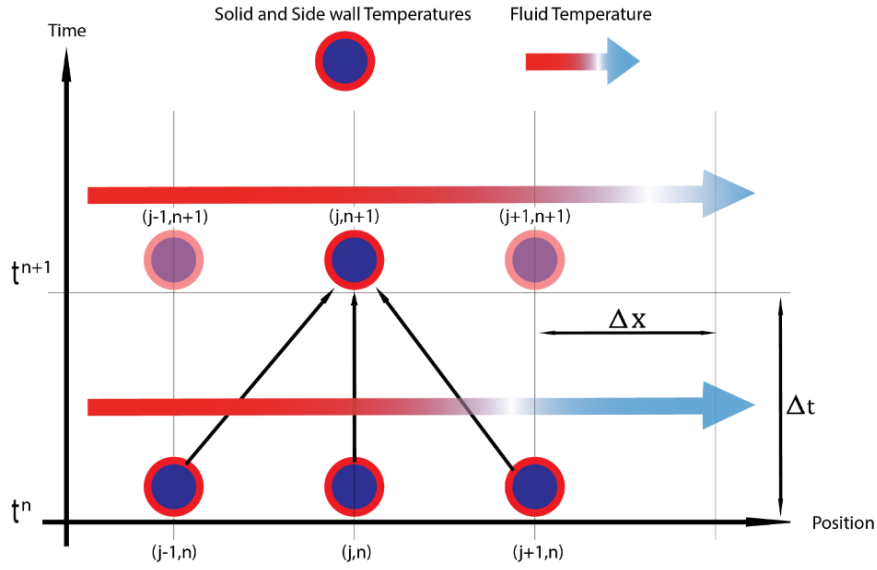
Figure 10.2 One-dimensional physical domain discretization.

The discretised equation can be written as:

$$T_{f,j}^n = \frac{(1 - R_{f1} - R_{f2})T_{s,j-1}^n + R_{f1}(T_{s,j}^n + T_{s,j-1}^n) + R_{f2}(T_{w,j}^n + T_{w,j-1}^n)}{(1 + R_{f1} + R_{f2})} \qquad 10.12$$

Where

$$R_{f1} = \frac{NTU_s.\Delta x}{2} \quad , \qquad R_{s1} = \frac{\lambda.\Delta t}{2\Delta x^2} \quad , \quad R_{s2} = \frac{NTU.\Delta t}{2}$$

$$R_{f2} = \frac{NTU_w.\Delta x}{2}, \quad R_{w1} = \frac{R_{tc}.\lambda_w.\Delta t}{2\Delta x^2}, and \quad R_{w2} = \frac{R_{tc}.NTU_w.\Delta t}{2} \qquad 10.13$$

By computing the fluid temperature T_f at t^n, the solid and side-wall temperatures distributed at t^{n+1} can be approximated in a time marching fashion using a forward explicit difference approximation. At a given time-step, the energy Equations 10.9, 10.10 can be constructed as:

$$T_{s,j}^{n+1} = 2R_{s1}(T_{s,j+1}^n - 2T_{s,j}^n + T_{s,j-1}^n) + 2R_{s2}(T_{f,j}^n - T_{s,j}^n) + T_{s,j}^n \qquad 10.14$$

$$T_{w,j}^{n+1} = 2R_{w1}(T_{w,j+1}^n - 2T_{w,j}^n + T_{w,j-1}^n) + 2R_{w2}(T_{f,j}^n - T_{w,j}^n) + T_{w,j}^n \qquad 10.15$$

Starting at the t^{n+1} time step, using the initial conditions and inlet boundary conditions, the distribution of the fluid temperature T_f at t^{n+1} can be obtained by reapplying Equation 10.12 again. This procedure continues to the end of the time nodes. This method is known as the explicit finite-difference scheme, which is second-order accurate in space, but is first-order accurate in time. Therefore, the initially approximated values of T_s and T_w were future corrected using the implicit Crank-Nicolson method. The energy Equations 10.9, 10.10 were further discretised and expressed respectively as:

$$\overline{T_{s,j}^{n+1}} = T_{s,j}^n + R_{s1}\left(\left(T_{s,j+1}^n - 2T_{s,j}^n + T_{s,j-1}^n\right) + \left(T_{s,j+1}^{n+1} - 2T_{s,j}^{n+1} + T_{s,j-1}^{n+1}\right)\right)$$

$$+ R_{s2}\left(\left(T_{f,j}^n - T_{s,j}^n\right) + \left(T_{f,j}^{n+1} - T_{s,j}^{n+1}\right)\right)$$

10.16

$$\overline{T_{w,j}^{n+1}} = T_{w,j}^n + R_{w1}\left(\left(T_{w,j+1}^n - 2T_{w,j}^n + T_{w,j-1}^n\right) + \left(T_{w,j+1}^{n+1} - 2T_{w,j}^{n+1} + T_{w,j-1}^{n+1}\right)\right)$$

$$+ R_{w2}\left(\left(T_{f,j}^n - T_{w,j}^n\right) + \left(T_{f,j}^{n+1} - T_{w,j}^{n+1}\right)\right)$$

10.17

➢ **Convergence and stability**

The convergence and stability are important in the finite-difference technique to ensure the technique is applicable and a reliable solution is achieved. Convergence of the numerical solution means Δx and Δt approach zero and the solution of the discretized equations tends the exact solution. In contrast, stability means the magnitude of error does not magnify in the course of the numerical solution process. The minimal time and position increments can be obtained by increasing the number of nodes in both the time and position directions. However, decreasing increments increases computational cost and time. It was reported that the explicit method is both convergent and stable if the diffusion factor $Di \leq 0.5$ where $Di = \lambda \Delta t / \Delta x^2$ [205]. The diffusion factor can be assessed in two different positions in the present model; in Equation 10.9 in which $Di = \lambda_s \Delta t / \Delta x^2$ and in Equation 10.10 where $Di = R_{tc}.\lambda_w \Delta t / \Delta x^2$. It has also been reported that if $Di \leq 0.5$, the solution might be stable and convergent, but the results might oscillate [205]. Setting $Di \leq 0.16$ to reduce the truncation error has also been recommended [205].

➢ Single-Blow Solution (MATLAB Coding)

A Matlab code was written to predict the outlet flow temperature response under various assumptions. The numerical code was written to be able to compute the maximum slope values for a wide range of modelling parameters and plotted against dimensionless time. The time increment was settled to be much lower than the distance increment to ensure the Di was much less than 0.16 at high flow rates and high thermal conductivities. By setting Δt at 0.0001 and Δx at 0.001 and applying three iterations for Crank-Nicolson correction, it was found that the solution was convergent, stable, and grid-independent. When the value of Δx was reduced further, the error was found to be ≤ 0.01%. The Matlab code was written as:

```
xx=250; %% Number of  intervals the length divided to
dx=1/(xx-1);%% Distance increment
tt=25000;%% Number of  intervals the time to
dt=0.0001;%% Time increment

NTU=10;%% NTUs value of the solid matrix
NTUw=0;%% NTUw value of the Side-wall
lambdas=0;%% Lambda of matrix
Rtc=0;%% Heat capacity ration of matrix to external wall
lambdaw=0;%% Lambda of Side-wall

A=1;% Wiebe function 1
B=1;% Wiebe function 2
tau=0.015153396;% time constant

%% constants for the solution
RS1=(0.5*lambdas*dt)/dx^2; %% soild constant 1
RS2=0.5*NTU*dt; %% soild constant 2
Rf1=0.5*NTU*dx;
RW1=(0.5*lambdaw*Rtc*dt)/dx^2; %% wall constant 1
RW2=0.5*NTUw*Rtc*dt; %% wall constant 2
Rf2=0.5*NTUw*dx;
%% matrix creation
tf=zeros(tt,xx);
ts=zeros(tt,xx);
tw=zeros(tt,xx);
tff=zeros(tt,xx);
tss=zeros(tt,xx);
tww=zeros(tt,xx);

%% time  and inlet fluid temperature calculations

t=linspace(0,tt*dt-dt,tt);
t=t.';
tf(1:end,1)=1-exp(-A*((t./tau).^B));

        for  i=2:tt
```

```matlab
        % explicit method

    for j=2:xx-1

        ts(i,1)= ts(i-1,1)+(NTU*dt*(tf(i-1,1)-ts(i-
1,1)))+((lambdas*dt*2*(ts(i-1,2)-ts(i-1,1))/dx^2)); % normal explicit for
any point at (t>0,x=0)..

        ts(i,j)= ts(i-1,j)+(NTU*dt*(tf(i-1,j)-ts(i-
1,j)))+((lambdas*dt*(ts(i-1,j+1)-2*ts(i-1,j)+ts(i-1,j-1))/dx^2)); % normal
explicit for any point at (t>0,L>x>0)..

        ts(i,xx)=(NTU*dt*(tf(i-1,xx)-ts(i-1,xx)))+ts(i-
1,xx)+((lambdas*dt*2*(ts(i-1,xx-1)-ts(i-1,xx))/dx^2)); % normal explicit
for a point at (t>0,x=L)..

        tw(i,1)= tw(i-1,1)+(NTUw*Rtc*dt*(tf(i-1,1)-tw(i-
1,1)))+((lambdaw*dt*2*(tw(i-1,2)-tw(i-1,1))/dx^2)); % normal explicit for
any point at (t>0,x=0)..

        tw(i,j)= tw(i-1,j)+(NTUw*Rtc*dt*(tf(i-1,j)-tw(i-
1,j)))+((lambdaw*Rtc*dt*(tw(i-1,j+1)-2*tw(i-1,j)+tw(i-1,j-1))/dx^2)); %
normal explicit for any point at (t>0,L>x>0)..

        tw(i,xx)=(NTUw*Rtc*dt*(tf(i-1,xx)-tw(i-1,xx)))+tw(i-
1,xx)+((lambdaw*dt*2*(tw(i-1,xx-1)-tw(i-1,xx))/dx^2)); % normal explicit
for a point at (t>0,x=L)..

    end
        for k=2:xx

        tf(i,k)=(((1-Rf1-Rf2)*tf(i,k-1))+Rf1*(ts(i,k)+ts(i,k-
1))+Rf2*(tw(i,k)+tw(i,k-1)))/(1+Rf1+Rf2);    % central difference scheme
for any point at (t>0,L>x>0).. .. see conduction in solid only

        end

        % Crank Neclson method

        for n=2:xx-1

        tss(i,n)= ts(i-1,n)+(RS1*(ts(i,n+1)-2*ts(i,n)+ts(i,n-1)+ts(i-
1,n+1)-2*ts(i-1,n)+ts(i-1,n-1)))+(RS2*(tf(i-1,n)-ts(i-1,n)+tf(i,n)-
ts(i,n))); % Crank Neclson for any point at (t>0,L>x>0).. see longitudinal
conduction in solid ref ..

        tww(i,n)= tw(i-1,n)+(RW1*(tw(i,n+1)-2*tw(i,n)+tw(i,n-1)+tw(i-
1,n+1)-2*tw(i-1,n)+tw(i-1,n-1)))+(RW2*(tf(i-1,n)-tw(i-1,n)+tf(i,n)-
tw(i,n))); % Crank Neclson for any point at (t>0,L>x>0).. see longitudinal
conduction in solid ref ..

        end

        ts(i,2:xx-1)=tss(i,2:xx-1);

        tw(i,2:xx-1)=tww(i,2:xx-1);
```

211

```
        for m=2:xx

        tf(i,m)=(((1-Rf1-Rf2)*tf(i,m-1))+Rf1*(ts(i,m)+ts(i,m-
1))+Rf2*(tw(i,m)+tw(i,m-1)))/(1+Rf1+Rf2); % central difference scheme for
any point at (t>0,L>x>0).. .. see conduction in solid only

        end
      end
 temp=tf(:,xx); % predicted temperature

 plot(t,temp) % predicted temperature vs time
```

➢ The validity of the solution

The accuracy of the numerical solutions was confirmed by comparing the output data with the numerical data for several modelling conditions available in the literature. The numerical data available for comparison shows the relationship between the maximum slope values and the number of transfer units. Therefore, the comparison was made based on this relationship and the response was compared with the published data in references [158][183][197]. Figure 10.3 shows excellent agreement between the current model solution and results published in references [183][197]for the ideal step change with and without the axial conduction effect. Figure 10.4 shows excellent agreement between the current model outputs and published numerical data that considers an exponential inlet temperature rise and non-adiabatic side-wall.

The theoretical results presented by Pucci et al. [183] are based on the numerical analysis conducted during the early 1960s when computer capability was limited. They solved the governing equations using the finite difference method. Early in the nineties, Chen et al. [13] obtained the solution using a similar implicit scheme. This scheme requires minor time and distance increments for an accurate solution. The governing equations were solved using the same method but with a time increment equal to 0.0001 and a distance increment of 1/1000, resulting in better accuracy. The purpose of this technical note is to explain the differences between the results of Pucci et al. [183], Chen et al. [13] and the present results shown in Figure 10.4.
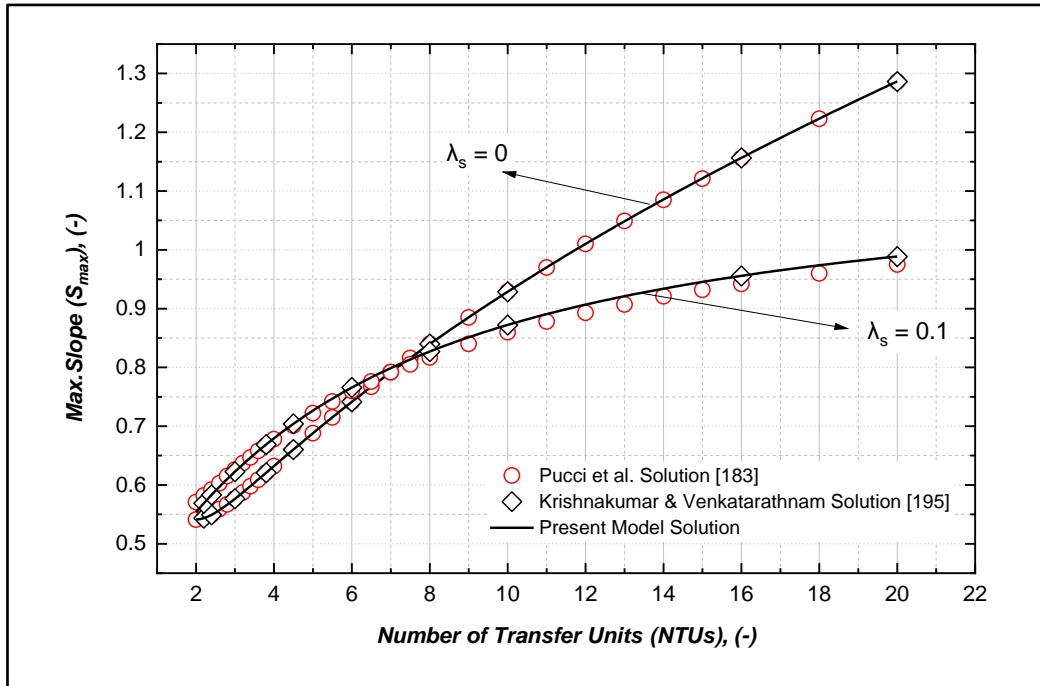
Figure 10.3 Validity of solution for different values of λ, adiabatic side-wall and ideal inlet fluid temperature.
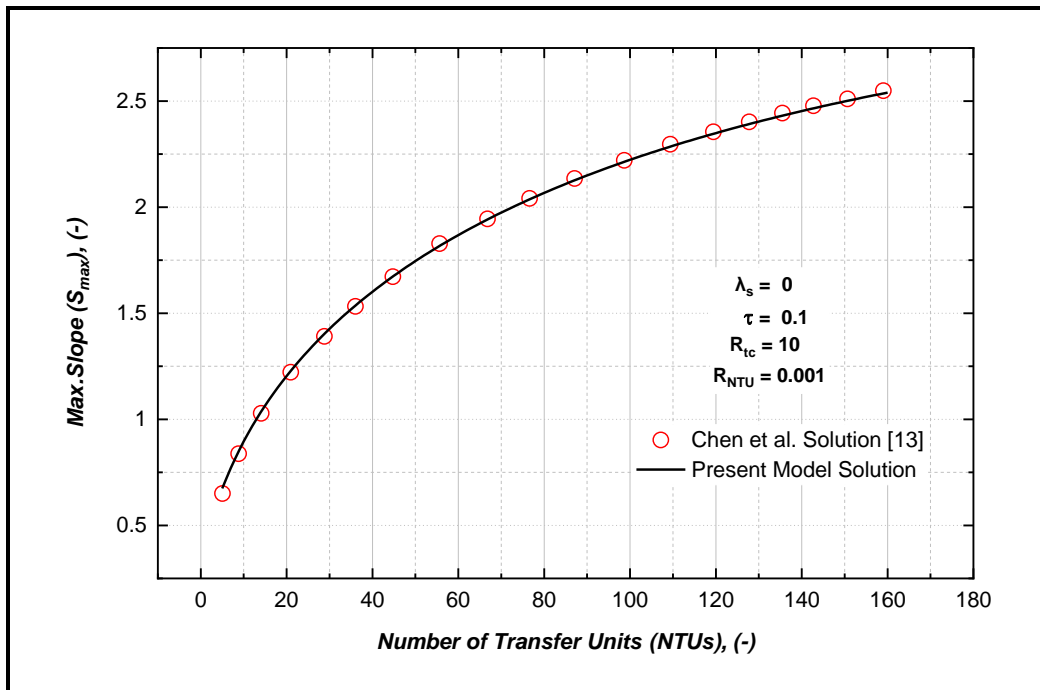
Figure 10.4 Validity of solution for non-adiabatic side-wall, no axial conduction and a step change for inlet fluid temperature.

213

Appendix 2: Orifice Plate Calibration

The micromotion was connected to the laboratory's compressed air source to measure the mass airflow rate as it passes through the system. The mass flow meter was connected to the Orifice plate using a 2.5m long PVC pipe with an internal diameter 51mm. The air density was calculated using the air pressure and temperature, measured downstream of the orifice plate. To obtain the meter coefficient, assumptions of the incompressible steady-state flow are made. If the friction loss is neglected, the conservation of energy equation (Bernoulli's equation) and the conservation of mass equation (the continuity equation) can be applied.

$$(P_1 - P_2) = 0.5 \, \rho \left(V_2{}^2 - V_1{}^2 \right)$$

$$A_1 V_1 = A_2 V_2$$

By Introducing the dimensionless factor β, which is the ratio of orifice hole area to pipe area, the theoretical volume flow rate can be given as:

$$q_v' = \frac{A_2 \sqrt{2(P_1 - P_2)/\rho}}{\sqrt{(1 - \beta^4)}}$$

The discharge coefficient is known as the ratio of the actual mass flow rate q_v to the theoretical mass flow rate q_v' and can be expressed as:

$$C = \frac{q_v \sqrt{(1 - \beta^4)}}{A_2 \sqrt{2\rho(P_1 - P_2)}}$$

In this study, the orifice plate, which has a 24.5 mm inner diameter, and the ratio of orifice hole area to pipe area equal 0.46, was calibrated. The actual mass flow rate, the pressure drop across the orifice plate, the pressure and temperature of the airflow was measured and tabulated below. The air density and the discharge coefficient were also obtained.
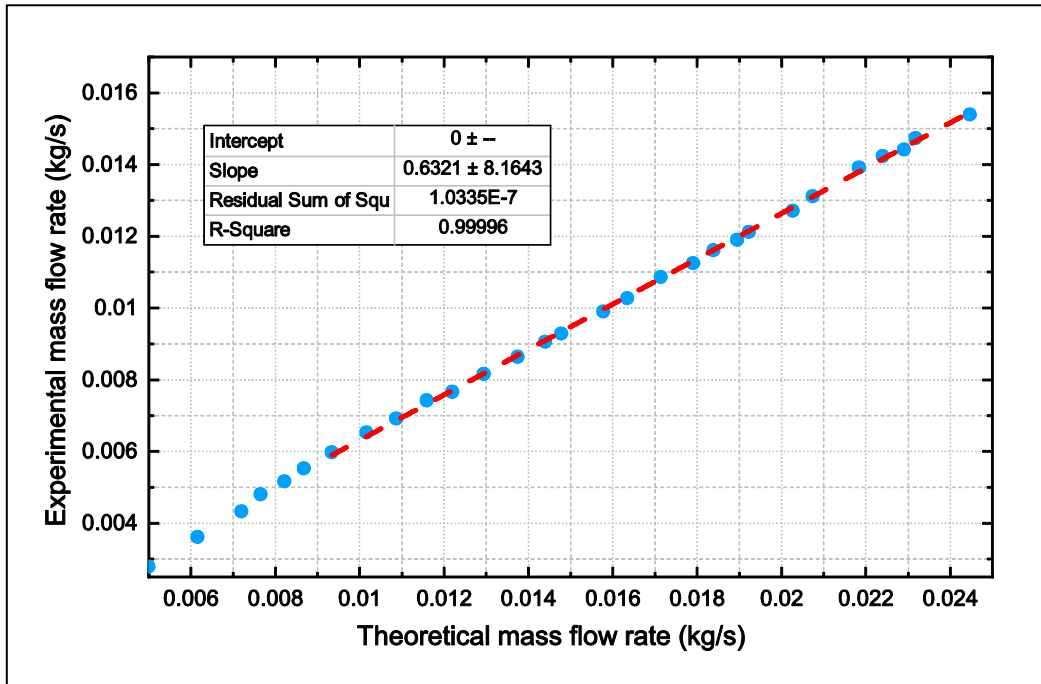
Figure 11.1 The orifice plate calibration data

	Calibration of Orifice plate					
Trial	Mass-flow reading (Kg/s)	Transducer reading (kPa)	Air pressure (kPa)	Air temperature (°C)	Density (Kg/ m³)	Discharge coefficient
1	0.00280	0.05	101.53	23.5	1.19	0.548
2	0.00362	0.07	101.57	23.5	1.19	0.589
3	0.00434	0.10	101.62	23.4	1.19	0.604
4	0.00481	0.11	101.65	23.8	1.19	0.630
5	0.00518	0.13	101.68	23.6	1.19	0.631
6	0.00554	0.14	101.71	23	1.20	0.638
7	0.00599	0.16	101.75	23.6	1.19	0.641
8	0.00628	0.18	101.78	23.7	1.19	0.643
9	0.00654	0.19	101.80	23.7	1.19	0.644
10	0.00678	0.21	101.83	23.6	1.20	0.643
11	0.00692	0.22	101.84	23.8	1.19	0.637
12	0.00716	0.24	101.87	23.6	1.20	0.640
13	0.00743	0.25	101.90	23.5	1.20	0.642
14	0.00767	0.28	101.93	23.5	1.20	0.629
15	0.00817	0.31	101.99	23.3	1.20	0.631
16	0.00865	0.35	102.05	23.6	1.20	0.630
17	0.00907	0.39	102.10	23.3	1.20	0.630
18	0.00930	0.41	102.14	23.2	1.20	0.629
19	0.00991	0.47	102.23	23.1	1.20	0.628
20	0.01028	0.50	102.29	23.3	1.20	0.629
21	0.01087	0.55	102.38	23.2	1.20	0.634
22	0.01125	0.60	102.45	23.4	1.20	0.629
23	0.01161	0.63	102.51	23.2	1.21	0.632
24	0.01190	0.67	102.56	23	1.21	0.628

25	0.01212	0.69	102.60	23	1.21	0.630
26	0.01272	0.77	102.72	23.1	1.21	0.627
27	0.01312	0.80	102.80	22.8	1.21	0.632
28	0.01392	0.89	102.96	22.9	1.21	0.637
29	0.01425	0.93	103.03	22.6	1.21	0.635
30	0.01442	0.97	103.07	23.8	1.21	0.630

Appendix 3: Thermal testing procedure

Once the pressure test was finished, both the sample and the test section were moved to the thermal apparatus, as shown in Figure 12.1. The PID controller was then adjusted to approximately 55°C, and the airflow was sucked at a high flow rate to warm up the system to minimize the heat loss from the hot air. The system needed to be left for about 20 to 30 minutes to warm up and reach the maximum inlet air temperature possible at the test section entrance. In this operation, the three-way valve was adjusted, allowing the hot air to flow through the detour section. Once the warming operation had finished, the three-way valve was switched toward the test section. This was essential: firstly, to adjust the flow rate to a desirable value by tuning the speed of the fans using the Variac; and secondly, to adjust the dummy valve in Figure 5.11.8 so it created similar flow resistance to that of the specimen to avoid a sudden flow reduction across the orifice plate.
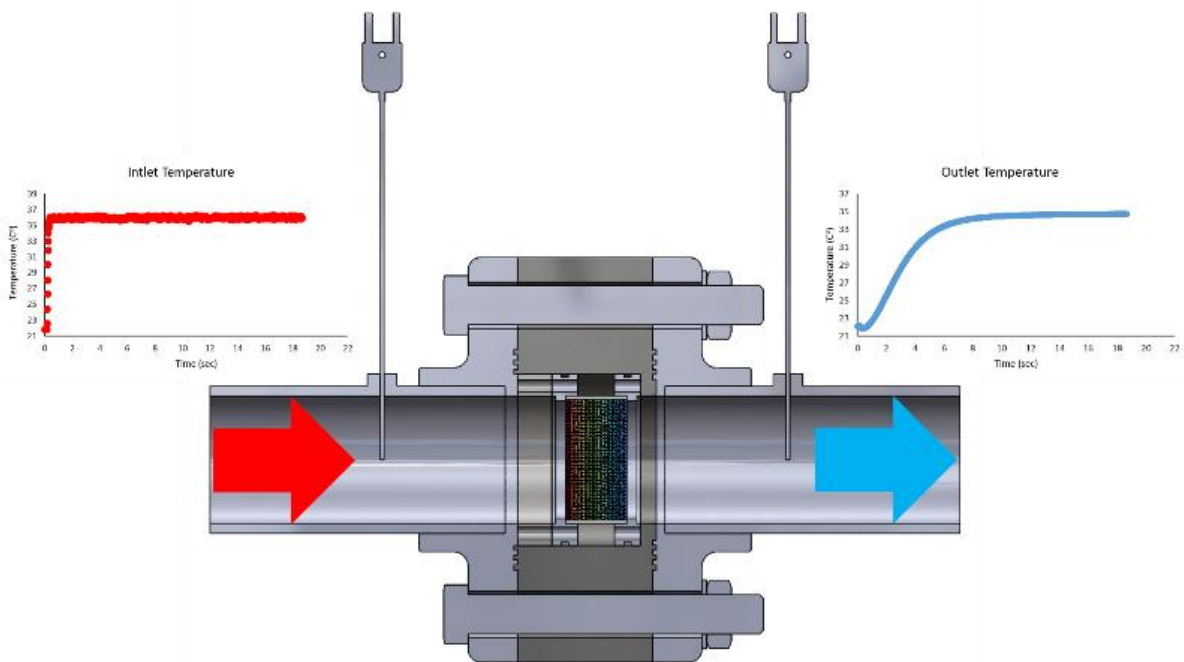
Figure 12.1 The sample inserted in a test section.

The adjustment operation caused an increase in the temperature of the specimen and the test section. As a result, the cooling operation occurred by allowing the cooled air through the system and achieving the lowest temperature possible in

the test section. The reduction of the temperature difference could be observed through an indicator built on the IV. Once the temperature difference had reached zero, the cooling line was switched off, and the three-way valve redirected the hot air towards the test section. It is always beneficial to start logging data before redirecting the three-way valve. This can help record the initial temperature in the test system and calculate at what time precisely the valve was opened. The data was recorded until the outlet fluid temperature showed no change with time, which usually takes less than 40 seconds. Finally, the Variac was adjusted to the next flow rate, and the process was repeated for six different flow rates.

Appendix 4: Calibration certificates

Omega Engineering, Inc.
Calibration Data Sheet
Certification Number: 171393

Sales Order Number:	SO337509
Serial Number:	156136
Model Number:	FMA-1613A-I
Software Version:	6v21.0-R22
Process Gas:	Selectable
Calibration Gas:	Air
Range:	1000 SLPM
Gas Temperature:	26.85°C
Ambient Humidity:	38.96%
Calibration Procedure/Rev. #:	DOC-AUTOCAL-GASFLOW/Rev. 92
Calibrated By:	Elyse Dobrydney
Calibration Date:	24-Aug-2017
Full Scale Pressure:	160.00 PSIA
Pressure Accuracy:	+/-0.5% of Full Scale
Temperature Accuracy:	+/-1.5°C
Standard Temp. & Pressure:	25.00°C, 14.69595 PSIA
Normal Temp. & Pressure:	0.00°C, 14.69595 PSIA
Calibration due 1 yr. after receipt:	

Equipment Used
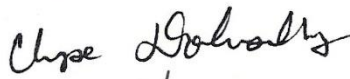
Flow:	TOOL-MOLBOX2	Pressure:	TOOL-PRESSURE8
Tool Due Date:	09-Feb-2018	Tool Due Date:	09-Mar-2018
Manufacturer/Model:	DH Instruments / Molbox 1 A700K-A	Manufacturer/Model:	010600 / P-100PSIG-D
Device Uncertainty:	NA \ Determined by Molbloc	Device Uncertainty:	+/- 0.2% of full scale
		Temperature:	TOOL-TEMP15
Flow:	TOOL-MOLBLOC7	Tool Due Date:	05-Oct-2017
Tool Due Date:	12-Oct-2018	Manufacturer/Model:	ASL / F200-A-2+Probe
Manufacturer/Model:	DH Instruments / 1E4-S	Device Uncertainty:	+/- 0.02°C
Device Uncertainty:	+/- 0.2% of reading		

Voltage:	TOOL-CMTR25
Tool Due Date:	19-Jun-2018
Manufacturer/Model:	Fluke / 87V
Device Uncertainty:	+/- (0.1% + 1 digit)

All test equipment used for calibration is NIST traceable.

Calibration

Uncertainty: +/- (0.8% of Reading + 0.2% of Full Scale)   Calibration Pressure: N/A
Units of measure: SLPM

Output 1 Configuration	Output 2 Configuration	Output 3 Configuration
mini-DIN Pin #1	mini-DIN Pin #2	mini-DIN Pin #6

D.U.T.	Actual	In Tolerance	Output 1	Output 2	Output 3
0	0	Yes	4.00 mA	5.12 Vdc	0.000 Vdc
251	250	Yes	8.02 mA	5.12 Vdc	1.255 Vdc
502	501	Yes	12.03 mA	5.12 Vdc	2.510 Vdc
750	750	Yes	16.00 mA	5.12 Vdc	3.750 Vdc
1001	1001	Yes	20.02 mA	5.12 Vdc	5.00 Vdc

Tech Signature:

QC Signature:

CS1 Rev 17 Last Modified 15-May-2017

This meter or controller is tested to and meets published specifications. After final calibration our products are stored in a controlled stock room and considered to be in bonded storage. Depending on environment and severity of use factory calibration is recommended every one to three years after initial purchase date.

Roxspur Measurement & Control Ltd.

Calibration Data Sheet

Certification Number: 123105

Sales Order Number:	SO324419
Serial Number:	119534
Model Number:	FFLM0035
Software Version:	5v11.0-R22
Process Gas:	Selectable
Calibration Gas:	Air
Range:	50.00 SLPM
Gas Temperature:	23.2°C
Ambient Humidity:	51%
Calibration Procedure/Rev. #:	DOC-AUTOCAL-GASFLOW/Rev. 87
Calibrated By:	Brian Wong
Calibration Date:	7/29/2015
Full Scale Pressure:	160.00 PSIA
Full Scale Pressure Accuracy:	+/-0.5% of Full Scale
Temperature Accuracy:	+/-1.5°C
Standard Temp. & Pressure:	25°C, 14.6959 PSIA
Calibration due 1 yr. after receipt:	

Equipment Used

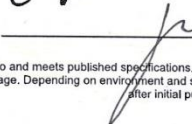|				
Voltage:	TOOL-CMTR12		Temperature:	TOOL-TEMP18
Tool Due Date:	7/1/2016		Tool Due Date:	6/14/2016
Manufacturer/Model:	Fluke / 87V		Manufacturer/Model:	SELCO
Device Uncertainty:	+/- (0.1% + 1 digit)		Device Uncertainty:	+/- 0.75°C
Flow:	TOOL-FLOW24		Pressure:	TOOL-PRESSURE8
Tool Due Date:	9/9/2015		Tool Due Date:	3/9/2016
Manufacturer/Model:	Alicat		Manufacturer/Model:	Alicat / P-100PSIG-D
Device Uncertainty:	+/- (0.3% Reading + 0.2% F.S.)		Device Uncertainty:	+/- 0.2% of full scale

All test equipment used for calibration is NIST traceable.

Calibration

Uncertainty: +/- (0.8% of Reading + 0.2% of Full Scale)   Calibration Pressure: N/A
Units of measure: SLPM

Output 1 Configuration mini-DIN Pin #6			Output 2 Configuration mini-DIN Pin #2	
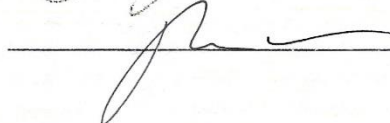
D.U.T.	Actual	In Tolerance	Output 1	Output 2
0.00	0.00	Yes	0.000 Vdc	5.12 Vdc
12.47	12.48	Yes	1.247 Vdc	5.12 Vdc
25.02	25.01	Yes	2.502 Vdc	5.12 Vdc
37.61	37.53	Yes	3.760 Vdc	5.12 Vdc
50.15	50.06	Yes	5.02 Vdc	5.12 Vdc

Tech Signature:

QC Signature:

CS1 Rev 16 Last Modified 01/18/2013

O M E G A   E N G I N E E R I N G   I N C.

PRESSURE TRANSDUCER
FINAL CALIBRATION

0.00 -   1.00 PSID
Excitation   24.000 Vdc

Job: WHS0011883	Serial: 469316
Model: PX409-001DDU10V	Tested By: JP
Date: 1/4/2017	Temperature Range: 0 to 185 F
Calibrated: 0.00 - 1.00 PSID	Specfile: PX409V10<=1G

Pressure PSID	Unit Data Vdc
0.00	0.000
0.50	4.999
1.00	10.008
0.50	5.001
0.00	0.001

Balance	0.000	Vdc
Sensitivity	10.008	Vdc

ELECTRICAL LEAKAGE: PASS
PRESSURE CONNECTION/FITTING: 1/4-18 NPT Male
ELECTRICAL WIRING/CONNECTOR: Integral Cable 4-Cond
BLACK = - EXCITATION
WHITE = + OUTPUT
GREEN = N/C
RED   = + EXCITATION

This Calibration was performed using Instruments and Standards that are
traceable to the United States National Institute of Standards Technology.

S/N	Description	Range	Reference	Cal Cert
801	PPC3 2.2 PSIG AUTO	0 - 1.00 PSID	C-1952	C-1952
US37034809	HP 34970A	Unit Under Test	C-3002	C-3002

Q.A. Representative : *John Piendl*   Date: 1/4/2017

This transducer is tested to & meets published specifications. After final
calibration our products are stored in a controlled stock room & considered in
bonded storage. Depending on environment & severity of use factory calibration
is recommended every one to three years after initial service installation date.

Omega Engineering Inc., One Omega Drive, Stamford, CT 06907
http://www.omega.com   email: info@omega.com   phone (800) 826-6342